Design, modeling, fabrication and characterization of a micro-device for the study of alternating flow - Application to energy harvesting and conversion

Jean Kovchar

THESE DE DOCTORAT DE L'ETABLISSEMENT UNIVERSITE BOURGOGNE FRANCHE-COMTE

PREPAREE A L'UNIVERSITE DE FRANCHE-COMTE

Ecole Doctorale n ° 37

Ecole Doctorale SPIM

Doctorat de Sciences pour l'ingénieur

Par

M. Jean KOVCHAR

Design, modeling, fabrication and characterization of a micro-device for the study of alternating flow - Application to energy harvesting and conversion

---

Design, modélisation, fabrication et caractérisation d'un micro dispositif pour l'étude des écoulements alternés - Application à la récupération et la conversion d'énergie

Thèse présentée et soutenue à Besançon, le 15/03/2024.

Composition du Jury :

Mr MARANZANA Gaël	Professeur des Universités, Université de Lorraine, LEMTA	Président
Mr BASROUR Skandar	Professeur des Universités, Université Grenoble Alpes, TIMA	Rapporteur
Mr COLIN Stéphane	Professeur des Universités, Université de Toulouse, ICA	Rapporteur
Mr DE LABACHELERIE Michel	Directeur de Recherche CNRS, FEMTO-ST	Directeur de thèse
Mme BARTHES Magali	Maître de conférences, Université de Franche-Comté, FEMTO-ST	Co-directrice de thèse
Mr LANZETTA François	Professeur des Universités, Université de Franche-Comté, FEMTO-ST	Co-directeur de thèse

Table of contents

NOMENCLATURE

Roman letters

$\bar{U}$	Time average velocity	(m s^{-1})
$\dot{m}$	Mass flow rate	(kg s^{-1})
$\dot{V}$	Flow rate	(m^3 s^{-1})
$\dot{V}$	Flow rate	(m^3 s^{-1})
A	Cross-section	(m^2)
a	Temperature coefficient	(K^{-1})
A_B	Bonding area	(m^2)
A_R	Dimensionless displacement	
c	Speed of sound	(m s^{-1})
C_f	Friction factor	
C_P	Specific heat capacity	(J kg^{-1} K^{-1})
c_{piston}	Piston stroke	(m)
D	Diameter	(m)
D_h	Hydraulic diameter	(m)
D_m	Bending swiftness	(kg m^2 s^{-2})
D_{cf}	Constricted flow diameter	(m)
E	Young's modulus	(Pa)
e	Thickness	(m)
e_b	Elongation at break	
e_M	Thickness of membrane	(m)
E_P	Signal acquired for pressure measurements	(V)
E_Q	Signal acquired for flow rate measurements	(V)
E_{piston}	Signal acquired for the detection of piston displacement measurement	(V)
E_{UV}	Dose of exposure	(J m^{-2})
F	Load force	(N)
f	Frequency	(Hz)
f_c	Cutting frequency	(Hz)
f_s	Sample rate	(Hz)
H	Full width at half maximum	
h	Height	(m)
I	Current	(A)
k	Thermal conductivity	(W m^{-1} K^{-1})
L	Length	(m)
L_e	Entrance length	(m)
M	Molar mass	(kg mol^{-1})
P	Pressure	(Pa)

P_{UV}	Power of the UV lamp	(W m^{-2})
r	radial position	(m)
R_G	Gas constant	(J mol^{-1} K^{-1})
r_G	Specific gas constant	(J kg^{-1} K^{-1})
R_h	Hydraulic radius	(m)
r_M	Radius of membrane	(m)
R_{elec}	Electrical resistance	(Ω)
S	Seebeck coefficient	(V K^{-1})
s	Etching selectivity	
T	Temperature	(K)
t	Time	(s)
t_c	Crystallite size	(m)
U	Velocity	(m s^{-1})
U_{max}	Maximum velocity	(m s^{-1})
V	Volume	(m^3)
V_{DC}	Voltage	(V)
v_{PR}	Etching rate of photoresist	(m s^{-1})
v_{Si}	Etching rate of Silicon	(m s^{-1})
V_{swept}	Volume swept by the piston	(m^3)
w	Width	(m)
w_M	Deflection of membrane	(m)
X	Fluid displacement	(m)
X_{max}	Fluid displacement	(m)

Dimensionless number

De	Dean number
Ec	Eckert number
Kn	Knudsen number
Ma	Mach number
Pr	Prandtl number
Re	Reynolds number
Re_c	Critical Reynolds number for transition laminar-turbulent regime
Re_ω	Frequency Reynolds number
Re_{max}	Reynolds number based on maximum velocity
Va	Valensi number
Wo	Womersley number

Greek letters

α	Aspect ratio	
β	Convergence / Divergence angle	(rad)
$\Delta\theta$	Phase lag	(°)
ΔT	Temperature difference	(K)
ΔP	Pressure difference	(Pa)
γ	Heat capacity ratio	
λ	Wavelength	(m)
λ_f	Mean free path	(m)
μ	Dynamic viscosity	(Pa s)
ν	Kinematic viscosity	(m^2 s^{-1})
ν_p	Poisson's ratio	
ω	Angular frequency	(rad s^{-1})
Φ	Viscous dissipation	(W m^3)
Π	Wet perimeter	(m)

ρ	Density	(kg m^{-3})
ρ_{elec}	Electrical resistivity	(Ω m)
σ	Residual stress	(Pa)
σ_B	bonding strength	(Pa)
σ_y	Yield strength	(Pa)
τ	Time constant	(s)
τ_w	Shear stress	(Pa)
Θ	Diffraction angle	(rad)
θ	Crank angle	(rad)
ε	Roughness	(m)
ε_r	Relative roughness	(m)
ζ	Coefficient of minor losses	

Operator

$\mid y \mid$	Module of complex number
∇	Nabla
∂	Partial derivative
FFT	Fast Fourier Transform
i	Complex number
J	Bessel function

Subscript

ch	Channel
comp	Compressible
elec	Electrical
exp	Experimental
in	Inlet
incomp	Incompressible
num	Numerical
osc	Oscillating flow
out	Outlet
std	Steady flow
th	Theoretical

RÉSUMÉ

La chaleur perdue inexploitée est devenue l'un des principaux enjeux de la récupération d'énergie au cours des dernières années. Selon un rapport publié en 2017 par l'Agence de l'environnement et de la maîtrise de l'énergie (ADEME) en France, la chaleur perdue issue des procédés énergétiques industriels (à des températures inférieures à 100 $°C$) représentait 36% de la consommation d'énergie industrielle, soit 117,9 TWh d'énergie non encore exploitée chaque année sous forme de déchets gazeux, liquides et diffus. En 2020, cette chaleur perdue ne représentait plus que 16% de la consommation d'énergie industrielle, soit 51 TWh. Bien que certains de ces rejets de chaleur aient été partiellement exploités en 2020, la quantité totale de chaleur perdue non exploitée s'élevait encore à 99,6 TWh, soit une réduction de 15,5%. Ces chiffres soulignent la nécessité de poursuivre les efforts pour augmenter la récupération de cette source d'énergie inexploitée et encouragent la conception de systèmes permettant son exploitation.

Des systèmes innovants de récupération et de conversion d'énergie à basse température (< 200 $°C$) ont été conçus et développés [1], [2], [3], [4]. Cependant, ces systèmes macroscopiques sont souvent trop volumineux, ce qui les rend difficiles à mettre en œuvre dans les systèmes industriels. Ils présentent également une proportion élevée de volume mort.
C'est dans ce cadre que s'est inscrit le projet MISITC, résultant de la collaboration entre l'université de Sherbrook (Canada), l'Université Grenoble-Alpes et l'Université de Franche-Comté, visant à concevoir un système de récupération d'énergie miniature afin de valoriser au mieux cette source d'énergie par l'intermédiaire de plusieurs machines placées en série. Cette machine repose sur le principe du cycle thermodynamique de Stirling et a fait l'objet de précédentes études. On peut notamment citer les travaux de thèse de Dellali [5] ayant contribué à la caractérisation d'un régénérateur miniature réalisé par des procédés de microfabrication, élément essentiel optimisant l'efficacité des machines Stirling puisqu'il permet de stocker la chaleur du fluide au cours du temps avant de le restituer. Les travaux de thèse de Diallo [6] ont permis de concevoir un prototype de machine miniature également réalisé par des procédés de microfabrication. Lors de la miniaturisation de ces machines, des défis technologiques se posent car les frottements (des pistons sur les parois, de l'écoulement des fluides au sein des volumes) deviennent prédominants et affectent l'efficacité de la machine. Afin de minimiser les frottements des pistons, ces derniers ont été remplacés par des membranes hybrides composées d'un élastomère et de silicium. Cette machine miniature a pu être testée dans des conditions proches du fonctionnement d'une machine Stirling en actionnant une des membranes par un système d'électro-aimant permettant un déplacement oscillant de la membrane générant ainsi un écoulement alterné de gaz se transmettant à d'autres membranes situées dans d'autres chambres. Néanmoins, on a pu observer une grande diminution de l'énergie transmise par la membrane actionnée vers les autres membranes suggérant que des pertes importantes d'énergie du fluide se produisaientt dans les canaux reliant les différentes chambres entre elles. Le manque d'information sur

les écoulements alternés de gaz au sein de conduites aux dimensions milli- et sub-millimétriques n'ont pas permis de confirmer si ces pertes d'énergie étaient attendues. En revanche, une estimation de ces pertes d'énergie a été effectuée en supposant un écoulement incompressible de gaz et utilisant les valeurs théoriques attendues à échelle macroscopique. La comparaison de ces estimations avec les pertes d'énergie observées a montré que les pertes d'énergie obtenues expérimentalement étaient jusqu'à 50 fois plus importantes que celles prévues par la théorie. Ceci pouvait être attribué aux faibles dimensions des conduites concernées, à la rugosité des parois dont l'influence est sensiblement plus importante dans des canaux de faibles dimensions. La compressibilité du fluide pouvait également être un élément pouvant être remis en cause dans nos estimations expliquant les écarts obtenus. Le dernier élément, pouvant expliquer les observations, concerne la présence de coudes dans le design des canaux de la machine miniature réalisée dûs à des limitations en termes de microfabrication et des procédés utilisés pour la conception de la machine.

Ces travaux de thèse portent donc sur l'étude des écoulements alternés dans des canaux de dimensions milli- et sub-millimétrique afin d'apporter une meilleure connaissance des phénomènes thermo-fluidiques mis en jeu à ces échelles. Ce manuscrit s'articule autour de 4 chapitres.

Le chapitre 1 présente un état de l'art des écoulements permanents et oscillants au sein de canaux de dimensions allant de l'échelle macroscopique à l'échelle microscopique. Cela nous a permis d'obtenir une vision globale de l'influence de certains paramètres qui a servi par la suite pour la conception des canaux.

Une première partie du chapitre est dédiée à la présentation des principales grandeurs caractérisant un écoulement de fluide ainsi que les équations qui décrivent son comportement mécanique (frottements visqueux) et thermique dans le temps et l'espace. Cette partie présente également les nombres adimensionnels couramment utilisés pour la caractérisation des écoulements.

- Le nombre de Reynolds Re : il traduit le rapport entre les forces d'inertie et les forces de viscosité du fluide en écoulement. Il permet de classifier l'écoulement selon plusieurs régimes en fonction de la valeur de ce nombre allant d'un régime laminaire dans lequel les forces de viscosité sont prépondérantes devant les termes inertiels jusqu'au régime turbulent dans lequel les forces visqueuses sont cette fois-ci négligeables devant la contribution des forces inertielles.
- Le nombre de Mach Ma : il est défini par le rapport entre la vitesse de l'écoulement et la vitesse locale du son dans le milieu. Il caractérise la contribution de la compressibilité du fluide sur l'écoulement considéré.
- Le coefficient de frottement C_f: il caractérise le frottement fluide et donc la perte d'énergie par frottement.

Par la suite, nous nous sommes focalisés plus particulièrement sur les écoulements dans des conduites de faibles dimensions ($< 1\ mm$) afin de faire le lien avec les canaux présents dans le design de la machine de récupération d'énergie miniature. Lorsque les dimensions des canaux diminuent, le libre parcours moyen du gaz devient de moins en moins négligeable par rapport aux dimensions caractéristiques de l'écoulement. Ceci a pour conséquence de changer considérablement le comportement du fluide, on parle alors d'écoulement raréfié. On peut classifier l'écoulement selon son degré de raréfaction en fonction de la valeur du nombre adimensionnel de Knudsen Kn, défini par le rapport entre le libre parcours moyen des molécules de gaz et la dimension caractéristique du canal. Les différents régimes de raréfaction vont d'un écoulement continu ($Kn < 10^{-3}$) pour lequel les effets

de raréfaction de l'écoulement peuvent être négligés et pour lequel les équations de Navier-Stokes permettent de décrire l'écoulement sans ajouter de condition supplémentaire, jusqu'à un écoulement moléculaire libre ($Kn > 10$). Entre ces deux régimes se trouvent un régime transitoire dans lequel des contributions de la raréfaction se distinguent au travers d'une vitesse de glissement et un saut de température à la paroi. La conception des canaux d'étude a été faite de sorte que l'on puisse considérer les effets de raréfactions comme étant négligeables ($Kn < 10^{-3}$).

L'état de l'art, concernant les écoulements permanents dans des canaux aux dimensions submillimétriques jusqu'à des canaux de dimensions micrométriques, a permis de mettre en évidence l'influence de certains paramètres. On observe ainsi une plus grande influence de la rugosité des parois puisque pour des rugosités relatives inférieures à celles pour lesquelles la contribution de la rugosité peut encore être négligée à échelle macroscopique, des écarts avec la théorie ont pu être relevés par certaines études. De la même manière, la contribution de la compressibilité du fluide semble apparaître pour de plus faibles valeurs du nombre de Mach. Enfin, l'influence du rapport d'aspect α du canal (rapport entre la hauteur et la largeur du canal) a également pu être mis en évidence.

La troisième partie du chapitre concerne les écoulements oscillants à échelle macroscopique ainsi que les quelques résultats d'études menées à échelles milli- et microscopiques. Ces écoulements se distinguent des écoulements continus (sans oscillation) par la variation des grandeurs caractéristiques telles que la vitesse, la pression et la température, mais aussi par la variation temporelle des propriétés du fluide (masse volumique notamment). Par conséquent, les nombres adimensionnels utilisés dans le cas d'écoulements permanents ne sont plus adaptés pour caractériser ce type d'écoulement. De plus, les écoulements qui nous intéressent sont des écoulements alternés caractérisés par une vitesse moyenne au cours du temps nulle, dû à l'alternance de sens dans lequel le fluide circule. Par conséquent, les études menées sur ces écoulements ont permis de définir divers nombres adimensionnels qui servent à caractériser ces écoulements instationnaires. On peut citer, le nombre de Reynolds fréquentiel Re_ω similaire au nombre de Reynolds Re en remplaçant la vitesse de l'écoulement par le produit de la pulsation des oscillations de l'écoulement et du diamètre hydraulique. Le nombre de Womersley Wo est également utilisé : il est égal à la racine carrée du nombre de Reynolds fréquentiel tout en remplaçant le diamètre hydraulique par le rayon hydraulique. Ce nombre de Womersley est également lié au nombre de Valensi Va dont seule la longueur caractéristique de l'écoulement change puisque le nombre de Valensi utilise le diamètre hydraulique tandis que le nombre de Womersley utilise le rayon hydraulique. D'autres études utilisent un nombre de Reynolds qui est défini avec la vitesse moyenne ou maximale de l'écoulement au cours du temps au lieu de la vitesse instantanée.

Les diverses études conduites sur des écoulements oscillants ont permis de mettre en évidence la singularité du profil de vitesse lorsque l'instationarité de l'écoulement est importante, avec des profils de vitesse dont la vitesse maximale se situe, non pas au centre de la conduite, comme c'est "classiquement" le cas mais est délocalisée proche des bords de la conduite.
On peut également observer un déphasage entre la variation de vitesse de l'écoulement au cours du temps avec celle de la pression. Les grandeurs de l'écoulement variant au cours du temps, contrairement aux écoulements permanents continus, il est possible d'observer une transition entre écoulement laminaire et écoulement turbulent au cours d'une période de l'écoulement.
Enfin, le coefficient de frottement est également différent celui utilisé pour des écoulements permanents continus, puisqu'il doit également tenir compte d'un terme dépendant du temps.

Cet état de l'art a donc permis la conception de canaux permettant l'étude de plusieurs paramètres. Le dimensionnement des canaux a fait l'objet de la première partie du second chapitre.

Le deuxième chapitre présente le dimensionnement qui a été réalisé concernant les canaux qui sont envisagés pour l'étude en accord avec l'état de l'art réalisé au chapitre précédent. Ce dimensionnement concerne :

- La largeur et la hauteur du canal qui permettent de faire varier le diamètre hydraulique du canal ainsi que son rapport d'aspect $\alpha < 1$ (rapport entre la hauteur et la largeur du canal). Cela permettra donc de déterminer l'influence du diamètre hydraulique dans la gamme 100 μm à 1 *mm*, et pour un rapport d'aspect variant entre 0.1 et 1.
- La longueur du canal, qui a été déterminée en fonction de la longueur d'entrée du canal permettant d'avoir un écoulement établi (dépend de la gamme de nombre de Reynolds testée). De plus, deux longueurs différentes ont été envisagées afin de permettre une étude de l'influence de la longueur sur les caractéristiques de l'écoulement.
- L'ajout de coudes dans certains canaux afin de déterminer leur influence. Cet ajout doit respecter une longueur équivalente avec les canaux sans coudes afin de pouvoir être comparés.
- L'adaptation des sections de passage entre le canal et les tubes du dispositif expérimental afin de permettre un raccordement dont la contribution est aussi faible que possible sur les caractéristiques de l'écoulement.

Une deuxième partie de ce chapitre est consacrée à un état de l'art des capteurs de pression et de température communément utilisés dans la littérature pour des mesures dans des canaux aux dimensions sub-millimétriques. Cela permet dans un troisième temps, de dimensionner nos capteurs qui seront envisagés pour des mesures aussi proches que possible de l'entrée et de la sortie du canal. Concernant les mesures de pression, la méthode retenue consiste à mesurer la déflexion d'une membrane à l'aide d'un capteur optique chromatique confocal. Le dimensionnement de ce capteur repose sur : i) le diamètre de la membrane, ii) le matériau de la membrane que l'on souhaite le plus élastique possible afin d'obtenir des mesures sur une large gamme de pression, iii) son épaisseur limitée par les propriétés mécaniques du matériau choisi mais aussi par la précision du capteur optique. Pour les mesures de température, le type de capteur choisi consiste en une piste résistive de Platine, dont la résistance varie en fonction de la température mesurée. Ce choix a été motivé par la grande stabilité de ces capteurs. Ces capteurs consisteront donc en une couche mince de Platine déposée d'une épaisseur de 200 *nm* et permettant d'obtenir une résistance d'au moins 100 Ω.

Le troisième chapitre est séparé en deux grandes parties. La première partie se focalise sur la présentation des étapes des procédés utilisés pour la conception des canaux, tandis que la deuxième partie concerne la caractérisation des capteurs de température réalisés. Dans un premier temps, nous avons présenté les procédés de fabrication utilisés pour la conception des canaux instrumentés (avec capteurs de pression et de température intégrés aux dispositifs) et de canaux non instrumentés. Ces deux procédés ont été utilisés en parallèle afin d'obtenir des canaux pouvant être testés rapidement avec un procédé de fabrication simplifié. Ceci permet d'obtenir des résultats exploitables malgré la complexité du procédé de fabrication des canaux instrumentés. Les étapes successives de fabrication sont détaillées pour chaque procédé. Concernant le procédé de fabrication des canaux instrumentés, les parois latérales des canaux sont réalisées par gravure profonde sèche sur un substrat en silicium. Un procédé Bosch a été utilisé permettant d'obtenir des flancs bien verticaux. Ce substrat est ensuite

assemblé par soudure anodique avec un substrat en verre constituant la paroi supérieure du canal. Les capteurs de température sont constitués d'une couche de Platine d'une épaisseur de 200 nm déposée par pulvérisation sur un autre substrat de Silicium. Une couche d'accroche de Chrome d'une épaisseur de 20 nm améliore l'adhérence de la couche de Platine ainsi déposée. Les capteurs de pression consistent en une couche de PDMS de 20 μm déposée sur la totalité de la surface. En effet, cette couche de PDMS est également envisagée pour être utilisée afin de réaliser l'assemblage entre les deux substrats de Silicium. Des ouvertures sont nécessaires sur la face arrière des dispositifs afin d'avoir un accès optique permettant de mesurer la déflexion des membranes. Cette étape, également réalisée par gravure sèche profonde, s'est révélée infructueuse car les procédés de gravure étant fortement énergétiques, un refroidissement du substrat est nécessaire. Or, la couche de PDMS constituant une isolation thermique, le refroidissement du substrat n'a pas pu être effectué correctement. Une solution a été d'utiliser une couche d'aluminium pour réaliser les accès optiques avant de déposer le PDMS puis d'enlever cette couche d'aluminium au niveau des membranes. Par la suite, l'assemblage des deux substrats a pu être testé en utilisant la couche de PDMS. Ce collage s'est également révélé infructueux bien qu'ayant montré satisfaction pour des substrats non structurés. D'autre part, la conception des canaux non instrumentés a été effectuée avec un procédé simplifié : i) assemblage des deux substrats de silicium par thermocompression Au-Au (les couches d'or étant déposées préalablement par évaporation), ii) gravure profonde sèche des canaux, iii) assemblage par soudure anodique avec le substrat en verre. Les canaux ont ensuite été découpés et ont pu être utilisés sur le banc expérimental.

La deuxième partie du chapitre présente la caractérisation des capteurs de température réalisés. Pour améliorer la stabilité et la sensibilité de ces capteurs, un procédé de recuit a été utilisé. Cette caractérisation permet d'analyser l'influence des paramètres du recuit (température, temps) sur les propriétés électriques, mécaniques et structurelles des capteurs. Il en résulte que pour un recuit à 450 $°C$, les contraintes résiduelles dans la couche augmentent fortement, le coefficient de température du capteur diminue, réduisant donc sa sensibilité. En revanche, pour un recuit à 250 $°C$, on observe une augmentation du coefficient de température, qui s'accompagne d'une augmentation des contraintes résiduelles bien que moindre que celle obtenue pour le recuit à 450 $°C$, faisant de cette solution un bon compromis pour nos besoins.

Le dernier chapitre présente l'analyse des résultats expérimentaux obtenus. La première grande partie de ce chapitre est consacrée à l'étude de caractérisation des écoulements permanents. L'état de l'art sur les écoulements permanents au sein de microcanaux ayant mis en évidence des désaccords entre différents auteurs notamment concernant l'influence de la rugosité sur les caractéristiques de l'écoulement, cette première étude a permis de comparer ces résultats par rapport à ceux prédis par la théorie et ceux obtenus expérimentalement dans la littérature. L'écoulement permanent est généré à l'aide d'une bouteille d'azote sous pression dont le débit est mesuré et contrôlé avec un débitmètre massique thermique. Pour cette étude, les canaux testés comportent des canaux avec deux diamètres hydrauliques différents, deux longueurs de canal différentes ainsi que des canaux rectilignes et des canaux avec coudes. La gamme de débit testée correspond à des nombres de Reynolds variant de 10 à 510. Cela permet ainsi de générer des écoulements permanents en régime laminaire sur l'ensemble de la gamme de débit et sur l'ensemble des configurations de canaux testées. A partir des mesures de pression et de température, la masse volumique est calculée à l'aide de la loi des gaz parfaits pour chaque mesure réalisée permettant de constater également qu'au vu de sa faible variation de masse volumique, le fluide peut également être considéré comme étant incompressible dans la gamme de nombre de Reynolds de la présente étude. Les mesures réalisées sur les écoulements permanents

incluent les pertes de charge obtenues par différence entre la pression à l'entrée et celle à la sortie du canal ainsi que la différence de température entre l'entrée et la sortie du canal. Les pertes de charge obtenues expérimentalement ont été comparées avec les valeurs calculées par la théorie. Il en résulte un bon accord entre les valeurs expérimentales et les valeurs théoriques. De plus, une discrimination entre les pertes de charge dûes aux sections convergentes et divergentes par rapport à celles générées par frottement fluide le long du canal a permis de mettre en évidence, l'influence grandissante des pertes de charge dûes aux sections convergentes et divergentes situées de part et d'autre du canal. Ces pertes de charge singulières deviennent de même importance que celles dûes au canal seul, aux débits les plus élevés. A partir des mesures de pression et de la détermination du gradient de pression entre l'entrée et la sortie du canal ainsi que des mesures de débit, le coefficient de frottement a pu être calculé et représenté en fonction du nombre de Reynolds. La variation du coefficient de frottement en fonction du nombre de Reynolds montre un bon accord avec les résultats issus de la littérature. Les différences observées pouvant être dûes à des conditions opératoires et des géométries de canaux différentes dans la littérature par rapport à celles de notre étude. Les résultats obtenus en écoulement permanent ont donc permis de conforter un bon accord vis-à-vis de la théorie et servira de base de référence pour l'étude paramétrique menées dans le cas des écoulements alternés.

La deuxième partie de ce chapitre est consacrée à l'analyse et à la discussion des résultats obtenus pour des écoulements alternés de gaz. Cette étude est réalisée au sein des mêmes canaux que ceux testés en écoulement permanent avec deux canaux supplémentaires permettant l'étude de l'influence du rapport d'aspect, indépendamment de l'influence du diamètre hydraulique. Les écoulements alternés sont générés par les déplacements de deux pistons déphasés de 180° qui sont raccordés au système composé du canal et des sections convergentes et divergentes.

Les variations temporelles de pression et de température sont similaires à celles observées à échelle macroscopique dans le cas d'écoulements alternés. De la même manière, on observe un comportement similaire de ces écoulements alternés au sein de nos canaux d'étude et des canaux aux dimensions macroscopiques. Parmi ces similitudes de comportement, on peut notamment citer, l'augmentation de l'amplitude de variation de pression et de température au cours du temps lorsque la fréquence d'alternance de l'écoulement augmente. Ceci s'explique par l'augmentation des vitesses de fluide au sein du canal, générant plus de frottements fluides et donc plus de pertes de pression qui se caractérisent par une augmentation de température sous forme de dissipation visqueuse. Les observations ont également conduit à considérer un dédoublement de la fréquence du signal pour les canaux de plus grand diamètre hydraulique et pour les plus faibles fréquences testées. Ce phénomène a déjà été observé précédemment par différents auteurs au sein de canaux macroscopiques ainsi que de canaux aux dimensions millimétriques et est attribué par les auteurs par une prédominance des effets inertiels. D'autre part, le déphasage entre les signaux de pression et ceux de température pour un même côté du canal ont été représentés en fonction du nombre de Womersley *Wo*. On peut observer une augmentation du déphasage lorsque la fréquence de l'écoulement augmente. Ceci semble être attribué aux effets de compressibilité du fluide. Le rapport d'aspect semble également exercer une influence augmentant ce déphasage lorsque le rapport d'aspect diminue, expliqué par le changement de section de passage du fluide et donc de la vitesse de l'écoulement qui n'est pas pris en compte dans le nombre de Womersley. Dans un second temps, les pertes de charge ainsi que les différences de température ont été représentées pour l'ensemble des configurations testées en fonction de l'angle de rotation du moteur d'entraînement. Les mêmes observations que celles menées sur les signaux de pression et de température, ont pu être effectuées. Les valeurs moyennes des pertes de pression et de différences de température au cours d'une période ont ensuite été calculées puis représentées en

fonction du nombre de Womersley. Ces valeurs moyennes ont été calculées sur la base d'un ensemble d'une cinquantaine de périodes. On peut observer un comportement similaire pour les canaux de diamètres hydrauliques 500 µm et 200 µm, avec les pertes de pression qui semblent tendre vers une valeur constante lorsque la fréquence augmente. Cela a également été observé à l'aide d'un modèle analytique simplifié, permettant de supposer que ce phénomène pourrait être dû au fait que le canal se comporte comme s'il était bouché. Cela se répercute alors sur les différences de température obtenues puisque si le débit de fluide diminue alors les frottements fluides diminuent également provoquant une baisse de la température du fluide. Cela montre les limitations, en termes de fréquence, du fonctionnement d'une machine miniature de Stirling en fonction du diamètre des canaux. La dernière partie du chapitre présente l'influence des paramètres étudiés sur les caractéristiques de l'écoulement. Tout d'abord, l'influence du rapport d'aspect montre une augmentation considérable à la fois des chutes de pression et de la différence de température lorsque le rapport d'aspect diminue. Ce comportement est dû à l'augmentation de la vitesse du fluide causée par le changement de section de passage entre les deux configurations de canaux. Ensuite, l'influence de la présence de coudes au sein du canal est moindre que celle observée par l'influence du rapport d'aspect. Enfin, l'influence de la longueur du canal est assez faible par rapport à l'influence du rapport d'aspect.

De cette étude, il apparaît que l'influence du rapport d'aspect semble bien plus significative que celle dû à la longueur du canal et surtout celle dûe à la présence de coudes dans le canal, contrairement à ce que l'on pouvait s'attendre. Le rapport d'aspect constitue donc un premier élément important à bien prendre en compte dans le design de la machine miniature de Stirling.

Nous avons constaté que la perte de charge semble tendre vers une valeur constante lorsque la fréquence augmente. Cela est à mettre en relation avec les résultats obtenus analytiquement avec un modèle constituant une première approche du problème bien que limité par des hypothèses fortes telles que la compressibilité du fluide qui est négligée dans le modèle tandis qu'il a été montré que cette hypothèse ne peut pas s'appliquer dans le cas d'écoulements alternés au vu des nombres de Mach estimés et des variations temporelles et spatiales importantes de masse volumique du fluide. Les effets de compressibilité pourraient, entre autre, expliquer la légère augmentation des pertes de charge lorsque la fréquence de l'écoulement augmente, contrairement à ce qui est observé analytiquement. Néanmoins, ces résultats montrent que le canal se comporte comme un canal bouché pour des fréquences plus élevées et limitent donc le fonctionnement d'une machine miniature de Stirling uniquement à des fréquences maximales de l'ordre de la dizaine de Hz. Une étude plus approfondie pour des plus grandes fréquences permettrait de confirmer ce résultat. Cette limitation, en termes de fréquence maximale de l'écoulement, semble être grandement impactée par le diamètre hydraulique. Cela montre qu'un compromis doit être trouvé entre les dimensions des canaux constituant la machine miniature de Stirling et la fréquence de fonctionnement de celle-ci.

À la suite de ces travaux, l'étude paramétrique du transfert thermique en écoulement alterné permettra de caractériser le comportement de la machine Stirling miniature, notamment au regard des diamètres hydrauliques et des rapports d'aspect des canaux.

REMERCIEMENTS

Quelle aventure ! Cette thèse fut une épreuve ambitieuse et enrichissante dont on ne peut qu'apprécier le dénouement après avoir tant investi sur son accomplissement. Mais ce fut également un ascenseur émotionnel dont la fréquence d'oscillation des émotions devenait de plus en plus forte, une longue traversée remplie d'émotions contradictoires. D'un début de capitulation à la rencontre de chaque obstacle à la tenacité de chercher sans cesse un moyen de contourner ces problèmes, du désespoir après chaque échec avant de retrouver rapidement foi et optimisme, et enfin de la souffrance, du désespoir et de la crainte à mesure que l'ultime deadline approchait jusqu'à la joie incommensurable d'en avoir terminé avec cette dernière épreuve de rédaction du manuscrit. A de nombreuses reprises, j'ai douté de voir un jour une issue favorable à la fin de ce cycle. Gravir cette grande montagne afin de voir ce que me réserve l'horizon de l'autre côté ne fut pas une mince affaire, et je n'y serais sans doute jamais arrivé tout seul. C'est pourquoi je tiens à remercier tous ceux qui m'ont aidé à gravir étape par étape cette obstacle. Et bien que cette thèse et la rédaction de ce manuscrit furent également par moment aussi chaotiques que la turbulence d'un écoulement, aussi compliqués que les équations caractérisant un écoulement alternés de gaz et aussi longues que le sommeil qui m'attend à présent que cette thèse est terminée, ce n'est rien en comparaison avec la lourde tâche au moment de rédiger cette partie. En effet, j'ai du mal à trouver les mots afin de remercier convenablement toutes les personnes qui m'ont accompagné au cours de cette thèse et grâce à qui cette thèse a pu aboutir. Je remercie du fond du cœur tous ceux qui ont contribué à la réussite de cette thèse.

Je tiens tout d'abord à remercier M. **Gaël Maranzana** pour avoir accepté de présider mon jury de thèse, M. **Stéphane Colin** et M. **Skandar Basrour** pour avoir accepté d'être les rapporteurs de ce long manuscrit.

Vient ensuite mes encadrants de thèse que je tiens à remercier très chaleureusement. **Michel De Labachelerie**, mon directeur de thèse, pour avoir accepté de me confier les travaux de cette thèse et qui m'a dispensé ses nombreux et précieux conseils tout au long de cette thèse et dont les nombreuses idées ont permis d'explorer de nombreuses pistes. Ce fut un grand plaisir de travailler sous ta direction. Je remercie ensuite mon co-directeur de thèse, **François Lanzetta** pour la contribution qu'il a su m'apporter en tant qu'enseignant tout en me confortant sur le chemin qui m'a amené à cette thèse. Tu m'as apporté ton aide et m'a guidé à plusieurs reprises sur la partie expérimentale, lorsque c'était nécessaire. Et enfin un très grand merci à ma co-directrice de thèse, **Magali Barthès** qui m'a accompagné humainement et scientifiquement tout au long de cette thèse en plus de partager sa bonne humeur et la dose de sucre qu'il me fallait pour être à 1000% de mon efficacité. Tu as été le matelot qui aidé le capitaine inexpérimenté que j'étais à ne pas faire naufrage, et tu as réussi à m'orienter dans la bonne direction malgré ma réticence parfois à suivre tes bons conseils... Ce long périple n'aurait

pas été possible sans ton soutien, tu as su me remotiver et me rassurer plus d'une fois mais aussi me mettre la pression lorsque c'était nécessaire.

Un grand merci à vous, J'ai apprécié ce long périple à vos côtés, je n'ai jamais abandonné et j'ai toujours continué à aller de l'avant grâce à vous. Ce fut une expérience enrichissante, pas toujours facile, mais dont j'en ressors grandit. Je vous remercie également de votre patience et de m'avoir aidé à voir la lumière au bout de ce long tunnel.

Je tiens ensuite à remercier très chaleureusement l'ensemble du personnel de la salle blanche pour leurs aide et contribution ainsi que leurs précieux conseils qui ont fortement contribué à la réussite de la fabrication des dispositifs. Qu'ils trouvent en ces mots ma profonde reconnaissance pour leur collaboration, en dépit de procédés parfois ambitieux et parfois également loin des procédés standards utilisés en salle blanche. Je remercie en particulier **Sylwester Bargiel**, **Djaffar Belharet**, **Samuel Queste**, **Laurent Robert**, **Stefania Oliveri**, **Lilian Arapan**, **Marina Raschetti**, **Guillaume Jutzi**, et **Marion Vieira**. Je remercie également **Alpha Diallo** qui m'a aidé à débuter dans l'univers de la salle blanche, et qui m'a montré des nombreuses astuces. Tout autant de remerciements à l'égard de **Rabah Zeggari**, **Florent Bassignot**, **Valérie Soumann** pour leurs précieux conseils.

Je suis également très reconnaissant envers **Thérèse Leblois** qui a su être une très bonne directrice de l'école doctorale et humainement à l'écoute de mes problèmes. Je te remercie également pour tes encouragements, tes conseils et pour avoir sauvé cette thèse lorsque le dénouement final approchait et qu'aveuglé par la rédaction, je me suis retrouvé en retard sur les démarches administratives de réinscription et pour le comité de suivi de thèse. Tu m'as permis d'arriver au bout de cette thèse et je t'en remercie sincèrement.

J'éprouve une profonde gratitude pour **Sandrine Chatrenet** qui m'a dépêtré plus d'une fois de désagréments mais m'a aidé à de nombreuses reprises à faciliter mes démarches administratives sur l'aspect financier de la thèse. Des remerciements également pour **Axelle Rabbe**, **Jocelyne**, **Ayoko**, **Marilyne Draps** qui ont facilité toutes mes requêtes administratives dans la bonne humeur malgré le fait qu'elles étaient overbookées. Une pensée vient ensuite à **Mireille Shwarz** et **Isabelle Christen**, pour toute la bonne humeur qu'elles ont su me partager, c'est toujours plus motivant de travailler lorsqu'une personne souriante et plein de gentillesse nous accueille à notre arrivée dés le matin.

Je remercie également **Vincent Tissot**, **Emmanuel Dordor**, **Laurent Callegari**, **Bernard Rothlisberger** pour leurs contributions sur la conception et la fabrication du banc expérimental. Je remercie également **Olivier Gaiffe**, **Franck Chollet**, **Vincent Humblot** et **Saber Hammami** pour leurs aides et précieux conseils. Je n'oublie pas **Virginie Moutarlier** qui a accepté de réaliser les mesures par DRX et SDL sur mes échantillons afin de pouvoir les caractériser, je tiens à te remercier pour ton aide.

Un grand merci également à **Jean-Marc Cote**. Pour tout le temps que tu as accepté de consacrer à m'aider à résoudre les nombreux problèmes rencontrés tout au long de la thèse. Tu m'a permis d'avancer en toute sérénité malgré les obstacles. Je te remercie également pour tes nombreux conseils et ta gentillesse.

Un grand merci à tout mes collègues du département chimie de l'IUT avec qui j'ai passé de bons moments et qui m'ont assisté pour mes débuts dans le domaine de l'enseignement. Je me suis toujours senti à l'aise dans ces locaux grâce à vous. Je remercie tout d'abord chaleureusement **Audrey Mandroyan** qui a accepté de me confier des heures d'enseignements au sein du département Chimie.

Je remercie ensuite **Nicolas Fatin-Rouge**, **Remy Viennet**, **Philippe Godani**, pour m'avoir accompagné pour mes débuts et qui m'ont montré leur petites astuces et conseils, **Catherine Sourlier** , pour sa bonne humeur communicative et avec qui j'ai pris plaisir de discuter, et également **Laurent Chanez** qui n'est pas sans reste non plus lorsqu'il s'agit de transmettre sa bonne humeur à travers tout l'établissement, sans oublier **Marielle Remery** grâce à qui j'ai pu enseigner ces travaux pratiques en toute sérénité.
Je n'oublie pas non plus **Coraline Lapre** qui a effectué les mêmes enseignements tout en partageant la même condition de doctorante et avec qui j'ai passé de bons moments.

Je remercie ensuite tous ceux avec qui j'ai partagé de bons moments : **Jean-Loup Skora**, **Fernando Ramirez** mes voisins qui ont su égayer le bureau avant de finalement quitter le navire à la fin de leur thèse respective, **Claude Humbert**, **Emmanuel Attal**, avec qui j'ai pu partager nombre de conversation autour de pause café qui souvent se prolongeait bien au-delà de la pause midi. **Sylvain Midrouet**, **Florian Jouy** et **Louis Guyon de Montlivaut** avec qui j'ai partagé de nombreux repas et conversations intéressantes, **Himanshi Kharkwal** dont je souhaite à présent lui donner courage et réussite pour son doctorat, je n'oublie pas les autres personnes avec qui j'ai passé de bons moments mais dont les passages au sein du labo étaient trop brefs : **Paresh Mahashptra**, **Victoria Duval**, **Marvin Tresse** et **Guillaume Ozout**. Merci à vous tous pour ces bons moments qui m'ont permis d'échapper pendant de rares mais plaisants moments à la morosité ambiante. Merci également à **Martin Quintanilla**, **Fatima El Mankibi**, **Julien Petitgirard** et **Theo Kziazyk** pour ces bons moments passés avec vous au cours de mes brefs voyages sur le site de Belfort lors de ma campagne de mesure expérimentale. Merci aux stagiaires **Marouane Yakob** qui a aidé au développement d'un programme permettant le filtrage des signaux et à **Abdelhamid Blidia** dont, malheureusement, les travaux numériques n'ont pu être comparés en raison de modifications dans le design final des canaux.

Des remerciements viennent ensuite aux compositeurs Borislav Slavov, dont les travaux musicaux m'ont accompagné tout au long de la rédaction de ce manuscrit. Cette symphonie mélodieuse, me rappelant aux bonnes heures de la Compagnie de Smaughetto, fut un refuge me permettant de continuer à avancer malgré la difficulté de la rédaction de ce manuscrit.

Comment ne pas remercier mes amis, avec qui je regrette de n'avoir pu passer plus de temps en cette fin de thèse pour des raisons évidentes. Merci à «**Douh8** »et le «**gitan** »pour ces soirées Yu-gi-oh! en compagnie de **DD**, ce fut de bons moments passés, même s'il y en a un qui n'est pas assez réactif et un autre qui l'est trop ... Remercions également les autres compagnons de soirée loin de tous les affres de cette thèse, **GG**, «**Chaos Max**», **Guigui**, «**Robinho**»ou «**Robinet**»on ne sait plus trop lequel était utilisé à l'origine... Merci à vous pour ces soirées loin de toute inquiétude liée à la thèse.

Merci également à ma famille et en particulier à mes parents, qui ont toujours cru en moi et m'ont toujours soutenu. Je suis fier de ce que j'ai pu accomplir grâce à votre soutien sans faille ! Merci profondément pour tout ce que vous m'avez apporté. Merci aussi à **Pascale** et **Jordane** pour votre bonne humeur et votre soutien qui m'a permis de garder le moral tout au long de cette thèse.

Enfin un grand merci aux membres de la Tour Noire, à **Sammael** l'éternel rêveur, et au **M'Hael** le souverain de la foudre dont les nombreuses conversations à la «Cascade à Vin»au sein du «Manethering»ont permis de trouver la force et le courage d'aller au bout de la forge des microcanaux, bien du point de vue de Sammael, tout ceci ne fassent point «rêver»... Merci de m'avoir accompagné tout au

long de cette épopéé que fut le confinement et cette thèse en général ! C'est sans nul doute grâce à votre indéfectible présence, les nombreuses anecdotes du GTR, les nombreux débats débutés par le M'Hael au détour d'une conversation en apparence anodine, que j'ai pu forcer la trame à être modelé selon mon envie ! D'Anor Londo à Rivellon, ce fut une longue aventure, qui m'a permis de rester sur le droit chemin fidèle à mes principes. Une lueur d'espoir à travers ce brouillard épais digne de Shadar Logoth. Aujourd'hui, je peux hisser la bannière bien haute et avec fierté car quel que soit le destin qui m'est réservé par le tissage de la Trame, je clame haut et fort :

Dovie'andi se tovya sagain ! Tai'shar Fesches-le-Chastelot ! Tai'shar Baidwé !

Jean Kovchar

INTRODUCTION

Unexploited waste heat has been one of the major challenges for energy recovery in recent years. In 2017, the French Environment and Energy Management Agency (ADEME) published that, in France, waste heat loss ($> 100\ °C$) from industrial energy processes accounted for 36% of industrial energy consumption, or 117.9 TWh of energy not yet exploited each year in the form of gaseous, liquid and diffuse waste. This waste heat represented only 16% of industrial energy consumption, amounting to 51 TWh heat lost each year in France in 2015. By 2020, this heat waste have been partially exploited. The total amount of remaining unexploited heat is equal to 99.6 TWh reducing it by 15.5 %. These values show that there is still work to be done to further increase the recovery of heat waste and confirm the importance of harnessing this remaining unused source of energy.

Innovative low-temperature ($< 200\ °C$) energy recovery and conversion systems have been designed and developed [1], [2], [3], [4]. However, these macroscopic systems are often too voluminous, making them difficult to implement in industrial systems. They also have a high proportion of dead volume. Consequently, previous studies [5], [6] have led to the design of a miniature device for low-temperature energy recovery and conversion, based on the principle of Stirling machines. When miniaturizing such machines, technological challenges arise as friction (of pistons, of fluid flow ...) becomes predominant and affects the machine's efficiency. To minimize piston friction, these pistons were replaced by hybrid membranes made from an elastomer and silicon during a previous thesis in our institute [6]. However, when the machine was tested in operation, a significant energy loss was observed during the transmission of energy from one membrane (set in oscillatory motion using an electromagnet) to the chambers and other membranes making up the Stirling micro-machine. Comparison of the estimated pressure drop with theoretical values for an incompressible steady flow [1] using macroscale correlations showed a significantly higher pressure drop for the miniature device: up to 50 times higher than those predicted by theoretical value at macroscale for incompressible flow. However, very few data are available for alternating flows on the scale of the micro-Stirling engine.

Several approaches need to be explored to understand the observed energy losses, which are much greater than those initially estimated. Possible explanations for these differences include compressibility effects. In the Stirling micro-machine, air was used as the working fluid. But by reducing the size of the machine, for oscillation frequencies of a few Hz, the fluid velocity can become greater than at the macroscopic scale, and compressibility effects are no longer negligible. Another possible explanation is the presence of right-angle bends, linked to microfabrication constraints to link the various chambers together. Indeed, by reducing channel dimensions, contributions neglected on the

[1] When speaking of steady flows, we will be referring to a flow whose characteristics and properties are independent of time.

macroscopic scale can have a greater influence on the smaller scale, with surface forces, for example, becoming increasingly important compared to volume forces.

Thus, the main purpose of this thesis is to study alternating gas flows within channels of similar dimensions to those involved in the miniature device, to obtain a clearer understanding of alternating flows and the influential contributions at this sub-millimeter scale. This study will then enable us to optimize the design of the miniature machine to improve its efficiency. This thesis work was co-financed by the project I-SITE ANTARES and by EUR-Eiphi. These projects were dedicated to obtain a better understanding of alternating flow at microscale to enhance the design of micro Stirling engine.

This thesis is structured around 4 chapters. The first chapter presents a state-of-the-art on steady flows at both macroscopic and microscopic scales. This gives an idea of the parameters whose influence is more pronounced as channel dimensions decrease. In the second part of this chapter, we present the state of the art of oscillating flows [2], highlighting the various flow characteristics that differ from steady flows, as well as the different parameters that allow us to characterize these flows in a similar way to steady flows.

The second chapter presents the channel design considered for this study. This design is based on channel dimensions close to those of the miniature device. To adapt these dimensions to the pipe dimensions of the experimental device, converging and diverging sections have been designed on either side of the channel, while minimizing their influence on the flow. Secondly, this chapter presents the pressure and temperature sensors planned to be implanted within the channels, to enable pressure and temperature measurements as close as possible to the channel ends. The design and sizing of these sensors will be presented.

The third chapter describes the manufacturing processes used to produce the channels. Given the complexity of the process used for making channels with integrated sensors, another process for the fabrication of channels without sensors was considered and used alongside the other process. These two processes will be described in detail one after the other. In the second part of this chapter, we present the characterization of the temperature sensors fabricated. This characterization enables us to determine the influence of the annealing process parameters (temperature, time), involved in the fabrication of these sensors, on the electrical, mechanical, and structural properties of the thin-film deposition of Platinum resistive tracks.

The fourth chapter presents first the experimental setup and the metrology and acquisition system used for the measurements. Secondly, this chapter concerns the results obtained for both pressure drop and temperature difference in the case of steady nitrogen flows. These results are discussed and compared with theoretical values, for which detailed calculations will also be presented. On the other hand, the results for the calculated friction factor are compared to the correlations from the literature. The last section of this chapter presents the results obtained for both pressure and temperature in the case of alternating [3] air flows. The pressure drop and temperature difference are also represented versus the Womersley number. These results are discussed regarding results from the literature for oscillating flow at the macroscale.

[2] Oscillating flow will refer to flows whose characteristics and properties vary periodically over time.

[3] Alternating flow refers to a specific case of oscillating flow in which the velocity will change direction over time (the average velocity of such flows over time is zero due to the reversal of the flow direction).

CHAPTER I

STATE OF THE ART OF STEADY AND ALTERNATE FLOWS AT MACRO- AND MICRO-SCALE

To enhance the performance and optimize the design of the miniature Stirling device [5], [6], a better understanding of gas flow, and more specifically of alternating gas flow, is required in channels at the milli and micro scales. Thus, this first chapter will present the parameters and dimensionless numbers that characterize flows. The behavior of incompressible and compressible flow at the macroscale will first be given. As the dimensions of channels get smaller and smaller, effects that are neglected at macroscale are more significant. Moreover, if the dimensions of the channel get close to the mean free path of the gas, rarefaction effects can be significant assuming the gas cannot be considered as continuous fluid anymore. As a result, a geometric requirement has been defined to ensure that rarefaction effects can still be neglected in the case of our study.

In the second part of this chapter, a review of the main characteristics of flow in microchannels will be presented focusing on non-rarefied flow since the dimensions of our test channels will ensure that the assumption of continuous flow is still valid. The review will highlight the influence of several parameters, for which the contribution at the macroscale is neglected. Indeed, the influence of the roughness of the wall of the channel on the flow behavior will be highlighted. Moreover, the compressibility effects are significant even for smaller values of the Mach number Ma (characterizing the compressibility of the fluid) than the values of Mach number at the macroscale for which the compressibility of the fluid starts to be considerable.

To improve the understanding of the flows generated within the miniature Stirling engine manufactured within the microfabrication technology facility of the FEMTO-ST Institute, the last part of this chapter will focus on the characteristics of oscillating flows at both macro- and microscales, considering unsteady gas flow occurring in Stirling engine. Oscillating flows are different from "classical" flow as the motion of the fluid can be expressed as a sinusoidal function. Therefore, velocity, pressure, and temperature but also density vary periodically, which results in differences in the characterization of these flows than to steady flows.

I.1 Characterization of fluid flows

The flow of an incompressible fluid is characterized by its velocity, pressure, and temperature. For compressible fluids, the characterization of the flow will also include the density. To determine these quantities, three equations are required (four equations for compressible flows).
The governing equations for fluid flow come from the equation of continuity, the conservation of momentum, as well as the conservation of energy. For gas flow, the equation of state will close the system of equations.

Considering that the fluid is a continuous medium and that gravitational, magnetic, and electrical effects can be neglected, fluid flows are therefore characterized by the following equations:

- Equation of continuity

  This equation describes the conservation of the mass flow rate and is expressed as follows:

$$\frac{\partial \rho}{\partial t} + \vec{\nabla}.(\rho \vec{U}) = 0 \tag{I.1}$$

  with ρ the density of the fluid and U the velocity of the flow.

- Equation of momentum balance

$$\rho \left(\frac{\partial \vec{U}}{dt} + (\vec{U}.\vec{\nabla})\vec{U} \right) = -\vec{\nabla} P + \mu \vec{\nabla}^2 \vec{U} \tag{I.2}$$

  with P representing the pressure, and μ the dynamic viscosity of the fluid.

- Equation of energy conservation

$$\rho C_p \left(\frac{\partial T}{\partial t} + \vec{U}.\vec{\nabla} T \right) = \frac{\partial P}{\partial t} + \vec{U}.\vec{\nabla} P + k \vec{\nabla}^2 T + \Phi \tag{I.3}$$

  with C_P the specific heat capacity, T the temperature of the fluid, k its thermal conductivity, and Φ the viscous dissipation function.

- Gas state equation

  Regarding gas flow in channels, the fluid is compressible and results in the variation of the fluid density. Another equation is thus required to determine the density of the fluid. Considering that the gas is ideal, the relation between density, pressure, and temperature of the gas can be expressed as:

$$P = \rho \ r_G \ T \tag{I.4}$$

  with P the pressure, ρ the density, r_G the specific gas constant, and T the temperature of the gas.

I.1.1. Dimensionless number

Usually, Reynolds number is used to characterize inertial and friction characteristics of flow regardless of working fluid and characteristic flow length. Mach number is commonly used to characterize compressible flows and the influence of compressibility effects in relation to inertial and viscous contributions.

I.1.1.1 Reynolds number

As it will be further highlighted, the dimensionless number $\frac{\rho_0 U_0 L_c}{\mu_0}$ which characterizes the influence of inertial force compared to viscous contribution is important to characterize flows. This dimensionless number is called Reynolds number and is defined as:

$$Re = \frac{\rho U L_c}{\mu} \tag{I.5}$$

with ρ representing the density of the fluid, U the velocity of the flow, and L_c a characteristic length of the flow, which is often represented by the hydraulic diameter defined as:

$$D_h = \frac{4A}{\Pi} \tag{I.6}$$

where A represents the cross-section of the fluid and Π is the wetted perimeter of the cross-section.

According to the value of the Reynolds number, the flow can be classified within the following regimes:

- laminar regime: this regime corresponds to low values of Re, where fluid flows are governed by the viscous forces
- turbulent flow: this regime corresponds to a high value of Re, where inertial forces are significantly higher than viscous forces.
- transition regime which is the range of Re between fully laminar flow and fully turbulent flow.

  The commonly used Reynolds number range for which the transition from laminar to turbulent regime occurs for flows in channel is typically between 2000 and 3500.

Regarding the present study, the working fluid involved will be air as well as nitrogen. Fluid compressibility can affect the characteristics of a flow, which is why it is essential to identify the influence of fluid compressibility on the flow.

I.1.1.2 Mach number

Compressible flows are characterized by large variations in fluid density. These variations in fluid density can lead to significant changes in flow velocity, resulting in local fluid acceleration. Therefore, this induces important local variations in fluid pressure and temperature.

The Mach number characterizes the compressibility effects and is defined as:

$$Ma = \frac{U}{c} \tag{I.7}$$

where c represents the speed of sound.

The speed of sound in a gas can be expressed by the equation:

$$c = \sqrt{\gamma \; r_G \; T} = \sqrt{\frac{\gamma \; P}{\rho}} \tag{I.8}$$

For compressible flow, the density of the fluid will vary according to the gas state equation (equation I.4). The variation of viscosity can also be important since it affects the friction characteristics of the fluid flow. The variation of viscosity with the temperature can be expressed using the kinetic theory. Different models (such as the hard-sphere kinetic theory, power-law force, the Sutherland model or the Lennard-Jones model) can express this variation at different level of accuracy. The Sutherland model offers the best compromise between accuracy in describing viscosity variation as a function of temperature and its ease of use. Therefore, in this thesis, the viscosity will be calculated using the Sutherland's law [7][8]:

$$\frac{\mu}{\mu_0} = \left(\frac{T}{T_0}\right)^{3/2} \left(\frac{T_0 + C_\mu}{T + C_\mu}\right) \tag{I.9}$$

with $T_0 = 273.15$ K and C_μ a constant depending on the gas, C_μ (air) = 113 K, C_μ (N_2) = 109 K.

The effects of compressibility become significant for $Ma \geq 0.3$. Oosthuizen and Carscallen [9] reported that at $Ma = 0.1$, the variation of density was theoretically equal to 1 % of the variation of velocity, while at $Ma = 0.33$ this variation was equal to 10 % of the variation of velocity. This is because the variation of density is related to the variation of velocity with the square of the Mach number. Therefore, at a Mach number below 0.3, the effect of compressibility is often neglected.

$$\frac{\partial \rho / \rho}{\partial U / U} = -Ma^2 \tag{I.10}$$

I.1.2. Dimensionless equations

The dimensionless form of these equations can be obtained by introducing the following dimensionless quantities, denoted by the superscript *.

$$\begin{cases} x^* = \frac{x}{L_c} & \overrightarrow{U^*} = \frac{\vec{U}}{U_0} & t^* = t\frac{U_0}{L_c} & \rho^* = \frac{\rho}{\rho_0} & \mu^* = \frac{\mu}{\mu_0} \\ C_P^* = \frac{C_P}{C_{P0}} & k^* = \frac{k}{k_0} & P^* = \frac{P}{\rho_0 U_0^2} & T^* = \frac{T - T_0}{\Delta T} & \Phi^* = \frac{L_c^2}{\mu_0 \; U_0^2} \; \Phi \end{cases} \tag{I.11}$$

L_c is a characteristic length of the fluid flow, for internal flow, the hydraulic diameter is commonly used. U_0 corresponds to the mean velocity in the cross-section (for oscillating flow as we will later see, it will be also either an average value over time or its maximum value). T_0 corresponds to the room temperature, and ΔT represents the temperature difference between the inlet and outlet of the channel. k_0, C_{P0}, ρ_0, and μ_0 represent the fluid properties at the room temperature. The dimensionless form of pressure here is only used for incompressible flow or flow at low Mach number

Replacing the introduced dimensionless quantities in the previous equations (I.1) - (I.3), we obtain the following dimensionless equations:

- Dimensionless equation of continuity

$$\left(\frac{\rho_0\ U_0}{L_c}\right)\frac{\partial\rho^*}{\partial t^*}+\frac{1}{L_c}\overrightarrow{\nabla^*}.(\rho_0\,\rho^*\,U_0\overrightarrow{U^*})=0 \tag{I.12}$$

This equation can be simplified as follows:

$$\frac{\partial\rho^*}{\partial t^*}+\overrightarrow{\nabla^*}.(\rho^*\,U^*)=0 \tag{I.13}$$

For incompressible flow, the term $\frac{\partial\rho^*}{\partial t^*}$ is equal to 0.

- Dimensionless equation of momentum conservation (for incompressible flow)

$$\rho^*\rho_0\left[\frac{U_0^2}{L_c}\frac{\partial\overrightarrow{U^*}}{\partial t^*}+\frac{U_0^2}{L_c}(\overrightarrow{U^*}.\overrightarrow{\nabla}^*)\overrightarrow{U^*}\right]=-\frac{\rho_0U_0^2}{L_c}\overrightarrow{\nabla}^*(P^*)+\mu_0\mu^*\frac{U_0}{L_c^2}\overrightarrow{\nabla}^{*2}\overrightarrow{U^*} \tag{I.14}$$

The equation I.14 can be simplified as follows:

$$\rho^*\left[\frac{\partial\overrightarrow{U^*}}{dt^*}+(\overrightarrow{U^*}.\overrightarrow{\nabla}^*)\overrightarrow{U^*}\right]=-\overrightarrow{\nabla}^*(P^*)+\left(\frac{\mu_0}{\rho_0U_0L_c}\right)\mu^*\overrightarrow{\nabla}^{*2}\overrightarrow{U^*} \tag{I.15}$$

With $Re=\frac{\rho UL_c}{\mu}$, the Reynolds dimensionless number, the equation of momentum conservation can finally be expressed as:

$$\rho^*\left[\frac{\partial\overrightarrow{U^*}}{dt^*}+(\overrightarrow{U^*}.\overrightarrow{\nabla}^*)\overrightarrow{U^*}\right]=-\overrightarrow{\nabla}^*(P^*)+\frac{1}{Re}\mu^*\overrightarrow{\nabla}^{*2}\overrightarrow{U^*} \tag{I.16}$$

- Dimensionless equation of energy (for incompressible flow)

$$\rho^*C_P^*\frac{\rho_0\,C_{P\,0}\,U_0}{L_c}\Delta T\left[\frac{\partial T^*}{\partial t^*}+(\overrightarrow{U^*}.\overrightarrow{\nabla}^*)T^*\right]=\rho_0U_0^2\frac{U_0}{L_C}\left[\frac{\partial P^*}{\partial t^*}+\overrightarrow{U^*}.\overrightarrow{\nabla}^*P^*\right]+\Delta T\frac{k_0}{L_c^2}k^*\overrightarrow{\nabla}^{*2}T^*+\frac{\mu_0U_0^2}{L_c^2}\Phi^* \tag{I.17}$$

After simplification of this equation, it gives the following equation:

$$\begin{aligned}\rho^*C_P^*\left[\frac{\partial T^*}{\partial t^*}+(\overrightarrow{U^*}.\overrightarrow{\nabla}^*)T^*\right]&=\frac{U_0^2}{C_P\,\Delta T}\left[\frac{\partial P^*}{\partial t^*}+\overrightarrow{U^*}.\overrightarrow{\nabla}^*P^*\right]\\&+\frac{k_0}{\mu_0\ C_{P0}}\frac{\mu_0}{\rho_0\ U_0\ L_c}k^*\overrightarrow{\nabla}^{*2}T^*+\frac{\mu_0}{\rho_0\ U_0\ L_c}\frac{U_0^2}{C_{P0}\Delta T}\Phi^*\end{aligned} \tag{I.18}$$

with $Pr = \frac{\mu C_P}{k}$, the Prandtl number and $Ec = \frac{U^2}{C_P \Delta T}$ the Eckert number, the dimensionless equation of energy can finally be expressed as:

$$\rho^* C_P^* \left[\frac{\partial T^*}{\partial t^*} + (\overrightarrow{U^*}.\overrightarrow{\nabla^*})T^* \right] = Ec \left[\frac{\partial P^*}{\partial t^*} + \overrightarrow{U^*}.\overrightarrow{\nabla^*}P^* \right] + \frac{1}{Pr\,Re} \overrightarrow{\nabla}^{*2} T^* + \frac{Ec}{Re}\ \Phi^* \tag{I.19}$$

- Dimensionless equation of momentum conservation (for compressible flow)

  For compressible, these dimensionless equations can be expressed in another form which includes the contribution of the Mach number.
  By substituting $P^* = P/P_0$ with $P_0 = \rho_0 r_G T_0 = \frac{\rho_0}{\gamma} \left(\frac{U_0}{Ma} \right)^2$, the equation I.2 becomes:

$$\rho^* \rho_0 \left[\frac{U_0^2}{L_c} \frac{\partial \overrightarrow{U^*}}{\partial t^*} + \frac{U_0^2}{L_c} (\overrightarrow{U^*}.\overrightarrow{\nabla^*}) \overrightarrow{U^*} \right] = -\frac{\rho_0}{\gamma L_c} \left(\frac{U_0}{Ma} \right)^2 \overrightarrow{\nabla^*}(P^*) + \mu_0 \mu^* \frac{U_0}{L_c^2} \overrightarrow{\nabla}^{*2} \overrightarrow{U^*} \tag{I.20}$$

  This equation can now be simplified as follows:

$$\rho^* \left[\frac{\partial \overrightarrow{U^*}}{dt^*} + (\overrightarrow{U^*}.\overrightarrow{\nabla^*}) \overrightarrow{U^*} \right] = -\frac{1}{\gamma Ma^2} \overrightarrow{\nabla^*}(P^*) + \frac{1}{Re} \mu^* \overrightarrow{\nabla}^{*2} \overrightarrow{U^*} \tag{I.21}$$

  This shows the importance of defining the characteristics and quantities representing the flow.

I.1.3. Friction factor

Fluid flows are characterized by the pressure drop that describes the amount of energy loss along the channel. It is defined by the difference between the pressure at the inlet of the channel and the pressure at the outlet of the channel. The pressure drop is related to the velocity of the flow through the following relation:

$$\Delta P = P_{inlet} - P_{outlet} = \frac{1}{2} C_f \rho U^2 \frac{L}{D_h} \tag{I.22}$$

with ΔP the pressure drop through the channel, C_f the friction factor, U the cross-sectional flow velocity. For flow in a circular cross-section, the friction factor is defined as the following relation:

$$C_f = \frac{8\tau}{\rho U^2} \tag{I.23}$$

τ represents the shear stress defined by:

$$\tau = \mu (\frac{\partial U}{\partial n})_{n=0} \tag{I.24}$$

with n the normal direction of the channel wall

The friction factor in eq. I.23 is called the Darcy friction factor and must not be confused with the Fanning friction factor which is used in numerous studies in the literature. The relation between these two friction factors is given by :

$$C_{f-Darcy} = 4\, C_{f-Fanning} \tag{I.25}$$

In the following, the friction factor C_f will correspond to Darcy's friction factor.

In addition to characteristic dimensions such as hydraulic diameter and channel length, at the macroscale, other parameters influencing pressure drop for a given fluid include roughness, aspect ratio, and compressibility.

I.1.3.1 Roughness influence on friction factor

For incompressible fluid flow at the macroscale, the theoretical values for the friction factor as a function of the Reynolds number are given by the following relations.

- Laminar regime ($Re \leq 2000$)

  For circular channels, the friction factor in laminar flow is independent of the surface roughness and is directly related to the Reynolds number by :

$$C_f = \frac{64}{Re} \tag{I.26}$$

- Turbulent regime ($Re \geq 3500$)

  It's important to note that there are a large number of correlations in the turbulent regime, with different areas of validity depending on the author. We will limit ourselves here to two of the most frequently cited cases.

  The friction factor as a function of roughness ε in the turbulent regime is given by the Colebrook-White relation[10]:

$$\frac{1}{\sqrt{C_f}} = -2log\left(\frac{2.51}{Re\sqrt{C_f}} + \frac{1}{3.7}\frac{\varepsilon}{D_h}\right) \tag{I.27}$$

  For smooth channel and $Re \leq 10^5$ the relation between the friction factor and the Reynolds number is given by the Blasius equation:

$$C_f = \frac{0.316}{Re^{0.25}} \tag{I.28}$$

I.1.3.2 Aspect ratio correction on friction factor

The aspect ratio α of the cross-section of a rectangular channel is given by $\alpha = \frac{h}{w}$ if $h \leq w$ and $\alpha = \frac{w}{h}$ if $h \geq w$, with h and w being respectively the height and the width of the channel. The aspect ratio is important as the influence of the boundary layer is much more significant for low aspect ratio values (geometry of channels close to the parallel plate model) than for channels with an aspect ratio close to 1 (geometry of channels close to square cross-section).

In laminar flow, for rectangular cross-section channels of aspect ratio α with width w and height h , Equation (I.26) becomes the following [11]:

$$C_f = \frac{96}{Re}\ (1 - 1.3553\alpha + 1.9467\alpha^2 - 1.7012\alpha^3 + 0.9564\alpha^4 - 0.2537\alpha^5) \tag{I.29}$$

From Equation I.29, the correlation for the case of square channels (α = 1) and parallel plate channels ($\alpha \to 0$) can be deduced[11]:

$$C_f = \frac{56.91}{Re} \qquad (square\,channels) \tag{I.30}$$

$$C_f = \frac{96}{Re} \qquad (parallel\,plate) \tag{I.31}$$

In the following when referencing the theoretical values of friction factor at macroscale, it will correspond to Equations I.26 - I.31 according to the cross-section of the channel and the regime of flow.

I.1.3.3 Friction factor for compressible flow

- Isothermal flow

  Regarding compressible flow, as the density can be significantly different between both extremities of the channel, another expression for the friction factor was proposed by Shapiro [12]. Considering an isothermal and steady flow of a perfect gas, the proposed equation was:

$$P_{in}^2 - P_{out}^2 = r_G T \left(\frac{\dot{m}}{A}\right)^2 \left(C_f \frac{L}{D_h} + 2ln(\frac{P_{in}}{P_{out}})\right) \tag{I.32}$$

  with r_G the specific gas constant, ΔP the pressure gradient between the inlet and outlet of the channel, P_{in} and P_{out} the pressure at the inlet and outlet of the channel and T the temperature of the gas.

  This results in the following expression for the friction factor in the case of isothermal compressible flow:

$$C_f = \frac{D_h}{L}\left[\left(\frac{P_{in}^2 - P_{out}^2}{r_G T(\frac{\dot{m}}{A})^2}\right) - 2ln\left(\frac{P_{in}}{P_{out}}\right)\right] \tag{I.33}$$

- Adiabatic flow

  Regarding a flow that can be considered adiabatic, the friction factor must take into account the contribution of temperature at both extremities of the channel in the friction factor [13], [14]. Therefore, the expression of the friction factor becomes:

$$C_f = \frac{2\,D_h}{L}\left[\left(\frac{P_{in}^2 - P_{out}^2}{R_g(T_{in}+T_{out})(\frac{\dot{m}}{A})^2}\right) - ln\left(\frac{P_{in}}{P_{out}}\right) + ln\left(\frac{T_{in}}{T_{out}}\right)\right] \tag{I.34}$$

I.2 Characteristics of gas and liquid flows inside microchannels

The interest in flows within microducts has only emerged in the last decades with the improvement of MEMS technologies, these flows at a microscopic scale are therefore less understood, although

many investigations have been undertaken. When the dimensions of the channels decrease, several authors report some scaling effects that change the characteristics and behavior of the flows inside these small channels. Therefore, a review of the main characteristics of gas and liquid steady flows at these microscales will be presented.

I.2.1. Scaling effect

Both gas and liquid flows inside microchannels have been widely studied during the last decades. These investigations were carried out to determine whether flow characteristics are different as channel dimensions decrease. Indeed, as dimensions decrease, surface forces become increasingly important compared to volume forces.

As far as studies with a liquid are concerned, we can cite, for example, the work of Pfahler *et al.* [15] who studied the flow of N-Propanol in 53 μm wide and 135 μm deep channel (*i.e.* $D_h = 76$ μm) as well as smaller channels with a width of 100 μm and a depth ranging from 0.7 μm to 1.8 μm (*i.e.* D_h ranging from 1.4 to 3.5 μm). The Reynolds number ranged up to 300. The authors observed that, as the dimensions of the channels became smaller, a deviation from the classical behavior could be seen. The friction factor for the large microchannel and the channel with a depth of 1.8 μm was in rough agreement with the theoretical value, while the friction factor was observed up to 3 times higher for the smaller channel. Judy *et al.* [16] investigated fluid flow inside circular and square channels with hydraulic diameters ranging from 22 to 149 μm using water, methanol, and isopropanol as working fluid. The authors, unlike Pfahler *et al.* [15], could not confirm the existence of any scale effects since the deviations observed were within the experimental uncertainties. The same conclusion came from the study of Gao *et al.* [17] with water as a working fluid through two parallel plates with a height ranging from 0.1 mm to 1 mm for friction characteristics being non-affected by scaling effect.

With regard to studies using gas as a working fluid, we can cite, for example, Yang and Lin [18] (D_h ranging from 123 to 962 μm) and Jung *et al.* [19] (D_h ranging from 100 to 133 μm). Yang *et al.* [20] also investigated the influence of the size of channels for gas flow (air as working fluid). The hydraulic diameter ranged from 86 to 920 μm. The authors observed no significant size effects or discrepancies within these ranges of hydraulic diameter.

Inconsistent conclusions appear between authors making it difficult to conclude on the influence of the change of dimension. These contradictions can be caused by differences between the experimental conditions of the study and the model used for comparison with the theory, the accuracy and errors of measurement becoming significantly larger than at the macroscopic scale. It could also be due to effects not taken into account at the macroscopic scale and whose influence is much more important at the microscopic scale, the surface forces becoming increasingly significant compared to the volume forces as the dimensions of the channels decrease. The main causes of these noticed deviations could be the rarefaction of the flow as well as the roughness of the walls whose influence at the microscale seems indeed much more important than its contribution to the flow characteristics at the macroscale. The next part focuses on rarefaction effects that become important when the channel dimensions approach the mean free path. These rarefaction effects do not allow us to consider the fluid as a continuous medium.

I.2.2. Rarefaction effects

When the dimensions of the channels become smaller and smaller and significantly close to the mean free path of the particles, so-called "rarefaction" effects of the fluid appear. This rarefaction

effect results in a change in flow behavior and affects both velocity and temperature in a boundary layer located near the wall of channels [21], [22]. This is represented in slip condition for velocity and jump temperature as boundary conditions on the wall of the channels unlike "classical" non-rarefied flows. Models have been developed based on statistical methods to characterize rarefied flows [23].

The degree of rarefaction of a flow is characterized by the Knudsen number Kn which is defined as the ratio of the mean free path of the particles λ_G to a characteristics length L_c of the flow:

$$Kn = \frac{\lambda_G}{L_c} \tag{I.35}$$

The mean free path represents the average distance traveled by a particle between two successive collisions with other particles. The values of the mean free path and resulting critical hydraulic diameter which ensure that rarefaction effects can still be neglected for different gases are given in the table I.1. The values of mean free path for dry air have been determined by Jennings [24] and is equal to 66.9 nm at a temperature of 25 ° and a pressure of 1.013 bar.

Different flow regimes can be classified according to the value of the Knudsen number as depicted in figure I.1. The transition value of Kn for which the assumption of continuous flow is reasonable is considered around 10^{-3} for Kandlikar *et al.* [25], Colin *et al.* [26] whereas for Dongari *et al.* [27] and Yu *et al.*[28] this value is around 10^{-2}. In the rest of this work, for all calculations, we will use the value of Kn given by Kandlikar *et al.* [25].

Table I.1: Mean free-path for different gas at 20 °C and 1 bar [1]

Gas	N_2	Ar	He	H_2
Mean free path (nm)	67	72	196	125
Critical D_h $(\mu$**m**$)$	67	72	196	125

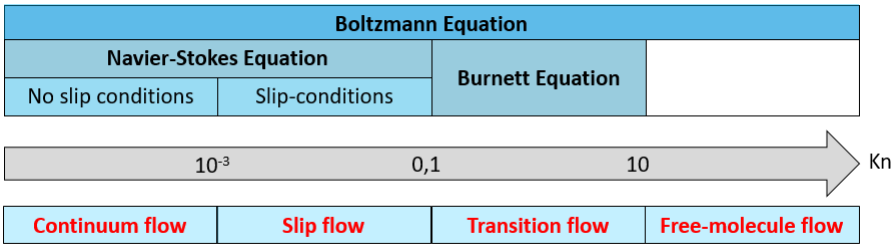

Figure I.1: Classification of rarefaction as a function of Kn

Assuming a Maxwell-Boltzmann distribution, the Knudsen number can also be related to the Reynolds and Mach number through the following relation:

$$Kn = \frac{Ma}{Re}\sqrt{\frac{\gamma\pi}{2}} \tag{I.36}$$

[0]http://www.leakdetection-technology.com/science/introduction-to-the-gas-laws/the-mean-free-path-for-some-gases-at-20-c-and-different-pressures.html

Hong *et al.* [29] observed the variation of the friction factor as a function of both Mach Ma and Knudsen Kn numbers and proposed the following correlation:

$$C_f.Re = \frac{96}{1+12Kn} + \frac{15.03Ma + 59.28Ma^2 + 414.31Ma^3}{(1+12Kn)^2} \tag{I.37}$$

As for the study in this thesis and to neglect rarefaction effects, the Knudsen number will be kept below the value of 10^{-3}. As for air, the mean free path is around 66.9 *nm* [24] at a temperature of 25 °C and a pressure of 1.013 bar., which results in the following condition for the hydraulic diameter as follows:

$$D_h = \frac{\lambda_{air}}{Kn} = \frac{66.9\ 10^{-9}}{10^{-3}} = 66.9\mu m \tag{I.38}$$

Therefore, the hydraulic diameter of channels that will be studied will be higher than 70 μm to consider that the rarefaction effect can be neglected. The state of the art of characteristics for flows at the microscale will consequently focus on non-rarefied flows. Fluid flows for both gas and liquid at the macroscale have been extensively studied for a long period and are well-known.

I.2.3. Influence of the roughness of the flows at microscale

Besides rarefaction effects, the question that arises with such small channel dimensions concerns the influence of other parameters that would be neglected on a macroscopic scale, such as the roughness of the channel's wall.

One of the first researchers to investigate gas flow in microchannels experimentally were Wu P. and Little W.A. [30] as part of the design of a miniature Joule-Thomson refrigerating device. They carried out their study on silicon and glass channels with different roughness. Their channel dimensions were about a few tens of micrometers, resulting in hydraulic diameters ranging between 45μm and 85μm. Nitrogen as well as helium and argon were used as working fluids. Their studies [30] focused on the variation of the friction factor and the heat transfer versus the Reynolds number for both laminar and turbulent regimes (Reynolds number ranging from 100 to 15 000). Their experimental data were compared with the theoretical correlations for macroscale channels and highlighted significant differences which the authors attributed to the roughness of the channel wall. Indeed, although they could not experimentally measure precisely the value of the roughness of their channels, they observed that the greater the roughness was, the greater the friction factor was and deviated from the classical correlations for macroscale flows. The friction factor for the roughest channel was three times larger than for the smoothest channel. It is important to note here that the smallest hydraulic diameter is at the limit of the slip flow regime (Table I.1), which could also partly explain the differences observed.

From this study, the roughness ε of the channels seems then to have a significant influence on the flows at the microscale even for laminar flow, unlike flows at the macroscale. Therefore, a review of the influence of the relative roughness ε_r for both gas and liquid flows inside microchannels will be presented below with relative roughness defined as:

$$\varepsilon_r = \frac{\varepsilon}{D_h} \tag{I.39}$$

with ε the roughness mean size along the channel.

I.2.3.1 Constricted flow hydraulic diameter

From numerous studies, it appears that roughness was not measured precisely or properly taken into account as it should be with the hydraulic diameter. Kandlikar *et al.* [31] proposed to take roughness into account using a constricted flow diameter defined as follows:

$$D_{cf} = D_h - 2\varepsilon \tag{I.40}$$

with D_h corresponding to the mean value of hydraulic diameter $\bar{D_h}$ (cf. Figure I.2) and ε corresponding to the mean roughness of the channel.

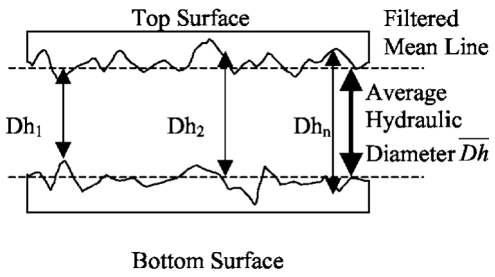

Figure I.2: Mean hydraulic diameter $\bar{D_h}$

Zhou *et al.* [32] reviewed the results from literature using the original constricted flow model, another constricted model with roughness distribution taken into account, and a third model using roughness and viscosity distribution. They compared the data from the literature with the three models: they found that the data from the original constricted model were within 15% of error compared to the literature data. This will result in calculating a new Reynolds number based on this constricted flow diameter. The friction factor can then be plotted versus the Reynolds number to correctly take into account the roughness of the wall.

I.2.3.2 Earlier transition laminar-turbulent regime

Many authors reported an earlier transition from a laminar to a turbulent regime. This transition was observed much earlier for rough microchannels than for smooth ones. For flow in channel, it is important to recall that this transition occurs for critical Reynolds number values Re_c between 2000 and 3500.

Wu *et al.* [30] observed an earlier transition from laminar to turbulence for rough microchannels ($Re_c \approx 400$) whereas the transition for smooth microchannels occurred around $Re_c = 1500$. Hao *et al.* [33] found transition $Re_c \leq 900$ for rough microchannels.

Vijayalakshmi *et al.* [34] studied both gas and liquid flow inside microchannels of hydraulic diameter ranging from 60.5 μm to 211 μm and observed also an earlier transition for both gas and liquid flow with Re_c between 1600 and 2300. This slight earlier transition was attributed to the influence of roughness on the characteristics of the flow in microchannels.

Natrajan *et al.* [35] found as well an earlier transition for rough microchannels. This transition was much more earlier as the roughness increased $Re_c = 1500$ for $\varepsilon = 1.25$ % whereas this value of transition is around 1300 for $\varepsilon = 2.5$ %. The transition occurred around $Re_c = 1900$ for smooth microchannels.

This earlier transition from laminar to a turbulent flow regime according to the above-mentioned investigation highlights another feature of roughness with higher influence on the flow in microchannels than at the macroscale.

Dai *et al.* [36] reviewed numerous studies of liquid flow inside mini- and micro-channels. Figure I.3, extracted from their work, highlights an earlier transition to turbulence depending on the roughness value, which was observed by numerous authors.

The transition from laminar to turbulent flow generally occurs for a Reynolds number in the range of 2000 to 3500, although this transition range may differ from authors in the literature depending on experimental conditions and channel geometry. Dai *et al.* [36] noticed that if relative roughness ε_r was low, there was no significant effect on the friction factor. As depicted in figure I.3, the authors suggested taking the value $\varepsilon_r = 1$ % as the separation between smooth and rough microchannel whereas at the macroscale, below relative roughness of 5%, the relative roughness is considered to not influence the friction characteristics of flow [37].

As there are many studies, we've only detailed a few here. However, a more complete summary can be found in Table I.2. This table summarizes the investigations carried out on both liquid and gas flow in microchannels and the influence of roughness on its characteristics within microchannels of various hydraulic diameters for a large range of Reynolds numbers. From this review of numerous investigations on the influence of the roughness of channel walls on flow at the microscale, it seems that the roughness has to be taken into account in the hydraulic diameter when the relative roughness is around and higher than 1%. The influence of the roughness can lead to variation in the friction factor up to 70% higher than theoretical values of friction factor at the macroscale. The roughness of the channel walls seems also to induce an earlier transition from a laminar to a turbulent regime. Nevertheless, many results obtained by different authors are not in agreement with each other. Thus, another explanation for the deviation observed in several investigations of flows in microchannels proposed by the authors is the effect of compressibility of the fluid. Indeed, due to the small dimensions of the channels, the velocity of the flow can reach high values approaching values of Mach for which the compressibility effect cannot be neglected. The large variation in the fluid density causes local acceleration of the fluid and therefore changes the behavior of the flow significantly compared to incompressible flow.

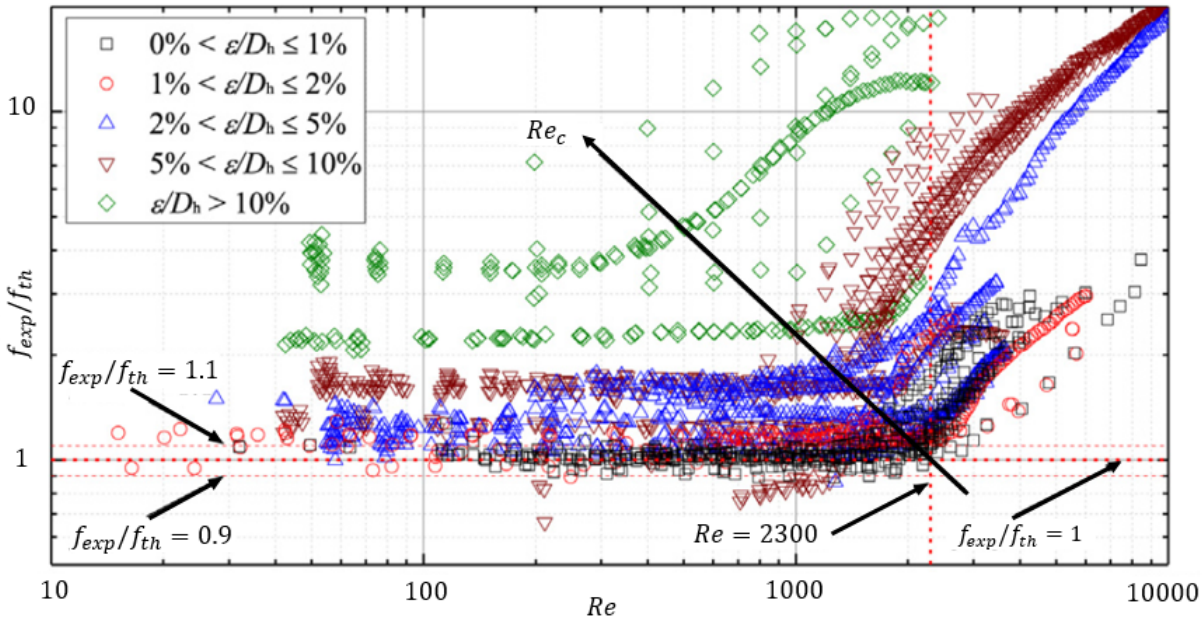

Figure I.3: Normalized friction factor against Reynolds number from the literature - Dai *et al.* [36] (2014)

Table I.2: Influence of roughness on liquid and gas flows in microchannels through literature investigations

Gas flow						
Authors	D_h (μm)	**Microchannel cross-section shape**	**Working fluid**	**Range of Re**	ε_r (%)	**Conclusion of the study**
Wu *et al.* [30] (1983)	45 - 85	Trapezoidal	N_2, Ar He	100 - 15000	20 - 30	Friction factor increased as roughness increased. Earlier transition to turbulence was observed.
Turner *et al.* [38] (2004)	5 - 96	Parallel plate	He, N_2	0.1 - 1000	0.4 - 3	No significant influence of roughness was observed on friction factor.
Kandlikar *et al.* [31] (2005)	325 - 1819	Rectangular	Air	200 - 7200	1 - 14	Both smooth and rough microchannels showed good agreement in the laminar regime using D_{cf} instead of D_h. Earlier transition to turbulence was observed for rough channels.
Tang *et al.* [39] (2007)	10 - 300	Circular	N_2, He	3 - 6200	2.4 - 5.9	Friction factor increased up to 70 % higher than theoretical value as roughness increased.
Lorenzini *et al.* [40] (2010)	26 - 508	Circular	N_2	20 - 14500	0.6 - 1.6	No significant influence for roughness on friction factor. No early transition to turbulent regime was observed.
Liu *et al.* [41] (2015)	400	Square	Air	200 - 2100	0.58 - 1.26	Friction factor increased as the roughness increased.
Yuan *et al.* [42] (2016)	400	Circular	Air	150 - 2800	0.21 - 0.25	C_f was higher in rough microchannels. C_f increased as roughness increased.
Liquid flow						
Authors	D_h (μm)	**Microchannel cross-section shape**	**Working fluid**	**Range of Re**	ε_r (%)	**Conclusion of the study**
Mala *et a.* [43](1999)	50 - 254	Circular	Water	40 - 2500	0.7 - 3.5	Deviation from theoretical value may be explained by a roughness-viscosity model.
Pfund *et al.* [44](2000)	125 - 1050	Rectangular	Water	60 - 3450	- -	$Cf_{exp} > Cf_{th}$ $\quad$ $Cf_{rough} > Cf_{smooth}$
Qu *et al.* [45](2000)	51 - 169	Trapezoidal	Water	10 - 1500	1.2 - 1.7	Experimental data are in agreement with roughness-viscosity model.
Li *et al.* [46](2003)	80 - 450	Circular	Water	250 - 2500	0.01 - 4.3	No significant difference observed for smooth microtubes with diameter > 80um. C_f is 15% to 37% higher than theoretical values at macroscale for rough microtubes.
Baviere *et al.* [47](2004)	199 - 585	Rectangular	Water	0.01 - 8000	0.01 - 2.6	Roughness of microchannels increased friction factor above the theoretical values at macroscale in the laminar regime. No early transition to turbulence was observed.
Kandlikar *et al.* [31](2005)	325 - 1819	Rectangular	Water	200 - 5700	1 - 14	Smooth and rough microchannels using D_{cf} showed good agreement for laminar flow. Earlier transition to turbulence was observed as the roughness of microchannels increased.

Liquid flow						
Authors	D_h (μm)	**Microchannel cross-section shape**	**Working fluid**	**Range of Re**	ε_r (%)	**Conclusion of the study**
Wang *et al.* [48](2005)	180		Water FC77	20 - 220	0.05 - 0.2	C_f increased as roughness of microchannels increased.
Croce *et al.* [49](2005)	50 - 150	Circular	R114	100 - 1500	0.05 - 2.65	C_f increased up to 16% higher for rough microtubes than for smooth microtubes. C_f increased as roughness increased.
Hao *et al.* [33](2006)	153 - 191	Rectangular	Water	100 - 2300	0.017 - 32	*Smooth microchannels:* No difference was observed compared to theoretical values at macroscale. *Rough microchannels:* Earlier transition to turbulence (Re_c = 900 for rough microchannels while Re_c = 2100 for smooth ones)
Shen *et al.* [50](2006)	436	Rectangular	Water	162 - 1257	4 - 6	Significant impact of roughness on friction factor in the laminar regime. The influence can be neglected for low value of Re.
Brackbill *et al.* [51](2007)	424 - 1627	Rectangular	Water	200 - 3000	0.12 - 27.6	Using D_{cf} instead of D_h showed good agreement between theoretical values for friction factor at macroscale and experimental data.
Hrnjak *et al.* [52](2007)	69.5 - 305	Rectangular	Water R134a	112 - 9180	0.14 - 0.35	*Smooth microchannels:* Cf is in good agreement with theory in the laminar regime. C_f is up to 30% higher in the turbulent regime. *Rough microchannels:* C_f is up to 9 % higher than for smooth microchannels in the laminar regime. An earlier transition to turbulence was observed. (Re_c = 1570)
Li *et al.* [53](2007)	50 - 1570	Circular	Water	20 - 2400	0.95 - 2.4	*Smooth microchannels:* C_f was in good agreement with theoretical value at macroscale for D_h down to 50 μm. *Rough microchannels:* C_f started to deviate from theoretical values at macroscale for ε > 1.5 %
Hakamada *et al.* [54](2008)	180 - 480	Circular	Water	200 - 3000	0.08 - 2.39	Earlier transition for rough microchannels was observed (Re_c = 1000).
Ghajar *et al.* [55](2010)	337 - 2083	Circular	Water	600 - 7000	0.27 - 3.7	C_f increased as D_h decreased and as er increased. Earlier transition to turbulence was observed for the rough microchannels.
Natrajan *et al.* [35](2010)	600	Rectangular	Water	100 - 5200	1.25 - 2.5	Earlier transition to turbulence was observed for rough microchannels compared to smooth microchannels. As roughness increased, the transition occured more and more earlier.
Tam *et al.* [56](2011)	750 - 2000	Circular	Water	700 - 7000	0.021 - 0.65	With increasing roughness, the range of Re where the transition from laminar to turbulent regime occurs was increasingly narrow.
Liu and Pang [57](2012)	230	Trapezoidal Circular	Water	100 - 9000	0.7 - 2	Friction factor increased as roughness increased.

I.2.4. Influence of the compressibility of the fluid

Araki *et al.* [58] investigated gas flow inside trapezoidal microchannel of hydraulic diameter ranging from 3 to 10 μm and observed that compressibility effect are significant even for low Mach number. Indeed, compressible friction factor was observed higher than incompressible friction factor for Mach number ranging from 10^{-4} to 0.1. This was due to the variation of the density along the channel, which was significant for a high-pressure ratio between the inlet and the outlet. Morini *et al.* [59] investigated nitrogen gas flow in microchannels with a diameter between 125 μm and 180 μm. The results led them to conclude that the relative roughness below 5 % did not influence the hydraulic resistance, despite the results of numerous studies mentioned in table I.2, discussed above. The authors justify the differences obtained with the other investigations by an incorrect consideration of the compressibility effect of the gas. To take into consideration the compressibility effect, the authors used the compressible friction factor defined in the equation I.33. The authors compared their experimental calculated friction factor with theoretical values and observed good agreement with the theory. Table I.3 summarizes complementary results from the literature (not all detailed in the text here) regarding the effect of the compressibility of gas flow in microchannels.

According to the literature, the effect of compressibility can occur even for a low Mach number below the classical value of $Ma = 0.3$ (at which the fluid is often assumed to be incompressible in the theory). Some authors observed variations in the gas density that generate local acceleration of the gas flow which would result in higher friction of the fluid. This was, for instance, observed by Chung *et al.* [60], who studied the flow of water and nitrogen in 100 μm diameter circular microchannels. While the authors found that the experimental and theoretical results were in agreement with water, for a gas, compressibility effects (producing a non-linear pressure distribution in the channel) had to be taken into account for the measured friction factors to agree with the theory. Asako *et al.* [61] studied nitrogen flow in fused silica microtubes with a diameter of 150 μm. Through this study, they investigated the influence of compressibility on the friction factor. They observed that the friction factor varied with the Mach number through the following correlation:

$$C_f = \frac{64 - 11.99Ma + 263.7Ma^2}{Re} \tag{I.41}$$

Hong *et al.* [29] as well as Tang *et al.* [62] conducted the same study on the effect of the compressibility of the fluid (air and nitrogen as working fluid) in microchannels with hydraulic diameter ranging from 2 μm to 50 μm and observed the same variation of friction factor as function of Ma. Vocale *et al.* [63] investigated numerically the effect of gas compressibility in rectangular microchannels with a hydraulic diameter ranging from 100 μm to 500 μm and aspect ratio of the rectangular shape of the channels ranging from 0.25 to 1. The numerical model was validated through a comparison with experimental data carried out in a rectangular microchannel with a hydraulic diameter equal to 295 μm and with an aspect ratio equal to $\alpha = 0.69$. The authors observed an increase in the friction factor as the Mach number increased. The highest friction factors were also obtained for microchannels with the lowest values of aspect ratio.

To conclude this section, it seems that for gas flows, even at low Mach numbers, compressibility effects must be taken into account and have an effect on friction coefficients. Based on the literature review, another parameter that can influence the flow is the aspect ratio which will be discussed in the next section.

Table I.3: Influence of the compressibility of gas on fluid flow in microchannels

Authors	D_h (μm)	Microchannel cross-section shape	Working fluid	Range of Re	Range of Ma	Conclusion of the study
Araki [58] (2002)	3 - 10	Trapezoidal	N2 He	0.04 - 4.2	10-4 - 0.1	Compressible friction factor is higher than incompressible friction factor and increased as Mach number increased
Ying-Tao [64] (2002)	26 - 39	trapezoidal	N_2	10 - 550	- -	Deviations from the theory with incompressible assumption were observed and therefore attributed to compressible effects.
Yang [65] (2003)	173 - 4010	Circular	Water R-134a Air	200 -15000	- -	Experimental results for both liquid and gas flow are in good agreement with theory in the laminar regime. C_f for gas flow deviated from theory at high Re.
Hsieh [66] (2004)	80	Circular	N2	2.6 - 89.4	0.001 - 002	Pressure drop showed non-linear behavior at low Ma ($Ma \leq 0.3$) unlike in larger channels due to compressibility effects.
Turner [38] (2004)	5 - 96	Parallel plate	He N_2	0.1 - 10000	0.05 - 0.35	C_f increased around 8 % as Ma increased
Asako [61] (2005)	100 - 150	Circular	N_2	- -	0.05 - 0.4	$C_f.Re$ increased as Ma increased. Correlation for $C_f.Re$ as function of Ma is obtained.
Kohl [67] (2005)	25 - 100	Rectangular	Water Air	5 - 19000	- -	*Liquid flow:* Good agreement with theory at macroscale. *Gas flow:* Compressible friction factor should be used to correctly characterize the friction characteristics of gas flow.
Tang [39] (2007)	50 - 200	Rectangular Circular	N_2 He	3 - 6200	0.01 - 0.6	C_f is higher than theoretical value due to compressibility effect.
Vijayalakshmi [34] (2009)	60.5 - 211	Trapezoidal	Water N_2	200 - 7000	- -	Compressibility effect are significant for Ma around the value of 0.3 and above but is not important for lower Ma.

I.2.5. Influence of aspect ratio on friction characteristics

As presented in the previous section, Vocale *et al.* [63] carried out a numerical study of gas flow in rectangular microchannels (D_h ranging from 100 μm to 500 μm) with various aspect ratios (ranging from 0.25 to 1). Their numerical results were validated through a comparison with experimental data in the case of a rectangular channel with D_h= 295 μm and $\alpha = 0.69$. They found the highest friction factors for the channels with the lowest values of aspect ratio. Indeed, as the aspect ratio decreases, the behavior of fluid flow in the microchannels is more likely similar to the fluid flow between two parallel plates. This results in the limitation of using hydraulic diameter alone to characterize flow.

In the case of a non-circular cross-section, a correction factor has to be added in the determination of the friction factor as shown in Equation I.29.

Papautski *et al.* [68] studied the flow of water inside rectangular metallic pipette arrays with width ranging from 150 to 600 μm and height ranging from 22.71 to 26.35 μm while the aspect ratio of the rectangular cross-section varied from 0.0379 to 0.1757. Re was in the range of 0.001 to 10. The authors observed a deviation of 20 % from theoretical values for a low aspect ratio.

Hrnjak *et al.* [52] investigated the flow of R-134a (liquid and vapor) in rectangular microchannels with hydraulic diameters ranging from 69.5 to 304.7 μm while the aspect ratio ranged from 0.09 to 0.24. Re varied from 112 to 9180. The experimental data were found in good agreement with the correlation of friction factor for rectangular channels defined in the equation I.29. This means that for liquid flows inside small rectangular channels, the friction factor correlation still ensures the characterization of the flows, therefore we will use this definition of friction factor for the calculation of our friction factor.

I.2.6. Entrance effect

Ahmad *et al.* [69] studied the influence of the scaling effect in the entrance region for liquid flow in the laminar regime. The hydraulic diameter of their channels ranged from 0.1 to 0.5 mm. The authors observed that for Re > 10, there was no significant effect of the dimension of the channel on the entry length and therefore only depends on the Reynolds number. They also proposed a general correlation for the entrance length:

$$\frac{L_e}{D_h} = \frac{0.60}{0.14Re + 1} + 0.0752Re \tag{I.42}$$

Galvis *et al.* [70] investigated on the influence of the aspect ratio on the entrance length in rectangular channels with hydraulic diameter in the range 0.1 - 0.5mm, aspect ratio ranging from 0.2 to 1. The Reynolds number ranged from 50 to 200. A general correlation is given below:

$$\frac{L_e}{D_h} = \frac{C_1}{C_2Re + 1} + C_3Re \tag{I.43}$$

From this correlation, the coefficients C_1, C_2, and C_3 are given in the table I.4 for different values of aspect ratio.

This overview of both liquid and gas steady flows in microchannels has highlighted the influence of various factors related to channel geometry, such as hydraulic diameter, wall roughness and aspect

Table I.4: Coefficient of the equation for different aspect ratio

Aspect ratio α	0.2	0.4	0.8	1
C1	1.1471	1	0.715	0.740
C2	0.034	0.098	0.115	0.09
C3	0.0818	0.9890	0.0825	0.0889

ratio, as well as other factors such as fluid compressibility, which must be taken into account even at lower Mach numbers than 0.3 unlike for flows on a macroscopic scale. As mentioned in the introduction, this paper is concerned with alternating flows, such as can be observed in Stirling engines. In the next section, therefore, we will focus on the studies carried out so far on alternating flows and outline the main characteristics of these flows. Nevertheless, the deviations observed by authors were also probably mainly due to the uncertainties of measured dimensions and accuracy of the used sensors. The deviations from theory decreased as well along with time.

I.3 Oscillating flow

We recall that the objective of this study is to provide a better understanding of flows generated inside the miniature Stirling engine [5],[6] to improve the design of these devices. These Stirling engines are characterized by alternating gas flows. Currently, alternating flows were studied mainly on a macroscopic scale, and in the presence of porous media (regenerator). Thus, unless otherwise stated, the majority of works in the literature presented here concern studies on a macroscopic scale and/or in a porous medium.
Oscillating flows are characterized by time-varying quantities (such as velocity, pressure, and temperature but also density as a consequence of gas flow). Alternating flows are a particular kind of oscillating flow for which the mean velocity along a period is null. As for these kind of flows, the displacement $X(t)$ of the fluid is defined by:

$$X(t) = X_{max} sin(\omega t) \tag{I.44}$$

where X_{max} corresponds to the maximum displacement of the fluid along a period, ω the angular frequency of the flow oscillation, and t the time.

I.3.1. Annular effect

At the macro-scale, these flows have been widely studied. The first investigations involving oscillating flows were undertaken by Richardson [71] on a Helmholtz acoustic wave resonator. The authors showed that the velocity profile of the flow exhibited a delocalized maximum at the edges of the circular orifice, in contrast to the classically localized velocity maximum at the center of the pipe. This phenomenon was explained by the authors as a consequence of the fluid's inertia. The greater the frequency of flow oscillation, the more pronounced the observed phenomenon [72], as can be seen in Figure I.4.

Interest in oscillating flows was further stimulated by studies in the fields of respiration and blood circulation. Lambossy [73] showed that the oscillating flow velocity profile was related to the dimensionless number n:

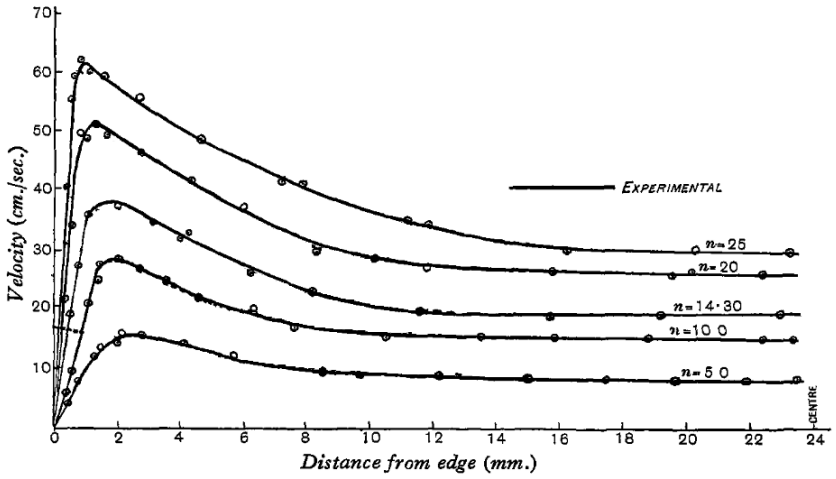

Figure I.4: Velocity profile in square section channel [72]

$$n = R\sqrt{\frac{\rho\omega}{\mu}} \tag{I.45}$$

where R is the radius of the pipe, ρ the density of the fluid, ω the angular frequency and μ the dynamic viscosity.

In addition to the annular effect, a phase lag between pressure and velocity values can be observed in oscillating flows: this is the subject of the following section.

I.3.2. Phase lag between pressure and velocity

Helps and McDonald [74] studied the oscillating flow of blood generated in dog arteries and observed a phase lag between velocity and pressure gradient. Following this study, Womersley [75] provided an exact solution of the equations of oscillating flow studied by Helps and McDonald and observed that the phase lag between velocity and pressure gradient (figure I.5) was related to a frequency dimensionless number:

$$Wo = R_h\sqrt{\frac{\omega}{\nu}} \tag{I.46}$$

where Wo represents the Womersley number, R_h the hydraulic radius (4 times lower than hydraulic diameter), ω represents the angular frequency, and $\nu = \frac{\mu}{\rho}$ the kinematic viscosity.

I.3.3. Velocity profile

Uchida [76] proposed an exact solution of oscillating incompressible flow in a circular pipe. Considering unidirectional flow with axial symmetry $U = U_x(x,r,t)$ and neglecting external forces, the following equations describe the behavior of the flow:

$$\begin{cases} \frac{\partial U_x}{\partial x} = 0 \\ \frac{\partial P}{\partial r} = 0 \\ \frac{\partial U_x}{\partial t} = -\frac{1}{\rho}\frac{\partial P}{\partial x} + \nu\left(\frac{\partial^2 U_x}{\partial r^2} + \frac{1}{r}\frac{\partial U_x}{\partial r}\right) \end{cases} \tag{I.47}$$

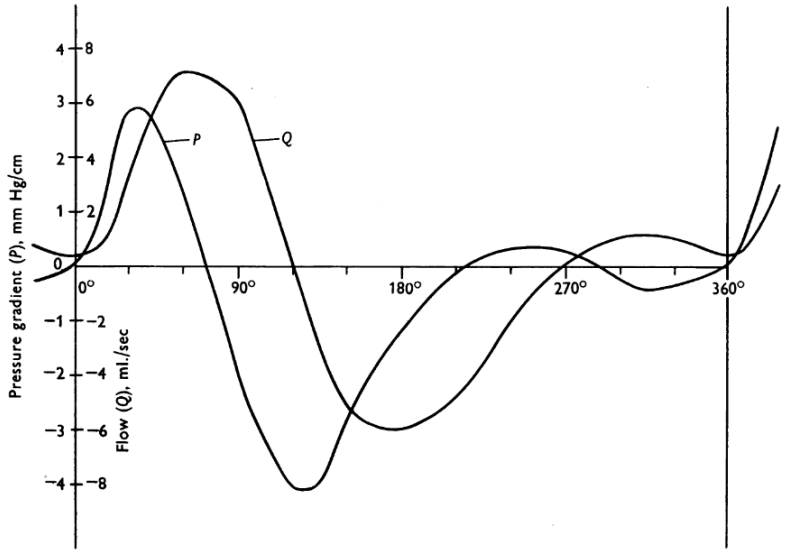

Figure I.5: Phase lag between flow rate (Q) and the pressure gradient (P) in the femoral artery of a dog [75]

Considering a sinusoidal pressure gradient, which can be expressed by:

$$-\frac{1}{\rho}\frac{\partial P}{\partial x} = P_{X0} + \sum_{n=1}^{\infty} P_{Xcn} cos(nt) + \sum_{n=1}^{\infty} P_{Xsn} sin(nt) = P_{X0} + \sum_{n=1}^{\infty} P_{Xn} e^{int} \tag{I.48}$$

The authors found an exact solution for the velocity:

$$U = \frac{P_{X0}}{4\nu}(R^2 - r^2) - \sum_{n=1}^{\infty} \frac{iP_{Xn}}{n}\left[1 - \frac{J_0(k\,r\,i)^{3/2}}{J_0(k\,R\,i)^{3/2}}\right] e^{int} \tag{I.49}$$

with J_0 the Bessel function of the first kind, $k = \sqrt{\frac{\omega}{\nu}}$, and R the radius of the channel.

This solution for the velocity of the fluid has been then represented for different Womersley numbers and is shown in Figure I.6 taken from the thesis of Meunier [77]. The different colors represent different dimensionless times of the period, from t^* = 0 to t^* = T by increment of 0.1 T, where T corresponds to the time period of the flow. These graphics showed again the annular effect observed by Richardson [71]. This annular effect was increasingly pronounced as the Womersley number increased.

I.3.4. Similarity parameters for oscillating flow

In the last decades with the growing interest in the Stirling engine and its application, alternating flow in porous media such as regenerators have been extensively studied at macro scales. Since alternating flows are characterized by unsteady quantities such as the velocity of the flow which varies along the period of oscillation of the flow, the classical definition of the Reynolds number cannot be used anymore to characterize the flows.

Ohmi *et al.* [78] used another definition of the Reynolds number based on the mean amplitude of the velocity to describe the characteristics of oscillating flow as follows:

$$\bar{Re} = \frac{|\bar{u}|D_h}{\nu} \tag{I.50}$$

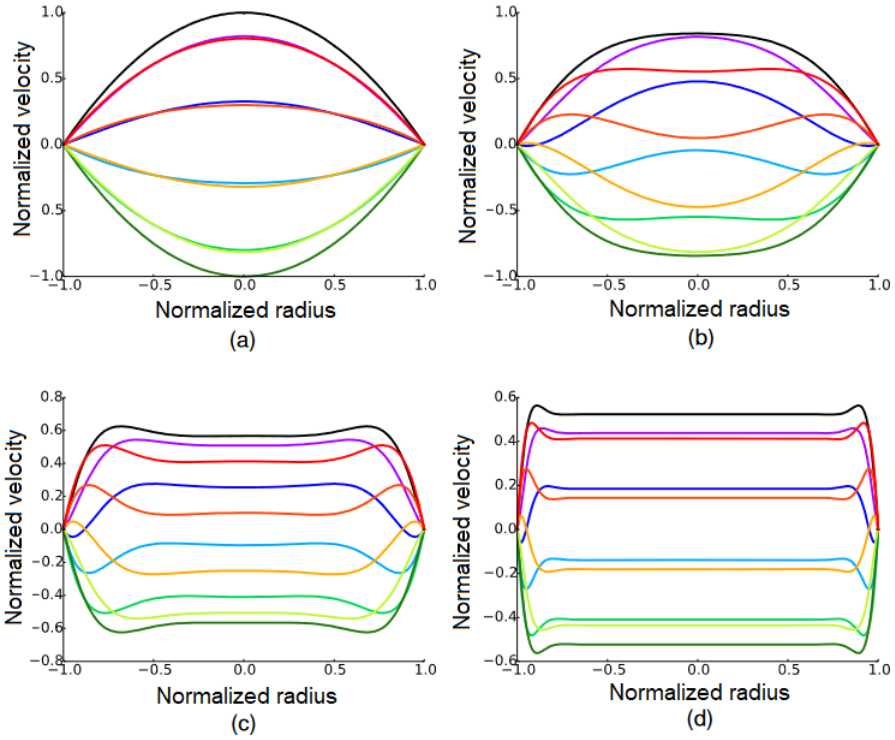

Figure I.6: Velocity profile for (a) $Wo = 1$, (b) $Wo = 4$, (c) $Wo = 10$, (d) $Wo = 30$ [77]

Where $\bar{Re}$ represents the Reynolds used for oscillating flow and $|\bar{u}|$ is the mean amplitude of the velocity.

However, as the mean velocity of alternating flow is equal to zero, the mean-velocity-based Reynolds number cannot be used to characterize the flows that are generated in the Stirling engine. Therefore, Simon and Seume [79] used a new definition of the Reynolds number based on the maximum velocity in the flow:

$$Re_{max} = \frac{U_{max} D_h}{\nu} \tag{I.51}$$

where Re_{max} represents the Reynolds number based on the maximum value of the fluid's velocity, U_{max} represents the maximum of the velocity and ν the kinematic viscosity.

I.3.4.1 Characterization of the unsteadiness of the flow

As mentioned earlier, the Womersley number is used to characterize the unsteadiness of the oscillating flow. This dimensionless number shows the influence of the frequency of flow oscillations on the behavior and characteristics of these flows. However, a different definition of this dimensionless frequency is used to describe the behavior of oscillating flow depending on the characteristics length used. The Womersley number used the hydraulic radius of the channel to characterize oscillating flow while the so-called frequency (or kinematic) Reynolds number used the hydraulic diameter and is defined as:

$$Re_\omega = \frac{\omega D_h^2}{\nu} \tag{I.52}$$

This frequency Reynolds number characterizes the unsteadiness of the flow and is related to the Womersley number by the following relation:

$$Re_\omega = 16\,Wo^2 \tag{I.53}$$

Other authors used the Valensi number which is defined and related to the Womersley number as:

$$Va = \frac{\omega R_h^2}{\nu} = Wo^2 = \frac{1}{16} Re_\omega \tag{I.54}$$

I.3.4.2 Dimensionless equations for oscillating flows

Simon and Seume [79] studied alternating flow inside Stirling engine heat exchangers They introduced the following dimensionless quantity: $t^* = t\ \omega_0$ and U_{max} instead of U_0 into the equation I.1, I.2 and I.3, to obtain the following dimensionless equations:

- Equation of continuity

$$\frac{\partial \rho^*}{\partial t^*} + \overrightarrow{\nabla}.(\rho^* U^*) = 0 \tag{I.55}$$

- Equation of momentum conservation

$$\rho^* \rho_0 \left[U_{max}\omega_0 \frac{\partial \overrightarrow{U^*}}{\partial t^*} + \frac{U_{max}^2}{L_c}(\overrightarrow{U^*}.\overrightarrow{\nabla^*})\overrightarrow{U^*} \right] = \frac{\rho_0 U_{max}^2}{L_c}\overrightarrow{\nabla^*}P^* + \mu^*\mu_0 \frac{U_{max}}{L_c^2}\overrightarrow{\nabla}^{*2}\overrightarrow{U^*} \tag{I.56}$$

After simplification, this results in:

$$\rho^* \left[\frac{\rho_0 \omega_0 L_c^2}{\mu_0} \frac{\partial \overrightarrow{U^*}}{\partial t^*} + \frac{\rho_0 U_{max} L_c}{\mu_0}(\overrightarrow{U^*}.\overrightarrow{\nabla^*})\overrightarrow{U^*} \right] = \frac{\rho_0 U_{max} L_c}{\mu_0}\overrightarrow{\nabla^*}P^* + \mu^*\overrightarrow{\nabla}^{*2}\overrightarrow{U^*} \tag{I.57}$$

By replacing Re_ω and Re_{max} in the dimensionless equation I.57 we obtain:

$$\rho^* \left[Re_\omega \frac{\partial \overrightarrow{U^*}}{\partial t^*} + Re_{max}(\overrightarrow{U^*}.\overrightarrow{\nabla^*})\overrightarrow{U^*} \right] = Re_{max}\overrightarrow{\nabla^*}P^* + \mu^*\overrightarrow{\nabla}^{*2}\overrightarrow{U^*} \tag{I.58}$$

- Equation of energy

$$\begin{aligned} \rho_0\,\rho^* C_{P0}\,C_P^* \left[\Delta T\,\omega_0 \frac{\partial T^*}{\partial t^*} + \frac{U_{max}\Delta T}{L_c}(\overrightarrow{U^*}.\overrightarrow{\nabla^*})T^* \right] = \\ \rho_0 U_{max}^2 \omega_0 \frac{\partial P^*}{\partial t^*} + \frac{\rho_0 U_{max}^3}{L_c}(\overrightarrow{U^*}.\overrightarrow{\nabla^*})P^* + \frac{k_0}{L_c^2}\overrightarrow{\nabla}^{*2}T^* + \frac{\mu_0 U_{max}^2}{L_c^2}\Phi^* \end{aligned} \tag{I.59}$$

After simplification, the equation I.59 gives :

$$\begin{aligned}\rho^* C_P^* \left[\frac{\rho_0 \omega_0 L_c^2}{\mu_0} \frac{\partial T^*}{\partial t^*} + \frac{\rho_0 U_{max} L_c}{\mu_0} (\overrightarrow{U^*}.\overrightarrow{\nabla^*}) T^* \right] = \left(\frac{\rho_0 \omega_0 L_c^2}{\mu_0} \right) \left(\frac{U_{max}^2}{C_{P0} \Delta T} \right) \frac{\partial P^*}{\partial t^*} \\ + \left(\frac{\rho_0 U_{max} L_c}{\mu_0} \right) \left(\frac{U_{max}^2}{C_{P0\Delta T}} \right) (\overrightarrow{U^*}.\overrightarrow{\nabla^*}) P^* + \frac{k_0}{\mu_0 C_{P0}} k^* \overrightarrow{\nabla}^{*2} T^* + \frac{U_{max}^2}{C_{P0} \Delta T} \Phi^*\end{aligned} \tag{I.60}$$

By replacing Re_ω and Re_{max} in the dimensionless equation I.57 we obtain:

$$\begin{aligned}\rho^* C_P^* \left[Re_\omega \frac{\partial T^*}{\partial t^*} + Re_{max} (\overrightarrow{U^*}.\overrightarrow{\nabla^*}) T^* \right] = Re_\omega Ec_{max} \frac{\partial P^*}{\partial t^*} \\ + Re_{max} Ec_{max} (\overrightarrow{U^*}.\overrightarrow{\nabla^*}) P^* + \frac{1}{Pr} \overrightarrow{\nabla}^{*2} T^* + Ec_{max} \ \Phi^*\end{aligned} \tag{I.61}$$

I.3.4.3 Dimensionless displacement

Simon and Seume [79] defined a dimensionless number characterizing the relative displacement in the case of an oscillating flow, in a Stirling engine:

$$A_R = \frac{X_{max}}{L_{ch}} \tag{I.62}$$

Where X_{max} stands for the maximal displacement of fluid during a period ($X_{max} = \frac{V_{swept}}{A_{ch}}$ with V_{swept} the volume swept by the piston during a period and A_{ch} the channel cross-section) and L_{ch} is the length of the channel.

- $A_R < 1$: The displacement of the fluid in a half-period is lower than the length of the channel. Therefore, some part of the fluid always remains in the channel.
- $A_R = 1$: The displacement of the fluid in a half-period is equal to the length of the channel
- $A_R > 1$: The displacement of the fluid in a half-period is higher than the length of the channel.

Since for a sinusoidal oscillating flow, $U_{max} = \frac{X_{max}\,\omega}{2}$, the dimensionless displacement can also be expressed as:

$$A_R = \frac{2\,U_{max}}{\omega\,L_{ch}} = \frac{2}{L_{ch}} \frac{U_{max}\,D_h^2/\nu}{\omega\,D_h^2/\nu} \tag{I.63}$$

Therefore, there is a relation between the dimensionless displacement A_R, the ratio $\frac{D_h}{L_{ch}}$ and both Re_{max} and Re_ω.

$$A_R = \frac{1}{2} \frac{D_h}{L_{ch}} \frac{Re_{max}}{Re_\omega} \tag{I.64}$$

I.3.4.4 Transition laminar-turbulent regime

Unlike steady flows for which the laminar/turbulent regime is determined by the value of the Reynolds number (and therefore determined by the flow velocity), for oscillating flows the Reynolds number fluctuates as a function of time, making the flow likely to undergo a transition from laminar to turbulent within an oscillation period, depending on the instantaneous flow velocity. Since the flow regime has a major influence on its frictional characteristics, it is necessary to understand its mechanism for an oscillating flow.

Tew *et al.* [80] reported that for oscillating flows, the critical Reynolds number for which the transition from laminar to turbulent regime occurs is a function of the Valensi number as shown in figure I.7 which shows the different limits of laminar and turbulent regimes for both steady and oscillating flow.
NB: figure I.7 is clearly plotted versus the Valensi number rather than Re_w. The two dimensionless numbers are proportional to each other with a factor equal to 4. As a general remark, it is important to be careful with the dimensionless numbers used, to avoid misleading interpretations of the results presented. For our study, we will only use the Womersley number to characterize oscillating flows.

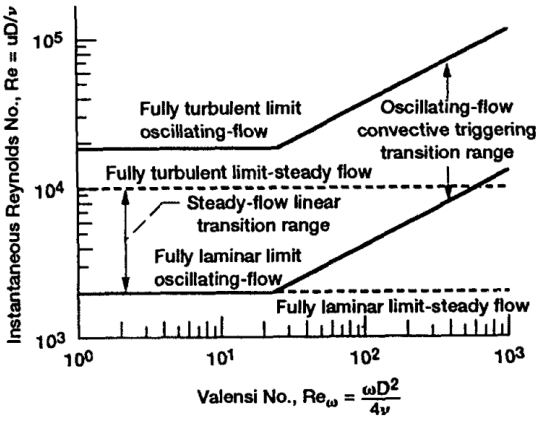

Figure I.7: Critical Reynolds number for which transition from laminar to turbulent regime occurs for both steady and oscillating flows [80]

Several authors have developed correlations between the Womersley number and the critical Reynolds number corresponding to the transition from laminar to turbulent flow. Other studies provided a correlation between Re_{max} and the Womersley number. These correlations are given in table I.5.

I.3.4.5 Correlation for friction factor

The friction factor for oscillating flows used for the comparison of friction characteristics of flow is often determined by its mean value during an oscillation period. This mean friction factor is also often represented as a function of Re_{max} or Re_ω which are characteristics of the oscillating flow.

Gedeon and Wood [87] observed that the friction factor under oscillating flow conditions could be expressed in the following general form:

$$C_f = \frac{a}{Re} + bRe^c \tag{I.65}$$

Table I.5: Correlation between critical Reynolds number and Re_{max} with Womersley number (or Re_ω)

Correlation Re max and Rew					
Authors	**Channel dimensions**	**Microchannel cross-section shape**	**Working fluid**	**Validity range**	**Corrrelation**
Sergev [81] (1966)	$D_h = 3.8 - 12.1\ mm$ $L = 17.5 - 100\ cm$	Circular	Water	$Wo = 4 - 40$	$Re_c = 700\,Wo$
Park and Baird [82] (1970)	$D_h = 6 - 18.9\ mm$ $L = 99 - 372\ cm$	Circular	Water	$Wo = 6 - 31.6$	$Re_c = 188\,Wo^{4/3}$
Iguchi [83](1982)	U-tube $D_h = 15.8\ mm$	Circular	Water + Glycerine mixture	$100 \leq Re_\omega \leq 800$	$Re_{max} = 800\,Re_\omega{}^{0.5}$
Ohmi [84] (1982)	$D = 50\ mm$ $L = 5\ m$	Circular	Air	$42 \leq Wo \leq 71$	$Re_{max} = 400\,Wo$
Ahn *et al.* [85] (1982)	$D = 50.4\ mm$ $L = 6000\ mm$	Circular	Gas	$1920 \leq Re_{max} \leq 60800$	$Re_{max} = (211\,Wo)^{8/7}$
Zhao *et al.* [86] (1996)	$D_h = 13.5\ mm$	Circular	Air	$Re_\omega = 81 - 540$ $A_{Dh} = 53.4 - 113.5$	$Re_{max} = 380.5\sqrt{Re_\omega}$

with a, b, and c constants to be determined according to experimental data. Zhao *et al.* [86], studied oscillating air flow inside tubes of hydraulic diameter equal to 13.5 *mm*, and Reynolds number ranging from 81 to 540. The dimensionless displacement ranged from 53.4 to 113.5. The authors proposed a correlation for the friction factor expressed as:

$$C_f = \frac{1}{A_{Dh}}\left(\frac{76.6}{Re_\omega^{1.2}} + 0.40624\right) \tag{I.66}$$

Other correlations were proposed by several authors, mainly for gas flows inside porous channels. These correlations and experimental conditions are given in Table I.6. Given the diversity of porous materials (wire screens, metal foams, etc.), experimental conditions, and dimensions tested, it is difficult to determine a general trend in these correlations. This being said it does enable us to determine a rough estimate for the friction factor.

I.3.5. Oscillating flows inside mini and micro-channels

Even though, numerous investigations have been carried out on the characteristics of oscillating flows at the macroscale, as far as we know these kinds of flows are still not well known and almost not investigated in sub-millimetric channels. Most of the work on oscillating alternating flow at milli or micro scale was carried out in porous media (see previous section), and cannot be directly extrapolated to empty channels. Moreover, many studies have proved difficult at these scales due to technical issues in achieving accurate and relevant measurements in the characterization of these kinds of flows. Consequently, we found very few references on the subject in the literature.

Karbashi *et al.* [97] studied numerically and experimentally oscillating water flow in a capillary with a diameter of 450 μm. Frequencies of the oscillation were ranging from 5 to 100 Hz. The authors observed the same phase shift between velocity and pressure as mentioned earlier in the range 5 - 60 Hz. For the experimental and CFD data, the authors represent this phase shift as a function of the frequency in figure I.8. They obtained good agreement between their model and experimental values.

Table I.6: Correlations for alternating flows inside porous channel

Correlation $C_f - Re_{max}$ and $C_f - Re_\omega$					
Authors	**Channel dimensions**	**Channel shape**	**Working fluid**	**Validity range**	**Corrrelation**
Tanaka *et al.* [88] (1990)	$D_h = 0.05 - 0.45\ mm$ $\varepsilon_p = 0.372 - 0.956$	Wire netting Sponge metal Sintered metal	Air	$Re = 4 - 4000$	$C_f = \frac{40.7413}{Re_{max}} + 0.5315$
Gedeon & Wood [87] (1996)	$d_w = 12.7 - 94\ \mu m$ $e_s = 7.5 - 22.1\ mm$ $\varepsilon_p = 0.623 - 0.841$	Woven screens Metal felts	Gas	$d_w = 0.053 - 0.094$ $d_w = 0.0127 - 0.051$ $Re_{max} = 0.45 - 6000$	$C_f = \frac{129}{Re_{max}} + \frac{2.91}{Re_{max}^{0.103}}$ $C_f = \frac{192}{Re_{max}} + \frac{4.53}{Re_{max}^{0.067}}$
Hsu *et al.* [89] (1999)	$d_w = 0.224 - 0.32\ mm$ $D_h = 0.509 - 1.213\ mm$ $\varepsilon_p = 0.694 - 0.792$	Woven screens	Air	$Re_{max} = 0.27 - 2600$	$C_f = \frac{109.3}{Re_{max}} + \frac{5}{Re_{max}^{0.5}} + 1$
Choi *et al.* [90] (2004)	$d_w = 30 - 52\ \mu m$ $D_h = 63.5 - 110.5\ mm$ $\varepsilon_p = 0.679 - 0.697$	Wire screen	Air	Re = 5 - 100	$C_f = \frac{39.52}{Re} + 0.01$
Leong *et al.* [91] (2006)	$d_l = 112.6 - 427.2\ \mu m$ $D_h = 1.01 - 4.32\ mm$ $\varepsilon_p = 0.9$	Al metal foam	Air	$Re_\omega = 0.46 - 57.9$ $ADh = 12.7 - 67.5$	$C_f = \frac{1}{A_{Dh}}(\frac{86.7}{Re_\omega^{0.19}} + 0.61)$
Shen *et al.* [92] (2008)	$D_h = 0.05 - 0.28\ mm$ $d_w = 0.025 - 0.1\ mm$ $\varepsilon_p = 0.67 - 0.735$	Woven screens	Air	$Re_{max} = 5 - 100$	$C_f = \frac{97.43}{Re_{max}} + 1.6665$
Jin *et al.* [93] (2008)	$d_l = 112.6 - 427.2\ \mu m$ $D_h = 1.01 - 4.32\ mm$ $\varepsilon_p = 0.9$	Al metal foam	Air	$Re_\omega = 0.46 - 57.9$ $ADh = 12.7 - 67.5$	$C_f = \frac{1}{A_{Dh}}\left(\frac{403.2}{Re_\omega} + 1789.1\right)$
Kahaleras *et al.* [94] (2014)	$D_h = 0.178 - 0.250\ mm$ $\varepsilon_p = 30\% - 40\%$	Stainless steel porous matrix	Air	$\varepsilon_p = 30\ D_h = 0.178$ $\varepsilon_p = 35\ D_h = 0.237mm$ $\varepsilon_p = 40\ D_h = 250mm$	$C_f = \frac{0.00689}{Re_\omega} + 0.791$ $C_f = \frac{0.00279}{Re_\omega} + 0.00186$ $C_f = \frac{0.00246}{Re_\omega} + 0.02962$
Xiao *et al.* [95] (2017)	$d_w = 30 - 150\ \mu m$ $D_h = 0.0596 - 0.551\ mm$ $\varepsilon_p = 66.5\% - 78.6\%$	Woven screens	Air	$Re_\omega = 0.00143 - 0.204$ $A_{Dh} = 4600 - 20300$ $Re = 2.7 - 553$	$C_f = \frac{134}{Re} + \frac{5.44}{Re^{0.188}}$
Dellali *et al.* [96] (2019)	$D_h = 2.1 - 3.7\ mm$ $\varepsilon_p = 80\% - 90\%$	Array of pillars lenticular shape	Air	$Re_\omega = 3.6 - 56.4$ $Re_{max} = 800 - 6200$	$C_f = 11.88 Re_{max}^{-0.262}$

d_w corresponds to the diameter of wire, which is related to the hydraulic diameter for flow inside porous media
d_l corresponds to the ligament diameter related to the hydraulic diameter for flow inside porous media constituted of metal foams
e_s corresponds to the thickness of the samples and ε_p represent the porosity of the media

Recently, Dellali [5] [96]investigated alternating flow in both milli- and micro-scale porous regenerators. The authors added a time-dependent term proportional to $\frac{\partial U}{\partial t}$ in the expression of the friction factor to take into account the unsteadiness of the alternating flow. The resulting friction factor was expressed as:

$$C_{f\,osc} = C_{f\,st} - \frac{2D_h}{U^2(t)}\frac{\partial U}{\partial t} \tag{I.67}$$

Considering an unsteady compressible and isothermal flow, the expression of the friction factor established in the equation I.33 becomes:

$$C_{f\,osc} = \frac{2D_h}{L}\left[\left(\frac{P_1(t)^2 - P_2(t)^2}{r_G[T_1(t)+T_2(t)](\frac{\dot{m}}{A})^2}\right) - ln\left(\frac{P_1(t)}{P_2(t)}\right) + ln\left(\frac{T_1(t)}{T_2(t)}\right) - \frac{D_h}{U^2(t)}\frac{\partial U}{\partial t}\right] \tag{I.68}$$

The results of the measurements carried out in the microscale porous regenerator were unsuccessful due to the small pressure drop along the regenerator. The acquired signals delivered by the pressure sensors did not provide reliable values for the pressure drop.

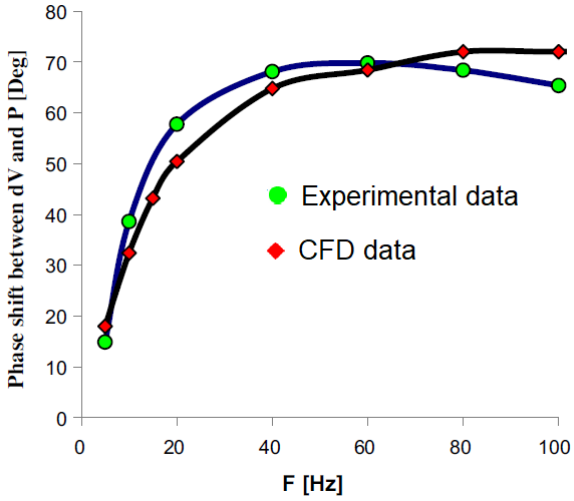

Figure I.8: Phase shift between inlet velocity and pressure through a capillary of D = 450 μm for different frequencies - Karbaschi *et al.*, figure 7 [97]

Chapter conclusion

In this chapter, we highlighted the contribution of both roughness and fluid compressibility when it comes to gas flows inside channels at the microscale. These contributions become significant for a larger range of respectively relative roughness and Mach number, which characterize the compressibility of the flow than for the case of flows at the macroscale. Regarding oscillating flows at the macro-scale, this review of literature investigations highlighted the importance of using mean or maximum quantities to be able to characterize these particular flows since quantities such as velocity, pressure, and temperature vary over time.

This review of results from the literature allowed us to design the microchannels as well as the sensors implemented within these microchannels. Our study will focus on the influence of hydraulic diameter, and other geometrical parameters as well as the impact of bends on flow characteristics. The study will include both gas steady and alternating flows to make a proper comparison between the impact of parameters for steady and alternating flows.

The design of the channels and the sensors used to carry out this study will be presented in the next chapter, the dimensions of the channel will ensure that rarefaction effects can still be neglected. Despite roughness will not be studied, a careful measurement of it will allow us to take its influence into account in our experimental results. These channels will allow the study of alternating flows within square and rectangular channels with hydraulic diameters ranging from 1 *mm* to 100 μm and aspect ratio in the range 0.1 to 1.

CHAPTER II

DESIGN OF THE MICROCHANNELS

This chapter will present the design of the microchannels and the sensors realized to enable the characterization of steady and alternating gas flows. As illustrated in the previous chapter, when the dimensions of the channels decrease, the contribution of the roughness of the channel walls as well as the effects of compressibility become significant for a relative roughness of about $\varepsilon_r = 1$ % [36] and low Mach number [58][66] unlike the "classical" flows at macroscopic scale for which these effects can be neglected (when $\varepsilon_r \leq 5$ % [37] for the effect of relative roughness, and when Ma ≤ 0.3 [9] for the effect of compressibility).

Studying the influence of roughness requires a method to control the parameters defining the roughness, which implies fabrication skills that are too complex to be studied in the framework of this thesis. Nevertheless, particular attention will be given to determining as precisely as possible the value of this average roughness along the channels for each configuration, to take into account as well as possibly the influence of this parameter.

The objective of the work will be to study the influence of several geometrical parameters (e.g. hydraulic diameter) on the steady and alternating flows. Moreover, for the miniature Stirling machine realized at the FEMTO-ST institute during a previous work [6], another relevant parameter that may decrease the efficiency of the system is the presence of bends in the channels' design, which probably led to increase the pressure losses. Therefore, some of the microchannels will be designed with bends to study their influence on the pressure drops.

This chapter will present first the choice of the microchannels' dimensions (hydraulic diameter, width, height, aspect ratio, and length), to perform the most relevant studies. In addition, the design of device that allows the adaptation of cross-section, will be presented.

In a second step, some metrology methods used in literature to achieve temperature and pressure measurements in mini- and micro-channels will be presented, followed by the sensors design that has been chosen for our study.

II.1 Design of the devices

Since the channels were manufactured using microfabrication technologies available at the FEMTO-ST cleanroom, a number of technology constraints had to be taken into account.

- We have chosen to use silicon and glass as manufacturing materials, because these are reference materials for microfabrication.
- Due to the microfabrication techniques chosen, the channels had a square or rectangular cross-section. This justified the use of the notion of hydraulic diameter presented below.
- In order to connect our microchannels to the fluid circulation system, a rectangular to circular cross-section transition, with a gradual change from millimetric to micrometric scale, had to be sized to limit its influence on the flow behavior.

Indeed, before reaching the microchannel, the fluid moves through a circular tube of several *mm* in diameter and then has to cross a sub-millimeter rectangular channel. In order to minimize the effect of the cross-sectional change, a "transition" section of pipe - that is specific to each type of microchannel - had to be designed. This transition section from millimeter to micrometer scale could not be considered simply by using microfabrication, because changes from circular to rectangular cross-section were not possible with the selected microfabrication techniques. Therefore, we have chosen an alternative solution based on two transition sections: one at millimeter scale fabricated in 3D using stereo-lithography (SLA) for the transition from a circular to a rectangular cross-section, followed by another section for the transition from millimeter to micrometer scale that was made using 2D microfabrication on silicon because SLA could not meet the resolution required for the smallest microchannels.

Figure II.1 shows the design of the fabricated devices, including the sections for the 2D cross-section change on either side of the microchannel. The latter is located at the center of the device (*C*) with a width w_{ch} and a length L_{ch}. At both ends of the microchannel (*B* and *D*), converging and diverging sections are used to match the dimension of the microchannel width to the diameter of the tube used in the circulating system. The length of these converging and diverging sections was sized to limit the disturbance on the flow as well as the minor pressure drop generated in a sharp transition. The determination of these lengths will be detailed further. Sections at the end of the device (*A* and *E*) were used to connect the device to the experimental bench via the parts manufactured by the SLA technique.

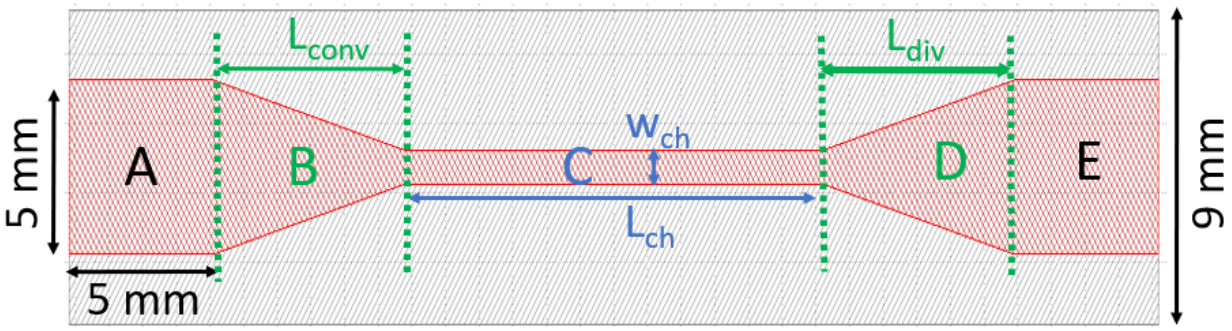

Figure II.1: Design of the micro-channels

II.1.1. Sizing and design of the micro-channels (Section *C*)

II.1.1.1 Hydraulic diameter and length of channels

Since the channels were rectangular or square in cross-section, the hydraulic diameter (cf. chapter I) was a relevant geometric parameter to use. The height of the microchannels was equal to the thickness of the wafer used for its fabrication. For this work, based on the literature review, five different configurations of hydraulic diameter were chosen ranging from 100 μm to 1000 μm. The chosen thicknesses corresponded to some standard dimensions of silicon wafers: 100 ± 5 μm, 200 ± 5 μm, 390 ± 5 μm, 500 ± 5 μm and 1000 ± 5 μm.

Regarding the available surface to length ratio on the 4-inch wafers, two different length configurations (25 mm and 50 mm) were selected. As mentioned in chapter 1, the entrance length is the length required for the flow velocity in the center line to reach 99% of the established velocity U_e. In the laminar regime, this entrance length depends on the hydraulic diameter and on the Reynolds number through the general form:

$$\frac{L_e}{D_h} = K_e\, Re \tag{II.1}$$

The study of Han *et al.* [98] provided a correlation that determined the value of the coefficient K_e for different aspect ratios. The values of K_e are given in table II.1.

Table II.1: Coefficient K_e in the correlation of the entrance length for different aspect ratios

Aspect ratio α	0	0.125	0.25	0.5	0.75	1
Coefficient K_e	0.0099	0.0227	0.0427	0.0660	0.0735	0.0752

Therefore, according to the Reynolds number range for the study, the channel length was chosen to obtain a dynamically established flow.

II.1.1.2 Aspect ratio

We recall that the aspect ratio α of the cross-section is given by α = h/w if h $\leq$ w and α = w/h if h $\geq$ w with h and w being respectively the height and the width of the channel. In order to investigate the influence of aspect ratio over flow characteristics at microscale, microchannels with different aspect ratios were designed, for the same hydraulic diameter and the same other geometrical and fluid flow parameters.

Since the height of the microchannels is determined by the thickness of the wafers, to modify the aspect ratio while keeping the same hydraulic diameter, the width of the microchannel had to be determined. Since the hydraulic diameter is defined for the rectangular channel by:

$$D_h = \frac{2\, h_{ch}\, w_{ch}}{h_{ch} + w_{ch}} \tag{II.2}$$

The relation between the width w_c, the hydraulic diameter D_h and the height h_c of the microchannel can be written as:

$$w_{ch} = \frac{h_{ch}\, D_h}{2\, h_{ch} - D_h} \tag{II.3}$$

Table II.2: Geometrical parameters of the microchannels

Height of channel h_{ch} (μm)	**Width of channel** w_{ch} (μm)	**Aspect ratio** α
$D_h = 100 \pm 6\,\mu m$ $L_{ch} = 25\,mm$		
100 ± 5	100 ± 2	1.00
200 ± 5	67 ± 2	0.335 ± 0.013
390 ± 5	57 ± 2	0.146 ± 0.006
500 ± 5	56 ± 2	0.112 ± 0.004
1000 ± 5	53 ± 2	0.053 ± 0.002
$D_h = 200 \pm 6\,\mu m$ $L_{ch} = 25\,mm$		
200 ± 5	200 ± 2	1.00
390 ± 5	135 ± 2	0.346 ± 0.007
500 ± 5	125 ± 2	0.250 ± 0.005
1000 ± 5	111 ± 2	0.111 ± 0.002
$D_h = 500 \pm 7\,\mu m$ $L_{ch} = 25$ and $50\,mm$		
390 ± 5	696 ± 2	0.560 ± 0.007
500 ± 5	500 ± 2	1.00
1000 ± 5	333 ± 2	0.333 ± 0.002
$D_h = 1000 \pm 5\,\mu m$ $L_{ch} = 25$ and $50\,mm$		
1000 ± 5	1000 ± 2	1.00

The width was determined by replacing in the previous equation all hydraulic diameters studied and all available values for the height of the microchannels according to the thickness of silicon wafers used in the clean room facility. Table II.2 summarizes the different dimensions of the channel considered for the study. The designed channels enabled the investigation of the influence of several geometrical parameters of both rectangular and square microchannels: with several hydraulic diameters ranging from 100 μm to 1000 μm, two channel lengths (25 *mm* and 50 *mm*) as well as aspect ratio ranging from 0.1 to 1 (square microchannels).

II.1.1.3 Sizing and design of micro-channels with bends

In order to study the minor pressure losses and their influence on the flow as well as their importance within micro-channels, two different configurations of channels were studied. Measurements with straight channel were compared to the ones for channel with bends and same hydraulic diameter and aspect ratio. Figure II.2 shows the design of the channels incorporating bends.

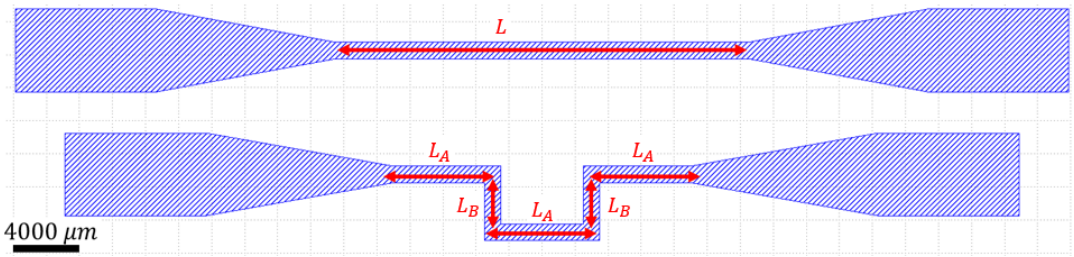

Figure II.2: Design of micro-channel without and with bends

The design of the microchannels with bends ensured that the total length L_{ch} of the channels remained the same for both configurations. According to figure II.2, the total length of the channels with bends is equal to $3\,L_A + 2\,L_B$ with L_A and L_B defined in figure II.2. This results in the following equation:

$$L_{ch} = 3L_A + 2L_B \tag{II.4}$$

Table II.3 shows the configuration of the microchannels with bends that will be studied.

Table II.3: Geometry of channels with bends

Width of channel $w_{ch}\,(\mu m)$	**Height of channel** $h_{ch}\,(\mu m)$	**Hydraulic diameter** $D_h\,(\mu m)$	**Length A** $L_A\,(mm)$	**Length B** $L_B\,(mm)$
1000	1000	1000	6	3.5
1000	1000	1000	8	0.5

II.1.2. Fabrication of device by stereo-lithography technique

As already mentioned, the change in channel cross-section was divided into two parts. The cross-section change to vary the width of the channels from w_{ch} to $5\,mm$ was integrated into the design of the parts realized through silicon micromachining, which will be detailed in chapter III. The change in cross-section to vary the height of the channels from h_{ch} to $5\,mm$, as well as the transition from rectangular to circular cross-section, was achieved through a device manufactured by stereo-lithography. This choice was motivated by the fact that stereolithography can be used to manufacture objects with complex geometries at high resolution and low cost.

The design of this device is shown in figure II.3. The microchannel was connected in the central part of the front side of the device (on the left in figure II.3). The pipes that made the connection to the experimental setup were connected in the central part of the back side of the device (on the right in figure II.3).

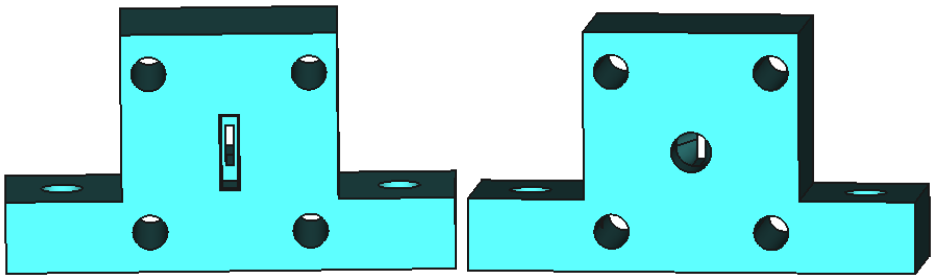

Figure II.3: Design of the device for the adaptation of the cross-section. On the left: front-side view. On the right: back-side view

II.1.2.1 Stereo-lithography 3D printing method

The concept of stereolithography was developed by Hull [99] in 1984. Lee *et al.* [100] developed a rapid system, which allowed fabricating of centimeter-scale 3D devices with microscale patterns by additive manufacturing. A laser with a power of $500\,mW$ and a wavelength of $405\,nm$ was used as a light source. A digital mirror reflected and projected the pattern on a photoresist. A z-axis displacement stage enabled the realization of several superimposed layers, making it possible to manufacture

3D devices. The smallest structures realized by the authors with this system were 50 μm thick walls. Channels realized by this method were limited to a width of about 200 μm due to the diffusion of the polymer according to the authors.

II.1.2.2 Choice of the photoresist

The part to manufacture had to be rigid enough to avoid disruption of the flow and be able to withstand a rather large temperature. Therefore the choice of the photoresist used for the manufacturing was important. The mechanical properties of available photoresists provided by the companies are given in table II.4. From this table, the photoresists with the best mechanical properties suitable for our needs were the Invicta-2020 and the Therma-DM210. Both photoresists have almost the same mechanical properties, however, the Therma-DM210 had the advantage of being used for applications over a large range of temperatures, which could be useful in further investigations, for instance, on both pressure drops and heat transfer characteristics under non-isothermal conditions. Therefore, the Therma-DM210 was used for the manufacturing of parts that connect and match the cross-sections of the channels to the pipes of the experimental setup.

Table II.4: Mechanical properties of photoresist for SLA process after UV curing (The values are taken from the technical data sheets of the company DWS)

Photoresist	**Elongation at break** $(\%)$	**Surface hardness (Shore D)**	**Flexural strength** (MPa)	**Flexural modulus** (MPa)	**Tensile strength** (MPa)	**Tensile modulus** (MPa)
Flexa GM08	20 - 65	25 - 27	-	-	-	-
Vitra DL375	6 - 10	-	80 - 105	2000 - 2500	45 - 55	1700 - 2200
Invicta 2020	3 - 10	90	90 - 150	2600 - 4000	40 - 75	2500 - 3600
Precisa 780	6 - 7	82 - 85	60 - 80	1500 - 1850	35 - 45	1700 - 2000
Therma DM210	1 - 4	85 - 90	50 - 135	1450 - 2800	20 - 45	1550 - 3100

II.1.2.3 Fabrication process of the devices

The system used for the stereolithography process (figure II.4) consisted of a UV laser system that focused the beam on the surface of the photoresist (z=0). The support platform was also placed at the surface of the photoresist at the beginning of the process. The laser exposed the resist at the required location to create the structures. When the first layer was completed, the platform moved up to begin the second layer of the device until the last layer was made.

II.1.2.4 Post-process treatment

Since support rods had to be added to the design to simplify the device manufacturing, it was necessary to remove them at the end of the process. It was then essential to smooth the roughened areas on which these rods were connected, to ensure a proper seal on the experimental bench. This step was carried out with sandpaper.

To enhance the mechanical properties of the cured photoresist, a post-curing with UV light was performed. Zguris *et al.* [101] studied the influence of the temperature and the time of the post-curing on the mechanical properties of the samples realized. The Young's modulus as well as the ultimate tensile strength increased with the post-curing time. The same trend was observed as the temperature at which the post-curing was performed increased. The Young's modulus increased from 1.3 GPa to

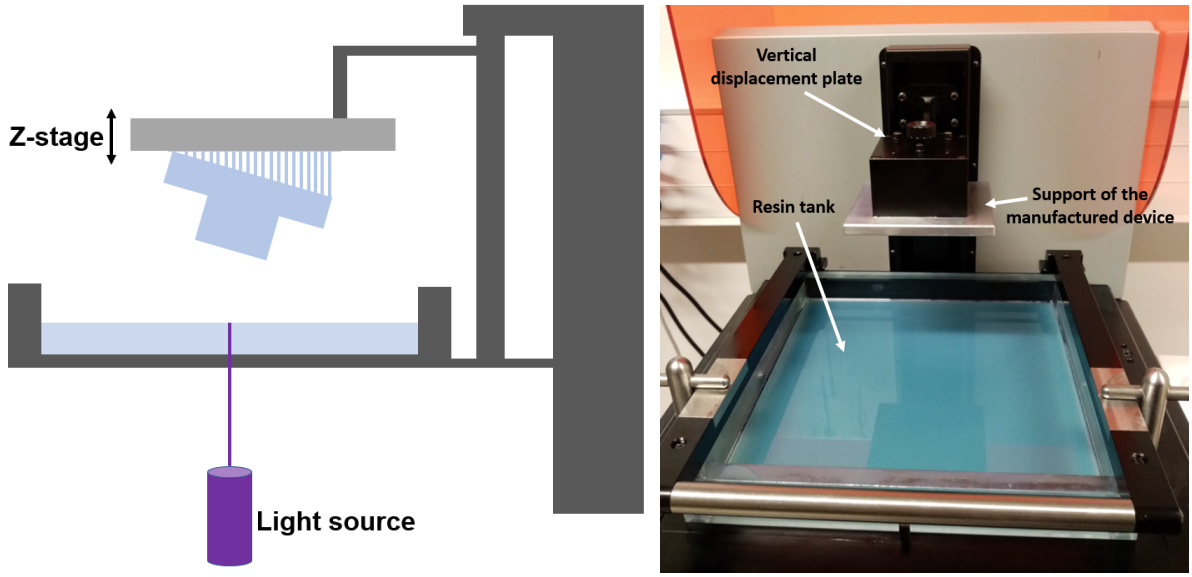

(a) (b)

Figure II.4: (a) Scheme of the stereolithography 3D printing method, (b) Picture of the system used to achieve stereolithography

2.8 *GPa* as the temperature increased from 25°*C* to 60°*C* while the ultimate tensile strength varied from 40 *MPa* to 70 *MPa*. The tensile strength and Young's modulus increase were respectively equal to 42 *MPa* and 410 *MPa* for 30 minutes of post-curing, while this increase was equal respectively to 50 *MPa* and 620 *MPa* for a post-curing time of 2 hours.

For the realization of our devices, a post-curing was performed with a 405 *nm* wavelength light source for 1 hour, which was a good compromise since the increase in mechanical properties was not significantly higher for higher post-curing time. Post-annealing was also performed at 120 °*C* for 30 minutes to obtain the maximum thermal resistance of the cured photoresist[1]. The mechanical properties of the photoresist after UV curing is given in table II.4

Five pairs of devices have been fabricated corresponding to the five different channel heights (figure II.5).

II.1.3. Design of converging and diverging parts of the micro-devices (Sections *B* and *D*)

As previously mentioned, converging and diverging sections (*B* and *D*) were implemented in the device on both sides of the microchannel test section in order to match the width *w* of the microchannel to the diameter of the pipes of the experimental bench (5 *mm* diameter circular tubes).

The design of converging and diverging sections was carried out to minimize the pressure losses generated by these singularities. Duryodhan *et al.* [102] studied the effect of aspect ratio in converging and diverging microchannels as well as the influence of the angle of converging and diverging sections. The aspect ratio α varied from 0.05 to 0.58, while the convergence/divergence angle varied from 2 ° to 14 °. As shown in figure II.6, the authors observed that for a given aspect ratio, the

[1]Technical Data Sheet of THERMA DM210 https://www.dwssystems.com/en/configurator/X/15/therma-dm210-en

(a)

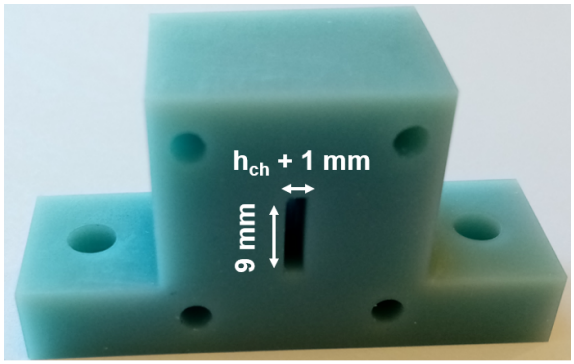

(b)

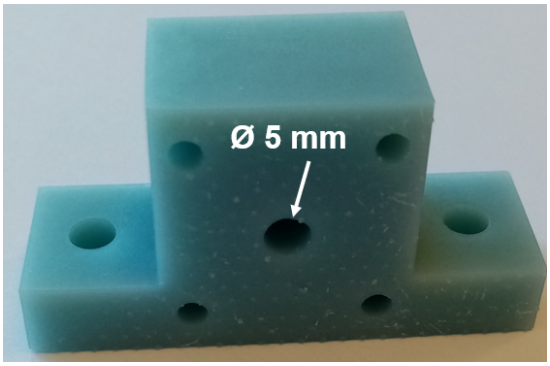

(c)

Figure II.5: Device fabricated by stereolithography (a) bottom-side view, (b) front-side view, (c) back-side view

pressure drop was independent from the angle for $\theta < 10$ °. For a larger angle of the converging or diverging sections, the pressure drop started to increase slowly as the angle increased. Also for a given angle, the pressure drop increased as the aspect ratio decreased. This increase in pressure drop was significant between $\alpha = 0.05$ and $\alpha = 0.19$ as the pressure drop was almost 20 times higher for α = 0.05. Moreover, as the authors observed in figure II.7, for angle θ = 10 °, C_f. Re was almost independent of the aspect ratio. For lower angle, C_f. Re increased when the aspect ratio decreased and inversely for angles higher than 10 °. According to this study, the optimal convergence angle seemed to be around 10 °. The design of sections B and D in figure II.1 had therefore been made in such a way as to obtain a convergence angle of 10 °.

Moreover, the convergence and divergence angles were identical for all channel configurations. Also, the total lengths of A + B parts as well as of E + D parts were kept identical for each configuration to have the same total length covered by the fluid. The 3D design of converging and diverging sections is shown in figure II.8. A simplified 2D scheme is also shown in Fig. II.9.

From the figure II.9, we get the following relation:

$$tan(\theta) = \frac{w_{pipe} - w_{ch}}{L_{conv}} \tag{II.5}$$

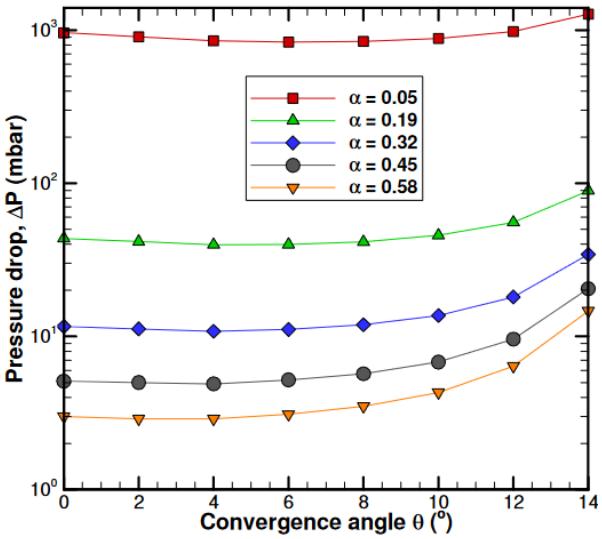

Figure II.6: Pressure drop versus convergence angle at different aspect ratio [102]

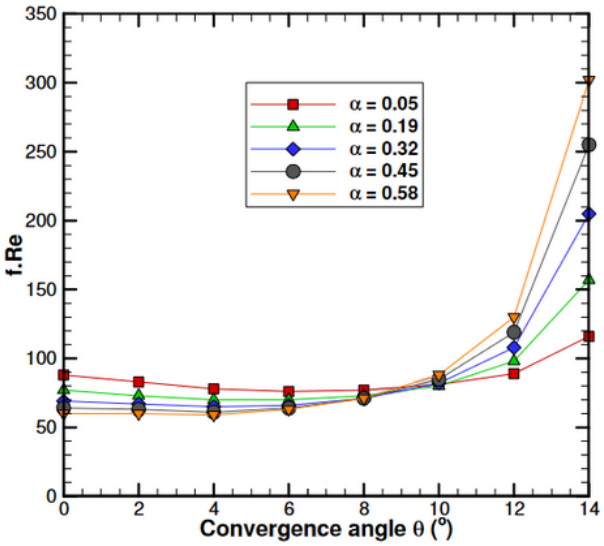

Figure II.7: C_f . Re versus convergence angle at different aspect ratio [102]

With w_{pipe} = 5 mm the width at the inlet of the converging section and outlet of the diverging section was equal to the inner diameter of all pipes of the experimental setup.

The following relation gives the length of the converging and diverging sections:

$$L_{conv} = \frac{w_{pipe} - w_{ch}}{tan\theta} \tag{II.6}$$

The width w_{pipe} and the angle θ were kept constant for each configuration, the length of the converging or diverging part depended only on the width of the channel. Table II.5 shows the different lengths of the convergent and divergent parts according to the width of the channel.

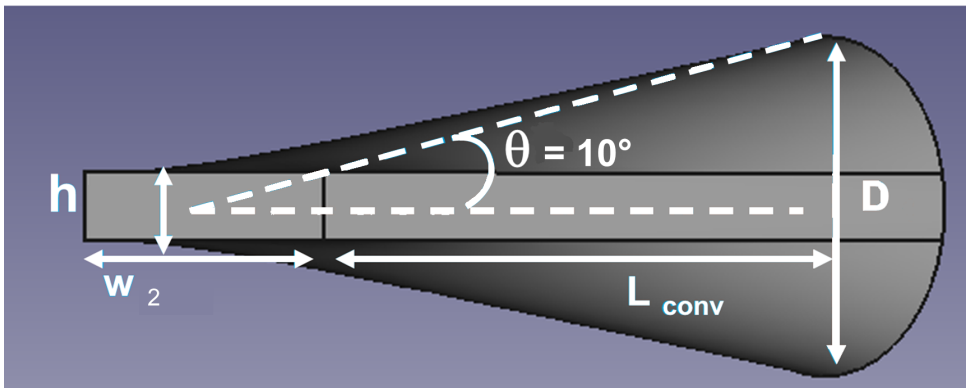

Figure II.8: 3D scheme of converging and diverging sections with adaptation of rectangular to circular cross-sections

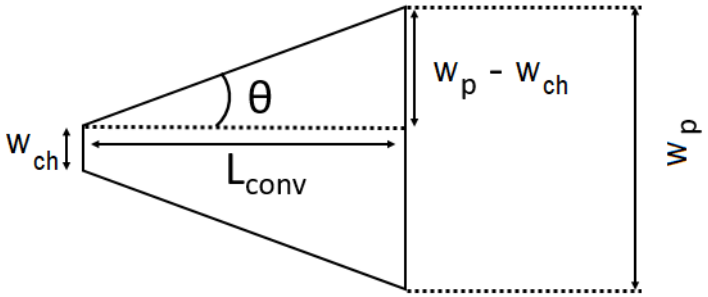

Figure II.9: Design of convergent and divergent parts

Table II.5: Length of the converging/diverging sections for different widths of channels

Channel width $w_{ch}\,(\mu m)$	100	200	500	1000
Converging and diverging length $L_{conv}\,(mm)$	13.87	13.58	12.73	11.31

The considered length of both converging and diverging sections added to the channel length, matched with the available surface on the wafer.

II.2 Temperature and pressure sensors

The converging parts on both sides of the microchannel generate pressure drops that are included into pressure measurements (P_1 and P_2 as shown in figure II.10). Therefore, the integration of sensors at the inlet and outlet of the microchannels to carry out pressure measurements (P_A, P_B) was considered to eliminate minor pressure drops generated upstream and downstream of the microchannel. Furthermore, cross-section changes induce a change in fluid velocity which can be determined by using the conservation of mass flow:

$$\dot{m} = \rho u A \tag{II.7}$$

This requires that the density is known at the location of velocity measurement as well as at the inlet and outlet of the microchannels. The density is calculated using the law of ideal gases:

$$\rho = \frac{P}{rT} \tag{II.8}$$

in which ρ is the density of the fluid, P the pressure, r_G the specific constant of perfect gas defined by $r_G = R_G$ / M (with R_G the gas constant and M the molar mass) and T the temperature. There-

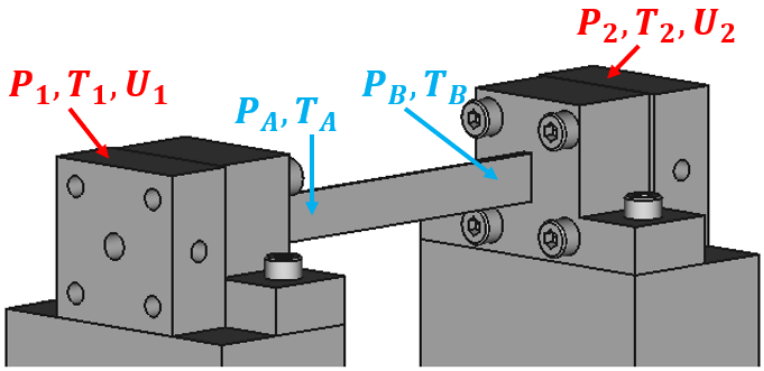

Figure II.10: Scheme of the device

fore, to characterize the flow, we needed to measure pressure, temperature, and flow velocity. These measurements included measurements at both ends of the channel (cross-section with micrometric dimensions denoted by A and B in figure II.10) as well as global measurements (cross-section with millimetric dimensions denoted by 1 and 2 in figure II.10).

Thermocouples fabricated at the FEMTO-ST institute were used for global temperature measurements at locations 1 and 2. Global pressure measurements located at the same location were carried out by using commercial transducers from the Kulite company.

Although commercial sensors can be used for global measurements, we strived to limit the disturbance of the flow caused by the presence of the sensors at the inlet and outlet of the microchannel. At the same time, the sensor's implementation in the microchannel should be as easy as possible. While low intrusive, optical methods were on the other hand not easily implemented in the experimental setup and had to be correctly designed to provide enough sensitivity for the required measurements.

In order to minimize the impact of the sensor's size on the flow, the following methods were considered either for pressure or temperature measurements.

II.2.1. State of the art of the measurements technique for pressure and temperature inside microchannels

II.2.1.1 Pressure measurements

- Pressure-sensitive paints (PSP) [103] [104]

  Huang *et al.* [105] used pressure-sensitive paints to measure pressure in the range 0.07 mbar - 2 bar with a spatial resolution of $\pm$ 5 μm using a layer of 1 μm thickness. This technique was based on a layer of polymer or a porous surface seeded with luminescent particles bonded to

the channel's wall. These luminescent particles were excited by a light source (UV lamp, blue or green laser). The excited particles emitted luminescence which was captured by an optical sensor as shown in figure II.11. The intensity of the signal measured by the sensor depended on the quantity of molecules of oxygen present in the layer. The more the number of molecules of oxygen, the weaker the intensity of the emitted signal. Considering that the proportion of oxygen in the air was known, the amount of oxygen molecules in the layer depended on the pressure of the gas at the measurement point. Li *et al.* [106] used Ni-PDMS conductive gel blocks as PSP to measure pressure in the range of 0 to 1 bar with a response time of a few seconds. Matsuda *et al.* [107] used PDMS and a luminophore layer to measure pressure in the range 0.12 bar to 0.2 bar with an accuracy of less than 0.4 mbar. Huang *et al.* [108] improved the range of their pressure measurement up to 0.07 mbar - 3.45 bar with a spatial resolution of $\pm$ 3 μm with a "pixel-by-pixel" calibration instead of the standard "single-point" calibration. The main limitation of this method was its oxygen-dependence, and therefore not suitable for applications where the working fluid did not contain oxygen.

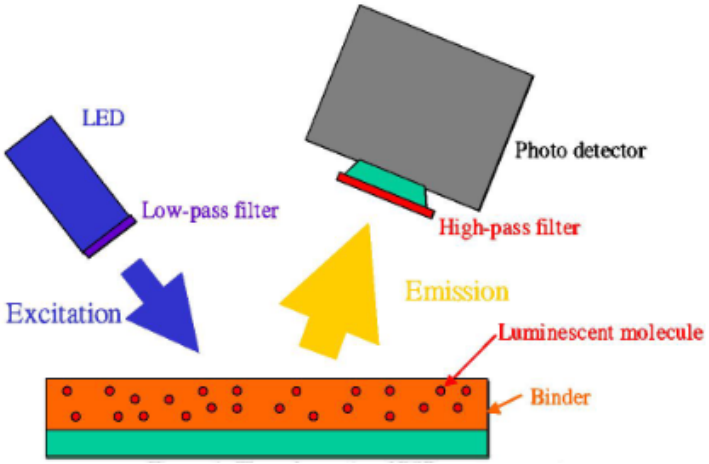

Figure II.11: Schematic of PSP measurement [105]

- Interferometric method

  Fultz *et al.* [109] used an interferometric method to provide pressure measurements This method relies on the division of a light beam in two paths, a reference path and a path that contains the microchannel. Both beams interfere after crossing the microchannel. The interface pattern depends on the local refractive index of the channel's wall and the refractive index of the working fluid, which depends on the fluid density. Therefore, the pressure can be determined if the temperature is known by using the ideal gas law.

- Deflection of a membrane [110]

  Zohar *et al.* [111] used a membrane with integrated piezoresistive sensors to carry out pressure measurements. The membrane deflection caused by pressure variations leads to a change of resistance of the piezoresistive elements. Molla *et al.* [112] fabricated a 100 μm thick PDMS membrane to measure pressure ranging from 9 bar to 27 bar with an accuracy of $\pm$ 400 mbar in a channel with a hydraulic diameter of 2 mm. Several authors used membranes of various

thicknesses to measure various ranges of pressure in microchannels. Chung *et al.* [113] used a 15 μm thick PDMS membrane to carry out pressure measurements in the range of 0 to 0.7 bar with an accuracy of $\pm$ 10 mbar and a time response $\tau < 0.25$ s, in microchannels with a hydraulic diameter of 160 μm. Song and Psaltis [114] used a 530 μ m thick PDMS membrane to measure pressures ranging from 0 to 0.7 bar with an accuracy of $\pm$ 2 % full scale in microchannels with a hydraulic diameter of 92.3 μm.

In this study, we decided to use membrane deflection for pressure measurement. The next section will be dedicated to a non-exhaustive state of the art of temperature measurement.

II.2.1.2 Temperature measurements

- Fluorescence thermometry [115] [116] [117], [118], [119], [120]

  This method consists in seeding the flow with fluorescent molecules which will be excited by a light source. The intensity of the radiation emitted by the particles will depend on the temperature of the particles. Coppeta and Rogers [121] investigated the dual emission laser-induced fluorescence to measure the temperature and pH of liquid flow. They measured temperature in the range 20 - 60 ° C, with an accuracy of $\pm$ 1.8 ° C. The sensitivity of this method was observed to vary from - 1.54 % per ° C to 2.43 % per ° C depending on the dye used to seed the flow. Sakakibara and Adrian [122] excited Rhodamine B particles with an Argon ion laser at a wavelength k = 514 nm. They obtained a sensitivity of - 1.95 % per ° C for temperature measurements in the range 15 - 40° C. Saeki and Hart [123] observed a sensitivity of -1.34 % per °C in the range of 25 °C to 85 °C using Rhodamine B excited at k=532 nm using Nd:Yag laser. Hu *et al.* [124] improved the sensitivity of this method by using another dye to seed the flow ($1-BrNp-M\beta CD-ROH$). They observed a sensitivity from 8.15% per °C to 18.2% per °C depending on the time delay between the laser pulse and the phosphor signal acquisition.

  Hu *et al.*[125] used this method to provide velocity as well as temperature measurements to characterize the transient behavior of an electro-osmotic flow in microchannels of hydraulic diameter 300 μm. By using with Rhodamine B, Chamarthy *et al.* [126] performed temperature measurements in the microchannels of a heatsink that were 500 μm wide and 200 μm in the range 20 - 50 °C and obtained an uncertainty in temperature measurements down to $\pm$1.25°C.

- Microthermocouple

  Thermocouples are widely used for performing temperature measurements based on the Seebeck effect. They are manufactured by welding together two different conductive materials [127]. A voltage is generated when there is a temperature gradient between the temperature measured by the thermocouple and a reference temperature achieved at the so-called "cold junction". Figure II.12 illustrates the temperature measurements by the meaning of a thermocouple.

  The voltage measured is related to the temperature through the following equation:

$$\Delta V_{measured} = \int_{T_{ref}}^{T_{measured}} S_{AB}(T)dT \tag{II.9}$$

  where $\Delta V_{measured}$ is the voltage generated by the Seebeck effect, and S_{AB} is the difference between the Seebeck coefficients of material A and B ($S_{AB} = S_B - S_A$).

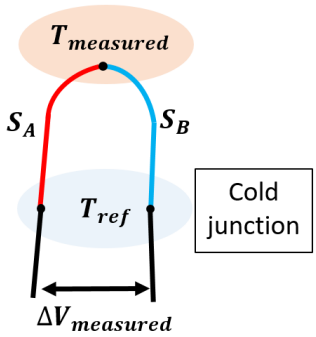

Figure II.12: Thermocouple measurements principle

Commercial thermocouples are however too invasive and voluminous to be used in microfluidic applications and studies. Nevertheless, Thiery *et al.* [128] have achieved the manufacturing of a Platinum/Platinum-Rhodium thermocouple with a junction diameter of $0,5\,\mu m$ which is referenced as a S-type thermocouple.
Lanzetta *et al.* [129] measured the temperature in a continuous gas flow of nitrogen within glass microchannels using 25.4 μm Chromel-Alumel K-type microthermocouples. Doghmane *et al.* [130] characterized K-type thermocouples in ceramic tubes with a metal deposition on the ceramic to realize the hot junction of the thermocouples (Gold, Chromium, and Tungsten were used as a metallic layer). Two thicknesses for the deposited metallic layers were tested (400 nm and 800 nm). The thermocouple was composed of a 50 μm diameter alumel wire and a 50 μ m chromel wire. The sensor with the 400 nm gold deposition gave the best result. The time constant of the sensors under laser excitation was equal to 10 μs for the rise-time and 80 μs for the decrease-time. The cut-off frequency of the probes was equal to 67 Hz. Dellali *et al.* [96] explored alternating flows at the inlet/outlet of microgenerators with K-type thermocouples, 7.6 μm and 12.7 μm in diameter. These low-intrusive sensors offer very low time constants (Table II.6).

Table II.6: Dynamic characteristics of S and K-type thermocouples [127]

Type	**Junction diameter** $d_{junction}\ (\mu m)$	**Time constant under laser heating** $\tau\ (ms)$	**Bandwidth** $\Delta f\ (Hz)$
S	0.53	0.07	2274
S	1.27	0.18	884
S	5.3	1.3	123
K	12.7	8.5	19
K	25.4	34	5
K	53	64	2.5

MEMS techniques have allowed the development of thermocouples allowing a spatial resolution on the order of a few micrometers and even sub-micrometers.

The time response of thermocouples has also been improved [131]. Cygan *et al.* [132] fabricated micro-thermocouple by e-beam deposition. The thermocouple is composed of a stack of

50 nm thick Copper layer with a 10 nm thick Titanium adhesion layer welded with a constantan layer electrodeposited on the substrate. The thermocouple had a sensitivity of - 62 μ V $\circ$ C^{-1}. After amplification of the signal, the sensitivity was -17.8 mV $\circ$ C^{-1}.

- Resistance Temperature Detectors (RTD)

  The principle of this measurement is based on the fact that the electrical resistance of a metal or semiconductor varies with temperature. As the temperature increases, it induces an increase in the movement of the atoms, which results in less freedom of movement of the electrons, resulting in higher electrical resistance of the material.

  The relationship between the electrical resistivity of the material and its temperature can be written as:

$$\rho_{elec}(T) = \rho_{0\,elec}\,[1 + a(T - T_0)] \tag{II.10}$$

  With a representing the temperature coefficient of the material, ρ_{elec} the electrical resistivity, T the temperature in $°C$ and $\rho_{0\,elec}$ the electrical resistivity at the temperature T_0. For platinum, these values are given in table II.7 [133].

Table II.7: Properties of Platinum at $T = 0°$C

Electrical resistivity $\rho_{elec}\,(\Omega.m)$	**Temperature coefficient** $a\,(°C^{-1})$
11 10^{-8}	3.92 10^{-3}

  Moser *et al.* [134] deposited 200 nm Platinum layer with 50 nm Titanium adhesion layer to realize a flexible temperature sensor ranging from 0 °C to 400 °C. Tiggelaar *et al.* [135] deposited 100 nm to 360 nm to obtain temperature sensors for high-temperature applications.

Other techniques have been used to measure pressure and temperature in microchannels. These other measurement techniques will not be detailed here since the methods were less well documented or not suited to our setup.

II.2.2. Design of the sensor inside the microchannels

II.2.2.1 Design of the temperature sensor

For the temperature measurements at the inlet and outlet of the microchannel, the Platinum Resistance Temperature Detector (RTD) was chosen because of its high stability over time and its good accuracy [136] [137]. It was also a type of sensor that was relatively easy to implement in the microchannel design with available technologies at the FEMTO-ST cleanroom. Since this sensor was composed of thin film deposited on the bottom wall of the channel with a thickness around 200 nm ($\leq$ 0.2 % of the smallest hydraulic diameter), it could be considered as low intrusive for the flows which were studied.

As illustrated in figure II.13, the thin film sensor was composed of meanders (the sensitive part of the sensor) in order to minimize its size. The meander width was w_{Pt} and the thickness of the thin Platinum layer was denoted e_{Pt}. The sensor film was ended on both sides by large pads that were used to connect it through external wires to a printed circuit board (PCB) linked to the acquisition system. This large surface of the pads ensured that the resistance of the connecting part could be neglected compared to the total resistance of the sensors.

To minimize the role of parasitic resistances, we strived to keep at least at 100 Ω the resistance of the thin film sensor at room temperature. Its electrical resistance was associated with the electrical resistivity of the material according to the relation:

$$R_{elec}(T) = \rho_{elec}(T)\frac{L_{Pt}}{A_{Pt}} \tag{II.11}$$

Where R_{elec} is the electrical resistance of the sensor, L_{Pt} is its total length and $A_{Pt} = w_{Pt}\ e_{Pt}$ is the cross-sectional area of the thin film.

The width of the tracks was initially set at 50 μm to limit the mechanical stresses resulting from the thermal expansion of the Platinum layer. The standard thickness of the platinum thin film deposition for temperature measurements application was around 100 nm to 300 nm.

Therefore, a thickness of 200 *nm* Platinum layer was considered for the temperature sensor. Since the width and thickness of the Platinum layer were set, the only parameter to calculate was the length of the tracks determined by the following relation:

$$L_{Pt} = A_{Pt}\frac{R(T)}{\rho_{elec}} \tag{II.12}$$

As illustrated in figure II.14, the length of each meander L_m was limited by the width of the channel and was equal to the channel width w_{ch} to which we removed 20 μm, to prevent short-circuit of the sensors with the silicon wafers, which were used for the fabrication of channels as it will be detailed in the next chapter. The required length of the tracks would result in a sensor that covers a too-large area for the smaller channels. Therefore, for the 100 μm and 200 μm wide channels, the track width was reduced to 10 μm. For the 500 μm channels, this width was equal to 30 μm. Table II.8 summarises the geometry of these sensors for each configuration.

Table II.8: Dimensions of the Platinum sensors

Channel width w_{ch} **(**μ**m)**	**Film thickness e** (*nm*)	**Track width w** (μ**m**)	**Track length** L_{Pt} (*mm*)	**Number of meanders**
100	200	10	1.8	18
200		10	1.8	10
500		30	5.4	12
1000		50	9.1	10

The connector part of the sensors induced an additional and undesirable resistance. By making a large connecting part, the additional resistance generated was limited. Moreover, it facilitated connection to the acquisition system by wire bonding.

The resistance of these sections can be determined by the following relation:

$$R_{conn} = \rho_{elec}\int_0^{L_1+L_2}\frac{dx}{S} \tag{II.13}$$

with $S = e\ w(x)$ the cross-section of the Platinum deposition. From the figure II.13, we can deduce that:

$$tan(\theta_1) = \frac{w_2 - w_1}{L_1} = \frac{w(x) - w_1}{x} \tag{II.14}$$

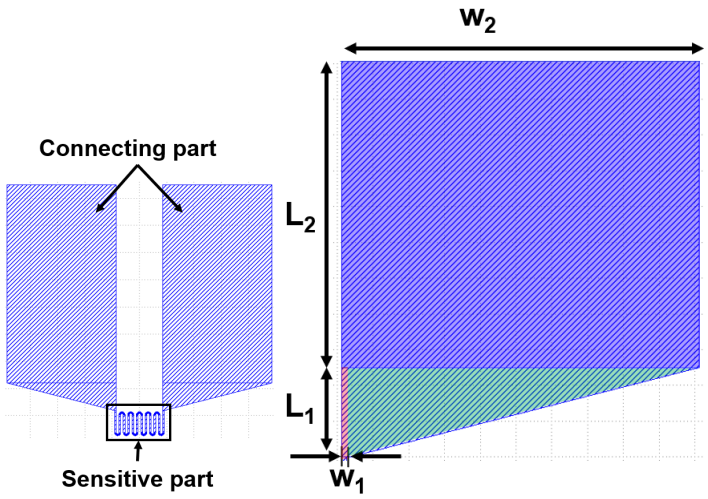

Figure II.13: Design of the connector part of the Pt sensors

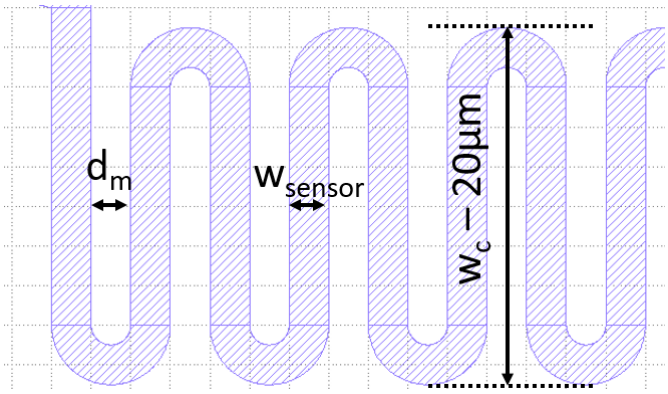

Figure II.14: Design of the connector part of the Pt sensors

Therefore, the width of the track $w(x)$ can be determined by:

$$\begin{cases} w(x) = w_1 + x\frac{w_2 - w_1}{L_1} & for\ x \in [0; L_1] \\ w(x) = w_2 & for\ x \in]L_1; L_2] \end{cases} \tag{II.15}$$

The resistance R_{conn} induced by this connector part could thus be written as:

$$R_{conn} = \rho_{elec}\left[\int_0^{L_1} \frac{dx}{e(w_1 + x\frac{w_2 - w_1}{L_1})} + \frac{L_2 - L_1}{e\ w_2}\right] \tag{II.16}$$

$$R_{conn} = \frac{\rho_{elec}}{e}\left[\frac{L_1}{w_2 - w_1}\left(ln(w_1 + L_1\frac{w_2 - w_1}{L_1}) - ln(w_1)\right) + \frac{(L_2 - L_1)}{w_2}\right] \tag{II.17}$$

$$R_{conn} = \frac{\rho_{elec}}{e}\left(\frac{L_1}{w_2 - w_1} ln(\frac{w_2}{w_1}) + \frac{(L_2 - L_1)}{w_2}\right) \tag{II.18}$$

The width w_2 was set equal to 2 mm, while L_1 was equal to 0.5 mm and L_2 was equal to 3.5 mm to get the connecting part at the edge of the device. The resistance of the connecting part was determined for each Pt sensor design to make sure that it did not contribute to more than 2% of the sensor's total resistance. The theoretical resistance of the connection pad for each Pt sensor design is given in table II.9.

Table II.9: Resistance of both connecting and sensitive parts of the Pt sensors

Channel width (μm)	**Resistance of Pt thin film** (Ω)	**Resistance of sensitive part of the sensor** (Ω)	**Resistance of connecting part of the sensor** (Ω)	**Contribution of connecting part in the total resistance** (%)
100	97.5	95.9	1.6	1.63
200	102.7	101.2	1.5	1.44
500	105.5	104.1	1.4	1.33
1000	106.4	105.1	1.3	1.21

II.2.2.2 Design of the pressure sensor

Pressure measurements at the inlet and outlet of the microchannel was considered to be achieved by measuring the deflection of a membrane incorporated in the microchannel structure. This choice was justified by the low intrusiveness of the membrane in the flow within the microchannel.

An optical sensor was considered to be used to measure the displacement of the center of the membrane. The sensor considered to be used was a chromatic confocal sensor IFS2405-6 from MicroEpsilon company. This type of sensor uses a polychromatic source whose different wavelengths are focused at different distances. The sensor measures the wavelength of the light beams reflected by the membrane whose displacement is to be determined. This wavelength is related to the distance separating the sensor from the center of the membrane. The measurement accuracy of the sensor used is $\pm$ 23 nm, with a beam diameter of 31 μm. The sensor's measuring range is around 6 mm with a focal length of 6 cm, enabling it to measure objects at a distance ranging from 5.7 cm to 6.3 cm.

The deflection of a membrane is related to the applied pressure according to the following equation [110]:

$$w_M = \frac{P\,r^4}{64\,D_m} + \frac{C_1\,r^2}{4} + C_2\,log\frac{r}{r_M} + C_3 \tag{II.19}$$

with P the pressure applied on the membrane, w_M the associated deflection of the membrane, r_M the radius of the membrane, r is the radial position, the bending swiftness $D_m = \frac{E\,e_M^3}{12\,(1-\nu_P^2)}$ and C_1, C_2, C_3 are determined by the boundary condition.

For membranes clamped at edges, the boundary conditions impose [110]:

$$\begin{cases} C_1 = -\frac{P\,r_M^2}{8\,D_m} \\ C_2 = 0 \\ C_3 = \frac{P\,r_M^4}{64\,D_m} \end{cases} \tag{II.20}$$

This results in the following relation between the pressure applied to the membrane and the associated deflection:

$$w_M = \frac{P}{64\,D_m}\left(r_M^2 - r^2\right)^2 \tag{II.21}$$

The maximum deflection of the membrane is obtained at the center r=0. This results in the deflection at the center of the membrane:

$$w_M = \frac{P\,r_M^4}{64\,D_m} \tag{II.22}$$

This equation considers that the pressure applied to the membrane is uniform over its entire surface. In reality, this pressure is not completely uniform along the length of the microchannel. Therefore it will be necessary to verify that this difference in pressure between the two edges of the membrane leads to a small error.

Therefore, the main parameters for the design of the membranes are (i) its radius, (ii) its material, and (iii) its thickness.

- Diameter of membranes

  The deflection at the membrane center increases with the diameter of the membrane, resulting in higher sensitivity of the sensor. However, this diameter cannot exceed the channel width. Therefore, the diameter of the membranes will be close to the width of the microchannels to obtain enough membrane deflection. Thus, the two parameters to define are the material and the thickness of the membranes.

- Choice of material

  The choice of membrane material is influenced by its mechanical properties, which determine the deflection of the membrane under uniform pressure. Indeed, the deflection of the membrane is related to the pressure applied with its Young's modulus E and Poisson's ratio ν_p. Table II.10 gives the mechanical properties of several materials which were considered for the membrane according to the available possible process that could be achieved in the FEMTO-ST cleanroom facility.

  The mechanical properties of PDMS depend on the thickness of the membrane [143]. Its Young's modulus is around 1,4 MPa for a membrane thickness around 100 μm while it drops down to 0.6 MPa for a PDMS membrane with a thickness larger than 1 mm. For our case, since thickness of PDMS membrane would be closer to 100 μm, it is the value of 1.4 MPa which was taken for the Young modulus in the calculation.

- Thickness of membranes The accuracy of the sensor mentioned earlier, which will be used to measure the deflection of the membrane, is around 34 nm. Therefore, a minimal displacement of 680 nm at the center of the membrane is required to obtain uncertainties on the pressure measurement below 5%. The other restriction regarding the thickness of the membrane is due to the yield strength of the material and elongation at break of material which are given in table II.10.

[1]Engineering ToolBox, (2003). Young's Modulus, Tensile Strength, and Yield Strength Values for some Materials. https://www.engineeringtoolbox.com/young-modulus-d_417.html

[2]Engineering ToolBox, (2007). Poisson's Ratios Metals. https://www.engineeringtoolbox.com/metals-poissons-ratio-d_1268.html

Table II.10: Mechanical properties of materials considered for the membranes

	Young modulus $E(MPa)$	**Poisson ratio** ν_p	**Yield strength** $\sigma_y(MPa)$	**Elongation at break** $e_b\,(\%)$
Al [1, 2] [138]	70.10^3	0.33	$15-20$	$3-8$
Si [139] [140]	190.10^3	$0.22-0.28$	$5000-9000$	-
PDMS [139] [141] [142] [143]	$0.3-1.5$	$0.45-0.55$	-	70
PMMA [139]	1500 - 5000	$0.34-0.4$	-	$3-10$

PDMS: PolyDiMethylSiloxane
PMMA: PolyMethylMethAcrylate

Table II.11: Thickness of membrane for the different materials considered, in the pressure range of the present study

Membrane material	Al	Si	PDMS	PMMA
Membrane thickness (μm)	0.01	0.01	10 - 50	0.05

The minimum and maximum pressure that might be measured by the deflection of the membranes is estimated by theoretical values and correlations for laminar, steady, and incompressible flows at the macroscale in square channels. Figure II.15 shows the pressure range that would be measured by the membranes for all considered materials and for different membrane thicknesses.

To be able to carry out pressure measurements in the range considered for our study, the required membrane thickness for each material can be determined from these graphs and is given in the table II.11.

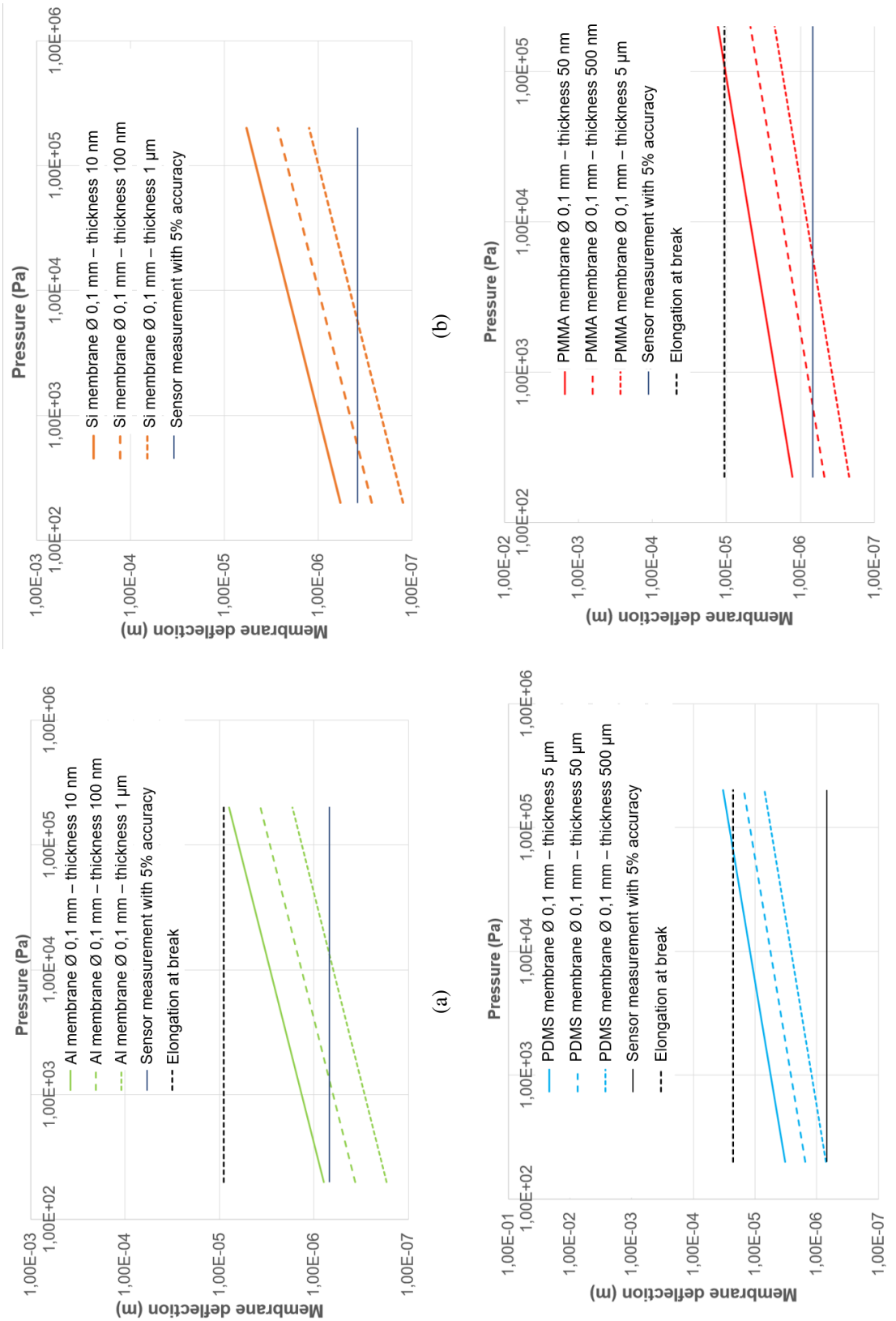

Figure II.15: Deflection of membrane for different thickness (a): Al, (b): Si, (c): PDMS, (d): PMMA

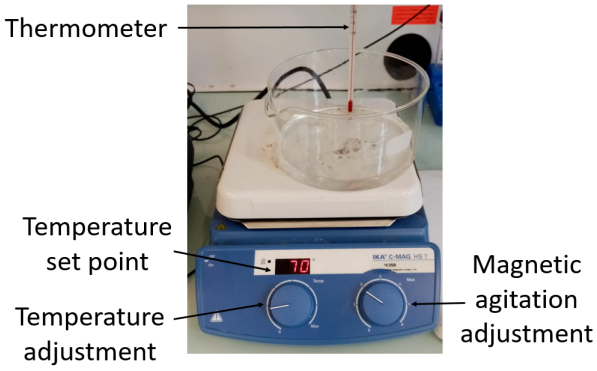

Figure II.16: Setup for the polymerization of PMMA

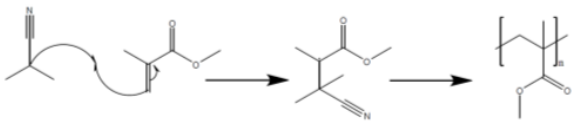

Figure II.17: Formation of PMMA from MMA and AIBN

From table II.15, we can notice that choosing membranes in silicon or aluminum would result in too-brittle membranes and would not be easy to realize since the required thickness should be as small as a dozen of nanometers.

Preliminary test of fabricating membrane made of PMMA was carried out. The polymerization of PMMA is done by mixing 2.7 mL of MMA (5 mol L^{-1}), heated at 70 ° C for 2 h, with 2.3 mL of Toluene and 16 mg of AIBN (Azobisisobutyronitrile, 0.02 mol L^{-1}) as shown in figure II.16.

Figure II.17 illustrates the formation of PMMA from MMA and AIBN. An activation of the surface by plasma O_2 is required before the immersion of samples in the mixing solution. The next step is heavily rinse the samples three times during 5 min in a mixed solution of toluene:acetone with a ratio of 2:1. The samples are then, rinsed during 10 min using de-ionized water before being dried with compressed air.

However, we did not reach to obtain a membrane with thickness of about 50 nm with this method. This can be due to insufficient parameters of plasma O_2 to achieve activating the surface. Another explanation could be due to the evaporation of the mixed solution which resulted in lower thickness of the membrane which we were unable to measure. Therefore, we will use PDMS for the fabrication of membrane with a thickness of 20 μm.

Chapter conclusion

In this chapter, the design of the microchannels, which will be fabricated, has been presented. The design will enable the investigation of the influence of several geometrical parameters of the rectangular and square microchannels: hydraulic diameter ranging from 100 μm to 1000 μm, two channel lengths (25 mm and 50 mm) as well as the aspect ratio of the microchannel cross-section ranging from 0.1 to 1 (square microchannels) for the same hydraulic diameter. The characteristics of alternating gas flow in straight channels will also be compared to those of channels with bends. The converging cross section has also been designed to generate the smallest allowable pressure loss. These converging sections will accommodate flow within rectangular and square microchannels (with hydraulic diameters ranging from 100 μm to 1000 μm) to 5 mm diameter pipes.

In the second part of this chapter, the design of the sensors which will be implemented for pressure and temperature measurements at both extremities of the microchannels was also introduced. Pressure measurements will be carried out by measuring the deflection of a 20μm thick PDMS membrane with an optical sensor. The choice of material as well as the diameter and thickness of the membrane determine the measurement range of these sensors. The temperature measurements will be performed using the temperature dependence of the platinum resistivity (RTD). The length and width of the tracks as well as the thickness of the thin film of deposited platinum were designed to obtain at least 100 Ω resistance of the sensor at room temperature. The large surfaces of the pads are designed to ensure that the additional resistance generated by these pads in the temperature measurement is below 2% of the total resistance of the sensors.

CHAPTER III

FABRICATION OF THE DEVICES

In this chapter, we will present the successive steps of the microchannel fabrication process with integrated pressure and temperature sensors. Their design was presented in the previous chapter. Using integrated pressure and temperature sensors should enable a more precise measurement since they sense flow parameters inside the channel, whereas external sensors will sense a flow that is modified by the connectors to external pipes with larger diameters. The integrated sensors will be located at both ends of the microchannel but could also be integrated anywhere in the channel for further studies. Temperature sensors are composed of Platinum thin layers deposited on the bottom wall of the channels with connection pads located outside the microchannels. Pressure sensors consist of a PDMS layer as a membrane, whose displacement caused by pressure variations will be monitored by an external optical sensor. Microchannels are fabricated using DRIE (Deep Reactive Ion Etching) on Silicon wafers.

Due to the difficulties encountered in the bonding of these devices, another process has been considered to fabricate microchannels without integrated sensors. These microchannels will still provide global measurements using sensors located on mechanical support attached to the microfabricated devices (using homemade microthermocouples for temperature, and commercial pressure sensors). Such measurements will however be less accurate than the measurements initially expected because, as mentioned in the previous chapter, these measurements include the changes in cross-section located on both ends of the microchannel, which modify the velocity, pressure, and density of the fluid in a proportion that can only be estimated using results from the literature for steady flows. However, the process carried out for the realization of these microchannels without instrumentation is much easier to perform. It will be detailed in the second part of this chapter.

The characterization of the temperature sensors realized with the deposited platinum layer will be presented in the third part of this chapter. These probes have been annealed to enhance their performance and stability. This characterization will allow us to determine the best annealing process for our application by comparing measurements carried out on samples with different annealing parameters. These measurements include X-ray diffraction (XRD) to characterize the crystallographic properties of the deposited platinum layer as well as the residual stress in the layer. Static and dynamic characterization is done to determine the electrical properties of the probes.

III.1 Microfabrication of the microchannels, with and without integrated sensors

In this section, we will present the manufacturing steps for both types of microchannel (with or without integrated sensors). We will start with the manufacturing steps, tests and problems encountered during the manufacture of microchannels with integrated sensors. In the second part, we will look at the manufacturing process for microchannels without integrated sensors, which was carried out alongside the tests carried out on the first manufacturing process.

To make the microchannels, three 4-inches wafers are assembled as illustrated in figure III.1. The wafer on top of the stack (W_{Glass}) is a glass ($BoroFloat33$) wafer with a thickness of 500 μm. This choice was motivated by the need for optical access (and the possible use of a flow velocity method, even though it will eventually not be implemented in this work due to the difficulty in seeding gas flow with micro-particles at the microscale). The wafer in the central part (W_{Si1}) is a silicon wafer and will be etched through its entire thickness h_{ch}. The patterns of the etched areas correspond to the channel geometry presented in the previous chapter. The wafer at the bottom of the stack (W_{Si2}) is a 500 μm thick silicon wafer that will be used to support the sensors located inside the microchannels. Regarding the channels without sensors, we keep the same silicon wafer at the bottom of the stack so that such potential interaction between the wall and the gas depending on the material of the wall will not influence the channels realized by the different manufacturing processes.

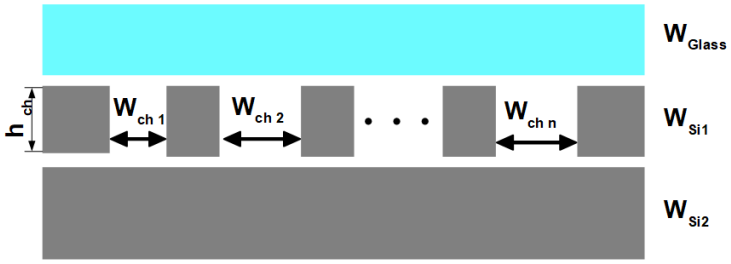

Figure III.1: Side view scheme of the assembled wafers

III.1.1. Process of fabrication of the microchannels with built-in temperature and pressure sensors

This manufacturing process was considered to provide both pressure and temperature measurements using membrane and platinum RTD as mentioned in Chapter II. Figure III.3 shows the top view of the assembled wafers. Temperature sensors are represented in red and microchannels in dark blue. The light blue surfaces correspond to glass, while the gray areas correspond to silicon surfaces of the wafer W_{Si2} that are visible at places where the glass wafer and silicon wafer W_{Si1} have been etched out. These channels have been designed to obtain both pressure and temperature measurements at both ends of the channels. Using more pressure sensors was considered but due to the optical sensor dimensions (used for the measurement of the membrane deflection), it was impossible to carry out at the same time pressure measurements at other locations than at the inlet and outlet of the channels.

Figure III.2 - detailed hereafter - presents the process flow for the fabrication of the channels with integrated sensors. The straight square-section microchannels, the rectangular-section microchannels,

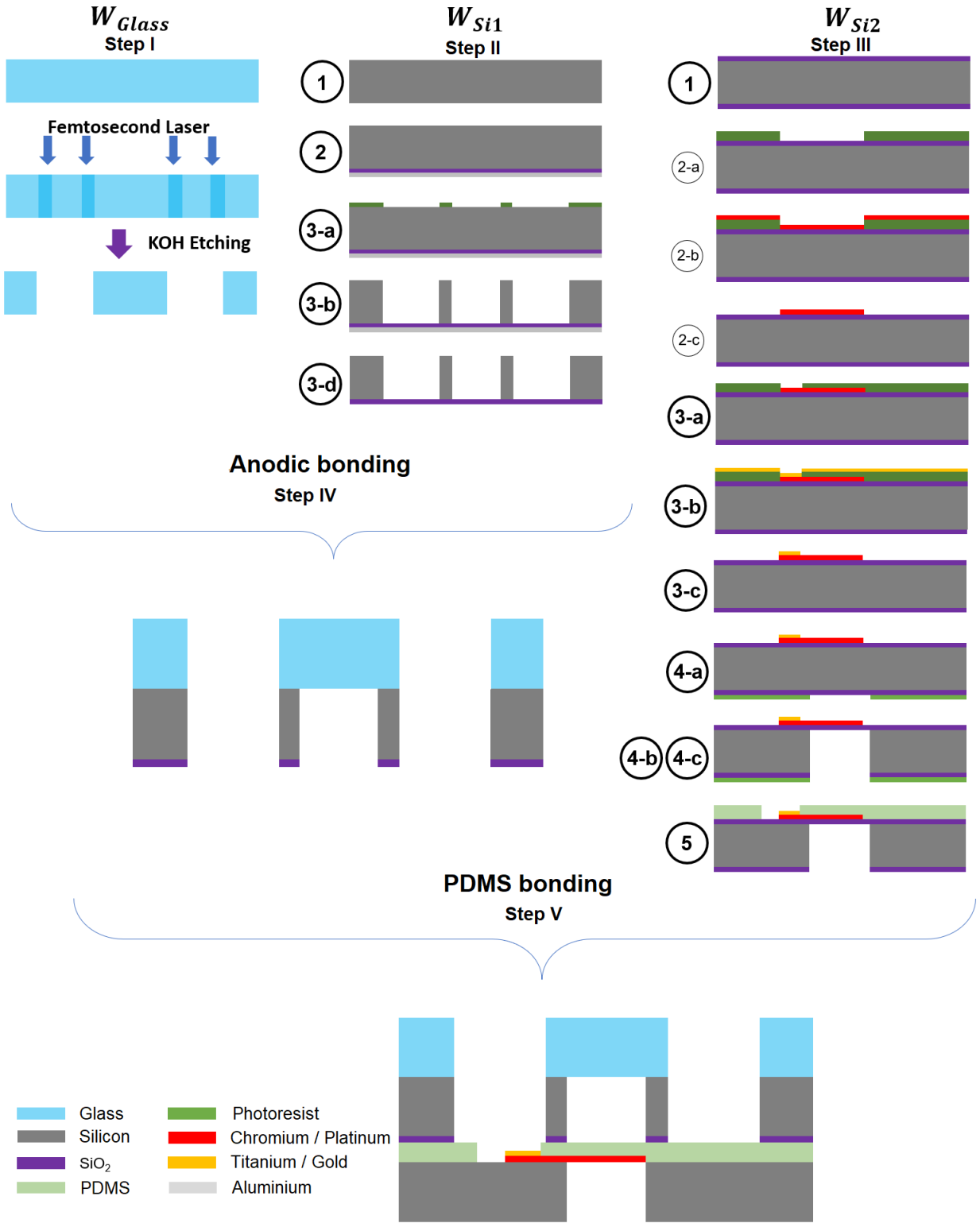

Figure III.2: Flowchart of the microchannel fabrication process with integrated sensors

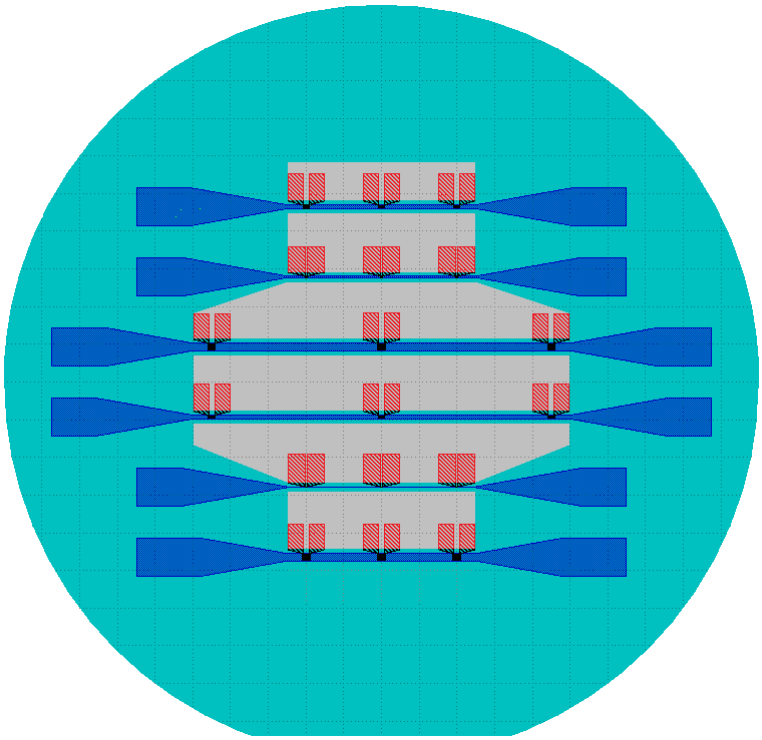

Figure III.3: Top view scheme of the assembled wafers

and the microchannels with bends are fabricated using the same process, but different masks for the silicon etching of wafer W_{Si1}.

III.1.1.1 Patterning of the glass wafer W_{Glass} (Step I)

The glass wafer must be shaped to enable access to the temperature sensor connectors. The design of the apertures created in the glass wafer is shown in figure III.3. These apertures are realized using chemical etching in a KOH solution assisted by a 1030 nm Yb:YAG femtosecond laser using a « f100 aHead Enhanced » system from the FEMTOprint company. The glass wafer is positioned and held on an XY-axis displacement stage. A 20x microscope objective is placed on a Z-axis displacement stage and used to focus the beam emitted by the laser. The laser exposes the glass wafer where the glass should be etched. The wafer is then immersed in a 10 $\mathrm{mol\,L^{-1}}$ KOH solution at a constant temperature of 80°C. The etch rate of the laser-modified areas using KOH is typically 2 $\mu\mathrm{m\,min^{-1}}$, while the etch rate of unmodified areas is around 0.01 $\mu\mathrm{m\,min^{-1}}$. Etch selectivity, defined by the ratio of the etch rate of exposed to unexposed glass areas is thus around 200.
To limit the time required to expose all areas that should be etched, only the edge of the rectangular and trapezoidal structures will be exposed by the laser. Wet etching is performed in an ultrasonic bath station, to enhance the release of the structures exposed by the laser. In addition, marks are also etched with this method to ensure proper alignment with the other substrates during the anodic bonding process which will be presented later, as well as marks that will be used for alignment when cutting the microchannels. The resulting wafer is shown in figure III.4.

Figure III.4: Glass wafer wet etched by KOH assisted by femtosecond laser

III.1.1.2 Patterning of the silicon wafer W_{Si1} (Step II)

The wafer W_{Si1} is used to make the microchannels. After cleaning the substrate with Acetone and Ethanol, followed by a cleaning with the « Piranha » mixture (*step n° II - 1*), a 350 nm thick layer of SiO_2 with a thickness of 350 nm with uniformity of $\pm$ 2.5% is deposited by PECVD (Plasma Enhanced Chemical Vapor Deposition) on the back side surface (*step n° II-2a*), to enhance the bonding strength of the PDMS bonding (step n ° V in figure III.2). Then, a 500 nm thick layer of Al, deposited by sputtering on the back side (*step n° II-2b*), will act as a stop layer for the deep dry etching step (*step n° II - 3* in figure III.2). Table III.1 presents the sequence of steps for the patterning of the wafer W_{Si1}.

Table III.1: Successive steps for the patterning of wafer W_{Si1}

Step n°	Process	Description of the process
II - 1	Substrate cleaning	Acetone + Ethanol Piranha mixing
II - 2a	SiO_2 layer deposition (backside)	SiO_2 deposition by PECVD[1] Thickness: 350 nm
II - 2b	Al layer deposition (backside)	Deposition of Al by sputtering Thickness: 500 μm
II - 3a	Photolithography	AZ10XT photoresist Thickness: 6 μm - 14 μm
II - 3b	Si Etching	DRIE[2] - Depth of etching is equal to the wafer thickness
II - 3c	Resist stripping	Acetone Ultrasonic bath
II - 3d	Al layer etching	Al etch mixture at 40°C

[1] Plasma Enhanced Chemical Vapor Deposition
[2] Deep Reactive Ion Etching

a) Photolithography step for etching process

The photolithography process is a critical step that is commonly used to transfer patterns from a mask to a photoresist layer deposited on the wafer surface.

A thin layer of « TI Prime » [3] as an adhesion promoter is first spin-coated onto the wafer surface to enhance the adhesion of the photoresist. Then, the photoresist is deposited by spin-coating on the wafer to obtain a layer of uniform and controlled thickness (*step n° II-3a*). The photoresist thickness is controlled by the speed at which the photoresist is deposited [144][145] [146]. The resulting photoresist layer is then exposed to a UV lamp through a mask. The masks are made of glass, with thin structured layers of Chromium on the areas where the resist should not be exposed. The mask used for the etching of the wafer W_{Si1} is shown in figure III.5.

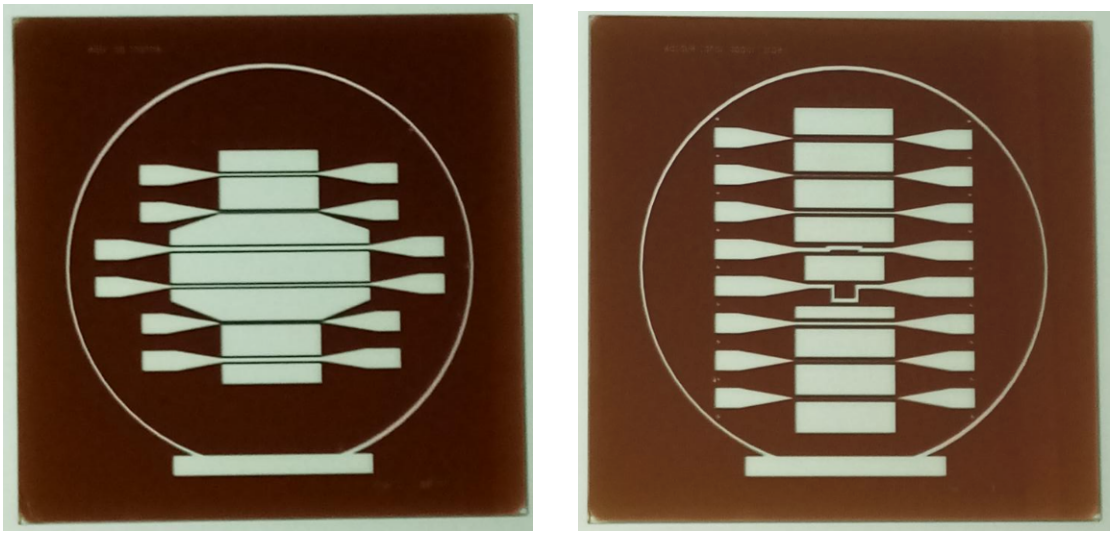

(a) (b)

Figure III.5: Photolithography masks for the Si etching used to fabricate the microchannels (light blue areas will be etched out), (a) Straight microchannels (b) Microchannels containing bends and microchannels designed for the study of the influence of the channel's aspect ratio on the flow.

The energy required for the exposure of the photoresist depends on the type of photoresist used and the thickness of the spin-coated layer. By measuring the power of the UV lamp, the exposure time t_{UV} can be calculated.

$$t_{uv} = \frac{E_{uv}}{P_{uv}} \tag{III.1}$$

With P_{UV} the power of the U.V. lamp and E_{UV} the required energy to expose the photoresist.

The wafer is then placed in a developer solution for a time which also depends on the thickness of the photoresist layer. The « AZ10XT » photoresist used is a positive thick resist, for which the developer will only remove the exposed areas. The solution used for developing the « AZ10XT » photoresist is a mixture of water and the developer « AZ400K1:4 » with a ratio of 4:1.

[3] https://microchemicals.com/micro/tds_ti_prime.pdf

The different parameters of the photolithography step are presented in Table III.2 according to the etching depth that should be achieved. The required thickness of the photoresist is determined according to the ratio of the dry etching rate between silicon and photoresist.

Table III.2: Parameters for the photolithography step

Etching depth (μm)	Thickness of photo-resist layer (μm)	Spin-coating speed (rpm)	Exposure energy ($mJ.cm^{-2}$)	Development time (min)
100	6	4800	280	3
200	6	4800	280	3
500	8	2500	350	4
1000	14	800	450	6

Once the photolithography step is achieved, a profilometer (« Stylus profilometer Dektak XT » from the Brucker company) is used to check if the deposited photoresist thickness meets the expectations. Then, a microscope (« Leica DM8000 » from the Leica-microsystems company) is used to also check the conformity of lateral dimensions of the patterns transferred to the photoresist.

b) Etching of Si (*step n° II-3b*)

Etching of the silicon wafer is performed using the dry etching process called Deep Reactive Ion Etching (DRIE). This process is typically used to etch structures with high aspect ratios. The process is highly anisotropic and allows obtaining extremely vertical sidewalls (with an angle close to 90°). Before the beginning of the etching process, the chamber is cleaned with oxygen gas and then conditioned with the gases used for the process.

The wafer is placed on a chuck with electrostatic clamping and inserted in the etching chamber. A chiller maintains the chuck temperature close to 0°C ensuring efficient cooling of the wafer during the high-energy etching process. A plasma using Argon gas is then generated in the chamber, to convert gas atoms into ions. The Bosch process[1], commonly used in deep etching, consists of a succession of steps after the plasma generation as illustrated by figure III.6 [2]:

- Deposition of an inert passivation layer (C_4F_8).

  Deposition of an inert passivation layer at the bottom of the cavity. This passivation layer protects the sidewalls from lateral etching.

- Etching step (SF_6).

  The etching step is divided into two sub-steps. The ions accelerate almost vertically toward the surface of the substrate and attack the passivation layer at the bottom of the cavity, removing the atoms of this layer (Physical etching). Then, the ions react with the substrate material at the bottom of the cavity generating another gas (Chemical Etching).

[1] https://www.freepatentsonline.com/6284148.html
[2] https://www.samco.co.jp/en/technews/2020/what-is-the-bosch-process.php

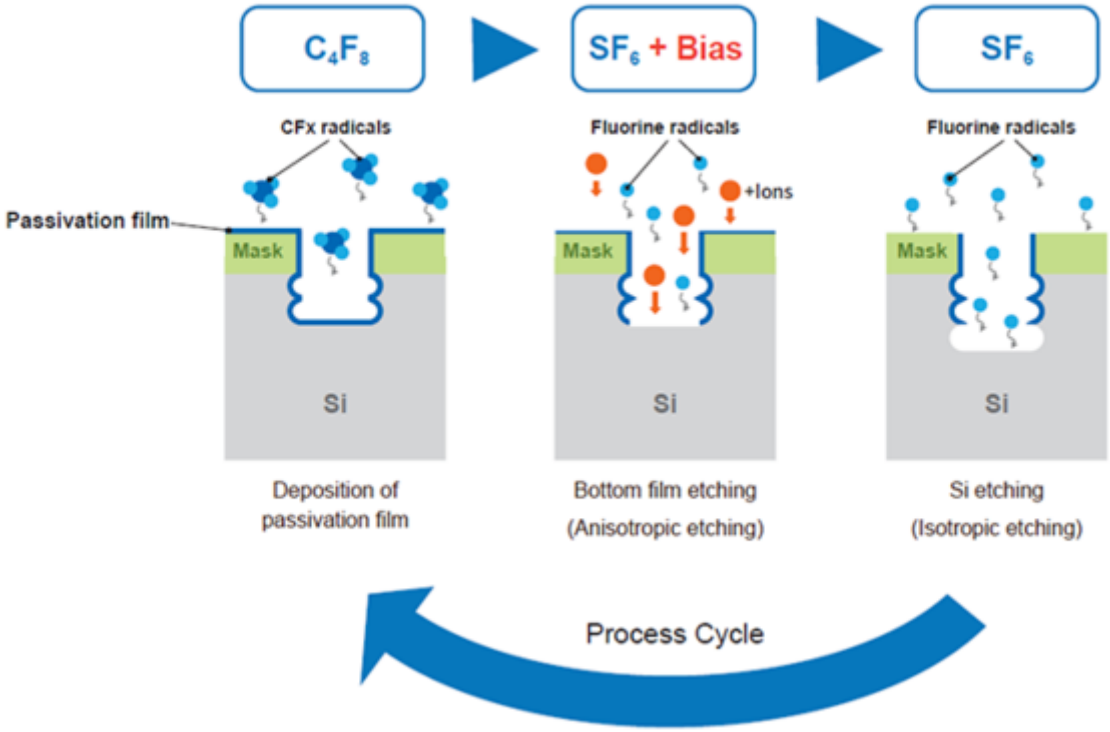

Figure III.6: Principle of Bosch process [2]

The parameters of the plasma during each step of the DRIE etching process are given in the table III.3.

Table III.3: Plasma parameters during each step of the etching process

Etching process step	Strike	Passivation layer deposition (C_4F_8)	Etching of passivation layer (SF_6)	Etching of Silicon (SF_6)
Gas pressure ($mTorr$)	40	40	40	75
Gas flow ($sccm$)	Ar: 200 C_4F_8: 400	C_4F_8: 300	SF_6: 450	SF_6: 450

These steps only take a few seconds and are repeated until the end of the etching process. The number of cycles required for each etching depth is shown in the table III.4.

Table III.4: Mean number of etching cycles for the different etching depths

Etching depth (μm)	100	200	500	1000
Mean number of cycles	175	300	700	1250

The photoresist used, as well as its thickness, are important parameters because it will also be etched by the DRIE process and may completely disappear before the end of the process. Therefore, thick resists are used for the deep etching process. The thickness of the photoresist required as a mask for the etching process depends on the etch selectivity defined by the ratio of the silicon etch rate to

the resist etch rate. By measuring the thickness of the photoresist layer before and after the etching process on test wafers, the thickness of the etched resist can be determined. The measurement of the etching selectivity of Silicon versus AZ10XT photoresist was determined equal to 98.6 $\pm$ 2.7. Figure III.7 shows a wafer after the DRIE etch-through process.

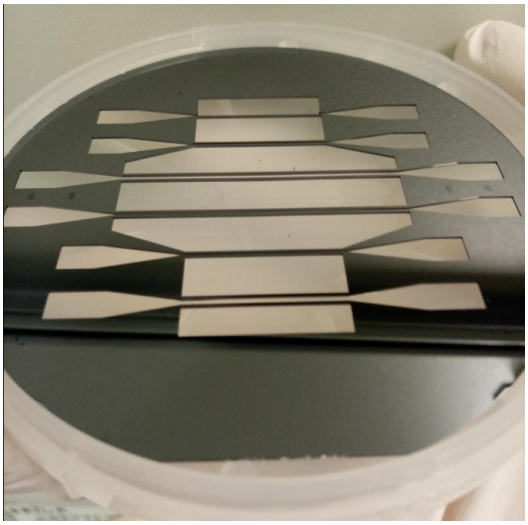

Figure III.7: Resulting wafer W_{Si1} after the deep etching process

The etching rate of silicon also depends on the width of trenches that are etched. Since there are microchannels with different widths on the same wafer, the etch-through process will be finished for some channels while others will take more time. Therefore, under-etching of the silicon on the back side can occur at the end of the etching process for the channels that are the first to be etched. To avoid this under-etching, a 500 *nm* thick Aluminum (Al) layer is sputtered on the back surface of the wafer before the photolithography step.

The end of the etching is detected using Claritas Optical Emission Spectroscopy (OES), which detects the change of plasma chemistry when it reaches the stop layer. Fig III.8 shows the signal detected by the OES system during an etching process. The signal increases at the beginning as the surface etched by the plasma increases. The signal decreases at the end of the process as the plasma meets more and more surfaces of the Al layer. Once all etched surfaces reach the Al layer, the signal remains constant meaning that the etching process is ended. The remaining photoresist is then stripped with Acetone and Ethanol (*step n° II-3c*).

c) Aluminum layer etching (*step n° II-3d*)

After the deep etching process of the silicon, the remaining aluminum layer deposited on the backside of the wafer as a stop layer for the etching process is no longer useful and must be removed to keep access to the temperature sensor connectors. This aluminum layer is etched by wet chemical etching using an « Aluminum etch » solution composed of 85% orthophosphoric acid (H_3PO_4), 100% acetic acid (CH_3COOH), and 68% nitric acid (HNO_3), with a volume mixing ratio of 29:5:1. This wet etching is performed at a temperature of 40°C, with an etching rate around 100 $\mathrm{nm\,min^{-1}}$.

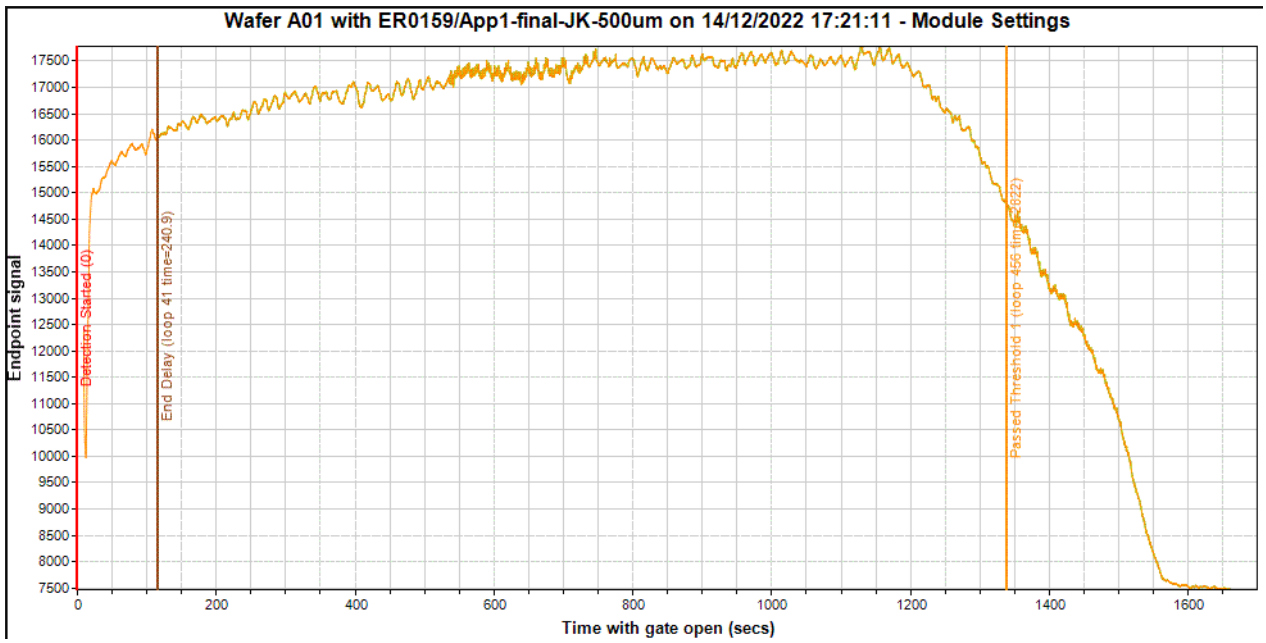

Figure III.8: Signal detected by the Claritas OES system during the DRIE process

III.1.1.3 Patterning of the silicon wafer W_{Si2} (*step n° III*)

The silicon wafer W_{Si2} is the wafer on which the pressure and temperature sensors will be implemented at both ends of the microchannels. Table III.5 presents the successive steps of this process.To obtain proper electrical and thermal insulation of the temperature sensors, oxidized silicon wafers are used for the implementation of the sensors within the microchannels (the thickness of the SiO_2 layer is about 1.3 μm on both sides of the wafer). Oxidized wafers are cleaned with Acetone and Ethanol before the beginning of the process (*step n° III - 1*).

a) Deposition of the metal layers

The deposition of Platinum layers as well as the deposition of Gold layers is performed by a sputtering process. This deposition method presented in figure III.9 consists of the biasing of a metallic target. An argon gas is injected into the chamber, this gas will be positively ionized (Ar^+) by collisions with electrons (e^-). The Ar^+ ions will then be attracted to the negatively polarized metal target (Cathode). The collision between the Ar^+ ions with the target will release the metallic particles which will be deposited on the wafer surface.

Regarding the deposition process, a layer of AZnLof photoresist is deposited on the wafer with a thickness of 1.3 μm (*step n° III - 2a* and *step n° III - 3a*) to achieve a « lift-off » process. Figure III.10 shows the masks used for the lift-off process of (a) Platinum and (b) Gold deposition.

Before performing the deposition process, the wafer is cleaned using a RF-Plasma (RadioFrequency plasma) with a power of 50 W and a bias of 80 V at a gas pressure of 0.9 Pa for 2 min. Then, to enhance the adhesion of Platinum on the wafer surface, a 20 nm thick adhesion layer of Chromium is first deposited on the surface (*step n° III - 2b*). In the same way, to promote the adhesion of the Gold layer, a Titanium layer with a thickness of 20 nm is deposited beforehand (*step n° III - 3b*).

Table III.5: Successive steps of the process for the temperature and pressure sensors realization

Step n°	Process	Description of the process
1	Substrate cleaning	Acetone + Ethanol Piranha mixing
2-a	Photolithography	AZnLof photoresist Thickness: 1.3 μm
2-b	Pt thin film deposition	Deposition of Pt by sputtering with Cr as an adhesion layer. Thickness: 200 *nm* (Pt) - 20 *nm* (Cr)
2-c	Lift-off	Resist striping Acetone + Ultrasonic bath
3-a	Photolithography	AZnLof photoresist Thickness: 1.3 μm
3-b	Au thin film deposition	Deposition of Au by sputtering with Ti as an adhesion layer. Thickness: 350 *nm* (Au) - 20 *nm* (Ti)
3-c	Lift-off	Resist stripping Acetone and Ultrasonic bath
4-a	Preparation of PDMS mixture	PDMS base : Curing agent mixing Mixing ratio 10:1
4-b	PDMS spin-coating	PDMS deposition by spin-coating Thickness: 15 μm
4-c	Polymerization of PDMS mixture	Post-baking Polymerization of PDMS
5-a	Photolithography (backside)	AZ10XT photoresist Thickness: 10 μm
5-b	Etching of SiO_2 layer (backside)	RIE for oxide etching Thickness of SiO_2 layer: 1.3 μm
5-c	Etching of Si (backside)	DRIE - Depth of etching: 500 μm (thickness of the wafer W_{Si2})

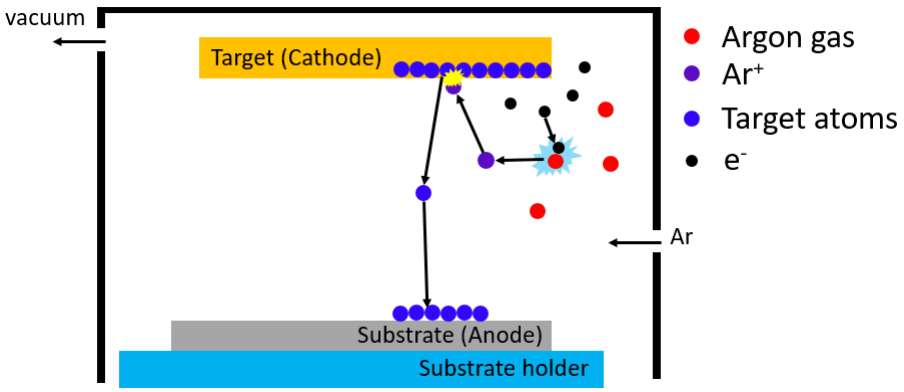

Figure III.9: Scheme of the deposition process by DC magnetron sputtering

The deposition rate of the metallic element is given in table III.6. Figure III.11 shows a picture of the wafer after the deposition process. Then, the remaining photoresist is stripped with Acetone and Ethanol to achieve the "lift-off" process removing the deposition of metallic thin film at the undesired locations on the photoresist layer. This lift-off process is realized using an ultrasonic bath to enhance the removal of both photoresist and metallic layers to prevent the probes from being short-cut.

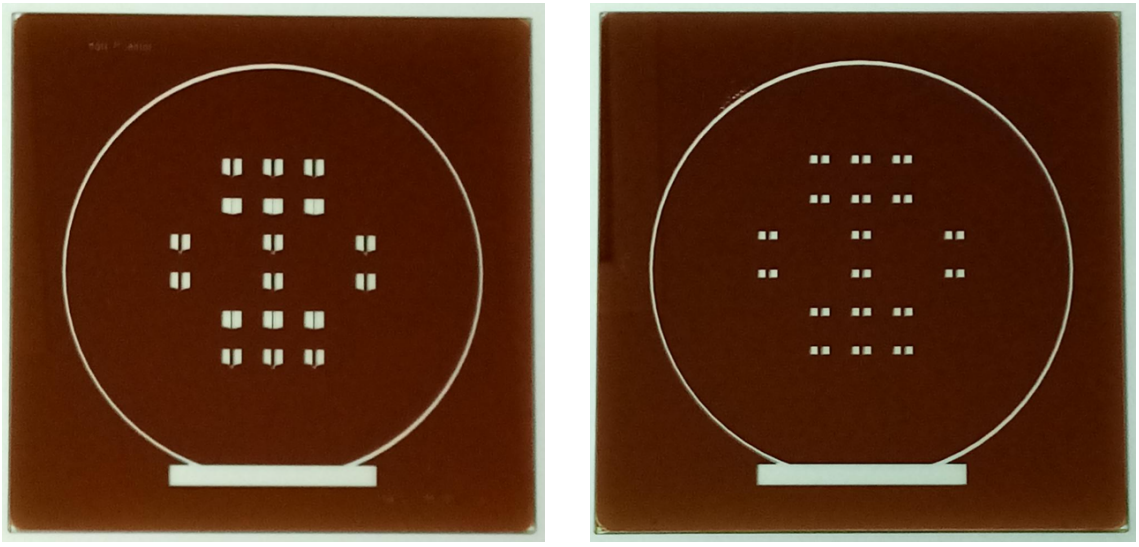

(a) (b)

Figure III.10: Photolithography masks used for (a) Platinum and (b) Gold deposition

Table III.6: Deposition rate, uniformity, and parameters of metallic deposition.

	Material	**Gas pressure process (Pa)**	**Current (A)**	**Power (W)**	**Deposition rate** $(nm.min^{-}1)$	**Uniformity**
	Cr	0.9	1	412	100	$\pm$ 10%
	Ti	0.9	1	370	50	$\pm$ 6.9%
(*step n° III - 2b*)	Pt	0.9	0.3	211	60	$\pm$ 11%
(*step n° III - 3b*)	Au	0.9	0.3	190	100	$\pm$ 12.5%

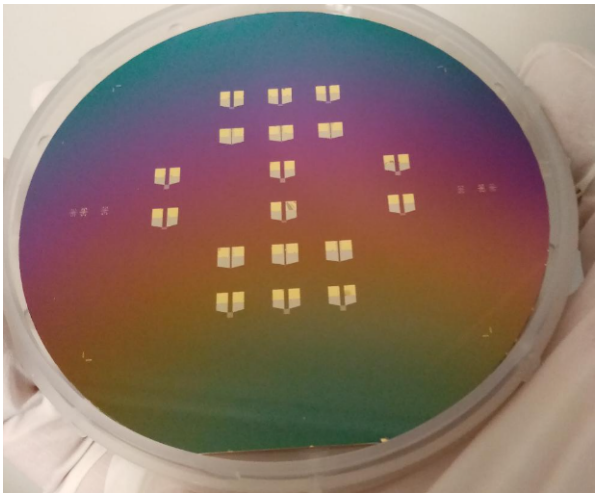

Figure III.11: W_{Si2} Wafer after the deposition processes

b) Deposition of PDMS thin films (*step III - 4*)

PDMS has been selected as a glue for the bonding of the silicon wafers and was expected to be used to make membranes for the pressure sensors. To manufacture the PDMS layer, the PDMS mixing needs to be prepared first. PDMS is obtained by mixing the Sylgard 184 silicone elastomer base with the curing agent in a 10:1 ratio. This ratio is obtained by measuring the mass of the elastomer base and curing agent, using a scale with an accuracy of $\pm 0.01g$ as shown in Figure III.12 (a). To obtain a uniform thick layer of PDMS, the quantity of PDMS elastomer base used for this process is 20 g, while the quantity of curing agent extracted and mixed with the PDMS elastomer base is 2 g. The solution is then mixed intensively for several minutes to homogenize it (*step III - 4a*). Once the solution is prepared, it is placed in a vacuum bell for about an hour to eliminate air bubbles inserted in the solution during the mixing phase as shown in Figure III.12 (b).

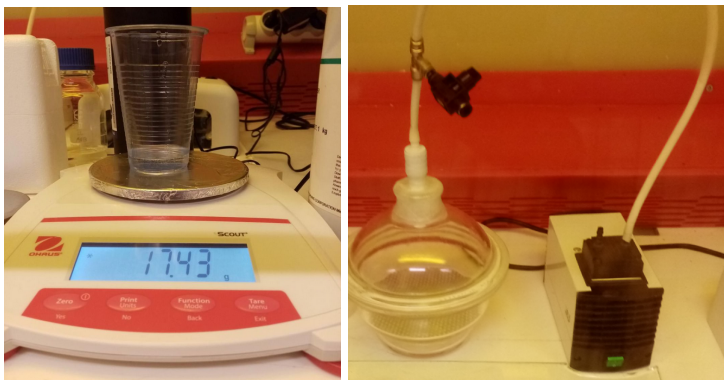

(a) (b)

Figure III.12: (a) Scale used to obtain the correct mixing ratio PDMS: Curing agent. (b) Vacuum bell used to eliminate air bubbles

Once the preparation of the PDMS mixture is done, PDMS is deposited on the wafer surface by spin-coating (*step III - 4b*). The PDMS solution is poured on the wafer surface as shown in Figure III.13 (a). The panel command used to define the parameters of the spin-coating is shown in Figure III.13 (b). The panel command allows controlling the speed and acceleration at which the deposition of PDMS is performed as well as the time of spin-coating.

The thickness of the resulting deposited PDMS thin film is a function of 3 parameters: speed of the spin-coating, time of the spin-coating, and mixing ratio PDMS: Curing agent. The thickness of the PDMS thin film deposited by spin-coating is represented as a function of the speed of the spin-coating in figure III.14. a [147], and as a function of the time of the spin-coating for different speeds in figure III.14.b [147]. In order to obtain the expected thickness around 20 μm of the deposited PDMS layer, the PDMS is spin-coated at 1500 rpm for 1 minute and 30 seconds (*step III - 4b*).

The curing of PDMS at room temperature is a long process. This time can be decreased by increasing the polymerization temperature. Table III.7 gives the recommended curing time from different sources for different curing temperatures. In addition, the Center of MicroNanoTechnology [1] (CMI) facility of EPFL also recommends a curing time of about 2 h at a curing temperature of 80 °C.

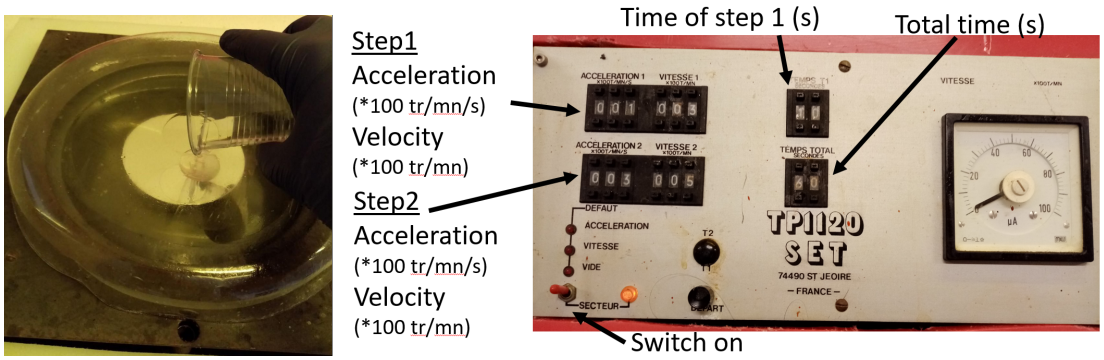

(a) (b)

Figure III.13: Substrate holder (a) and Panel command (b) for the spin-coating of PDMS

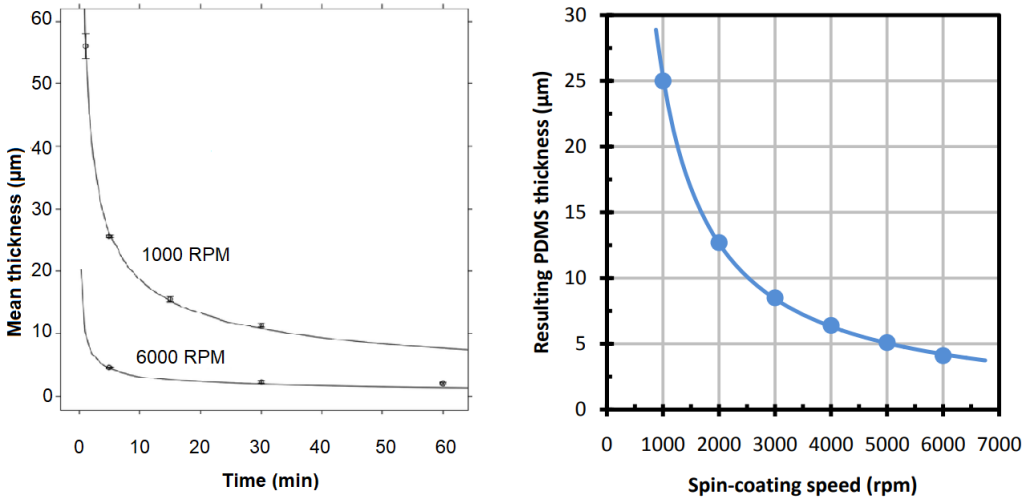

(a) (b)

Figure III.14: Mean thickness of PDMS layer as (a) function of spin-coating time [147] (b) spin-coating speed for a spin-coating time of 5 minutes [1]

For the curing of the deposited PDMS layer, we used the same parameters as the one recommended by the CMI facility of EPFL (*step III - 4c*).

Table III.7: Curing time of PDMS versus curing temperature

	Curing temperature (°C)	25	100	125	150
Dow Corming [2]	Curing time	48 h	35 min	20 min	10 min
Johnston *et al.* [148]		48 h	53 min	38 min	28 min
Prabowo *et al.* [149]		48 h	45 min	35 min	25 min

[1] https://www.elveflow.com/microfluidic-reviews/soft-lithography-microfabrication/pdms-membrane-thickness-of-a-spin-coated-pdms-layer/

[2] https://www.epfl.ch/research/facilities/cmi/equipment/packaging-miscellaneous/pdms-line/

[3] https://www.dow.com/en-us/document-viewer.html?docPath=/content/dam/dcc/documents/en-us/productdatasheet/11/11-31/11-3184-sylgard-184-elastomer.pdf

c) Release of the PDMS membrane (*step III - 5*)

Optical apertures are made through the silicon wafer W_{Si2} using deep dry etching of the substrate with circular patterns whose diameters are equal to the width of each microchannel. Since the wafer will be placed on an electrostatic chuck during the etching process, a thin layer of Titanium is deposited on the PDMS layer as shown in figure III.15 (a). This layer will also limit the contamination of the chuck by the PDMS layer. After less than 5 min of Silicon dry etching, all the photoresist deposited on the back-side of the wafer was burned (figure III.15 (c)) as well as a significant area of the PDMS layer (fig III.15 (b)). This may be due to the thermal insulation provided by the PDMS layer, which prevents the heat generated by the etching process from being dissipated.

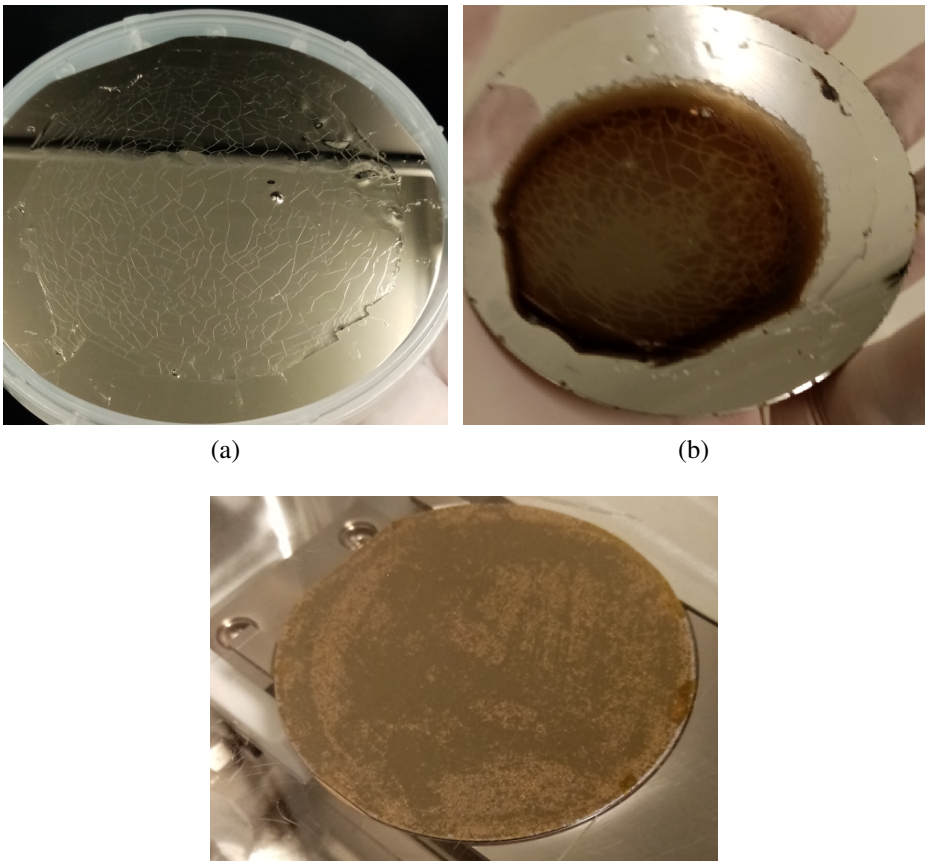

(a) (b)

(c)

Figure III.15: Surface condition of front-side wafer (a) before etching process, (b) after 5 minutes of etching process. (c) Surface condition of back-side wafer after 5 minutes of etching process

Therefore, to avoid issues caused by the presence of the PDMS layer during the Silicon dry etching process, it was decided to spin-coated the PDMS only after wafer etching. For this purpose, before silicon etching, a 2 μm thick Aluminum layer was deposited locally on the wafer front side around the membrane locations to hold the PDMS layer after etching the Silicon wafer. Precautions were taken to make sure that the Aluminum layer does not create a short circuit of the temperature sensors.

After etching the optical window used to monitor the deflection of the membrane, the PDMS layer is deposited by spin-coating on the aluminum layer. Then, the aluminum layer is removed by wet etching using the Aluminum etch solution mentioned earlier.

III.1.1.4 Bonding of the wafers W_{Glass} - W_{Si1} (*Step IV*)

The bonding of the wafers W_{Glass} and W_{Si1} is performed by anodic bonding. The principle of anodic bonding is illustrated in figure III.16.

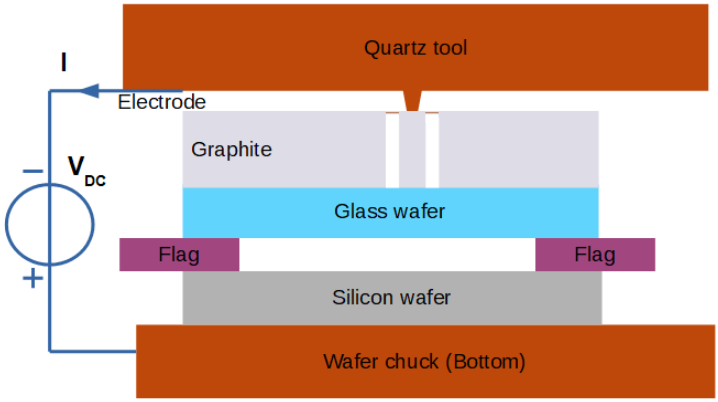

Figure III.16: Scheme of anodic bonding

a) Anodic bonding process

Anodic bonding have been used in numerous study and is well known [150] [151] [152] [153]. Before anodic bonding, the glass and Silicon surfaces to be bonded must be thoroughly cleaned. Then, the silicon wafer is placed at the bottom of the stack, while the glass wafer is placed at the top. Flags with a thickness of 50 μm are placed between the two wafers. A graphite disk and a quartz tool are placed above the stack to force the contact between both wafers. The chamber is put under vacuum (pressure $\leq 10^{-4}$ mbar) before decreasing the separation between the two wafers down to 0.3 mm.

The wafers are aligned before making contact between the two wafers with an applied force set to about 100 N $\pm$ 5 N. Once the contact is made, the wafers are heated with a halogen lamp to a temperature of 350°C $\pm$ 2 °C at which the bonding will be performed, with a ramp of 10° C min^{-1}. The temperature difference between the top chuck and the bottom chuck is maintained below 5°C to limit the thermal stress that can occur for higher values. A voltage of 600 V is applied, with current limited to 4 mA.

This applied voltage will force the positive ions Na^+ contained in the glass wafer to move towards the cathode (to the top of the stack) while the negative O^{2-} will move towards the bonding interface and will react with the silicon wafer creating a thin layer of SiO_2, this oxide layer will ensure a strong connection between wafers. The bonding process takes approximately 15 min. This results in an electric charge of 1500 - 2000 mC transferred, depending on the bonded surface. Figure III.17 shows the evolution of the current and the voltage during the bonding.

The bonded substrates are then cooled down to room temperature. This cooling is done by an initial ramp of $-5°C/min$ down to $250°C$ and then - 10 ° C min^{-1} from 250 °C to 150 °C ended

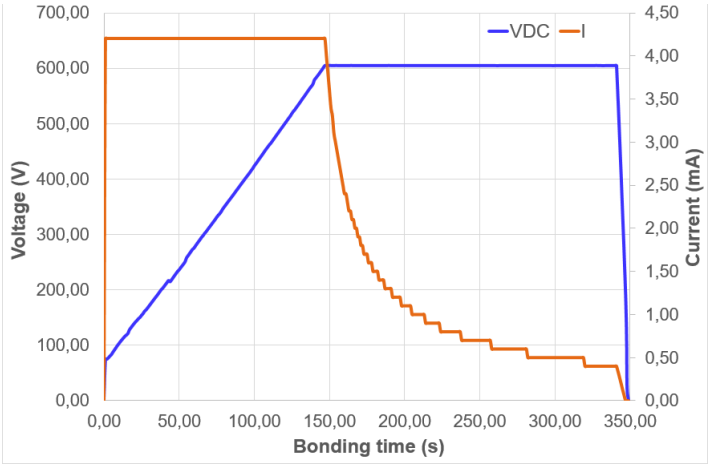

Figure III.17: Voltage and current during the bonding process

by free cooling, with nitrogen gas injected into the chamber. The resulting stack is shown in figure III.18.

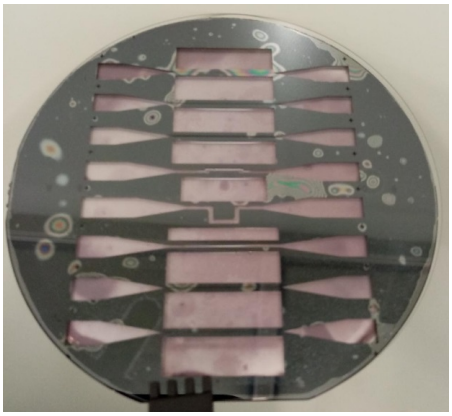

Figure III.18: Result of the anodic bonding process using the initial recipe

Many bonding defects are visible in the picture, which might be due to an imperfect cleaning of the substrates or poor contact between the wafers. The contact can be insufficient if the total variation of the wafer thickness is significant or if the curvature of the wafers is large. Particular attention was therefore given to the above-mentioned parameters while the bonding parameters have been modified to improve the bonding process.

b) Improvement of the anodic bonding process

To overcome the difficulties observed previously with the anodic bonding process, the applied voltage during bonding is increased from 600 V to 700 V. In addition, the contact force between the substrates is also increased from 100 N to 250 N to compensate for the wafers bending, which leads to poor contact between the wafers.

As cracks were also observed at various places on the wafer surface, the cooling has been modified to allow a more gradual cooling. In the new cooling process, there is an initial ramp of - 2°C min^{-1} down to 250°C, followed by a ramp of - 5°C until the temperature reaches 200°C which ends with the same free-cooling after injecting nitrogen gas in the chamber.

The resulting wafers are shown in figure III.19. The picture shows breaks on the edge of both wafer stacks and poor bonding on a circular surface of about 5 mm diameter in the middle of the 1.5 mm thick wafer stack.

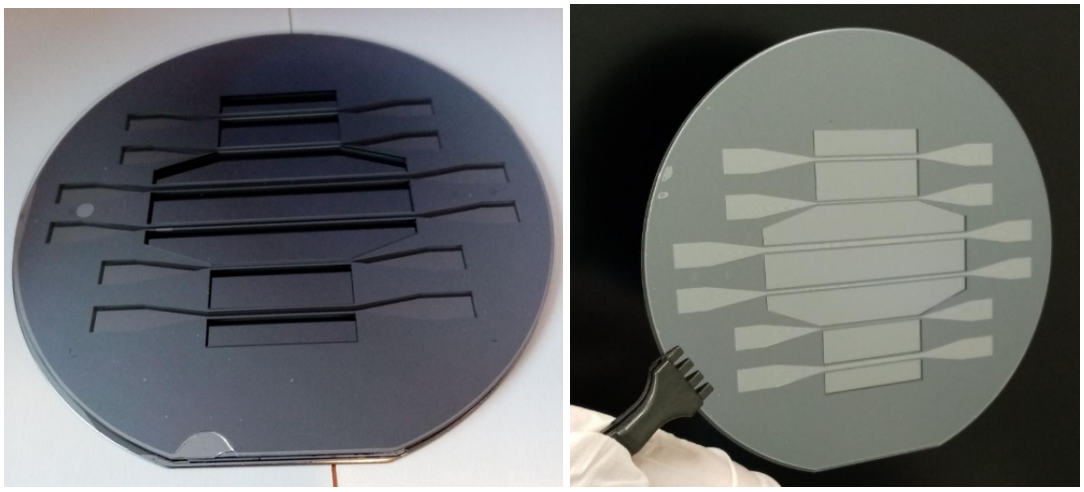

(a) (b)

Figure III.19: Result of the anodic bonding process using the improved recipe, with a 0.5mm thick glass wafer and (a) a 1 mm thick silicon wafer, (b) a 0.5 mm thick silicon wafer

Despite these minor defects, the bonding process succeeded in bonding the rest of the surface of both wafers properly. The improvements made to the recipe of the anodic process result in a proper bonding between the glass wafer and the silicon wafer.

III.1.1.5 Bonding of the stack W_{Glass} - W_{Si1} with the wafer W_{Si2} (*Step V*)

The critical step of the wafers bonding is the bonding between the two Silicon wafers W_{Si1} and W_{Si2}. Indeed, due to the presence of the thin layers of the temperature sensors, which go under the sidewalls of the microchannels, the « classical » Si-Si bonding (direct bonding) cannot be used. Two types of bonding were tested: the first with dry photoresist film; and the second with PDMS. These are presented below.

a) Adhesive bonding with lamination of dry photoresist film (20 μm thick)

Initially, the bonding between the stack composed of W_{Glass} and W_{Si1} wafers with the wafer W_{Si2} was done using an adhesive bonding technology. To do so, a dry resist film was used. First, this film must be thermally glued on the surface of the wafer etched by the DRIE process. Then, the bonding is performed by making a contact between W_{Si1} and W_{Si2} at a moderate temperature of 60 °C.

For this purpose, a dry resist film is cut to the dimensions of the wafer. The protective film is then removed and the adhesive part is placed in contact with the wafer. The temperature of the chuck on which the stack is placed is raised to 90 °C and contact is ensured by applying a force of 150 N. The stack is then cooled to room temperature. The dry resist film is then peeled off, structuring the resist layer that will be bonded to the W_{Si2} wafer, enabling access to the temperature sensor connectors. The stack is then placed on the bottom chuck of the bonding machine while the W_{Si2} wafer is placed on the top chuck, the wafers are then put in contact to ensure the bonding. Bonding is performed at a temperature of 120 °C with a contact force of 200 N for 5 min. The cooling is done by a ramp of - 2

°C min^{-1} to 50 °C followed by a free cooling to room temperature. The bonding setup is presented in figure III.20.

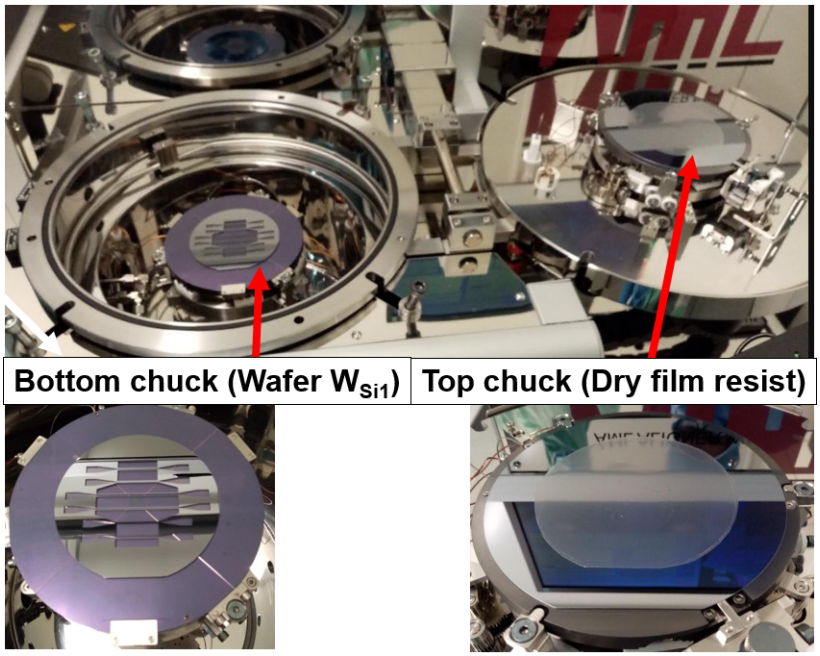

Figure III.20: Dry film resist bonding setup

The bonding quality is evaluated with two unprocessed wafers. The bonded wafers are cut into 10 mm x 10 mm samples to measure the bond strength. These samples are glued using a cyanoacrylate glue (Loctite 380) on two supports, located on each side of the sample as shown in figure III.21. This gluing ensures a greater adhesion than the bonding adhesion. The measurements are achieved with the Nordson DAGE 4000Plus bond tester in the stud-pull mode using a 200 kg cartridge. The movement of the mechanical gripper generates a force on the bonded sample, that is gradually increased until the samples are detached.

The bonding strength is related to the load force:

$$\sigma_B = \frac{F}{A_B} \tag{III.2}$$

where σ_B corresponds to the bonding strength, F = m g is the load force with m the load and g the gravity acceleration, and A_B corresponds to the bonding area. The results will be expressed in Newton unit corresponding to the load force as well as Pascal unit corresponding to the bonding strength The bond strength of each of the eight tested samples is given in the table III.8. The mean bond strength is equal to 2.81 $\pm$ 0.46 MPa.

Figure III.22 represents: (a) the configuration before the adhesive bonding with the dry film resist placed on a 6-inch support, while the stack made of the glass wafer bonded to the silicon wafer is placed above, (b) picture of the resulting surface after peeling off the dry film resist.

Figure III.22 shows that the structuring of the resist when the dry resist film is peeled off is not perfect, in particular around the patterns etched by DRIE. The modification of the parameters (contact

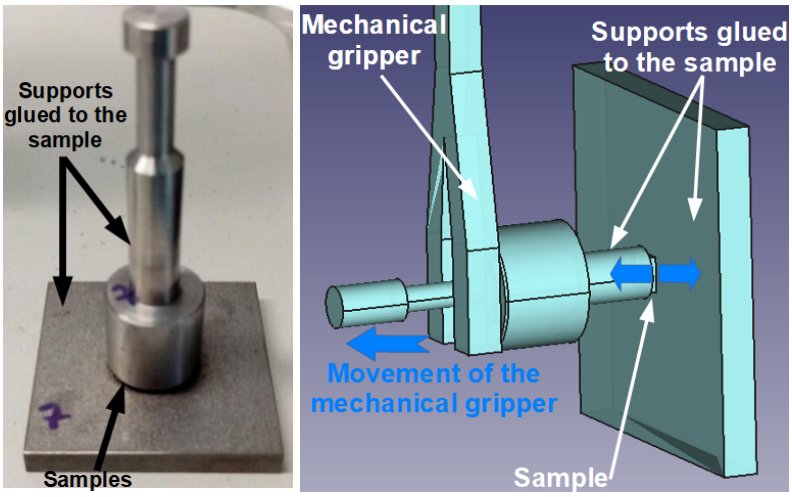

(a) (b)

Figure III.21: Samples setup for bonding strength measurement

Table III.8: Bond strength of dry film resist bonding

Samples	1	2	3	4	5	6	7	8	**Mean value**	**Standard variation**	**Uncertainties**
Load force (N)	246.59	214.96	335.13	279.73	328.89	301.53	227.77	309.03	**280.45**	**45.99**	$\pm$ *1.23*
Bond strength (MPa)	2.4659	2.1496	3.3513	2.7973	3.2889	3.0153	2.2777	3.0903	**2.8045**	**0.460**	$\pm$ *0.0123*

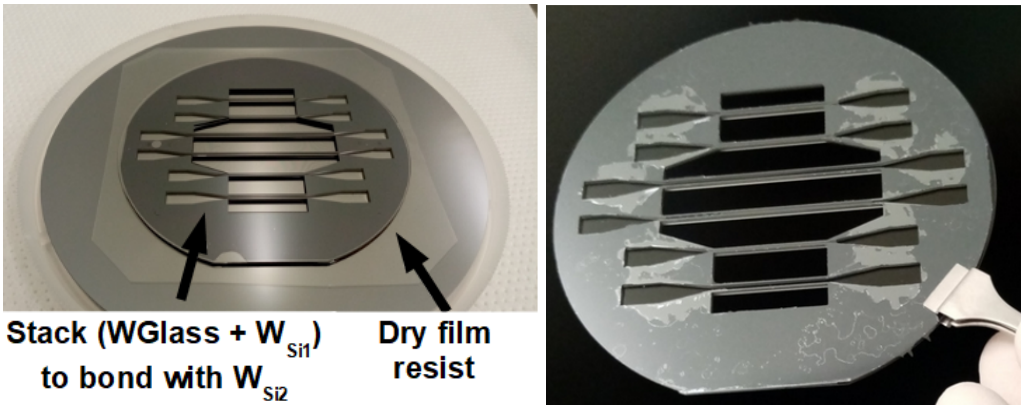

(a) (b)

Figure III.22: (a) Transferring dry film resist pattern on the back side surface of wafer W_{Si1}, (b) Surface condition after peeling off the film of dry resist

force, temperature at which the dry resist film is glued on the wafer surface) has succeeded in making a slightly better bonding but it remains imperfect as shown in the pictures taken by microscope in Figure III.23. In these pictures, issues of the dry film resist bonding can be observed. In the picture

(a), some parts of the resist have been peeled off on the surface to bond which will result in poor bonding at this location. In the picture (b), the presence of resist at the bottom of the microchannel cavities is an issue as it will disturb the flow of gas. This poor bonding can be explained by the large thickness of this dry-resist film (20 μm). Other tests carried out with 5 μm thick dry resist films have shown better results but not sufficient to provide good satisfaction on this bonding technique.

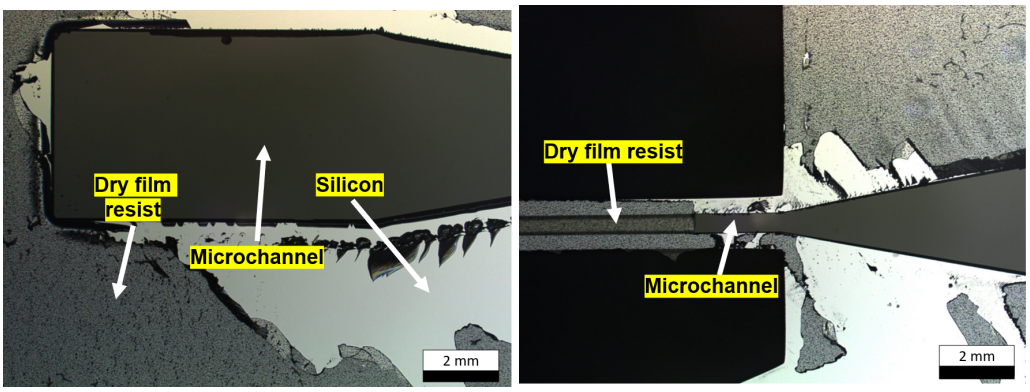

(a) (b)

Figure III.23: Zoom on etched structures after peeling off the dry film resist (a) resist peeled off on bonding surface, (b) presence of resist at the bottom of the microchannel cavities

Although the bonding of two unprocessed wafers with the lamination of dry photoresist films is successful with a bonding strength of 2.81 $\pm$ 0.46 MPa, this bonding method remains non-reliable for patterned wafers, probably due to the thickness of the film too important to allow a good structuring of the bonding surface. Therefore, another bonding technique has been tested using the PDMS layer which is used for the pressure sensor as a layer for the bonding step. PDMS has been used by several authors as an intermediate layer for the bonding of two silicon wafers.

b) PDMS bonding

i- Presentation of the PDMS bonding process

The first step in this bonding process is to activate all surfaces to be bonded with an Oxygen plasma to make all of them hydrophilic. This applies to PDMS and silicon surfaces as can be seen in Figure III.24. By putting the surfaces in contact, the elimination of Hydrogen gas leads to a strong oxygen bond between the two wafers as illustrated in figure III.24. Various studies have been carried out involving bonding between glass and/or silicon using PDMS as an intermediate layer for the bonding [154] [155]. Several investigations about PDMS bonding have been conducted. Kersey *et al.* [156] determined the adhesion strength of PDMS bonding on different materials. The authors observed that without an adhesion promoter, the PDMS bonding strength was higher for silicon with 468 $\pm$ 128 kPa while only 161 $\pm$ 37 kPa for glass substrate. However, with an adhesion promoter, the bonding strength was almost equal for both silicon and glass substrates with 841 $\pm$ 155 kPa and 847 $\pm$ 152 kPa respectively. The parameters of the oxygen plasma used to activate the surface are presented in table III.9. These parameters correspond to parameters used in previous investigations of

bonding between PDMS and several materials [157]. This bonding shows sufficient bonding strength for our study.

Then, the surfaces are aligned, and a moderate force of 100 N is applied to achieve the bonding. Finally, the bonded substrates are placed in an oven at 70 °C for one hour.

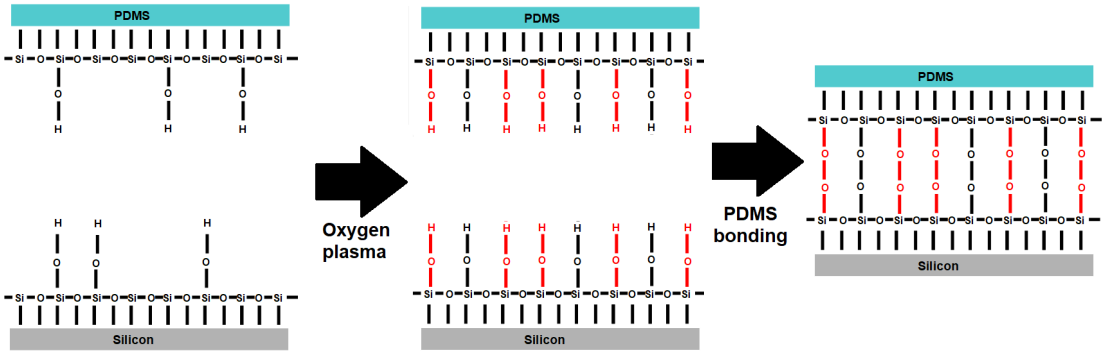

(a) (b) (c)

Figure III.24: PDMS bonding mechanism: (a) initial wafers, (b) wafers after Oxygen plasma treatment, (c) wafers after bonding

Table III.9: Parameters of the O_2 plasma for the surface activation to achieve PDMS bonding [157]

Plasma power (W)	**O_2 flow rate** $(sccm)$	**Gas pressure** $(Torr)$	**Plasma time** (min)
100	80	0.8	1

ii- Success and issues of the PDMS bonding

The PDMS bonding was first tested to bond two unprocessed silicon wafers. Then it was tested with structured wafers. Regardless of the bonding process used, an alignment between the two substrates to be bonded must be performed. Alignment marks were therefore etched or deposited. The alignment step of the bonding process is shown in figure III.25. The accuracy of the alignment is $\pm$ 1 μm.

For the bonding of two unprocessed silicon wafers, a 350 nm thick SiO_2 layer was deposited by PECVD on both wafer surfaces. Then, PDMS was spin-coated onto one of the wafers using the process detailed in the PDMS deposition section. The PDMS bonding procedure is the same as described above. Once both wafers were bonded, they were cut into 10 mm x 10 mm samples to characterize the bond strength. The results of the characterization of the bonding strength of the samples are given in Table III.10. The samples 9 and 10 were not glued enough and resulted in low bonding strength measured. These two samples will not be considered in the calculation of the mean bonding strength. The mean bonding strength of PDMS bonding is equal to 1.26 $\pm$ 0.6 MPa.

From Table III.10, we can observe a slight difference in the bonding strength measured between samples that were located at the edge of the wafer compared to the samples located at the center. This can be due to the non-uniformity of the PDMS deposition caused by its high viscosity. Similar values of bonding strength have been observed [157] with bonding between PDMS samples and Ga/As

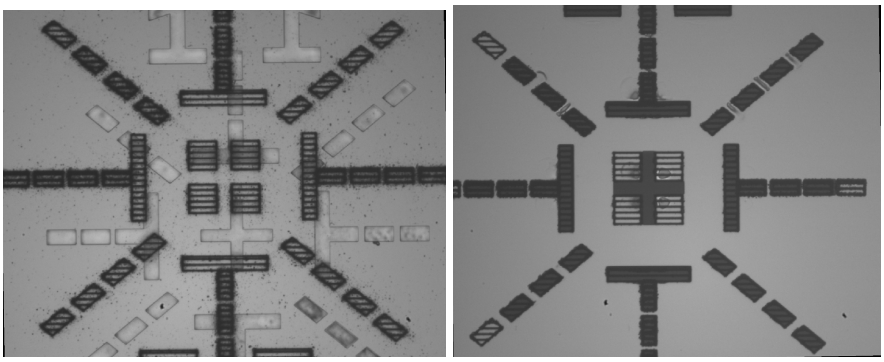

(a) (b)

Figure III.25: Alignment step (a) non-aligned wafer, (b) aligned wafer

samples with Silicon oxide SiO_2 layer deposited and acting as an intermediate layer to enhance the bonding to the PDMS sample.

Table III.10: Adhesion strength of PDMS bonding with non-patterned samples

Samples	1	2	3	4	5	6	7
Load force (kg)	9.480	13.301	20.226	19.631	20.542	8.750	13.079
Bonding strength (MPa)	0.930	1.304	1.984	1.925	2.015	0.858	1.283
Samples	8	9	10	11	Mean value	Standard variation	Uncertainties
Load force (kg)	60.297	0.349	0.389	4.846	12.876	6.109	0.050
Bonding strength (MPa)	0.591	0.034	0.038	0.475	1.263	0.599	0.005

PDMS bonding was successful to bond two unstructured Silicon wafers, providing a bonding strength sufficient to support the gas pressure considered for our study. However, PDMS bonding with structured silicon wafers with the whole process did not succeed in completely bonding the stack ($W_{Glass} + W_{Si1}$) with the wafer W_{Si2}. When cutting the stack to obtain the realized microchannels, silicon wafers were detached from each other. This detachment was more pronounced at the edge of the stack than at the center. It could be explained by the surface of the bonding being too small (the wall of microchannels is 500 μm thick) to correctly bond the wafers. Another explanation could be that PDMS quickly recovers its hydrophobic nature after surface treatment with Oxygen plasma and cannot ensure a proper bonding if the alignment step is done. Indeed, between the activation of the surface by Oxygen plasma and the bonding process, the wafer should be brought to another machine to perform the alignment step. An optimization of the time necessary to perform the alignment step as well as an optimisation of the surface activation process could perhaps lead to a better bonding.

Given the problems we expected to encounter during the manufacturing stages of instrumented microchannels with integrated temperature and pressure sensors, in parallel with the work presented above, we also decided to undertake a simpler process for manufacturing microchannels without integrated sensors. Although these microchannels will not allow localized measurements along the channel, they will provide valuable results by providing global pressure and temperature measurements upstream and downstream of the microfabricated devices. The following section describes the steps involved in manufacturing these microchannels.

III.1.2. Fabrication process for channels without integrated sensors

In this section, we are presenting the fabrication process of microchannels without integrated sensors. To realize microchannels without integrated sensors, glass unprocessed wafer W_{Glass} and silicon unprocessed wafer W_{Si2} are used. These wafers are bonded with the etched silicon wafer W_{Si1}. The successive steps of this simplified process are shown in figure III.26 and table III.11.

Table III.11: Successive steps of the microchannel fabrication process without sensors integrated into the microchannel

Step	Process	Description of the process
A	Substrates cleaning	Acetone + Ethanol Piranha mixing
B-1	Al/Ti/Au Deposition	Deposition of Al - Ti - Au by sputtering Thickness: 150 nm - 20 nm - 350 nm
B-2	Thermocompression Au-Au bonding	Bonding of wafer W_{Si1} with W_{Si2}
C-1	Photolithography	AZ10XT photoresist Thickness: 6 um - 14 um
C-2	Silicon etching	DRIE - Depth of etching equal to thickness of wafer W_{Si1}
C-3	Resist stripping	Acetone + Ethanol
D	Anodic bonding	Bonding of wafer W_{Glass} with the stack $W_{Si1} - W_{Si2}$

The main challenge for the process of microchannel fabrication with integrated sensors is the bonding between the two silicon wafers W_{Si1} - W_{Si2}. Without the issues that occur due to the presence of these sensors, other possibilities to bond the two silicon wafers can be considered. Among all available solutions, we have selected the bonding by thermocompression Au-Au. This bonding process is well mastered at Mimento's technology center, and ensures good bonding adhesion at high pressures without complex additional steps, making it the right choice for our fabrication process.

III.1.2.1 Thermocompression Au-Au bonding (*Step B*)

This step consists in the bonding of the substrates W_{Si1} et W_{Si2} [158]. First, an aluminum stop layer for the silicon etching is deposited on the back side of the W_{Si1} wafer, with a thickness of 150 nm. Then a 350 nm layer of gold is deposited on the back side of the W_{Si1} wafer and the front side of the W_{Si2} wafer. To improve the adhesion of this gold layer, a 20 nm thick Titanium adhesion layer was first deposited (*step B-1*). The bonding must be performed right after the deposition of the gold layers. The wafers are transported in clean transport boxes to limit as much as possible the deposition of impurities on the gold layers. The wafers are then placed on the top and bottom chuck of the assembly machine as shown in figure III.27

The bonding is achieved at a pressure below 10^{-5} Pa and a temperature of 320 °C with a ramp of 10 °C min^{-1} (*step B-2*). The contact force applied for this bonding is 40 kN. The contact force is gradually increased in 10 kN steps with a stabilization time of 1 minute between each step. The bonding time is set to 15 min. The stack is then cooled down to 250 °C with a ramp of -2 °C, followed by a ramp of - 5 °C until the temperature reaches 200°*C*. The wafers are finally freely cooled down

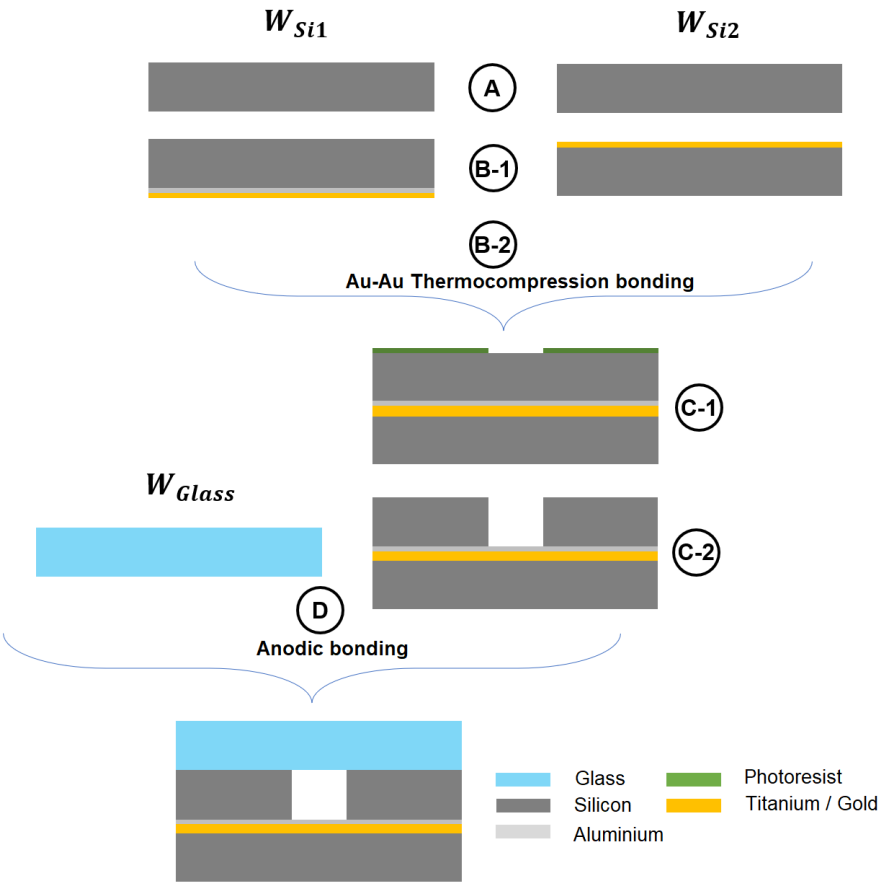

Figure III.26: Flowchart of the microchannel fabrication process without integrated sensors

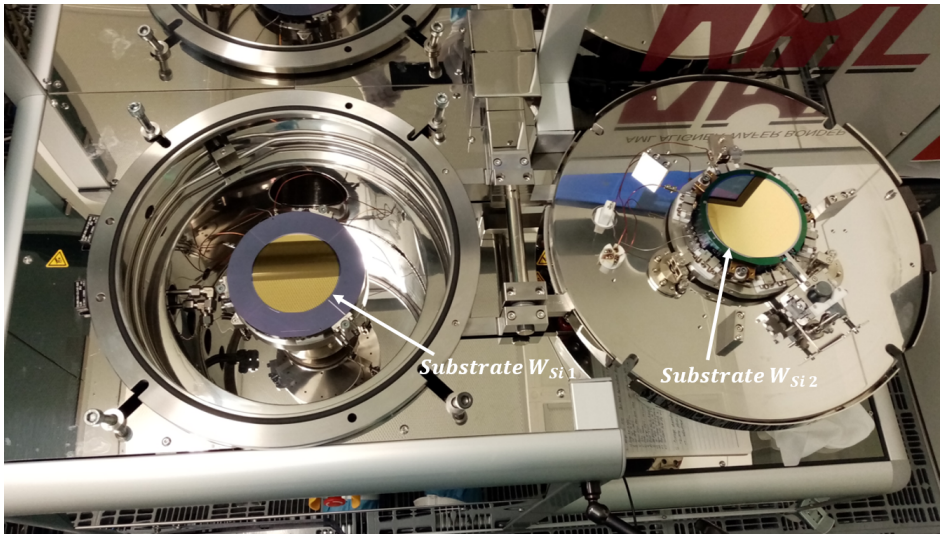

Figure III.27: Au-Au thermocompression bonding setup

to room temperature by injecting nitrogen into the chamber. No accurate alignment is required this time for the bonding steps since the glass and silicon wafers (W_{Glass} and W_{Si2}) which are bonded to the silicon wafer W_{Si1} are only used to enclose the microchannels. The silicon etching process

(step C), as well as the anodic bonding (step D), remain as previously presented for the fabrication of microchannels with integrated sensors. Once the thermocompression bonding, the etching, and the anodic bonding are achieved, the stack is diced using saw-cutting technology. The saw used to cut the wafers into several microchannels is 300 μm thick. Figure III.28 shows the microchannels after the cutting step.

(a) (b)

Figure III.28: Microchannels after the cutting step (a) straight channel, (b) channel with bends

III.2 Characterization of the micro-channels and of the sensors

In this section, we present the characterization of the fabricated microchannels. In the first part, we will look at effective dimensions and roughness. Secondly, we will focus on the characterization of temperature sensors, quantifying the influence of annealing, and determining the TCR and dynamic cutoff frequency of our sensors.

III.2.1. Characterization of the realized microchannels

III.2.1.1 Dimensions of microchannels

The dimensions (width w_{ch} and length L_{ch}) of the realized microchannels were determined with an optical microscope Leica DM8000 from Leica Microsystems company. This microscope has an accuracy of $\pm$ 5 μm. The measured dimensions of all realized channels are given in the table III.12.

Table III.12: Dimensions of the test channels

Channel	Width (μm)	Height (μm)	Length (mm)
1	101.2	104.4	24.999
2	133.3	392.8	25.001
3	670.1	392.8	25.001
4	1000.8	1005.4	24.999
5	999.7	1005.4	50.000
6	1003.4	1008.1	24.998
7	1001.7	1008.1	24.996
Accuracy	$\pm 5\mu m$	$\pm 2\mu m$	$\pm 5\mu m$

Channels from 1 to 5 are straight, whereas Channels 6 and 7 are channels with four 90° bends. The length of the channel given in Table III.12 corresponds to the measured distance between the inlet and outlet of the channels. We recall that (as presented in Chapter II and in Figure II.2) the total length covered by the fluid in the channels with bends (i.e. Channels 6 and 7) is the same as the length for the small straight channels. Therefore, the measurements of the length for these channels are carried

out on the center streamline of these channels for all five straight parts of the channels (*q.v.* Figure II.2). Therefore, the uncertainty for these channels length with bends is equal to $\pm$ 25 μm.

III.2.1.2 Roughness of microchannels

Another important parameter to determine, according to the review of the literature (chapter I), is the roughness of the channels. The roughnesses were determined for the top/bottom faces of the channel as well as for the lateral edges.

- Roughness of top and bottom walls

  The roughness of both the top and bottom walls was determined using a stylus profilometer with an accuracy of a few nanometers. The mean roughness measured ranged from 5 to 20 nm. The roughness was measured after the etching process but before any bonding process.

- Roughness of sidewalls

  The roughness of the side walls is mainly due to scalloping resulting from the etching process because of the deposition of the passivation layer. This scalloping was measured with a scanning electron microscope (SEM). Figure III.29 shows SEM picture of the channel sidewall before zooming on the structures. The pictures of the scalloping effect are shown at different wafer locations in figure III.30. We can observe the same pattern on each wafer location. However, the heights of the structures are considerably different. This can be explained by the difference in etching rate at the edges and the center of the wafer but also by the difference in surface exposed by the plasma. The measured roughness (due to the scalloping effect) ranges from approximately 200 to 400 nm. This represents relative roughness below the value of 0.5 %. Even though, for such low values of relative roughness, the literature review of investigations showed that the influence of roughness could be neglected, for the present study the roughness will still be taken into account in the hydraulic diameter of all realized channels by

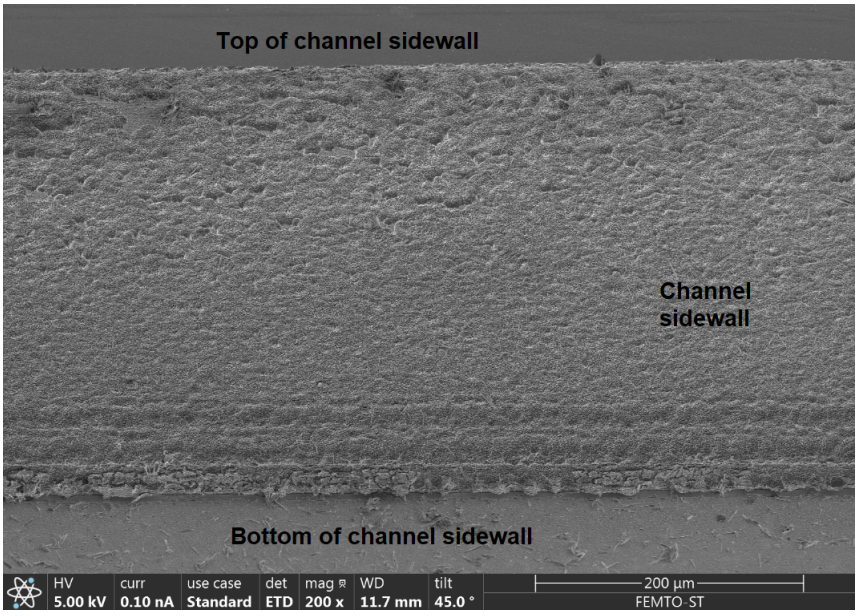

Figure III.29: SEM picture of channel sidewall

using the constricted flow hydraulic diameter D_{cf} defined in chapter I, which take into account the reduction of the cross-section due to the roughness of the channel walls.

III.2.2. Annealing process to enhance the stability of Platinum sensors

The desired features for the platinum sensors are almost non-intrusiveness, stability, and accuracy. Annealing must be taken into account for its influence on the sensors. Indeed, it was shown by Tiggelaar *et al.* [135] that annealing parameters (annealing time, temperature as well as the ambient in which the annealing is performed) influenced the structural properties (crystallographic orientation, crystallite size, alloy formation, and surface roughness), mechanical properties (residual stress, adhesion of the platinum layer) and electrical properties (TCR and resistivity of the metallic layer). For instance, Wang *et al.* [159] designed a temperature sensor composed of a stack of Ti/Pt/Cr/Au thin layers. They tested annealing temperatures ranging from 200°C to 800°C. They observed a reduction of the stack resistance for annealing temperatures below 350°C. For the annealing temperature above $350°C$, an increase in the resistivity of the stack was observed. The annealing was performed under a nitrogen atmosphere resulting in the reaction and formation of compounds such as titanium nitride (TiN) changing the electrical properties of the sensor.

Since Platinum cannot adhere well to silicon dioxide or another insulating layer (as previously mentioned), an intermediate adhesion layer must be applied (using less noble metal) to improve the Platinum adhesion on the wafer surface. However, due to this intermediate layer, several studies [160] reported thermal degradation of the probes for temperature above 500°C. Other studies [161], [162] reported diffusion of the adhesive layer into the Pt layer for annealing temperature above 450 °C. Delamination of the layer was also observed for intermediate to high-temperature [163] [164]. These issues are due to the change of the structural and mechanical properties of the layers depending on the sensor operating temperature.

Therefore, for our study, an optimal annealing process has to be determined to realize temperature sensors with good agreements with the desired features.

To do so, we tested different annealing temperatures and times, based on previous results [165] obtained in the MIMENTO facility of our institute. The different tested operating conditions are given in table III.13. Note that all the annealing processes were conducted in a neutral nitrogen atmosphere to limit the interaction with the metal layer. In this table :

- Samples marked "NS" are samples for which the deposited platinum was not patterned: the platinum was deposited on the full surface of the first test wafer. These are samples NS10 to NS23. They were cut into 20 mm x 20 mm test elements.
- Samples marked "T" correspond to those deposited on the second test wafer. In this case, the platinum deposit was structured according to the design shown in figure II.13 (chapter II). The samples were cut into 10mm x 10mm sections. These are numbered T1-1 to T6-3.
- In the table, when temperature and annealing time are not indicated (denoted "–" in the table), this means that these samples were not annealed.

III.2.2.1 Dimensions of the Pt sensors

Thicknesses of the deposited layers are measured after the Cr deposition and after the Pt deposition with the Stylus Profilometer Dektak XT. Fig. III.31 presents an example of measurements carried out by the profilometer. The thickness of the layer is measured along the entire length of a single sen-

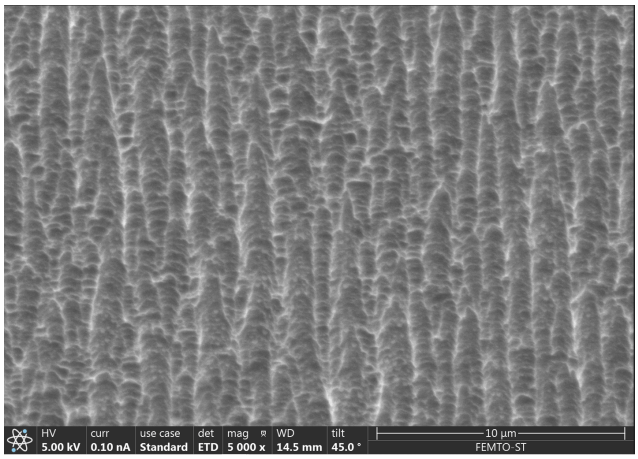

(a)

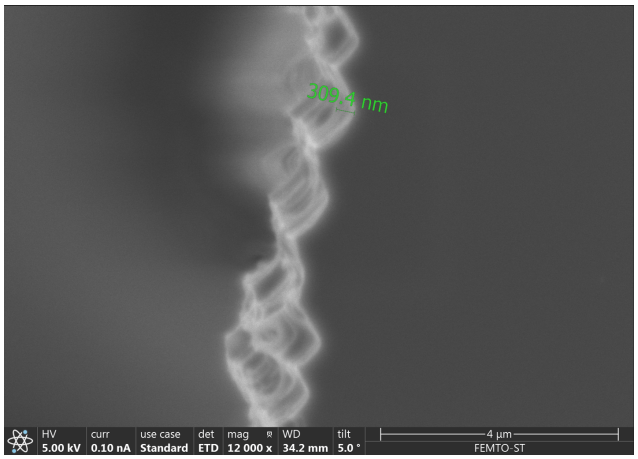

(b)

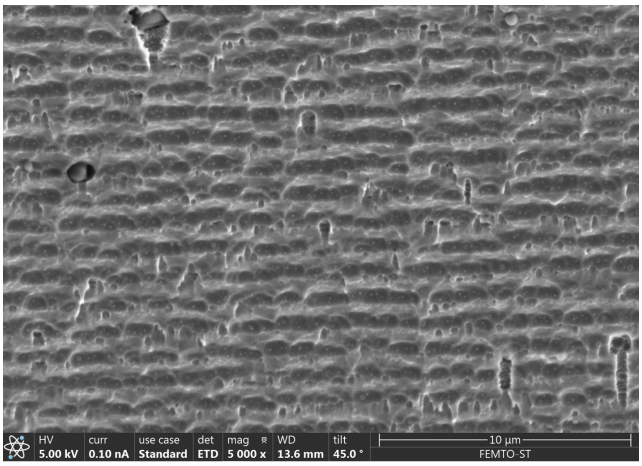

(c)

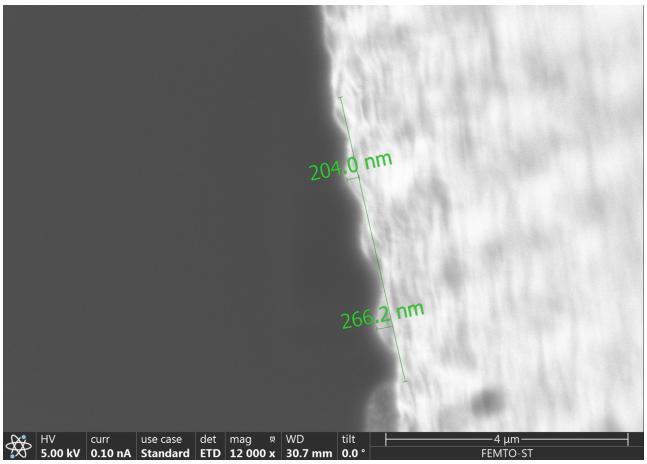

(d)

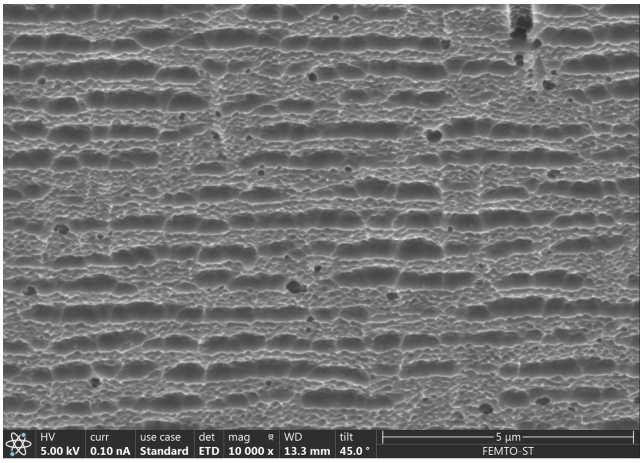

(e)

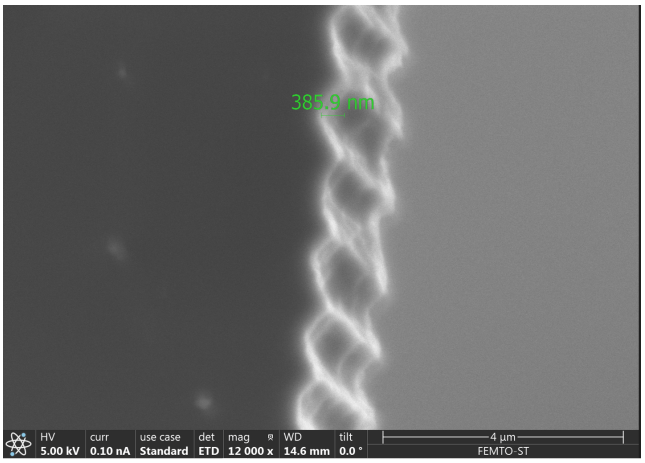

(f)

Figure III.30: SEM picture of the side wall (a) side view at the center of the wafer, (b) top view at the center of the wafer, (c) side view at the right part of the wafer, (d) top view at the right part of the wafer, (e) side view at the top part of the wafer, (f) top view at the top part of the wafer

Table III.13: Temperature and time parameters of the annealing process for the characterization of Pt probes

	Annealing conditions Pt sensor (structured wafer)				**Annealing conditions Pt layer without structuring**						
Sample name	T1-1 T3-3 T4-1 T6-3	T1-2 T2-3 T5-3 T6-1	T1-3 T2-1 T3-2 T4-3 T5-1	T2-2 T3-1 T4-2 T5-2 T6-2	C10 C11	C20 C21	C16 C17	C12 C13	C18 C19	C14 C15	C22 C23
Annealing temperature (°C)	–	250	250	450	–	150	250	250	300	450	600
Annealing time (*h*)	–	6	12	6	–	6	1	6	6	6	6

sor. From Fig. III.31, we can observe repeatable patterns of the same thickness for a single sensor. Thicknesses of Pt sensors ranged from 175 nm to 205 nm ± 20 nm due to the non-uniformity of the deposition on the whole wafer's surface which is equal to 11 %.

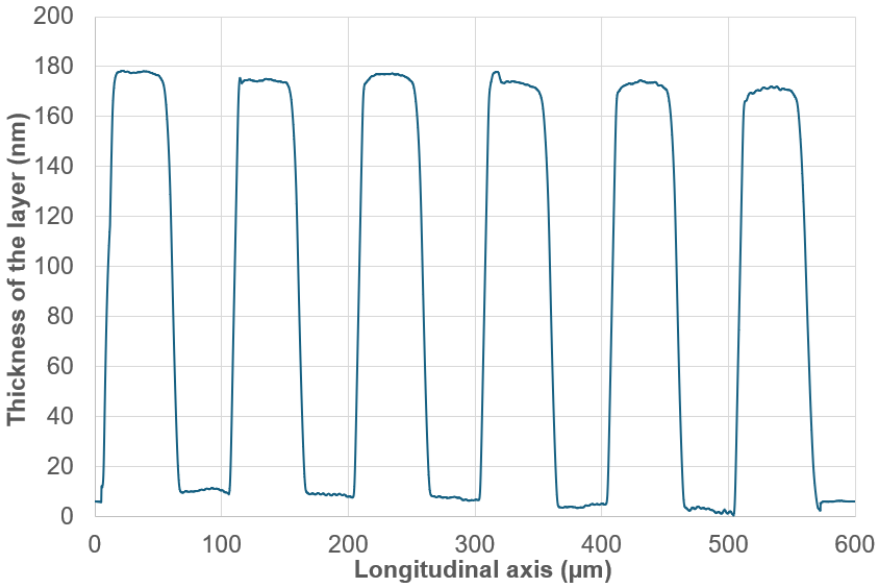

Figure III.31: Exemple of measurement carried out by profilometer

III.2.2.2 Resistance of the Pt sensors

Pt probe resistances were measured using *EPS150COAX* measurement system from the Microtron company. This system includes a chuck holding the wafer, coaxial wire tips connected to a *Keithley 6221* DC AND AC source, and further coaxial wire tips connecting the Platinum probes to a *Keithley 2182A* nanovoltmeter. Figure III.32 shows how the measurements were carried out systematically with all the probes. The probes are supplied with a current of 0.1 mA to limit self-heating, which

can have a significant influence on measurement at higher excitation currents as it was observed by Aymen *et al.* [165].

Systematic measurement of the resistances revealed a difference up to 30 % of the calculated theoretical resistance: this may be due to non-uniformity in the thickness of the platinum deposit, as well as to a small change in the probe design to limit the mechanical stress due to right angles in the calculation of probe dimensions whereas in the fabrication of the temperature sensor, the angles of the meanders are in a rounded shape.

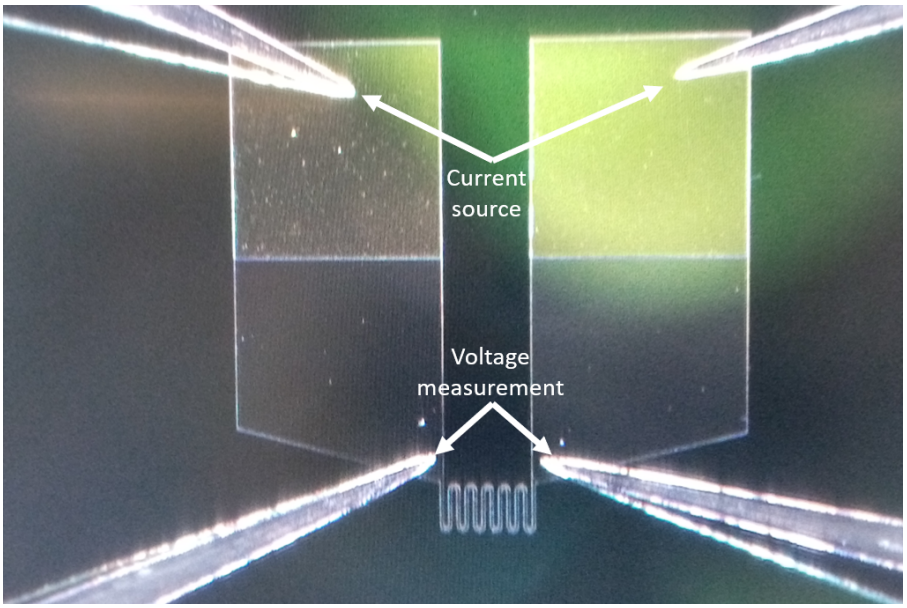

Figure III.32: Setup for the resistance measurement

Average resistance values before and after annealing were determined, and their evolution as a function of the annealing process and temperature is shown in Figure III.33. ΔR corresponds to the mean difference between the average value of the resistance after annealing, and the value of the resistance before annealing.

We can observe a decrease by around 40 Ω for the samples with annealing at 250 °C for both 6 h and 12 h. A slight difference can be seen as a function of the time of the annealing. However, for the samples with annealing at 450 °C, the resistance increases by more than 100 Ω. This is consistent with the observation carried out by Schmid *et al.* [166] with the resistivity of the thin film which decreased for annealing temperature up to 300 °C whereas the resistivity increased for an annealing temperature of 450 °C and higher. Regarding electrical properties, annealing at a temperature of 450 °C and higher is better as it will increase the sensor sensitivity.

III.2.2.3 Residual stress of the Pt layer

Another important parameter that will help select the annealing process is the residual stress of the Pt layer. This stress was measured by X-ray diffraction method (XRD). The XRD method involves incident X-rays irradiating a material and optical probes measuring both the intensity and scattering angle of the X-rays scattered out of the material. The XRD method is also a method that can be used to determine the molecular or atomic structure of a crystal.

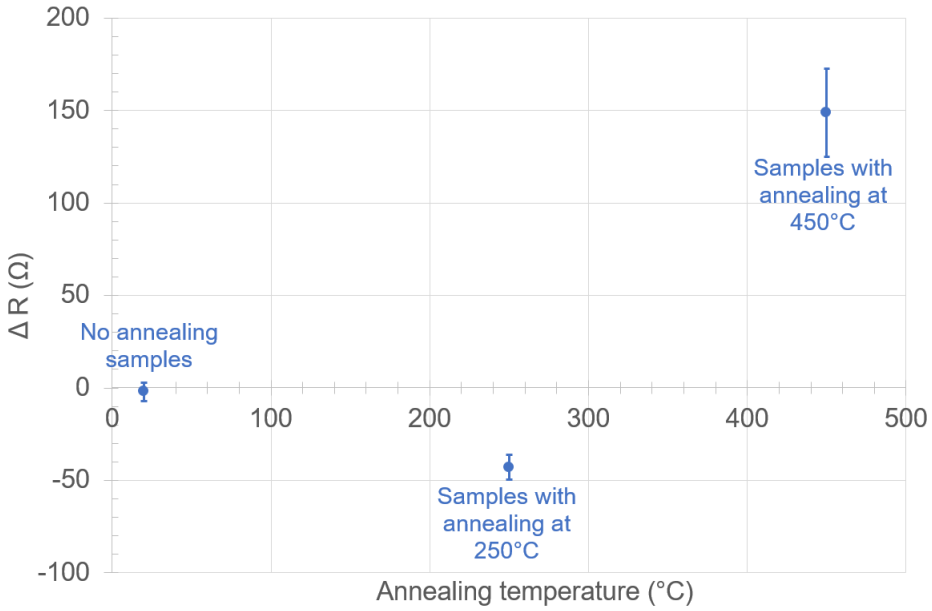

Figure III.33: Variation of the resistance of Pt sensors before and after annealing depending on the different annealing processes

The measurements were carried out by Virginie Moutarlier at the UTINAM Institute, with D8 Discover from BRUKER. X-rays are generated via a copper anode bombarded by electrons. The wavelength of the X-rays generated is thus equal to 1,54 Å. The measurements were done in a micro-XRD configuration using a 1mm collimator, which allows focusing on small areas of the sample and thus obtaining more accurate measurements. The intensity was measured for scattering angles ranging from 30° to 90° with an interval of 0.02° and a speed of 0.5s per increment of the scattering angle.

Measurement repeatability was checked: measurements were repeated on the same area of the same sample, with the sample being repositioned between measurements. An example of a repeated measure is shown in figure III.34. This figure shows that the curves (overall and at the zoomed-in peaks) overlap very well. On each occasion, the values were very close, validating the repeatability of the measurements.

Measurements were conducted on several samples: with no annealing and with annealing at temperatures of 250 °C and 450 °C. Figure III.35 shows the measurements carried out on the samples, the curves in blue correspond to samples without annealing, the ones in green correspond to samples with annealing at 250 °C while the ones in red correspond to samples with annealing at 450 °C.

In figure III.35, we observe two peaks measured by the XRD method, one located between 39 and 40° corresponding to the scattering of the rays due to the platinum lattice with the crystal orientation (111). The second peak located near 69 ° corresponds to the scattering of the rays due to the silicon lattice. In this figure, we can see a difference in intensity between the peaks: this is because in the area measured, the silicon surface is significantly higher than the deposited platinum surface. For all samples and annealing temperature, the silicon peak remains at 69.2 °. On the other hand, there is a shift in the position of the platinum peak as a function of annealing temperature (but no influence of annealing time was observed). Without annealing, it is located at 36.62 $\pm$ 0.01 °, for annealing

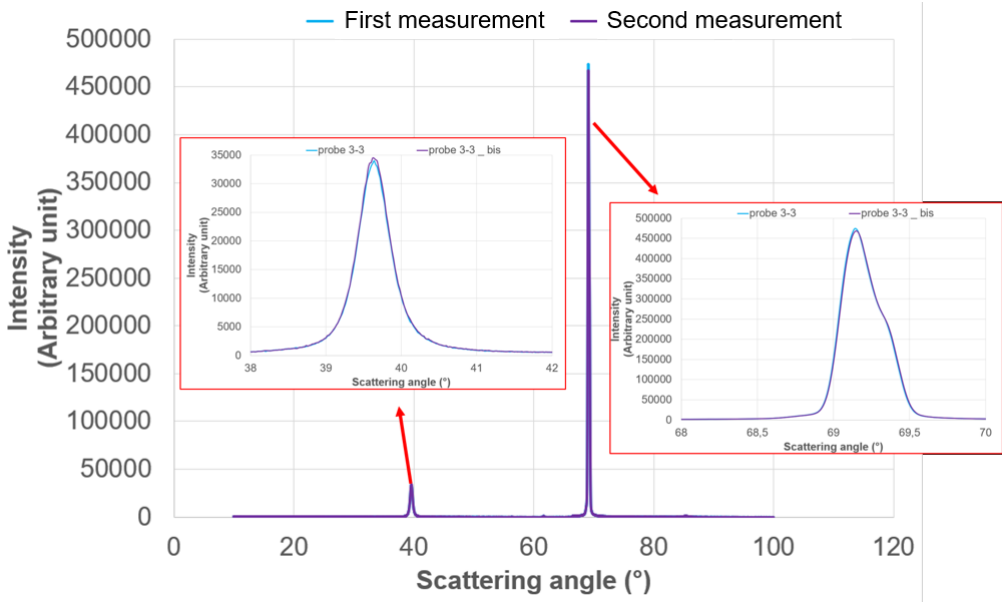

Figure III.34: Repeatability of XRD measurements

at 250°C, for all tested annealing times, it is located at 39.72 ± 0.01 ° and at 450 °C, it is located at 39.81± 0.01 °.

The displacement of the peak can be explained by a change in stresses. According to Bragg's law:

$$n\lambda = 2d\,sin(\Theta) \tag{III.3}$$

With n the scattering order, λ the wavelength of the ray, d the distance between two crystallographic planes, and Θ the scattering angle.

Therefore, a shift to the left in the graphic corresponds to increasingly extensive stress (decrease of Θ results in an increase of the distance d), while a shift to the right corresponds to increasingly compressive stress in the lattice (decrease of the distance d). Therefore, we can observe from figure III.35 that as the annealing temperature increases, the stress of the Pt layer gets more and more compressive.

In addition, the strain stress can be determined by the relation [167]:

$$\varepsilon_{\psi\phi} = \frac{1+\nu_p}{E}\sigma_\phi sin^2(\psi) - \frac{\nu_p}{E}(\sigma_1+\sigma_2) \tag{III.4}$$

where $\varepsilon_{\psi\phi}$ represents the strain stress, E represents Young's modulus, ν_p the Poisson's ratio, ϕ, and ψ corresponds to the angle represented in figure III.36.

Table III.14 gives the calculated values of the residual stress for samples with different annealing temperatures. The negative value of this stress means that the stress is compressive while a positive value corresponds to extensive stress. We can observe a low dispersion of the value except for annealing at a temperature of 450 °C.The residual stresses of the deposited platinum layer increase slightly with the annealing temperature up to an annealing temperature of 300 °C. Then, residual stresses sharply increase for samples annealed at 450 °C. This was found to be mainly due to the change in

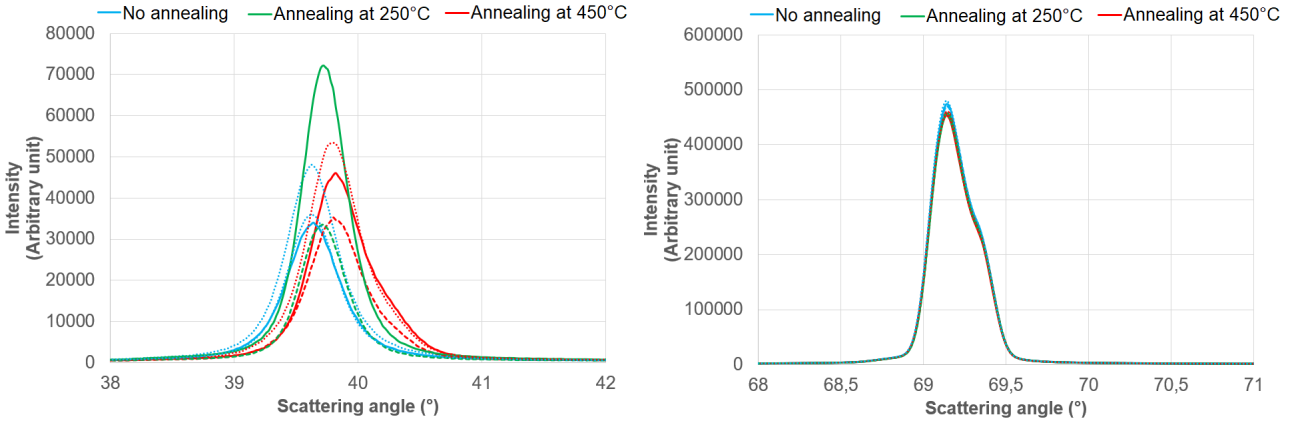

Figure III.35: XRD measurements: (a) zoom on Platinum peak between 36 and 42° (b) zoom on Silicon peak between 68 and 71 °. Blue curves : samples without annealing; Green curves : samples with an annealing at 250 °C ; Red curves: samples with an annealing at 450 °C

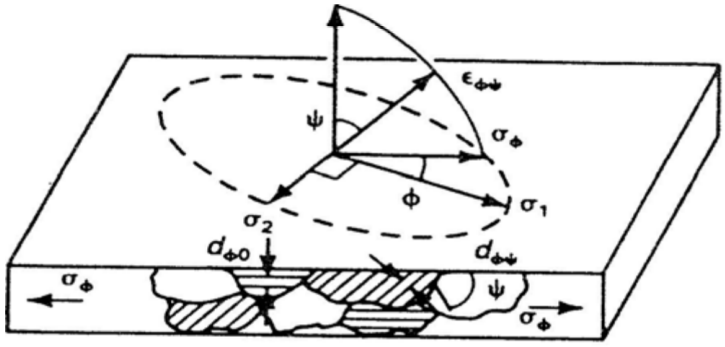

Figure III.36: Plane stress elastic model [167]

the deposited multilayer composition, as we will later see with the measurements carried out by the Glow Discharge Optical Emission Spectroscopy (GDOES) method.

Table III.14: Residual stresses measured for samples with different annealing temperatures

Pt sensor (structured wafer)				
Annealing conditions	No annealing	250°C 6 h	250°C 12 h	450°C 6 h
Mean residual stress (*MPa*)	-2020 ± *190*	-2880 ± *165*	-3075 ± *125*	-8810 ± *550*

Pt layer without structuring						
Annealing conditions	No annealing	150°C 6 h	250°C 6 h	300°C 6 h	450°C 6 h	600°C 6 h
Mean residual stress (*MPa*)	-2373 ± *245*	-2515 ± *230*	-2453 ± *310*	-3133 ±*275*	-5975 ± *370*	578 ± *130*

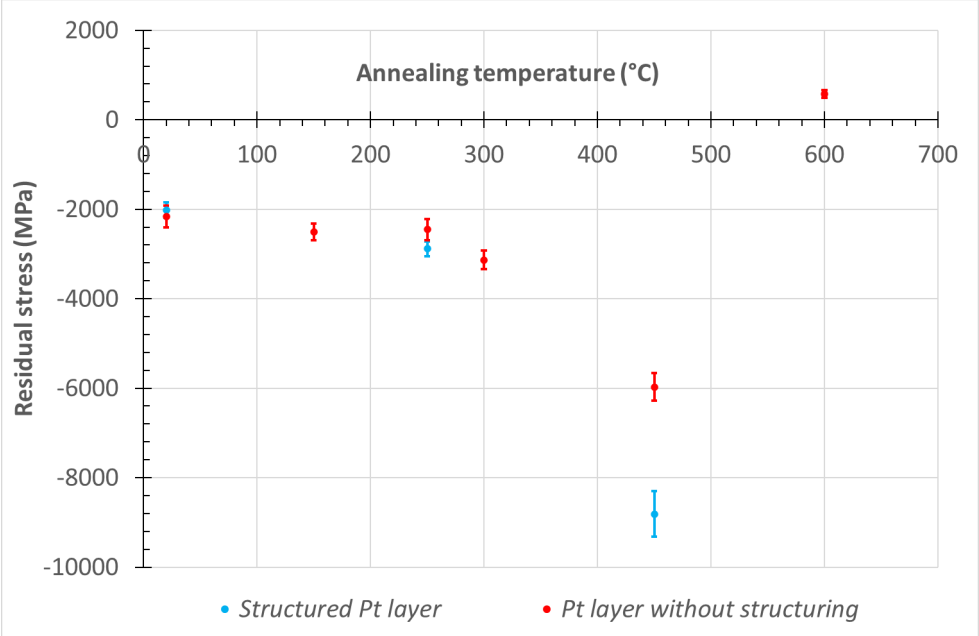

Figure III.37: Residual stresses of the Pt thin film as a function of the annealing temperature (for 6 h of annealing process)

III.2.2.4 Size of the crystallites of Pt layer

The crystal size can be estimated by the empirical Scherrer equation [168]:

$$t_c = \frac{k\lambda}{H cos\theta} \tag{III.5}$$

with t_c the mean size of the crystallite (nm), k is a form factor, λ is the wavelength of the X-ray (nm), H is the full width at half maximum (rad), θ is half of the scattering angle (rad).

The size of the crystallite for the different samples is given in table III.15.

Table III.15: Crystal size of the Pt structure as a function of annealing temperature

Pt sensor (structured wafer)			
Annealing conditions	No annealing	250°C	450°C
Mean crystallite size (*nm*)	17.8 ± *0.4*	20.3 ± *0.1*	16.9 ± *0.3*

From this table III.15, we can see that the size of the crystallites rises with annealing at 250 °C but for samples with annealing at 450 °C it decreases lower than for the samples without annealing. This is consistent with the investigations of Sreemany *et al.* [169] on the influence of annealing temperature on the electrical and structural properties of Pt thin film. The authors observed that the crystal size increased as the annealing temperature increased. The decrease in crystal size we observed for an annealing temperature of 450 °C could be explained by the use in our case of the Chromium layer as an intermediate layer to improve adhesion. Additional measurements have been carried out to observe the composition of the layer structure for the different annealing temperatures tested.

III.2.2.5 Characterization of the composition of the layers in-depth

To investigate the influence of the annealing temperature on the composition of the layers in-depth, glow discharge optical emission spectroscopy (GDOES) measurements were carried out by V. Moutarlier at the UTINAM Institute. GDOES measurement provides information on elemental concentrations as a function of the depth of analysis in the sample.

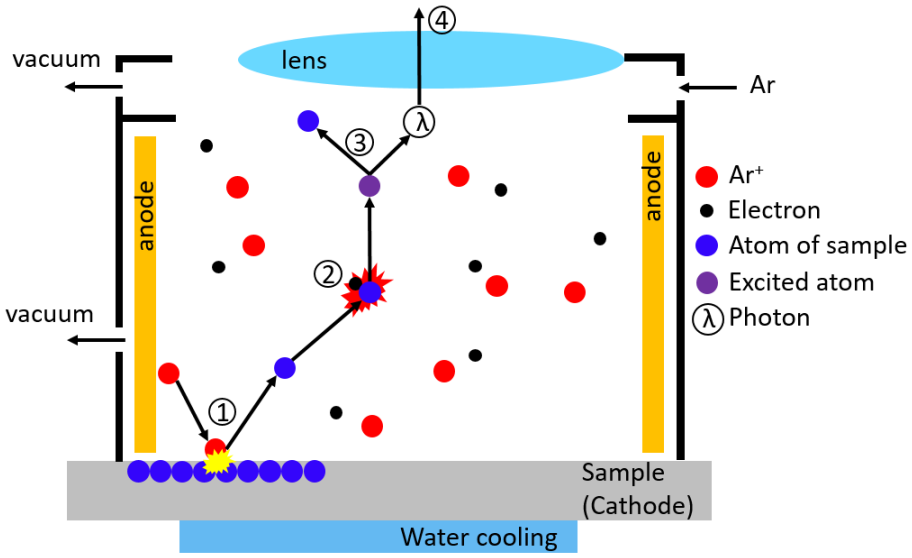

Figure III.38: Scheme of the different steps of the GDOES method

Figure III.38 illustrates the different steps of the GDOES method. For these measurements, Argon gas was injected into the chamber. The polarization of the chamber created Ar plasma which will strike the surface of the sample ①, and the atoms of the sample are torn off layer by layer. These atoms are then excited by collision with the ions or electrons of the plasma created ②. During their de-excitation, these atoms will emit photons whose wavelength is characteristic of the element ③. The radiation emitted during the de-excitation of the atoms is detected by photomultipliers ④. The signals are then processed to obtain the distribution of the elements according to the duration of the plasma erosion.

The device used to perform these measurements was a GD Profiler from HORIBA JOBIN YVON. The erosive power for the measurements was 20 W. The wavelengths of the spectral lines were 130 nm for oxygen, 283 nm for Platinum, 288 nm for Silicon, and 425 nm for Chromium. Given the constraints of the measuring instrument, only non-structured samples were analyzed in this section.

The profiles presented in figure III.39 represent the light intensity as a function of the erosion time. Multiplicative factors were chosen arbitrarily to represent on the same graph the evolution of each element.

Figure III.39 (a), (b) show that there is no significant difference observed between samples without annealing and samples with annealing at 300 °C. However, for the samples with annealing at 450 °C, a diffusion of Cr into the Pt layer near the surface of the sample can be noticed. A slight peak on the oxygen curve can also be observed near the surface which could suggest the presence of chromium oxide.

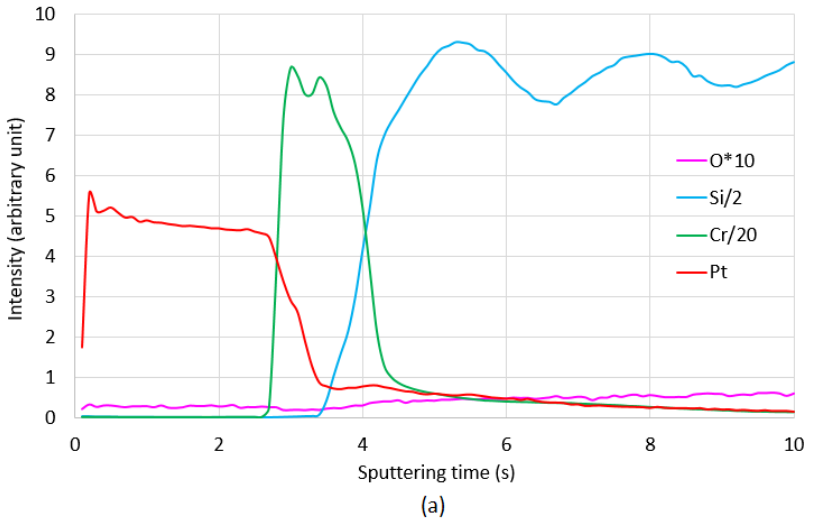

(a)

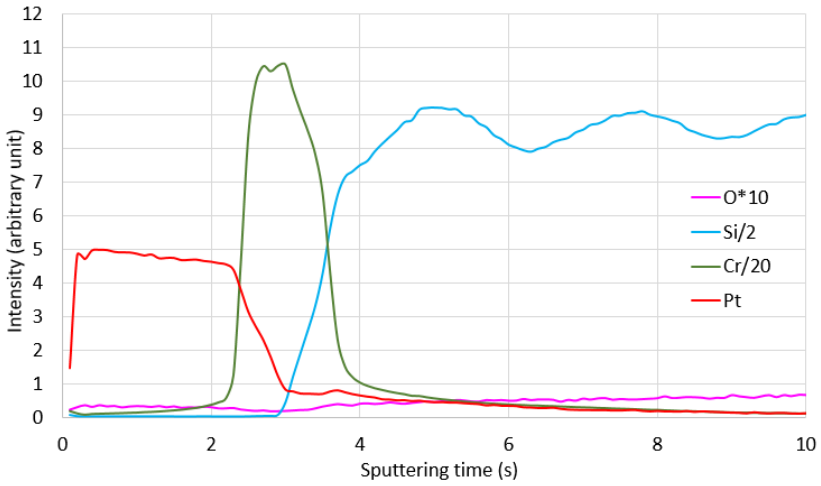

(b)

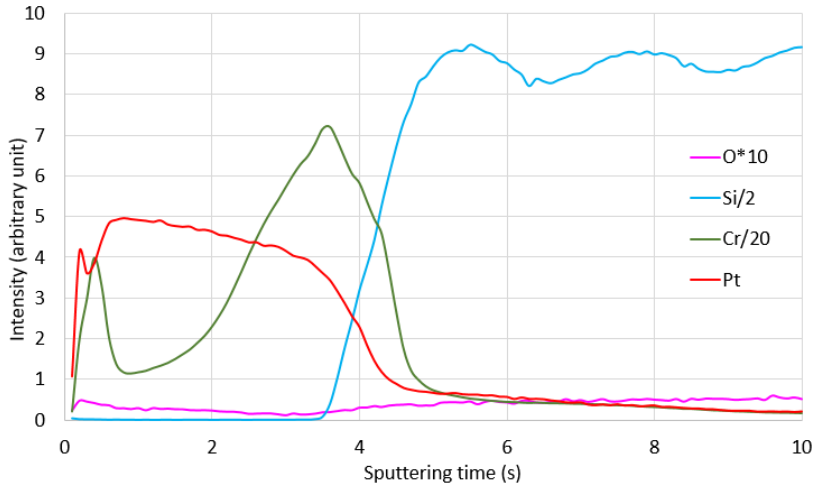

(c)

Figure III.39: Composition of the layers in-depth for samples (a) without annealing, (b) annealing at 300 °C, (c) annealing at 450 °C

This could explain the large variation observed regarding both mechanical (residual stress) and electrical (electrical resistivity) properties of Pt probes between samples annealed at 450 °C and the other samples.

III.2.2.6 Temperature coefficient of resistance and dynamical response of the temperature sensors

Regarding the performance of the probes, both sensitivity and time response of the sensors are required to measure temperature in microchannels. Therefore, the probes were characterized statically and dynamically.

1. **Temperature coefficient of resistance as a function of annealing temperature** The resistance of the samples is measured as a function of the temperature to determine the temperature coefficient resistance for all samples. Measurements were carried out using an oven (see figure III.40) for temperatures ranging from room temperature to 100 °C. The real temperature in the oven near the Pt probes was measured by a calibrated reference sensor (K-type thermocouple).

Figure III.40: Setup for the static characterization of the probes

Electrical resistances measured by the probes are plotted against the temperature measured by the reference thermocouple in Fig. III.40. Keeping in mind that the resistance of these sensors is a function of temperature according to the following relationship:

$$R_{elec}(T) = R_0\,(1 + \kappa T) \tag{III.6}$$

with R_{elec} the electrical resistance of the sensor, R_0 its electrical resistance at temperature T_0 = 0 °C, κ the temperature coefficient of resistance and T the temperature measured by the sensor.

Therefore, a linear regression y = ax + b is used to determine the resistance R_0 given by the y-intercept "b". The temperature coefficient of the probes κ was determined by the ratio between the slope of the curve "a" and R_0:

$$\begin{cases} R_0 = b \\ \kappa = \frac{a}{R_0} \end{cases} \tag{III.7}$$

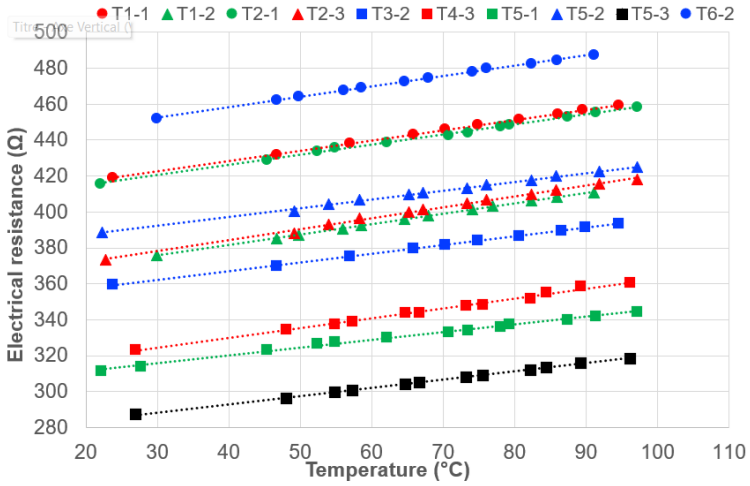

Figure III.41: Resistance measured by Pt probes as a function of the temperature

Average TCR values, together with their standard deviation, were determined from the different samples (without annealing, with annealing at 250°C for 6 hours, and at 450 °C for 6 h). These values are summarized in Table III.16. We can observe that the TCR of Pt probes increases by around 20 % with annealing at 250 °C with an increasing value from 0.00141 to 0.0017. However, for annealing of the Pt layer at 450 °C this value decreases by around 7 % below the value for samples without annealing, resulting in less sensitive sensors.

This consolidates the fact that annealing at 450 °C is not ideal in our case, unlike results from the literature for which TCR increased with increasing annealing temperature. This is due to the presence of the Chromium layer, which diffuses into the Platinum layer at annealing temperatures of 450 °C, considerably altering the sensor's electrical properties.

Table III.16: Temperature coefficient resistance as a function of annealing temperature

	No annealing	With annealing at 250°C / 6 hours	With annealing at 450°C / 6 hours
Mean value of TCR ($°C^{-1}$) (± standard deviation)	$1.408\ 10^{-3}$ ($\pm 0.011\ 10^{-3}$)	$1.665\ 10^{-3}$ ($\pm 0.032\ 10^{-3}$)	$1.307\ 10^{-3}$ ($\pm 0.017\ 10^{-3}$)

2. **Dynamical response of probes under convective condition**

The dynamical response of probes was conducted under pulsed forced convective hot air flow. A hot-air blower coupled with a chopper supplied by a motor generated the pulsed hot-air flow with a frequency ranging from 0.01 Hz to 2 Hz. The setup is shown in figure III.42. A converging section was added to limit the dispersion of the heat flux and focus it on the nearby sample. Temperatures were measured thanks to calibrated thermocouples. Both sample and thermocouples were held by a mechanical clamp with insulating foam. The temperature at

the end of the converging section was around 50 °C while the temperature measured near the sample was around 45 °C.

The results obtained for some frequencies are shown in figure III.43. We can observe that above a frequency of around 1 Hz, the uncertainties on the resistance measured by the Pt sensors are too high compared to the variation of the resistance of the sensors due to the heat transfer. This suggests that the sensors will not be able to follow the dynamic of the alternating flow which can be due to the high thermal inertia of the sensors.

One solution that was considered, but not implemented due to lack of time, would be to test with a sinusoidal signal (for the resistor measurement). After signal processing, this could eliminate noise and still provide a temperature value.

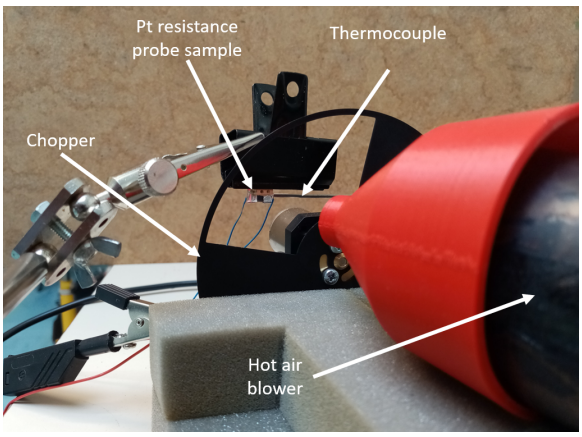

Figure III.42: Setup for the dynamic characterization of Pt probes.

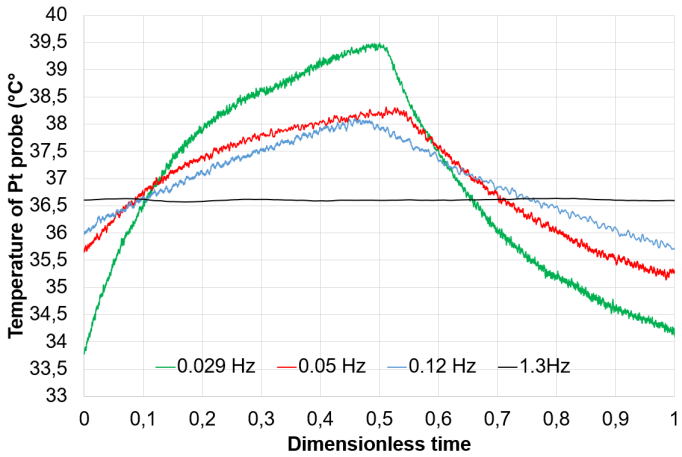

Figure III.43: Dynamic response of Pt probe under forced convection of hot air for different frequencies.

The results of the characterization of the crystallographic, mechanical, and electrical properties of platinum sensors as a function of annealing temperature have shown that samples with annealing at temperatures up to 250 °C enhance the properties of the probes with an increase of the temperature coefficient resistance up to 20 % higher. Up to temperatures of 300°C, the

residual stress in the thin layer of Pt increases up to around 1.5 times higher. The annealing at a temperature of 450 °*C* and higher, in contrast, exhibits a decrease of the temperature coefficient resistance 7 % lower than samples without annealing. In addition, the residual stress increases significantly (almost up to 5 times higher) compared to samples with annealing at lower temperatures. Therefore, an annealing process at a temperature of 250 °C seems reasonable for the requirements of the Pt probes for this study and was thus chosen.

Chapter conclusion

In this chapter, microfabrication process of microchannels with integrated pressure and temperature sensors was presented. The temperature sensors were Pt temperature probes fabricated by depositing a thin film of Platinum on the wafer at the bottom of the stack. Pressure sensors were made with a deposited PDMS layer on the whole surface of the wafer with optical access at both extremities of the microchannel. The microchannels were fabricated by etching the silicon wafer located in the middle of the stack. The bonding of the glass wafer W_{Glass} with the etched silicon wafer W_{Si1} was performed using anodic bonding, while the bonding of the stack composed of W_{Glass} and W_{Si1} with the other silicon wafer W_{Si2} holding the temperature and pressure sensors was performed using first dry photoresist thin film adhesive bonding. This bonding was, however, not fully satisfactory since the patterning created holes on the edges of the microchannels, resulting in gas leakage in the flow. Another bonding was performed using PDMS as an adhesive layer for the bonding. This assembly was not able to achieve proper bonding as well. The wafers assembled in this way were separated during the cutting process despite the good adhesion force observed on unstructured wafers.

To provide at least global measurements of flow inside the microchannels we designed, a simplified fabrication process without integrated sensors was developed. The successive steps of this process was presented in the second part of this chapter. This time, the bonding between silicon wafers W_{Si1} and W_{Si2} was performed using Au-Au thermocompression bonding. Then, the silicon wafer W_{Si1} was etched to make the microchannel. The final step of this process was to cover the top of the channel by bonding the stack composed of the two silicon wafers with a glass wafer using anodic bonding.

Although assembly of the wafers with temperature and pressure sensors integrated into the microchannel was unsuccessful due to the PDMS layer disbanding during cutting, characterization of the temperature sensors was carried out. The characterization included measurements of structural (profilometers, crystal size), electrical (resistance, TCR), and mechanical properties (residual stress). This characterization allowed us to determine the ideal annealing process to provide the best compromise between all requirements expected for the sensors. Annealing temperature up to 300 °C, increased the electrical properties while only increasing slightly the residual stress, whereas, for annealing at 450 °C, the electrical properties decreased as long as a high increase of stress.

With the channels made, the next step is to mount them on the experimental setup and characterize both steady and alternating flow with the same devices.

CHAPTER IV

EXPERIMENTAL SETUP, RESULTS AND ANALYSIS

This chapter is divided into three parts. First, we will introduce the setup used to characterize both steady and alternating flow. The metrological resources used for pressure and temperature measurements at both extremities of the device including the converging and diverging cross-sections (as it was discussed in the chapter II) will also be presented.

Then, the second part will focus on the experimental results obtained for steady flow. The influence of the flow rate on pressure and temperature will be discussed. The experimental data will be compared to the theoretical ones, based on the incompressible flow assumption at the macroscale in a rectangular channel. This assumption of incompressible flow seemed reasonable since the relative variation of fluid density between the lowest and highest Reynolds number was below 2%. The pressure drop due to the converging and diverging cross-section was also taken into account in the calculation of the theoretical values since the contribution of these parts cannot be neglected in the total pressure drop measured, as will be shown in this chapter. Friction factors have been calculated and compared with correlation from the literature.

Finally, the third part will concern results obtained for alternating flows. Variations of both pressure and temperature over a period, with corresponding pressure drop ΔP and temperature difference ΔT between both ends, will be presented for all the channel configurations and different frequencies. The results will be compared with those in the literature. The intention is to study the influence of various parameters (such as hydraulic diameter, the presence of bends, channel length, etc.) on pressure drop, in the field of reciprocating flows at the milli- and micro-scales. Based on the results obtained, we should be able to identify the critical features on which we need to focus in the manufacturing steps of the miniature device. Therefore, this work should provide the basis for optimizing the design of micro-motors for energy harvesting, such as, for instance, the micro-Stirling engine.

IV.1 Experimental setup and data post processing

IV.1.1. Experimental setup and metrology

The global experimental setup used for both steady and alternating flows is shown in figure IV.1.

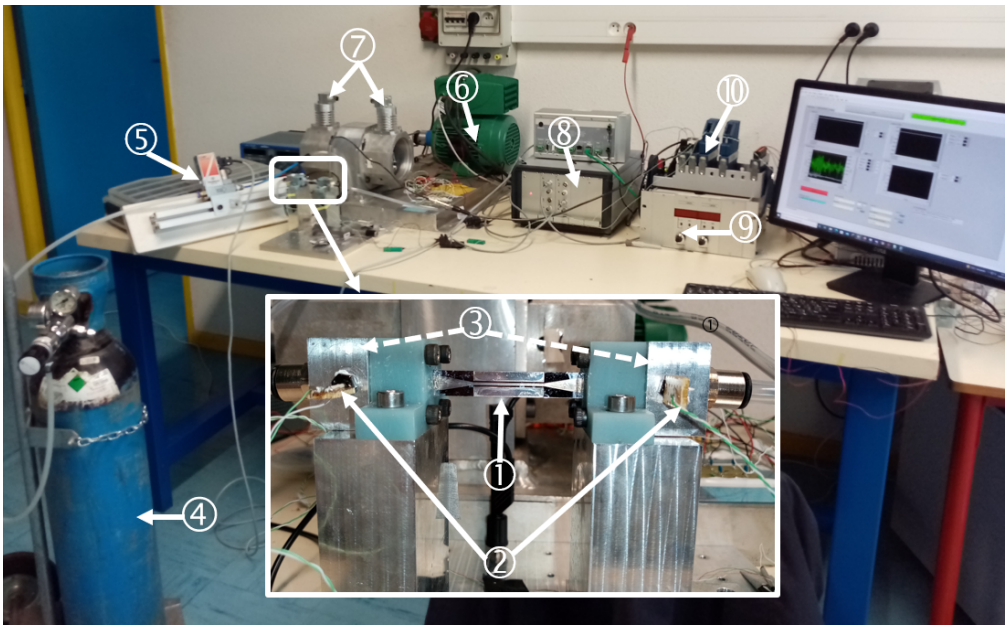

Figure IV.1: Experimental setup - 1: Test channel, 2: Thermocouples, 3: Pressure sensors, 4: Compressed nitrogen, 5: Mass flowmeter, 6: Electric motor, 7: Piston chamber, 8: Pressure signal conditioner, 9: Acquisition system of the mass flowmeter signal, 10: Labview acquisition system

The test channel, denoted (1) in the picture, is connected to the devices realized using stereolithography (chapter II). These devices enable the rectangular or square cross-section of the channel to match the circular cross-section of the pipes in the experimental setup. These printed plastic devices are fixed to a mechanical device supporting the sensors used for pressure (3) and temperature (2) measurements:

- **The pressure sensors** (3) are KULITE XCQ-055-10 BARA-8068-3-661 and were mounted on a screw which was fixed to the metal part holding the sensors as illustrated in figure IV.2. The signal from these sensors was amplified using a conditioner. This system can measure absolute pressure up to 10 bar with a sensitivity of 1 V bar^{-1} and an accuracy of $\pm$ 0.5 % full scale. Pressure sensors were calibrated in the range P_{atm} to 5 bar with the system DRUCK from GE company shown in figure IV.3.
- **The temperature measurements** were carried out by 12.7 μm type K thermocouples (2), which were realized and characterized in our laboratory by using a capacitive discharge method for forming the thermocouple junction. A transient convective method was used to characterize the thermocouples and to determine the time constant [170]. For a 12.7 μm type K thermocouple, the time constant is around 8 ms and the corresponding cut-off frequency is 20 Hz [5]. Each thermocouple was inserted inside a ceramic tube which passes through a screw as illustrated in figure IV.2. The extremity of the ceramic was sealed with glue to prevent gas from entering the two holes. The tip of the thermocouple was located inside the channel as close as possible to the center of the cross-section. This screw was then fixed to the metal part holding the sensors.

Teflon wrapped around the screws, for both pressure and temperature sensors, ensured a good airtight seal.

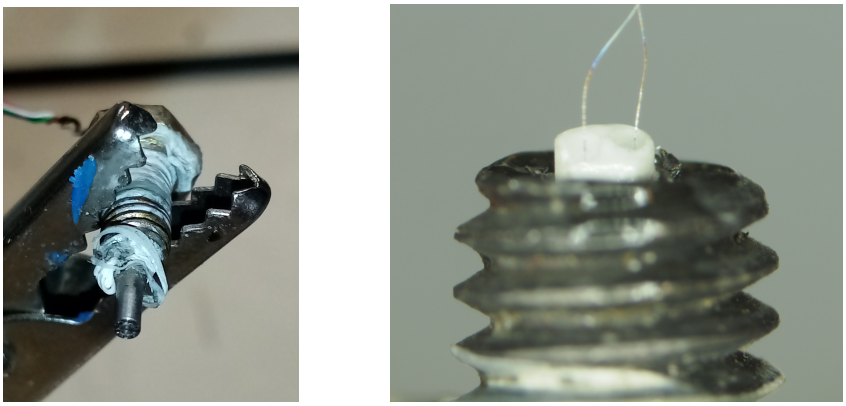

(a) (b)

Figure IV.2: (a) Pressure sensor passing through the screw, (b) Thermocouple passing through a ceramic tube fixed inside a screw

(a) (b)

Figure IV.3: (a) System used for the calibration of pressure sensors, (b) Pressure sensors

Since our study concerns steady flows as well as alternating flows, the fluidic circuit must be adapted according to the study :

- **System used to generate steady flows inside the channels**: the setup consists of a tank (4) where nitrogen is stocked at 200 bar before being expanded at a pressure of 5.5 bar. The gas then flows through an EL-FLOW F-201C-FAC-33-V mass flow meter from BRONKHORST (5), which measures and regulates the gas mass flow rate. This mass flow meter (Figure IV.4) ranges from 0 to 300 mL min^{-1} with an accuracy of $\pm$ 0.1%.

- **System used to generate alternating flows**: it is composed of a motor LEROY SOMER (6) which actuates a rod-crank system that moves two pistons (7), out of phase by 180°, to generate an alternating flow of gas (air). Flexible tubes connect the piston chambers (7) to the device.

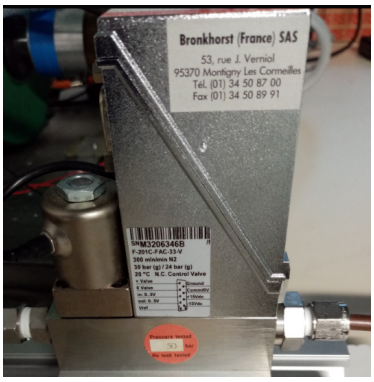

Figure IV.4: Mass flow meter for the flow rate measurement and control in steady flow configuration

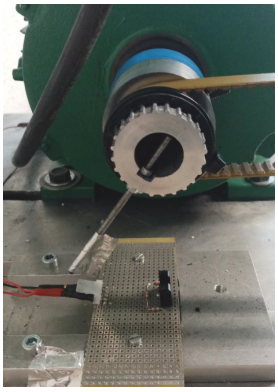

Figure IV.5: Optical sensor for the detection of the piston when reaching its top dead center

To ensure identical experimental conditions, the same lengths of the tube were used, regardless of the configuration (steady flow or alternating flow configuration), to connect the channel to either the piston chambers or the nitrogen cylinder. In addition, to prevent leaks, silicone rubber and O-rings were used on all connecting parts.
Sensor signals for temperature, pressure, flow rate, and piston position were recorded by acquisition systems (9), (10) :

- **For temperature measurements**: the acquisition was done using a NI 9212 module at a sampling rate of 100 samples per second. Other operating modes were available, enabling high-resolution measurements, but at a sampling rate limited to 2 samples per second. The high-speed mode was therefore used for these measurements, to give priority to the number of measurement points per signal period.

- **For pressure, flow rate, and piston position measurements**: the acquisition was carried out using a NI 9215 module, at a sampling rate of 100 samples per second and up to 1000 samples per second for oscillation flow frequencies higher than 5 Hz. An optical sensor, shown in figure IV.5, measured the displacement of the piston (7). A metal rod was linked to the displacement of the piston and moved in front of the optical sensor when the piston n° 1 was at its top dead center delivering a 5 V signal. This measurement allows the detection of the period of fluid oscillation. Considering that the displacement of the piston is sinusoidal, the piston displacement can be reconstructed using a sinusoidal function. Figure IV.6 represents the motion of the piston during a period of fluid oscillation.

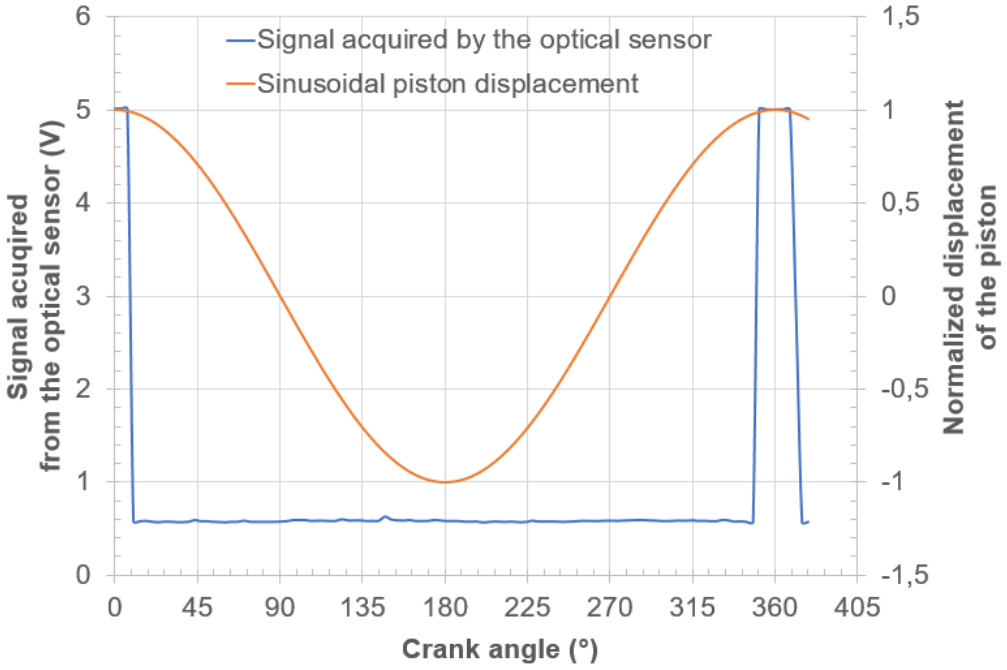

Figure IV.6: Signal acquisition from the optical sensor and related piston displacement

IV.1.2. Operating conditions

Table IV.1 gives the different configurations of the channels studied. Channel C-500-25-0.57-B corresponds to the channel with four bends in the channel design. All configurations were tested in steady and alternating gas flow except Channels C-200-25-0.11 and C-200-25-0.33 which were only tested with alternating flow. The accuracy for the width and the length of the channels is equal to $\pm$ 5 μm, while the accuracy for the height is $\pm$ 2μm.

Table IV.1: The different configurations of channels studied

Channel n°	C-0.2-25-0.1	C-0.2-25-0.3	C-0.5-25-0.6	C-1-25-1	C-1-50-1	C-0.5-25-0.6-B
Width of the channel (μm)	108.7	132.1	670	1003.5	999.7	699
Height of the channel (μm)	1019	396	396	1005	1005	396
Length of the channel (mm)	25	25	25	25	50	25
Hydraulic diameter (μm)	196	198	498	1004	1002	506
Aspect ratio α	0.1	0.3	0.6	1	1	0.6

- **For permanent flow:**
  - Working fluid: nitrogen
  - Flow rate range: 0 to 255 mL min^{-1}
  - Reynolds number range: 10 to 510

The Reynolds number is calculated using the experimental values of the flow rate. The mean cross-sectional velocity U of the flow inside channel with cross-section A is related to the flow rate $\dot{V}$ by the relation:

$$\dot{V}_{std} = U\,A \tag{IV.1}$$

Therefore, the relation between the Reynolds number and the flow rate is:

$$Re = \frac{\rho\ \dot{V}_{std}\ D_h}{\mu\ A} \tag{IV.2}$$

Thus, since the Reynolds number ranges from about 10 to 510, we can considered that the flow will remains in the laminar regime over the entire flow rate range.

- **For alternating flow:**
  - Working fluid: air
  - Frequency range: 0.3 Hz to 15 Hz
  - Rough estimated mean Reynolds range: 10 to 3400. Since we had no velocity measurement for alternating flow (as the hot wires provided had broken during the experiments and could not be replaced in time, it was not possible to measure velocity at the inlet and outlet of the channel), only a rough estimation could be done based on the volume swept by the piston and under the incompressible gas assumption. This rough estimation of the mean flow rate $\bar{\dot{V}}_{osc}$ is given by:

$$\bar{\dot{V}}_{osc} = 2\,f\,c_{piston}\,\pi\,r^2_{piston} \tag{IV.3}$$

with f the frequency of flow oscillation, c_{piston} the piston stroke and r_{piston} the radius of the piston.

Therefore, the mean Reynolds number expression is:

$$\bar{Re} = \frac{\bar{\rho}\ \bar{\dot{V}}_{osc}\ D_h}{\bar{\mu}\ A} \tag{IV.4}$$

The mean value $\bar{\rho}$ and $\bar{\mu}$ of respectively density and viscosity of the fluid are obtained by calculation of mean density and viscosity over the signals period followed by the calculation of mean value between each end of the system.

  - Womersley range: $0 < Wo < 0.67$

$$Wo = \sqrt{\frac{\bar{\rho}\ 2\pi\ f\ R_h^2}{\bar{\mu}}} \tag{IV.5}$$

Both fluids have close but different properties, which are given in table IV.2 at room temperature (T_0 = 20 °C) and atmospheric pressure (P_0 = 1 bar). Later on, the physicochemical properties of the

Table IV.2: Fluid properties at room temperature (T_0 = 20 °C) and atmospheric pressure (P_0 = 1 bar)

	Fluid density ρ $(kg.m^{-3})$	**Molar weight** M $(g.mol^{-1})$	**Specific gas constant** r_G $(J.kg^{-1}.K^{-1})$	**Dynamic viscosity** $*10^5$ μ $(Pa.s)$	**Kinematic viscosity** $*10^5$ ν $(m^2.s^{-1})$
N_2	1,1946	28,013	296,81	1,7573	1,527
Air	1,204	28,965	287,06	1,813	1,506

working gases will be used at the experimental temperatures and pressures corresponding to the test case under consideration.

Hereafter, pressure P_1 and temperature T_1 will refer to the values carried out on the left side of the channels (inlet of the system for steady flow), while pressure P_2 and temperature T_2 will refer to the values measured on the right side (outlet of the system for steady flow). In the same way, piston n° 1 will refer to side 1 while piston n° 2 will refer to the one on side 2.

IV.1.3. Data post-processing

Depending on the operating conditions, experimental data obtained from sensors can exhibit a low signal-to-noise ratio, especially at low frequencies. To smooth the curves and reduce the noise in the signal, the Savitzky-Golay algorithm was used to filter both pressure and temperature signals. The Savitzki-Golay filter smoothes data to improve accuracy, using a polynomial that fits each point according to adjacent points using linear least squares. This method has the advantage of preserving the shape of the signal while reducing noise. Compared with other filters such as Butterworth or Chebyshev, this choice of filter gives a better signal-to-noise ratio and reduces the phase shift that can occur with these other filters. When filtering a signal, it is important not to lose any important information. Therefore, special care was taken by adjusting the parameters of the filter (polynomial order, length of the window) to ensure that the data filtering does not shift the curves temporally or reduces significantly the amplitude of the signal. Figure IV.7 shows an example of a signal without and with filtering post-processing for both pressure and temperature measurements.

The alternating flow part required more data post-processing to shift the temporal signal onto a periodic signal as a function of crank angle θ, which is defined as:

$$\theta = 360\left(f\left[t-t_0\right] - INT\left(f\left[t-t_0\right]\right)\right) \tag{IV.6}$$

with f the frequency of the signal, INT the floor function, and t_0 the time of the beginning of the first period. The piston frequency was precisely determined from the piston position sensor signal and verified from the Fourier transform of the filtered pressure signals. A minimum of 50 periods was recorded for each test measurement, to ensure stability and accuracy.

IV.2 Steady gas flow: results and analysis

This section deals only with steady flows. We characterized the behavior of steady gas flow by determining both pressure and temperature variations between the inlet and outlet of the device. Mea-

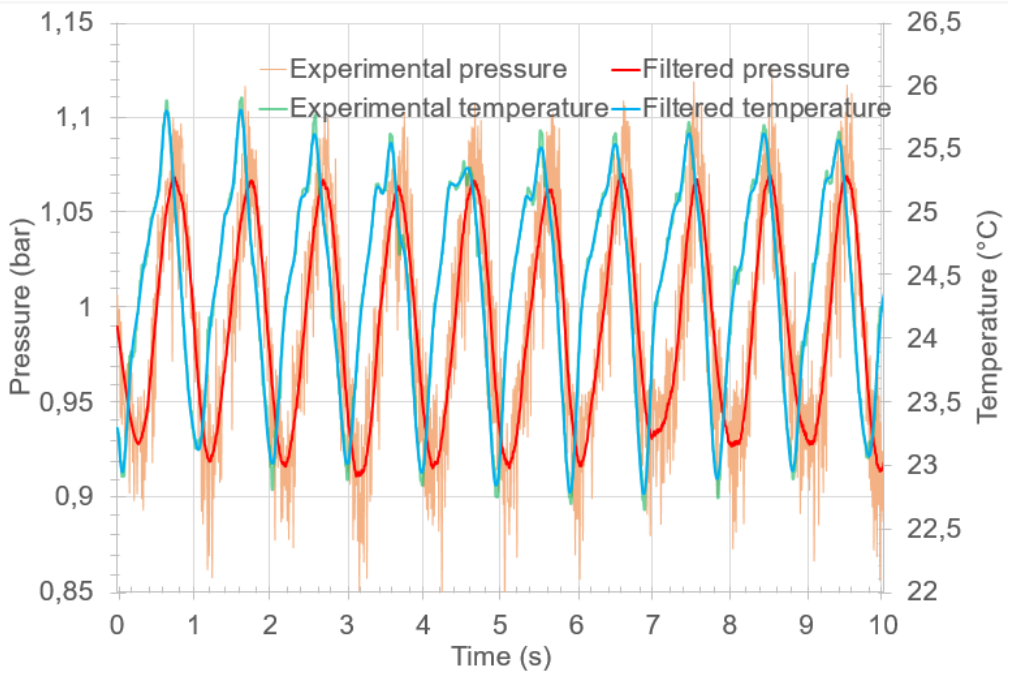

Figure IV.7: Data post-processing: example of filtered pressure and temperature. Curves called "Experimental" are the ones before filtering.

surements will be compared to the theoretical values. Then, the friction factor will be calculated and compared to correlations from the literature.

IV.2.1. Experimental conditions and fluid properties variation

IV.2.1.1 Density and viscosity variation

To determine the fluid properties under our operating conditions, we used the temperature measurements obtained at the channel inlet and outlet, over the entire range of tested flow rates (presented later in this chapter). From these experimental values, the density was calculated using the ideal gas law, while the viscosity was calculated using Sutherland's law [171], [11], [8] which expression is recalled:

$$\mu = \mu_0 \left(\frac{T}{T_0}\right)^{3/2} \left(\frac{T_0 + C_\mu}{T + C_\mu}\right) \tag{IV.7}$$

with C_μ = 113 K (air), and C_μ = 109 K (nitrogen) at temperature T_0 = 273.15 K.

Values of density at the inlet and outlet of the system are given in Table IV.3 at the lowest and highest flow rate for each channel configuration. From this table, we can observe that the variation of fluid density, over the flow rate range, only increases up to 2.4 % between the inlet and outlet of the channels. In the same operating conditions, the maximum increase in the fluid viscosity is 0.2 %. Therefore, for all cases covered in this study with steady flow, we can assume that the variation in fluid density and viscosity is negligible.

Table IV.3: Variation of fluid density between the inlet and the outlet of the device at different flow rates for steady flow

	$D_h = 500\ \mu$m, $\alpha = 0.6$, $L_{ch} = 25$ mm, Straight channel			$D_h = 500\ \mu$m, $\alpha = 0.6$, $L_{ch} = 25$ mm, Channel with 4 bends			$D_h = 1$ mm, $\alpha = 1$, $L_{ch} = 50$ mm, Straight channel		
	$\dot{V}_{min}$	$\dot{V}_{max}$	$\frac{\rho_{max}-\rho_{min}}{\rho_{mean}}$	$\dot{V}_{min}$	$\dot{V}_{max}$	$\frac{\rho_{max}-\rho_{min}}{\rho_{mean}}$	$\dot{V}_{min}$	$\dot{V}_{max}$	$\frac{\rho_{max}-\rho_{min}}{\rho_{mean}}$
Flow rate $\dot{V}$ $(mL.min^{-1})$	0	255	-	0	255	-	0	255	-
Inlet density ρ_{in} $(kg.m^{-3})$	1.114	1.135	1.9 %	1.104	1.123	1.7 %	1.144	1.156	1.05 %
Outlet density ρ_{out} $(kg.m^{-3})$	1.115	1.119	0.36 %	1.096	1.097	0.09 %	1.143	1.144	0.087 %
Relative variation in fluid density (%)	0.09 %	1.4 %	-	0.73 %	2.4 %	-	0.087 %	1.05 %	-
Inlet viscosity $\mu_{in}x10^5$ **(Pa.s)**	1.8676	1.8642	0.18 %	1.8650	1.8631	0.10 %	1.8674	1.8661	0.070 %
Outlet viscosity $\mu_{out}x10^5$ **(Pa.s)**	1.8666	1.8629	0.20 %	1.8627	1.8616	0.06 %	1.8661	1.8654	0.04 %
Relative variation in fluid viscocity (%)	0.06 %	0.07 %	-	0.12 %	0.08 %	-	0.07 %	0.04 %	-

IV.2.1.2 Range of Reynolds and Mach number

In addition, for each channel configuration tested, Reynolds and Mach numbers ranges have been calculated based on the experimental values of temperature and pressure, and their values are given in the table IV.4. We can observe that the Reynolds number is below 510 for all channel configurations. This is sufficiently low to consider the flow to be in the laminar regime.

Furthermore, the Mach number ranged from 0 to 0.027. Since it is well below the value of 0.3, this seems to support the validation of the hypothesis of an incompressible flow. Nevertheless, as we saw in Chapter 1, the condition on the Mach number is not sufficient to assert that the flow is indeed incompressible since compressibility effects have been observed for Mach number values below 0.3.

Table IV.4: Range of Reynolds and Mach number for the channels tested in steady flow

Channels	$D_h = 500\ \mu$m, $\alpha = 0.6$, $L_{ch} = 25$ mm, channel with bends	$D_h = 500\ \mu$m, $\alpha = 0.6$, $L_{ch} = 25$ mm	$D_h = 1$ mm, $\alpha = 1$, $L_{ch} = 25$ mm	$D_h = 1$ mm, $\alpha = 1$, $L_{ch} = 50$ mm
Range of Reynold number	30 - 507	30 - 490	15 - 280	15 - 275
Range of Mach number	0 - 0.027	0 - 0.027	0 0.013	0 - 0.013

IV.2.2. Pressure drop

Regarding the total pressure drop, it corresponds to the sum of all losses due to straight lengths (major losses) and those due to singularities (minor losses). In the theoretical part that follows, we will discriminate between each type of pressure loss to determine the total theoretical pressure loss.

IV.2.2.1 Theoretical pressure drop

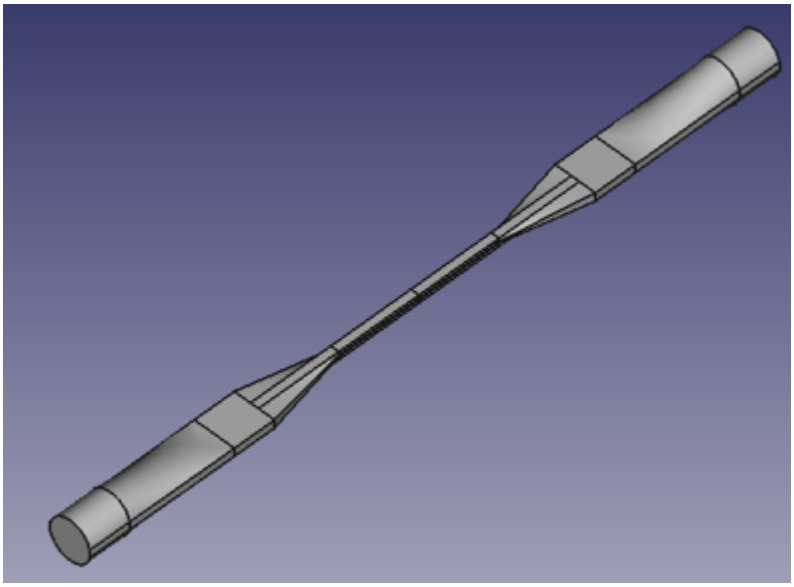

(a)

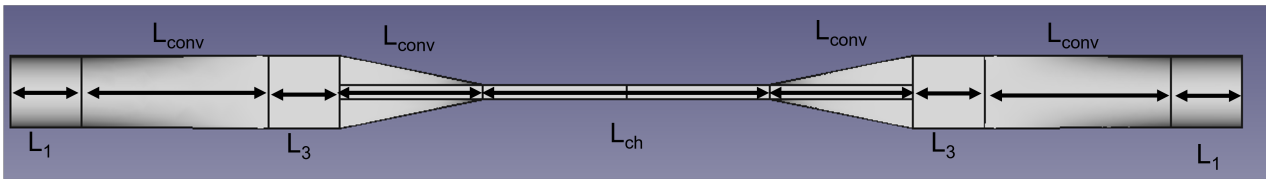

(b)

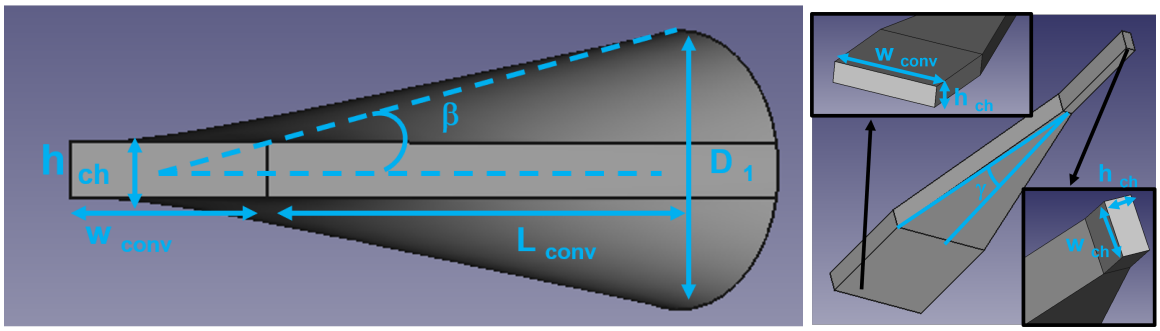

(c) (d)

Figure IV.8: (a) 3D scheme of the cross-section involved in the experimental setup, (b) top view, (c) Scheme of sections 2 and 7 (*cf.* figure IV.9) , (d) Scheme of sections 4 and 5 (*cf.* figure IV.9)

In this section, the theoretical pressure drop was estimated by its "classical" value for incompressible fluid flow in circular channels, or rectangular channels depending on cross-section, on a macroscopic scale.

Furthermore, based on the Reynolds number calculated above, the correlations used are those valid for laminar flow.

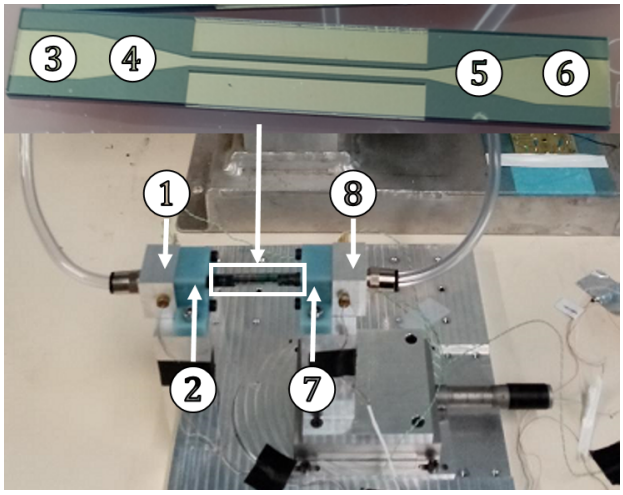

Figure IV.9: Picture of the various sections involved in the calculation of theoretical total pressure drop corresponding to the pressure difference measured experimentally

Figure IV.8 illustrates schematic views of the channel with the converging and diverging sections (a,b), dimensions and parameters of converging and diverging cross-sections (c,d).

All contributions to the pressure drop due to local singularity (minor loss), such as converging and diverging cross-sections, were calculated using reference formulas from [172]. Figure IV.9 shows the different cross-sections involved in the calculation of the total pressure drop, corresponding to the experimentally measured pressure difference. The parts numbered 1, 3, 6, and 8 correspond to friction losses (major losses), individually identified as ΔP_1, ΔP_3, ΔP_6 and ΔP_8, and whose sum corresponds to ΔP_f. On the other hand, the parts numbered 2, 4, 5, and 7 correspond to convergent and divergent sections, *i.e.* minor losses respectively noted ΔP_2, ΔP_4, ΔP_5 and ΔP_7, and whose sum corresponds to ΔP_m. To these must be added the contribution of the channel which corresponds to friction loss (ΔP_{ch}) and, if present, the bends corresponding to minor loss (ΔP_{bend}). Therefore, the total theoretical value of the pressure drop ΔP_{tot} (between 1 and 8 on figure IV.9) is given by the equation:

$$\Delta P_{tot} = \Delta P_f + \Delta P_m + \Delta P_{ch} + \Delta P_{bend} \tag{IV.8}$$

We recall that the pressure drop due to friction (friction or major loss) is given by the relation:

$$\Delta P_f = \frac{1}{2} C_f \rho U^2 \frac{L}{D_h} \tag{IV.9}$$

with C_f the friction factor, ρ the fluid density, U the flow velocity, L the length of the part, and D_h the hydraulic diameter. The theoretical pressure drop due to fluid encountering obstacles (minor loss)

is given by the relation:

$$\Delta P_m = \frac{1}{2}\zeta \rho U^2 \tag{IV.10}$$

with ζ empirical coefficient that can be determined according to the obstacle encountered. These coefficients have been determined experimentally for various obstacles at the macroscale.

1. Theoretical pressure drop due to friction in the channel

   The dimensions of the channel are given by its width w_{ch}, height h_{ch}, and length L_{ch}. The pressure drop due to friction in the channel is therefore given by:

$$\Delta P_{ch} = 0.5\,\rho\, U_{ch}^2\, C_f(\alpha)\, \frac{L_{ch}}{D_h} \tag{IV.11}$$

   Since we have channels with different aspect ratios, the correlation used for the friction factor will be the one proposed by White [11], which has been defined in chapter I. This correlation seems to be the most adapted regarding our experiment since it takes into account the influence of aspect ratio. We recall its expression here:

$$C_f(\alpha) = \frac{96}{Re}\ (1 - 1.3553\alpha + 1.9467\alpha^2 - 1.7012\alpha^3 + 0.9564\alpha^4 - 0.2537\alpha^5) \tag{IV.12}$$

2. Theoretical pressure drop due to converging and diverging cross-section

   - Sections 1 and 8 (*cf.* figure IV.9):

     Sections 1 and 8 consist of a circular cross-section with an inner diameter D_1 of 5 mm and a length L_1 of 12 mm. The theoretical value for C_{f1} will be taken assuming incompressible fluid flow in a circular channel which is equal at macroscale to $\frac{64}{Re}$ (since the flow is laminar for the tested flow rates).

$$\Delta P_1 = \Delta P_8 = 0.5\,\rho\, U_1^2\, C_{f1}\, \frac{L_1}{D_1} \tag{IV.13}$$

     This equation can be expressed with the measurements carried out and simplified as follows:

$$\Delta P_1 = 128\, \frac{\dot{V}\, L_1\, \mu}{\pi D_1^4} \tag{IV.14}$$

     with $\dot{V}$ the flow rate defined as $\dot{V} = U_1\, A_1$ (A_1 being the cross-section of the considered section).

   - Section 2 (*cf.* figure IV.9): Section 2 consists of a converging cross-section with a change of cross-section shape from circular (inner diameter: 5 mm) to rectangular (width: 5 mm and height is equal to the height of the channel). The length of this section ranges from 11.31 mm to 13.87 mm according to the height of the channel studied. The angle of converging cross-section β is the angle of the enlargement in the width of the channel while the angle γ will refer to the angle of the enlargement in the height of the channel. The pressure drop of the section B is given by [172]:

$$\Delta P_2 = 0.5\,\rho\,U_2^2\left[\zeta_2\left(1-\frac{A_2'}{A_2}\right)+\zeta_2'\right] \tag{IV.15}$$

With ζ_2 and ζ_2' coefficients (determined with the geometrical parameters of the converging cross-section), and A_2' and A_2 being respectively the smallest and the largest cross-section of the converging section 2.

From diagram 3-6 in [172], the coefficient ζ_2 was determined depending on the angle of the converging cross-section and the ratio L_{conv} to D_{h2} (where L_{conv} is the length of the converging section and D_{h2} is the hydraulic diameter of the smallest cross-section). As mentioned in chapter II, the half-angle of both converging and diverging cross-section was equal to 10 °. The ratio of L_{conv} to D_{h2} in our case is higher than 1 for all configurations. Therefore, we will take the value of $\zeta_2 = 0.18$ even though, the real values might be smaller.

The coefficient ζ_2' was determined using (diagram 5-3 [172]):

$$\zeta_2' = \frac{C_{f2}(\alpha_2)}{16\,sin(\beta/2)}\left[1-\left(\frac{A_2'}{A_2}\right)^2\right]+\frac{C_{f2}(\alpha_2)}{16\,sin(\gamma/2)}\left[1-\left(\frac{A_2'}{A_2}\right)^2\right] \tag{IV.16}$$

with $C_{f2}(\alpha_2)$ the friction factor, which depends on the aspect ratio of the cross-section.

Since the angle $\gamma = 0$ ° for the section 2, the equation can be simplified:

$$\zeta_2' = \frac{C_{f2}(\alpha_2)}{16\,sin(\beta/2)}\left[1-\left(\frac{A_2'}{A_2}\right)^2\right] \tag{IV.17}$$

Finally, the pressure drop ΔP_2 can be expressed as:

$$\Delta P_2 = \frac{\rho}{2}\left(\frac{\dot{V}}{A_2'}\right)^2\left[0.18\left(1-\frac{A_2'}{A_2}\right)+\frac{C_{f2}}{16sin(\frac{\beta}{2})}\left(1-\left(\frac{A_2'}{A_2}\right)^2\right)\right] \tag{IV.18}$$

- Section 3 and 6 on figure IV.9:

  Sections 3 and 6 consist of a rectangular cross-section with a width equal to 5 mm, a length equal to 5 mm, and a height equal to the channel's height h_{ch}.

$$\Delta P_3 = \Delta P_6 = 0.5\,\rho\,U_3^2\,C_{f3}(\alpha_3)\frac{L_3}{D_{h3}} \tag{IV.19}$$

with $C_{f3}(\alpha)$, the friction factor, which depends on the aspect ratio α_3 of this cross-section Which can be expressed as follows:

$$\Delta P_3 = \frac{C_{f3}(\alpha_3)}{2}\,\frac{L_3\,\mu}{D_{h3}^2}\,\frac{\dot{V}}{h_{ch}w_{conv}} \tag{IV.20}$$

This last equation can be simplified as:

$$\Delta P_3 = \Delta P_6 = \frac{C_{f3}(\alpha_3)}{2} L_3 \, \mu \, \frac{\dot{V} \, (h_{ch} + w_{conv})^2}{(h_{ch} w_{conv})^3} \tag{IV.21}$$

The theoretical value for C_{f3} for incompressible fluid flow at macroscale in a rectangular channel depends on the aspect ratio and is equal to $\frac{96 f(\alpha)}{Re}$, where f(α) is the function defined in equation I.29 (*cf. chapter I*).

- Section 4 (*cf.* figure IV.9):

Section 4 provides a convergent section to adapt the channel width from w_{conv} = 5 mm to the width w_{ch} of the channel, while the height of this section remains equal to h_{ch}. The length of this section ranges from 11.31 mm to 13.87 mm according to the height of the studied channel. The angle of converging cross-section β in the height of the channel is equal to 0°, while the value for the angle γ in the width of the channel is equal to 20°. In the same way, as for section 2, the pressure drop generated by section 4 is expressed by the relation:

$$\Delta P_4 = 0.5 \, \rho \, U_4^2 \left[\zeta_4 \left(1 - \frac{A'_4}{A_4} \right) + \zeta'_4 \right] \tag{IV.22}$$

With ζ_4 and ζ'_4 coefficients (determined with the geometrical parameters of the converging cross-section) and A'_4 and A_4 being respectively the smallest and the largest cross-section of the converging section 4.

Since the value of the angle of convergence and the ratio L_{conv} to D_{h4} are identical to the ones for section 2, the coefficient ζ_4 is unchanged and equal to 0.18. The coefficient ζ'_4 can be determined using (diagram 5-4 [172]) :

$$\zeta'_4 = \frac{C_{f4}}{4 sin(\gamma/2)} \left[\frac{w_{ch}}{L_{ch}} \left(1 - \frac{A'_4}{A_4} \right) + 0.5 \left(1 - \left(\frac{A'_4}{A_4} \right)^2 \right) \right] \tag{IV.23}$$

Therefore, the pressure drop generated by the section 4 can be expressed as:

$$\begin{aligned} \Delta P_4 = \frac{\rho}{2} \left(\frac{\dot{V}}{A'_4} \right)^2 \Bigg[& 0.18 \left(1 - \frac{A'_4}{A_4} \right) \\ & + \frac{C_{f4}}{4 sin(\frac{\gamma}{2})} \left(\frac{w_{ch}}{L_{ch}} \left(1 - \frac{A'_4}{A_4} \right) + 0.5 \left[1 - \left(\frac{A'_4}{A_4} \right)^2 \right] \right) \Bigg] \end{aligned} \tag{IV.24}$$

- Section 5 (*cf.* figure IV.9):

Section 5 consists of a diverging cross-section with identical geometrical parameters as section 4. The pressure drop for this section can be determined by the relation:

$$\Delta P_5 = 0.5 \, \rho \, U_5^2 \left[\zeta_5 \left(1 - \frac{A'_5}{A_5} \right)^2 + \zeta'_5 \right] \tag{IV.25}$$

Both coefficient ζ_5 and ζ'_5 were determined using diagram 5-4 [172]:

$$\zeta_5 = 3.2tan(\frac{\gamma}{2})\sqrt[4]{tan(\frac{\gamma}{2})} \tag{IV.26}$$

$$\zeta'_5 = \frac{C_{f5}}{4sin(\gamma/2)}\left(\frac{w_{ch}}{L_{ch}}\left[1-\frac{A'_5}{A_5}\right]+0.5\left[1-\left(\frac{A'_5}{A_5}\right)^2\right]\right) \tag{IV.27}$$

The pressure drop generated by section 5 can therefore be expressed as:

$$\begin{aligned}\Delta P_5 = 0.5\,\rho\left(\frac{\dot{V}}{A'_5}\right)^2\Bigg[3.2tan(\frac{\gamma}{2})\sqrt[4]{tan(\frac{\gamma}{2})}\left(1-\frac{A'_5}{A_5}\right)^2 \\ +\frac{C_{f5}}{4sin(\gamma/2)}\left(\frac{w_{ch}}{L_{ch}}\left[1-\frac{A'_5}{A_5}\right]+0.5\left[1-\left(\frac{A'_5}{A_5}\right)^2\right]\right)\Bigg]\end{aligned} \tag{IV.28}$$

- Section 7 (*cf.* figure IV.9):

  Section 7 consists of a diverging cross-section with identical geometrical parameters as section 2. The pressure drop for this section can be determined by the relation:

$$\Delta P_7 = 0.5\,\rho\,U_7^2\left[\zeta_7\left(1-\frac{A'_7}{A_7}\right)^2+\zeta'_7\right] \tag{IV.29}$$

  Both coefficient ζ_7 and ζ'_7 were determined using the diagram 5-3 [172].

$$\zeta_7 = 4tan(\frac{\gamma}{2})\sqrt[4]{tan(\frac{\gamma}{2})} \tag{IV.30}$$

$$\zeta'_7 = \frac{C_{f7}}{16sin(\beta/2)}\left[1-\left(\frac{A'_7}{A_7}\right)^2\right] \tag{IV.31}$$

  The pressure drop generated by section 7 can therefore be expressed as:

$$\Delta P_7 = 0.5\,\rho\left(\frac{\dot{V}}{A'_7}\right)^2\left[4tan(\frac{\beta}{2})\sqrt[4]{tan(\frac{\beta}{2})}\left(1-\frac{A'_7}{A_7}\right)^2+\frac{C_{f7}}{16sin(\frac{\beta}{2})}\left(1-\left[\frac{A'_7}{A_7}\right]^2\right)\right] \tag{IV.32}$$

3. Theoretical pressure drop due to sharp bends (90 °) ΔP_{bend}

The theoretical pressure drop due to a sharp bend can be determined by using diagrams 6-7 [172].

$$\Delta P_{bend} = \frac{1}{2}\,\zeta_{bend}\,\rho\,U^2 \tag{IV.33}$$

With ζ_{bend}, a coefficient equal to $C_1\,C_2\,C_3$.
C_1 is a function of the aspect ratio of the channel (height to width ratio) and can be determined with

table from the book [172]. C_2 and C_3 are coefficients that depend on the angle of the bend. All bends involved in the design of our channels are 90 ° bends. Therefore, C_2 = 0.99 and C_3 = 1.20, resulting in the simplification of equation IV.33:

$$\Delta P_{bend} = 0.594\, C_1\, \rho\, U^2 \tag{IV.34}$$

To conclude this section, the theoretical pressure drop will be calculated by summing the various elements mentioned above. These theoretical values will then be compared with the experimental values in the following section.

IV.2.2.2 Experimental pressure drop measurement

Experiments performed: During permanent flow experiments, the total pressure drop (between sections 1 and 8 in figure IV.9) was determined experimentally by the following relation:

$$\Delta P = P_{in} - P_{out} = P_1 - P_2 \tag{IV.35}$$

Each test was repeated at least three times to ensure repeatability and to isolate any measurement artifacts. Thus, the experimental results presented in this section are expressed as the average of at least three tests performed systematically for each channel configuration and flow rate covered.

Figures IV.10 and IV.11 show the evolution of the pressure difference ΔP measured between the inlet and outlet of the system for the channel configurations tested with steady nitrogen flow for a flow range from 0 mL min^{-1} to 255 mL min^{-1}. The error bars in figures IV.10 and IV.11 represent the standard deviation of the measurements over time (This represents a sufficiently large amount of measurement data to use the standard deviation, since measurements were taken for around 10 s for each flow with a sampling frequency of 100 Hz). The pressure difference obtained with equation IV.35 were compared with theoretical pressure drops derived from the equation IV.8. We recall that the theoretical pressure drops take into account the respective contribution of the converging and diverging sections on either side of the channel since the pressure drop generated along these sections is included in the pressure difference measured.

Discussion: i) Influence of channel length: Figure IV.10 focuses on the effect of channel length alone on pressure drop (the other converging, diverging *etc.* elements being identical for both geometries). The channels compared here had an aspect ratio α and hydraulic diameter D_h of respectively 1 and 1mm. The inserts at the top right correspond to zoom, as these pressure drops are relatively small compared with those of a smaller hydraulic diameter (Figure IV.11).

It was observed that for channels with a hydraulic diameter of 1 mm, pressure drops were low and close to the accuracy of pressure sensors, which explains the large error bars and wide dispersion of the data. Despite this wide dispersion of values, the experimental data were fitted with a 2nd-order polynomial corresponding to the form expected according to the theoretical pressure drops we had calculated.

Next, we attempted to represent this trend curve by the sum of two theoretical contributions described by the formulas listed above (the contribution of the channel and the one for the converging and diverging sections). For the 50 mm channel, the experimental curve appears to be fairly well described by the sum of the theoretical contributions. This is less the case for the 25 mm long channel, with deviations between experimental and theoretical reaching 100 % for the highest flow rates. This

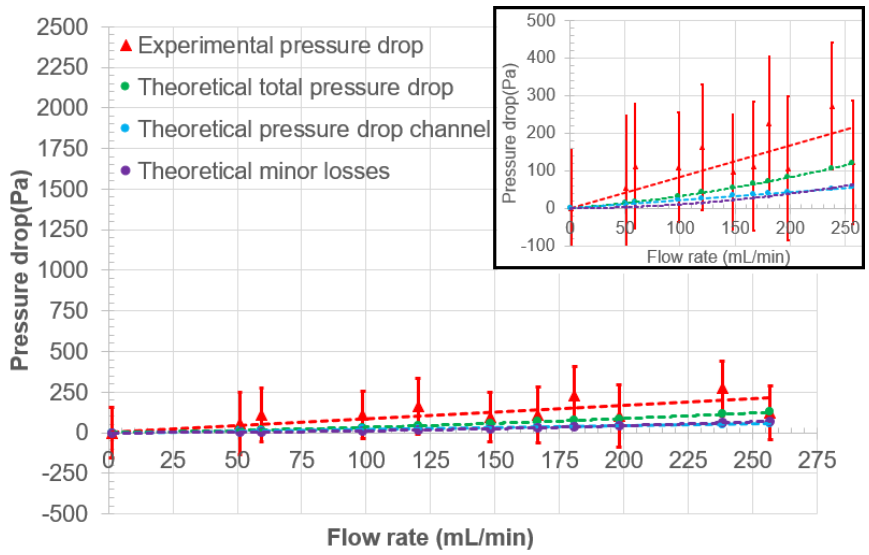

(a)

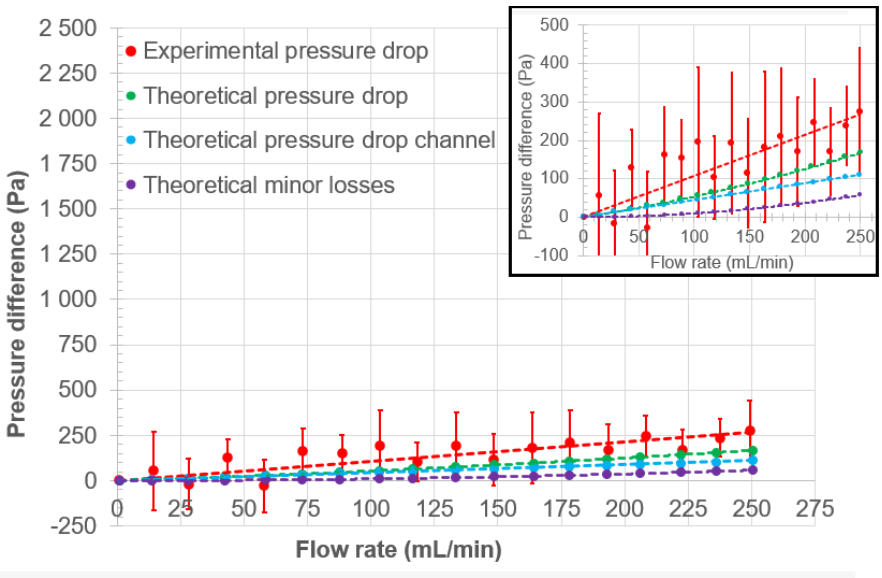

(b)

Figure IV.10: Influence of channel length: pressure drop as a function of flow rate for the channel with D_h = 1 mm and α =1, (a) L_{ch} = 25 mm, (b) L_{ch} = 50 mm

can also be seen in the coefficient of determination, which is lower for this channel than for the 50 mm long channel. This is to be expected, since pressure drops are necessarily lower for this channel, and the relative uncertainty of the measurements is therefore greater.

ii) Influence of bends: Figure IV.11 focuses on the influence of bends for otherwise identical channels (same length, hydraulic diameter, aspect ratio, etc.). The channels compared here have a channel length of 25 mm, aspect ratio of 0.6 and hydraulic diameters of 500 μm.

It can be seen that the measurements on these channels were much more representative, with error bars much smaller in proportion due to the greater pressure drops obtained. The variation in pressure

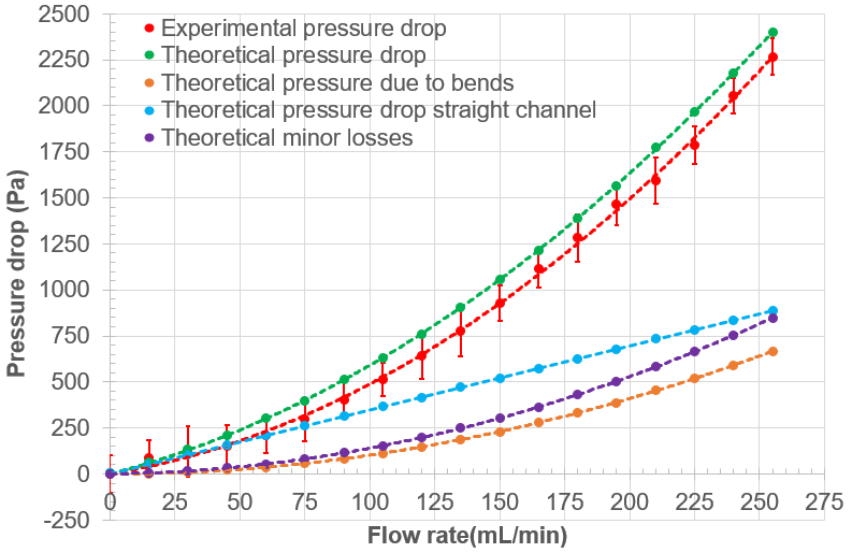

(a)

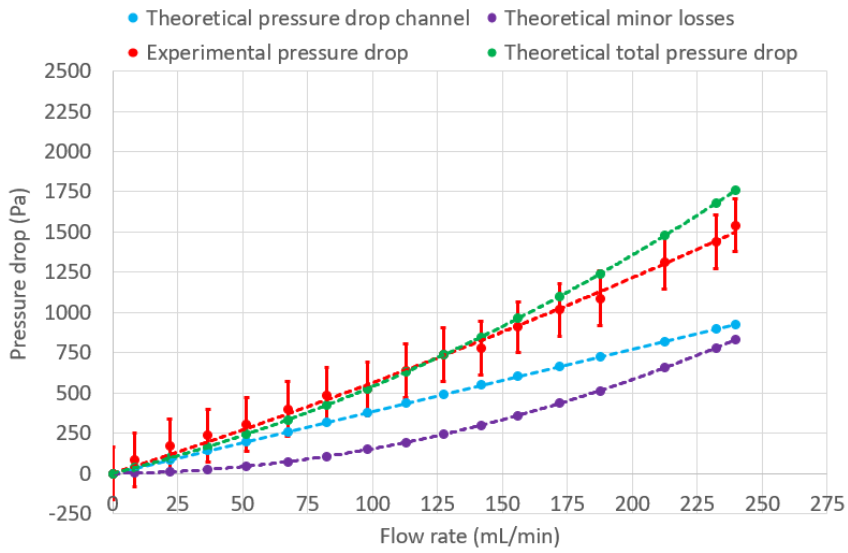

(b)

Figure IV.11: Influence of bends: pressure drop as a function of flow rate for channels with $D_h = 500$ μm, $\alpha = 0.6$, $L_{ch} = 25$ mm (a) channel with bends (b) straight channel

drops with the flow rate also follows much more regular curves, due to the lower dispersion of the measurements.

We can also observe a good agreement between the experimental pressure drops and the theoretical ones. This shows the need to take into consideration several contributions to the theoretical pressure drops (the importance of these contributions were of the same order of magnitude for the highest flow rates tested):

- The influence of the channel: This contribution was a linear function of the flow rate because we have assumed a theoretical friction coefficient inversely proportional to the Reynolds number.

- The influence of converging and diverging sections: As we assumed as a first approximation that the coefficients of these obstacles did not depend on the speed of the flow, consequently this contribution is proportional to $\dot{V}^2$. This hypothesis, as can be seen in figure, makes it possible to properly describe the experimental curves. Nevertheless, for the highest flow rates, it can be seen that the theoretical curve tends to deviate from the experimental curves, which could suggest that the contribution of the converging/diverging sections is perhaps rather in $\dot{V}^k$ ($1 > k > 2$) that in $\dot{V}^2$. This could also be due to an overestimation of the contribution of converging and diverging sections (in particular values of ζ_2 and ζ_4) which are very smooth and long transition of cross-section (high ratio of converging and diverging length to hydraulic diameter $L_{conv}/D_h >> 1$).
- The influence of bends, when present in the channel, is of the same shape and order of magnitude (although lower) than the contribution of converging/diverging sections. We nevertheless see that at high flow rates, the contribution of the converging/diverging parts moves further and further away from that provided by the bends, which suggests that the influence of the converging/diverging sections would become the major contribution and would tend to reduce the relative influence of the bends on the total pressure losses for higher flow rate .

Keeping in mind that values obtained for channel with hydraulic diameter of 1 mm is not completely reliable, by comparing IV.10 (a) and IV.11 (b), we can also estimate the influence of the hydraulic diameter and aspect ratio. The pressure drop obtained for the channels (without bends) with hydraulic diameter of 500 μm and aspect ratio of 0.6 increases up to almost 1500 Pa as the flow rate increases up to 255 mL min^{-1}, while for the channels with hydraulic diameter of 1 mm and aspect ratio of 1, it increases up to only about 200 Pa. This is consistent with theory since the pressure drop is inversely proportional to $D_h^2 A$:

$$\Delta P = 48\,\mu\,C(\alpha)\,\frac{\dot{V}}{A}\frac{L_{ch}}{D_h^2} \tag{IV.36}$$

where $C(\alpha)$ is the function defined in equation IV.12 which takes into account the aspect ratio of the channels, $\dot{V}$ being the flow rate.

Both A and D_h^2 are nearly 4 times higher for the channels with a hydraulic diameter of 1 mm compared to the channels with a hydraulic diameter of 500 μm, which results in a pressure drop around 16 times lower for the channels with a hydraulic diameter of 1 mm. This is consistent with what we obtained if we remove the contribution due to converging and diverging sections.

Next, we have removed the theoretical contribution due to converging and diverging sections from the experimental total pressure drops measured. This had allowed to compare only the contribution of the channel and thus determined the influence of bends on the channel pressure drops. Figure IV.12 shows the experimental channel pressure drop versus Reynolds number. Results for the channels with D_h= 1 mm, have not been displayed because our confidence in their accuracy is low (see comments on fig. IV.10).

We can observe that the contribution of bend in the pressure drop starts to be significant for Reynolds above 300. For lower Reynolds numbers, the pressure drop measured for the two channels with a hydraulic diameter of 500 μm are very close.

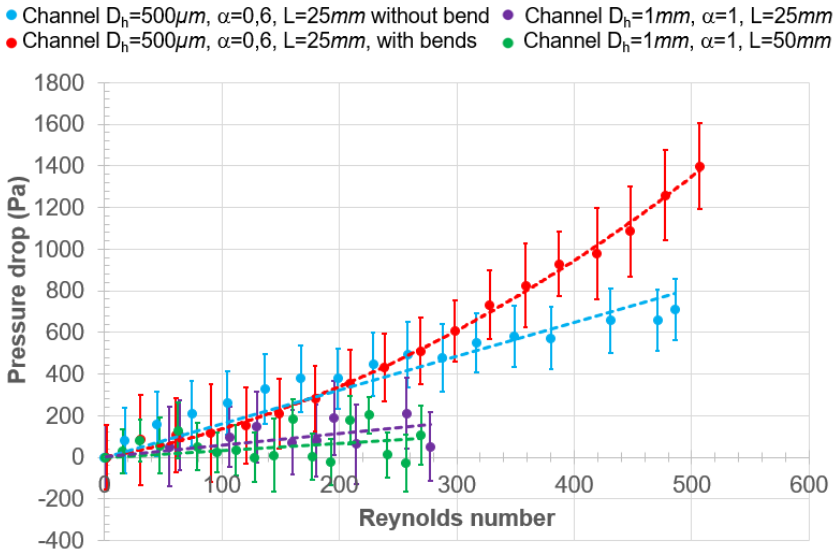

Figure IV.12: Pressure drop for each channel configuration as a function of Reynolds number

IV.2.3. Temperature difference

Experiments performed: First of all, we recall that the temperature measurements were carried out before the converging section (inlet temperature) and after the diverging section (outlet temperature). Figure IV.13 shows the variation in inlet and outlet temperature for channel with D_h = 500 μm, α = 0.6 and L_{ch} = 25 mm with bends and for the channel with D_h = 1 mm, α = 1 and L_{ch} = 50 mm (temperature could not be measured for the last tested channel -D_h = 1 mm, α = 1, L_{ch} = 25 mm -in steady flow configuration due to technical issues). Each measuring point here corresponds to the average of at least 3 tests. Furthermore, each test value is itself a time average throughout the data acquisition. Measurements were also carried out with increasing flow rate then with decreasing flow rate ensuring that no hysteresis effect is observed.

Discussion: The temperature variations are surprising and cannot be explained with absolute confidence.

i) Outlet temperature: The higher temperature at the outlet seems consistent if we consider that fluid friction will increase the temperature of the fluid along the channel. This was observed by Koo *et al.* in modeling the viscous dissipation in channels studied by Pfahler *et al.* [173] with a hydraulic diameter ranging from 1 μm to 43.6 μm. The authors observed that viscous dissipation can make non-negligible contributions to temperature rise, even at low Reynolds numbers. A temperature difference up to 30 $°C$ was observed for the channel with the lowest hydraulic diameter, D_h = 1 μm for a Reynolds number of 0.01. Regarding the channel with the highest hydraulic diameter, D_h = 43.6 μm, the temperature difference was observed only up to 1 $°C$ for a Reynolds number of around 100. This showed the large influence of hydraulic diameter in the contribution of viscous dissipation in the temperature rise. Since our tested channels have a much higher hydraulic diameter (D_h = 500 μm and D_h = 1 mm), the temperature difference is expected to be much smaller.

ii) Inlet temperature: On the other hand, the inlet temperature variation is more difficult to explain. The decrease in temperature was observed for increasing flow rates up to 100 $mL.min^{-1}$ seemed to be the opposite of what was expected since pressure at the same position increased as a function of

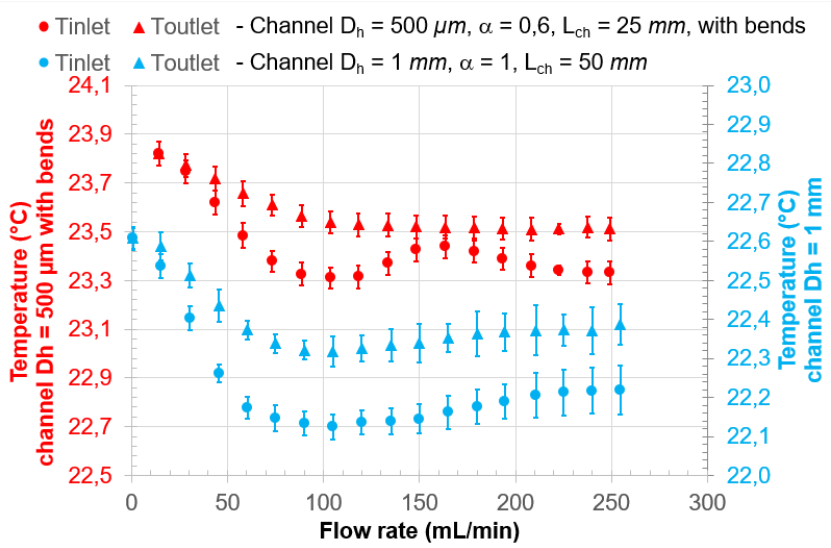

Figure IV.13: Variation of temperature at the inlet and outlet of the device for the channels with D_h = 500 μm, α = 0.6, L_{ch} = 25 mm. Circular points correspond to inlet temperature while triangular points correspond to outlet temperature.

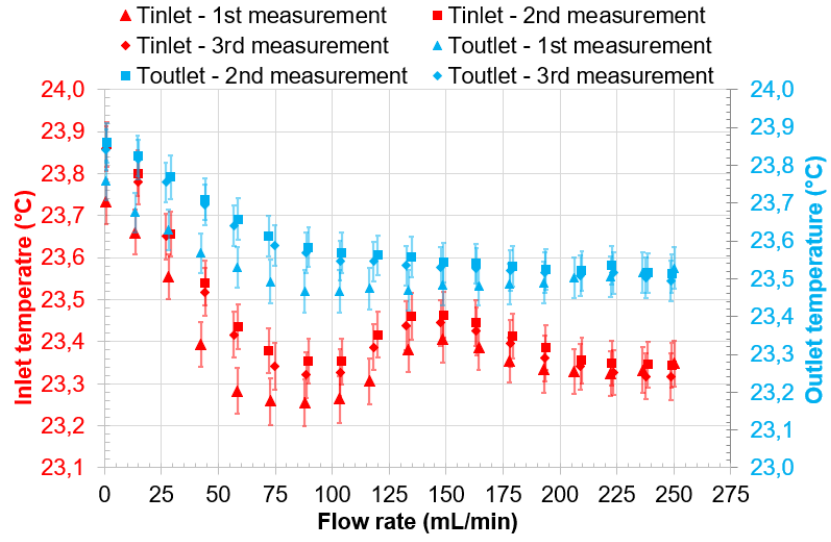

Figure IV.14: Repeatability of temperature measurements for the channel with D_h = 500 μm, α = 0.6, L_{ch} = 25 mm and with bends

flow rate. By using the law of ideal gas, if the pressure increases, the fluid temperature should also increase. One explanation might be that this was the result of a measurement artifact, a variation in room temperature, or an error due to sensor accuracy. However, these measurements were repeated two more times with the same variation observed, as shown in figure IV.14, which should suggest that this hypothesis does not explain the variation observed.

A decrease in inlet temperature with increasing flow velocity was also observed by Hong *et al.* [174], but the authors did not give any explanation on this behavior. They studied gas flow in channels with a hydraulic diameter ranging from 150 μm to 200 μm and length of channel equal to 27 mm,

for Re ranging from 500 to 16 000 and Ma ranging from 0.1 to 0.6. However, in their case, the flow could be assumed to be adiabatic, whereas in our case this assumption cannot be considered, since our channels are not thermally insulated. Thus, this decrease in inlet temperature could be explained by heat transfer which occurs at the wall of channels. Indeed, the heat transfer coefficient increases with the increasing velocity. This would result in a larger thermal exchange as the flow rate increases.

The increase in inlet temperature observed in the flow rate range of 100 - 150 $mL.min^{-1}$ could be due to a competing contribution from fluid friction and heat transfer. The fact that the outlet temperature is not as strongly impacted by these inlet temperature variations could also be explained by the pressure drop between the inlet and outlet, which contributes to lowering the fluid temperature under the assumption of incompressible flow. The fact that we did not observe the same variation at the outlet suggests that this is due to a contribution that occurs in the channel. However, we could not explain the decrease in inlet temperature observed for a flow rate higher than 150 $mL.min^{-1}$.

iii) Temperature difference: Figure IV.15 represent temperature difference ΔT between inlet and outlet versus Reynolds number for each tested channel configuration. ΔT was determined experimentally by:

$$\Delta T = T_{in} - T_{out} = T_1 - T_2 \tag{IV.37}$$

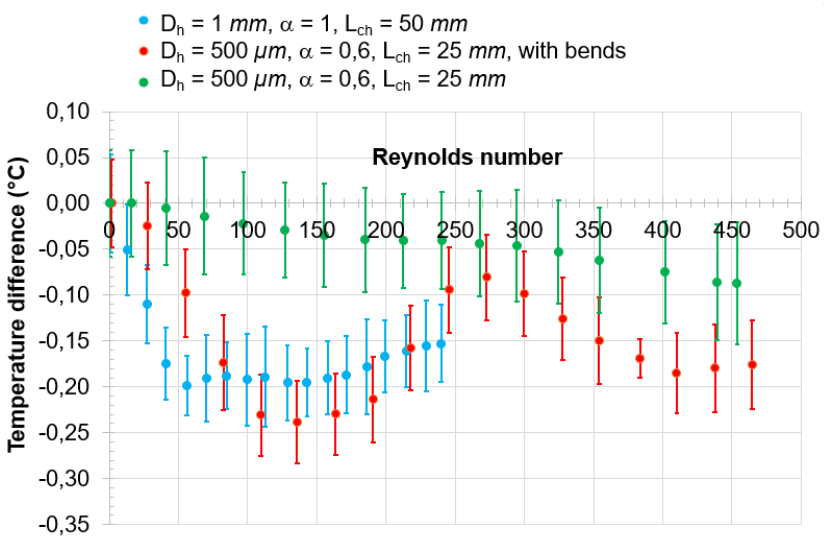

Figure IV.15: Temperature difference as a function of Reynolds number for each tested channel configuration in a steady flow.

As shown in figure IV.15, the channels affected by the inlet temperature variation mentioned above are the one with D_h = 1 mm, α = 1 and L_{ch} = 50 mm and the other with D_h = 500 μm, α = 0.6 and L_{ch} = 25 mm with bends. We can also observe that for both channels, the change in temperature variation occurs in almost the same Reynolds number range. This would suggest once again that this is related to viscous forces, however, this remains a supposition that cannot be confirmed with absolute confidence. The channel with D_h = 500 μm, α = 0.6, L_{ch} = 25 mm without bend seems not as much affected, the temperature difference between the inlet and outlet decreases as the flow rate increases. This could be mainly due to the contribution of fluid friction that increases the fluid temperature along the channel.

By comparing both channels with D_h = 500 μm, α = 0.6 and L_{ch} = 25 mm, we can deduce the influence of bends. The temperature difference is higher for the channel with bends. This is consistent with the expected behavior since the bends should increase the friction contribution and therefore increase much more the outlet fluid temperature

IV.2.4. Friction factor

Since the measurements we carried out include also the converging and diverging parts located at both ends of the test channel, to determine the friction factor, we had first to remove the contributions of these parts. To do so, we used their theoretical values, previously calculated, to estimate the experimental pressure drop through the channel. Given that our experimental pressure drop results were very close to those of the theory, the above approximation seemed relevant to us.

Furthermore, in the case of channels with bends, the contribution due to the bends was also removed from the measured pressure drop (in addition to the removed contribution from the converging and diverging sections). This makes it possible to compare the friction factor obtained for the two channels with the same hydraulic diameter D_h = 500 μm, aspect ratio α = 0.6, and channel length L_{ch} = 25 mm.

Figure IV.16 shows the variation of friction factor versus Reynolds number for two channels with a hydraulic diameter of 500 μm, aspect ratio α equals 0.6, and channel length L_h of 25 mm. The channel denoted C-500-25-0.59 has no bends, whereas the channel denoted C-500-25-0.56-B has four bends. For incompressible flow, the classical theoretical value for the friction factor is related to the Reynolds number by:

$$C_f = \frac{96 f(\alpha)}{Re} \tag{IV.38}$$

We recall that:

$$f(\alpha) = 1 - 1.3553\alpha + 1.9467\alpha^2 - 1.7012\alpha^3 + 0.9564\alpha^4 - 0.2537\alpha^5 \tag{IV.39}$$

Therefore, we have determined the correlation for the friction factor in the following form:

$$C_f = \frac{C}{Re} \tag{IV.40}$$

with C a constant determined by fitting the curves of friction factor versus the Reynolds number using a power trend curve, to match the "classical" theoretical correlation between friction factor and Reynolds number, which is commonly used in laminar flow.

From the experimental data, we obtained the following correlation for the friction factor as a function of the Reynolds number:

- Channel without bend: $C_f = \frac{86.54}{Re}$
- Channel with four bends: $C_f = \frac{87.63}{Re}$

The experimental correlations obtained are close, which was expected as the hydraulic diameter, aspect ratio, and channel length are the same for these two channels, and as we removed the contribution of all the minor losses. However, the experimental correlations of these two channels show a

large difference with the theoretical value of the friction factor in a rectangular channel with an aspect ratio of 0.6, $C_f = \frac{96f(\alpha)}{Re} = \frac{60.4}{Re}$.

This can be explained, as mentioned above, by the fact that these friction factors are only estimated (assuming theoretical values of pressure drop through converging and diverging sections are close to experimental values). These friction factor correlations are represented as function of Reynolds number in Fig. IV.16.

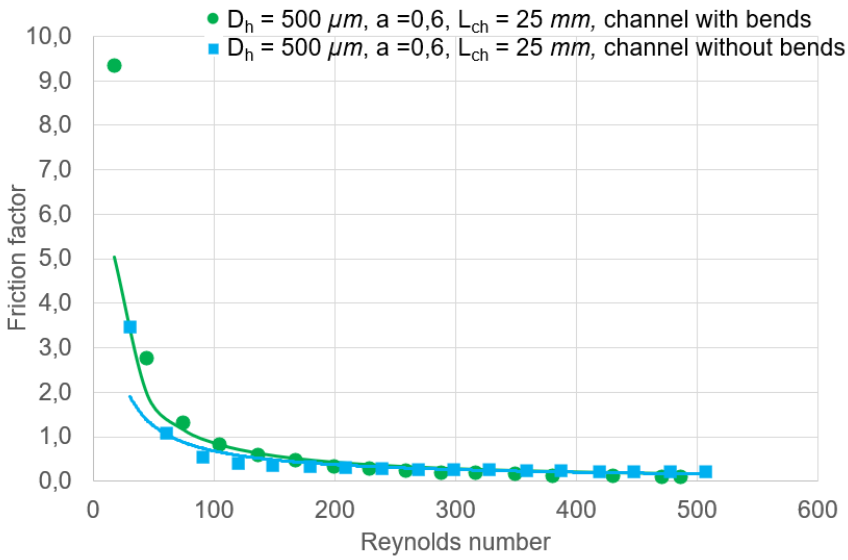

Figure IV.16: Comparison of experimental friction factor versus correlation of friction factor in the literature. Based on experimental results on channels with D_h= 500 μm, α =0.6 and L_h =25 mm

To conclude this section on steady flows, we carried out the characterization of channels with different geometries (hydraulic diameter, length, and bends). We found that the measured head losses were broadly in line with the values obtained from theory. By identifying the contribution of head losses generated by fluid friction (major head loss) and those generated by the presence of obstacles, i.e. converging and diverging sections, as well as bends for the channel that includes them (minor head loss), we were able to highlight the fact that minor head losses are increasingly significant as the mass flow rate increases.

Fluid temperatures follow a similar pattern to those observed in the literature in some studies concerning energy dissipation by viscous fluid friction, even if we were unable to explain certain trends with any certainty. Finally, a comparison of the friction factor with correlations from the literature for cases as close as possible to our experimental conditions and channel dimensions confirms that our values are close to the behavior observed in the literature.

This characterization of steady flows aimed to obtain reference values for flows documented in the literature, associated with our micro-devices. This will serve as a basis for alternating flows, which are much less well-studied at micro-scale. The good match between the literature and our steady-state experiments leads us to conclude that the results to be presented for alternating flows should only deviate from those for steady flows due to the difference in behavior of alternating flow due to its unsteadiness.

IV.3 Alternating gas flow

IV.3.1. Data post processing and general remarks

IV.3.1.1 Data post processing regarding alternating flows

To ensure comparability and consistency, measurements for alternating flows were made here with the same channels, converging/diverging sections, tube lengths, sensors, etc. as those used in the previous section. The basic distinction between steady and alternating flow is the variation over time of the parameters used to characterize the flow (P, T, U, ρ). Consequently, as mentioned in chapter I, it is necessary to use mean or maximum values of these quantities to characterize unsteady flow. As described in the data post-processing section, all our signals were temporally recalibrated as function of crank angle defined by:

$$\theta = 360\Big(f\big[t-t_0\big] - INT\Big(f\big[t-t_0\big]\Big)\Big) \tag{IV.41}$$

with θ the crank angle, f the signal frequency determined by the Fast Fourier Transform (FFT), t the time, t_0 the time at the beginning of the first period, and INT the floor function.

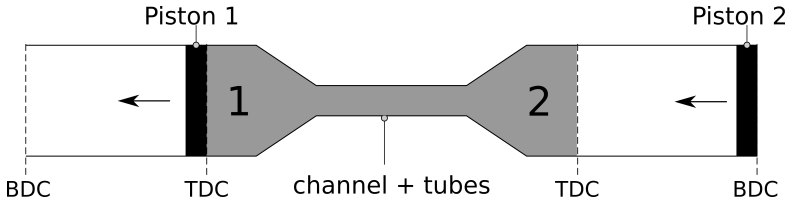

Figure IV.17: Schematic view of piston location side (1) and side (2) for a crank angle of 0 °. Piston (1) being at the TDC (Top Dead Center) while piston(2) is at the BDC (Bottom Dead Center)

A crank angle of zero corresponds to the piston (1) at top dead center (TDC) and the piston (2) at bottom dead center (BDC) (*cf.* figure IV.17). In order to simplify the experiments carried out on alternating flow, the pistons were only out of phase by 180° instead of the 120° which characterized the flow in the Stirling engine manufactured by Diallo [6].

The mean values of pressure drop and temperature difference being zero through a whole period, we will calculate the average of the absolute values of these quantities:

$$\bar{\Delta P} = \frac{1}{N}\sum_{i=1}^{i=N}|\Delta P_i|, \quad \bar{\Delta T} = \frac{1}{N}\sum_{i=1}^{i=N}|\Delta T_i| \tag{IV.42}$$

with N the number of measurement points over the period, while i and ΔP_i correspond respectively to the discrete values of crank angle and pressure drop over the period.

Then an average was calculated using previous values obtained for K periods (K is at least equal to or higher than 50). Thus, the average variation in pressure or temperature for each test was calculated as follows:

$$\bar{\Delta P}_a = \frac{1}{K}\sum_{j=1}^{j=K}\bar{\Delta P}_j, \quad \bar{\Delta T}_a = \frac{1}{K}\sum_{j=1}^{j=K}\bar{\Delta T}_j \tag{IV.43}$$

For instantaneous pressure and temperature values, once the signal had been recalibrated according to crank angle, a sliding average was applied. This section will present the filtered signals (temporally recalibrated according to the crank angle) then filtered with the sliding average.

IV.3.1.2 Variation of fluid density and viscosity

By contrast with steady flows, for which density variation could be neglected (relative variation < 2 % between minimum and maximum flow rate), in the case of alternating flows the effects of fluid compressibility are no longer insignificant, as shown in the figure IV.18. The viscosity and density of the fluid were calculated, at each instant using the pressure and temperature signals, which will be presented in the next section. We recall that the density was determined by the gas state equation (eq. I.4) whereas the viscosity was calculated using Sutherland's law (eq. I.9).

The relative variation in density is of the order of 13% for the channel with the largest hydraulic diameter (channel with D_h = 1 mm, α = 1, and L_{ch} = 50 mm) at a frequency of 3.8 Hz. These variations can reach 60 % for the channel with lower hydraulic diameter (channel with D_h = 500 μm, α = 0.6, L_{ch} = 25 mm) at a frequency of 12 Hz. As the signals between each end of the device are 180° out of phase, this generates a significant difference in fluid properties at a given time between each end of the channel.

The same applies to the viscosity of the fluid, which was nearly constant (relative variation < 0.2 %) in the case of steady flow. For alternating flows, this relative variation of viscosity remains not significant for the channels with the highest hydraulic diameter (D_h= 1 mm, α = 1, L_{ch} = 50 mm) with a relative variation of 0.9% at a frequency of 3.8 Hz. But this variation can reach 7 % for alternating flow, as can be seen in the case of the channel with lower hydraulic diameter (D_h = 500 μm, α = 0.6, L_{ch} = 25 mm) at a frequency of 11.9 Hz. As viscosity is related to the frictional characteristics of the flow, this variation can be important to take into account to correctly describe the behavior of these flows. Thus, in the remainder of this work, for alternating flows, fluid viscosity and density will be calculated for each experimental temperature and pressure value (*i.e.* at each crank angle), to enable the calculations in which these quantities are involved.

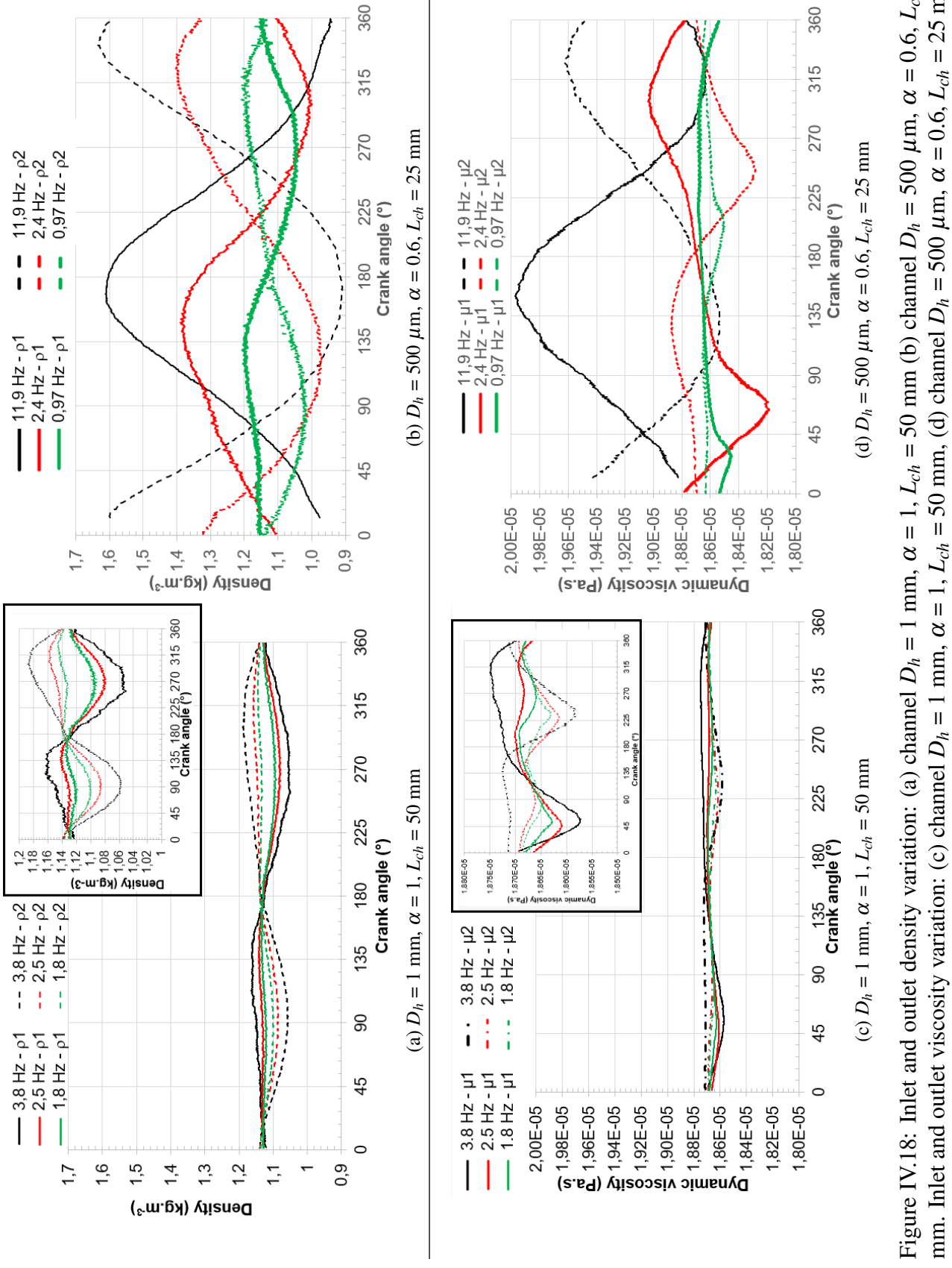

(a) $D_h = 1$ mm, $\alpha = 1$, $L_{ch} = 50$ mm

(b) $D_h = 500$ μm, $\alpha = 0.6$, $L_{ch} = 25$ mm

(c) $D_h = 1$ mm, $\alpha = 1$, $L_{ch} = 50$ mm

(d) $D_h = 500$ μm, $\alpha = 0.6$, $L_{ch} = 25$ mm

Figure IV.18: Inlet and outlet density variation: (a) channel $D_h = 1$ mm, $\alpha = 1$, $L_{ch} = 50$ mm (b) channel $D_h = 500$ μm, $\alpha = 0.6$, $L_{ch} = 25$ mm. Inlet and outlet viscosity variation: (c) channel $D_h = 1$ mm, $\alpha = 1$, $L_{ch} = 50$ mm, (d) channel $D_h = 500$ μm, $\alpha = 0.6$, $L_{ch} = 25$ mm

IV.3.2. Pressure and temperature signals

First, we checked the repeatability of our measurements and the temporal stability of our flow. Figure IV.19 represents the pressure measurements P_1 and P_2 for the same experimental test but over several periods which are superimposed in the same graphics. To obtain reliable mean values for our signals and to calculate both pressure and temperature differences between the two ends of the system, numerous periods were recorded. In addition, for each operating conditions, the experiment was repeated at least three times, with a potential slight variation in frequency between each run due to imperfect repeatability in terms of piston frequency.

Pressure and temperature measurements were recorded as a function of time. As previously presented, so that results can be compared, all measurements are presented as a function of the crank angle. In this way, all signals have been periodically recalculated on the crank angle which is link to the time basis of the signal corresponding to the position of the piston : signals (over at least 50 periods recorded) are shown with the light blue and red dots in figure IV.19. The dark blue and red points on the graph correspond to the sliding averages of the measurement points : it reduces the influence of noise or other external factors. The error bars take into account the accuracy of the sensors and the standard deviation of the measurements. This figure shows the repeatability, accuracy as well as the standard deviation of the measurements carried out for the alternating flows. Since numerous period were recorded and each test for a given operating condition was carried out at least three times, this should increase the reliability of the results presented.

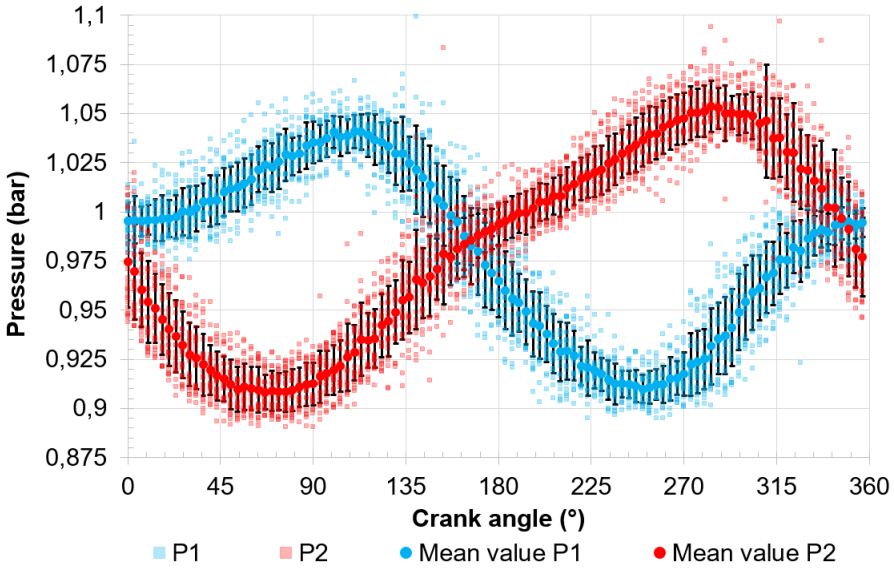

Figure IV.19: superimposition of the pressure measurements P_1 and P_2 for all periods measured

Table IV.5 gives the range of frequency tested for each channel configuration, with an increment of around 0.5 Hz between each frequency. Associated mean Reynolds and Mach number, are also given and calculated with mean values of velocity, density and viscosity over time. The mean velocity calculation have been detailed previously. We recall its expression here:

$$\bar{V} = 2\, f\, c_{piston}\, \pi\, r_{piston}^2$$

Bearing in mind that Reynolds and Mach numbers were rough approximation, we could nevertheless saw that the study range here is wider than in steady flow. Indeed, Mach number are almost 20 times higher than those observed in steady flow. Therefore, under the experimental conditions tested, the flow can no longer be considered incompressible (unlike in the case of steady flow). Regarding the range of Reynolds number estimated, we can observe that transition from laminar to turbulent flow can occur at several of the highest frequencies.

Table IV.5: Range of frequency and Womersley number tested for each channel configuration along with estimation of both Reynolds and Mach number.

Channel configuration	D_h = 200 μm α = 0.1 L_{ch} = 25 mm	D_h = 200 μm α = 0.3 L_{ch} = 25 mm	D_h = 500 μm α = 0.6 L_{ch} = 25 mm channel with bends	D_h = 500 μm α = 0.6 L_{ch} = 25 mm	D_h = 1 mm α = 1 L_{ch} = 25 mm	D_h = 1 mm α = 1 L_{ch} = 50 mm
f_{min}	0.69	0.31	1.24	0.67	0.28	0.54
f_{max}	9.74	11.44	12.20	14.12	15.76	13.52
Wo	0.02 - 0.09	0.02 - 0.11	0.07 - 0.3	0.08 - 0.28	0.13 - 0.67	0.13 - 0.31
mean Re range	100 - 1400	200 - 3450	175 - 1800	100 - 2100	20 - 1200	40 - 1050
mean Ma range	0.02 - 0.34	0.05 - 0.76	0.02 - 0.16	0.009 - 0.2	0.001 - 0.06	0.002 - 0.05

IV.3.2.1 Obtained results

Figures IV.20 to IV.24 show the variations of both pressure and temperature (except for figure IV.23, for which one temperature sensor was broken) at both ends of the experimental system during a period of the signal for different frequencies for some of the tested micro channels. Note that in these figures, we have not shown all the frequencies tested in order to maintain clarity.

We can notice that the pressure as well as temperature signals on side 1 are out of phase with the signals on side 2 by an angle of about 180°. This corresponds to the phase shift imposed between the two pistons located on each end of the channel, which are out of phase with each other by the same angle of 180°. We can also observe an increase in the amplitude of pressure signals as frequency increases. This is consistent with the fact that as the frequency increases, so does the variation of the associated velocity of the fluid within the channel. Thus the fluid frictions should increase and so should the pressure amplitude (variation of pressure). The same observation can be made with temperature variation, which is related to the viscous friction and the pressure variations.

Other things can be seen on these curves: for certain diameters and certain frequencies, a double frequency can be observed. This is the case, for example, in Figure IV.24 for the channel of D_h = 1 mm, at a frequency of 0.68 Hz. Furthermore, when comparing these curves, we note a shift in the extrema as a function of frequency. These two remarks are the subject of the next two sections.

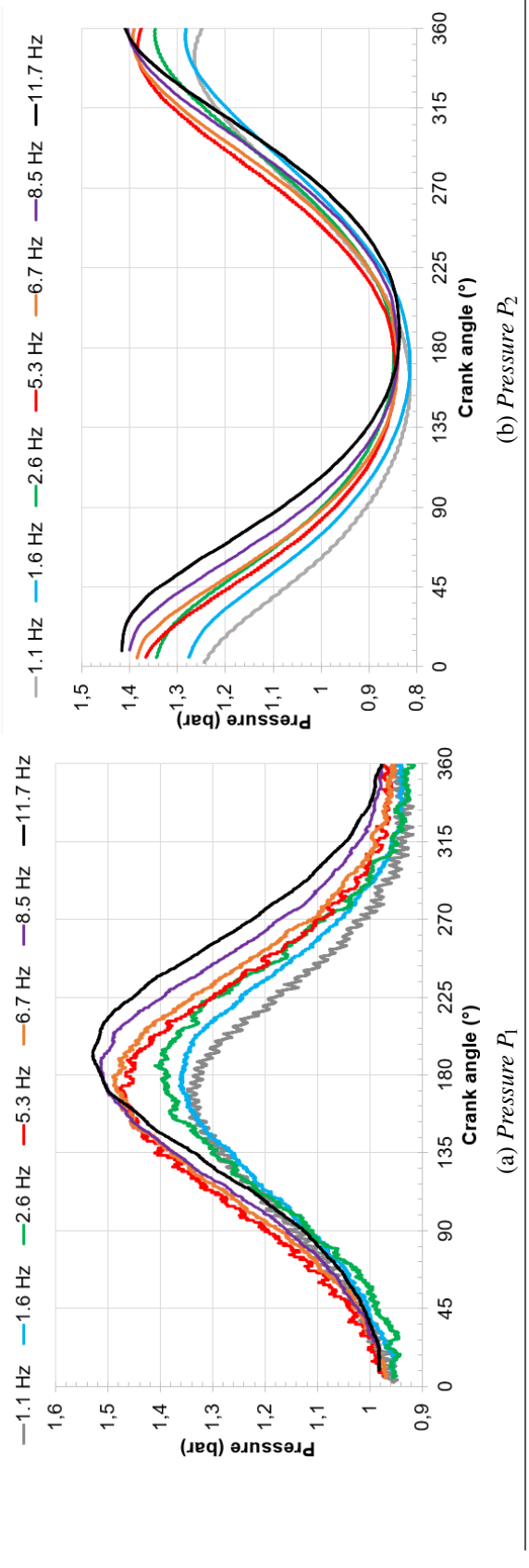

(a) *Pressure* P_1 (b) *Pressure* P_2 (c) *Temperature* T_1 (d) *Temperature* T_2

Figure IV.20: Measurements along a period for different frequencies for the channel with $D_h = 200\ \mu$m, $\alpha = 0.3$ and length of 25 mm. (a) Pressure P_1, (b) Pressure P_2, (c) Temperature T_1, (d) Temperature T_2

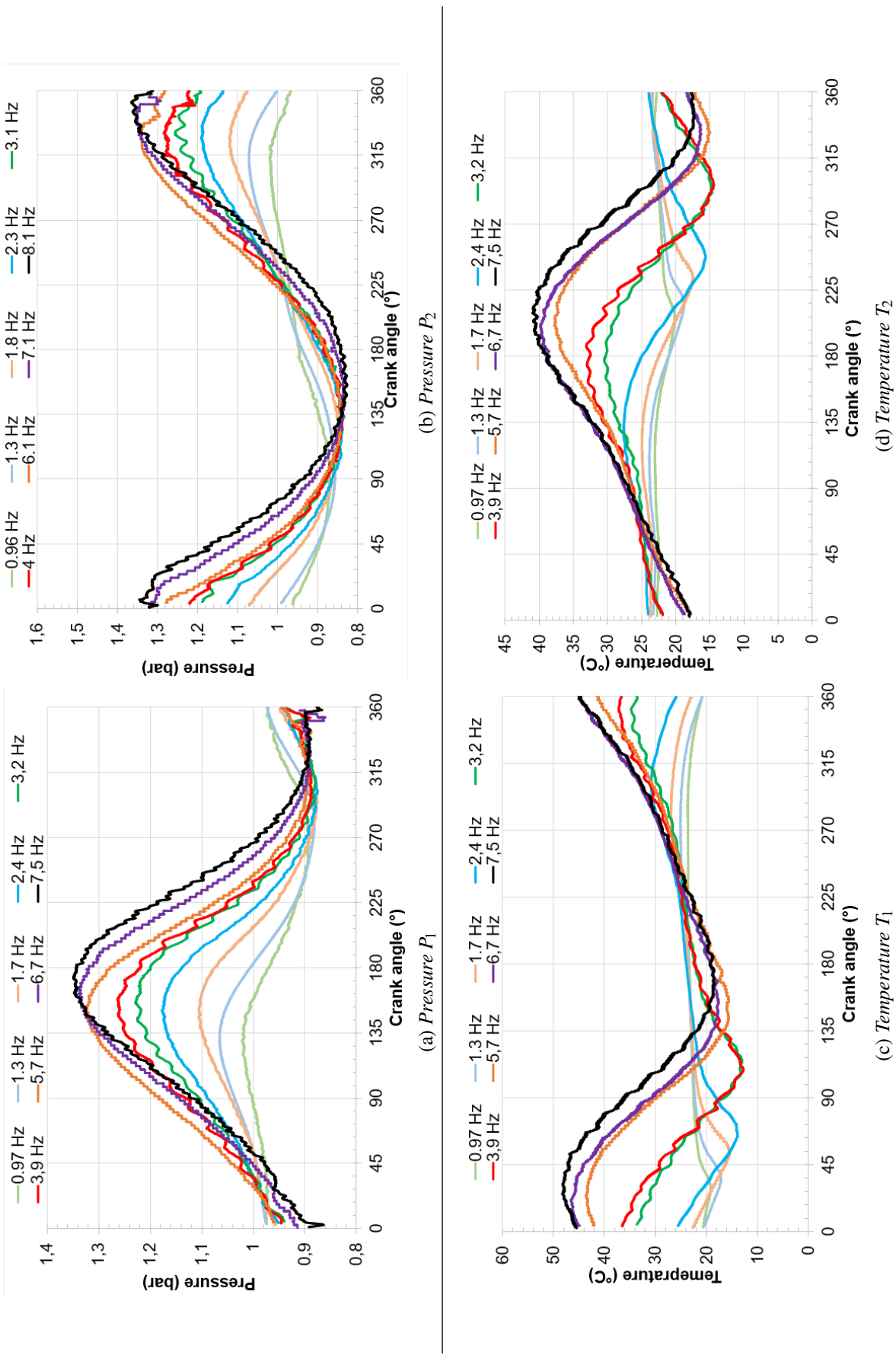

(a) *Pressure* P_1 (b) *Pressure* P_2

(c) *Temperature* T_1 (d) *Temperature* T_2

Figure IV.21: Measurements along a period for different frequencies for the channel with $D_h = 500\ \mu$m, $\alpha = 0.6$, and length of 25 mm. (a) Pressure P_1, (b) Pressure P_2, (c) Temperature T_1, (d) Temperature T_2

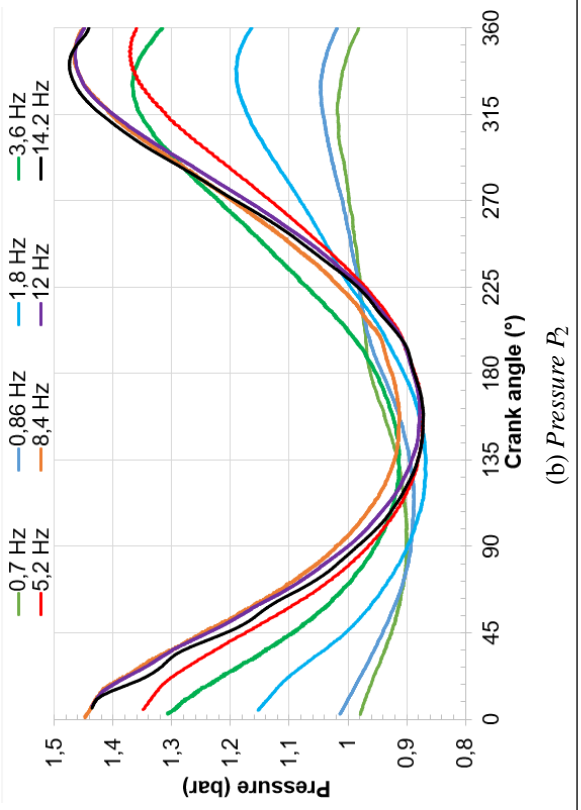

(a) *Pressure* P_1

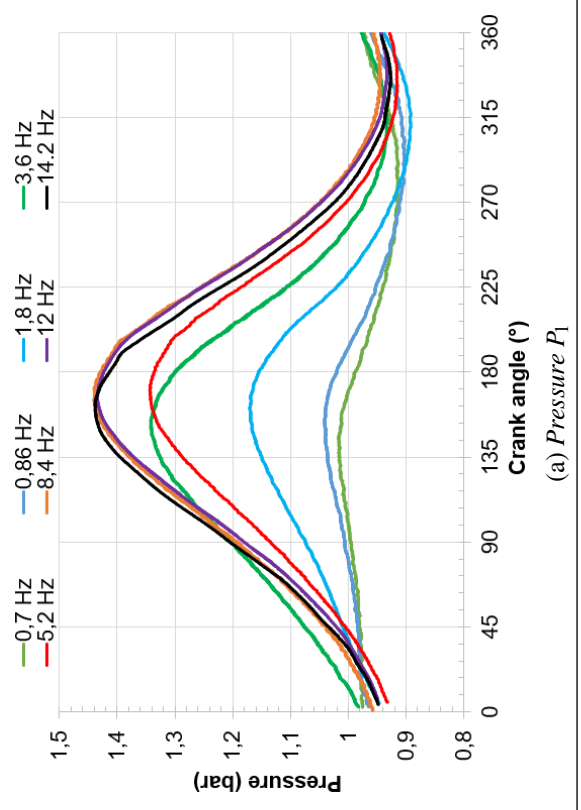

(b) *Pressure* P_2

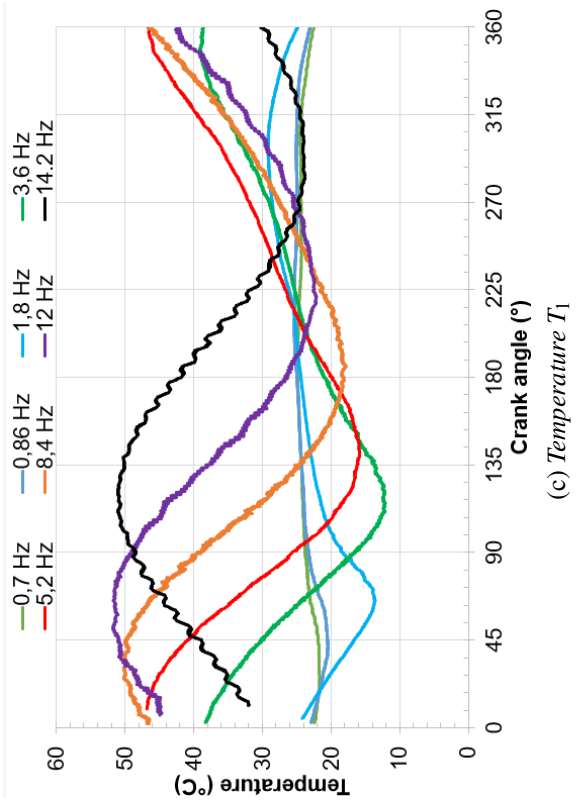

(c) *Temperature* T_1

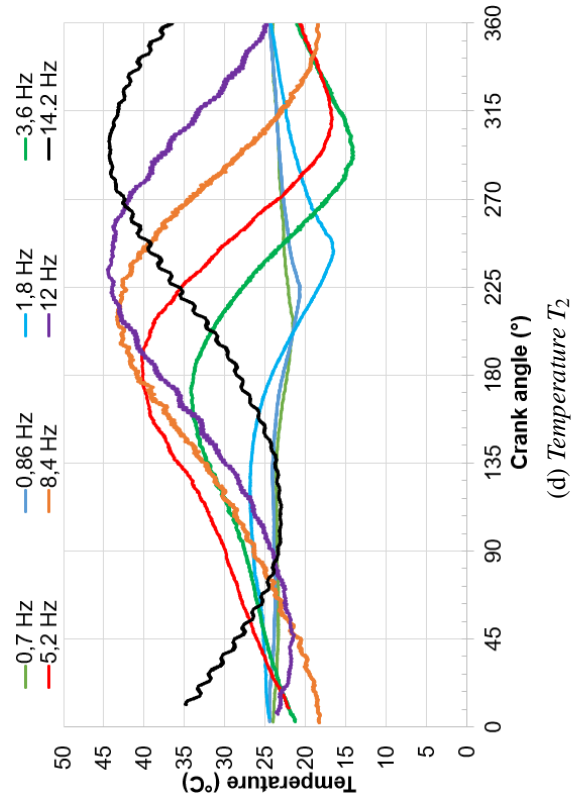

(d) *Temperature* T_2

Figure IV.22: Measurements along a period for different frequencies for the channel with four bends $D_h = 500\ \mu m$, $\alpha = 0.6$, length of 25 mm. (a) Pressure P_1, (b) Pressure P_2, (c) Temperature T_1, (d) Temperature T_2

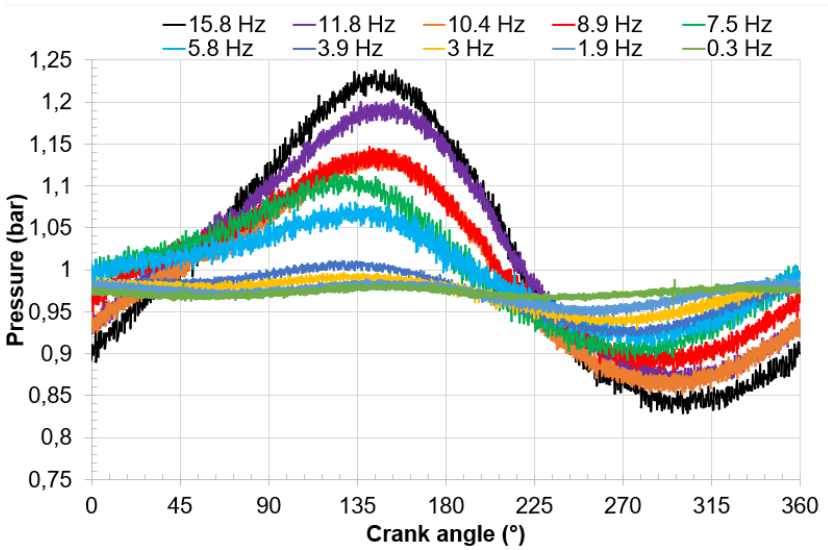

(a) *Pressure* P_1

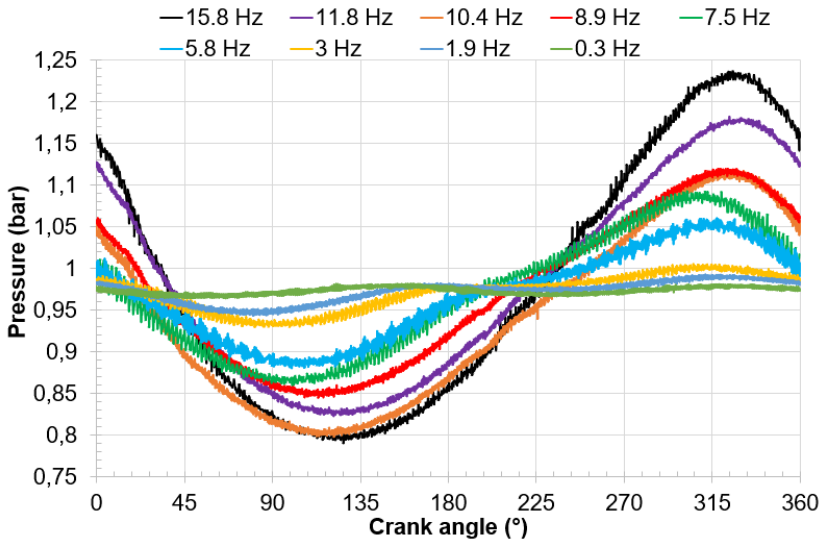

(b) *Pressure* P_2

Figure IV.23: Measurements along a period for different frequencies for the channel D_h = 1 mm, α = 1, L_{ch} = 25 mm. (a) Pressure P_1, (b) Pressure P_2

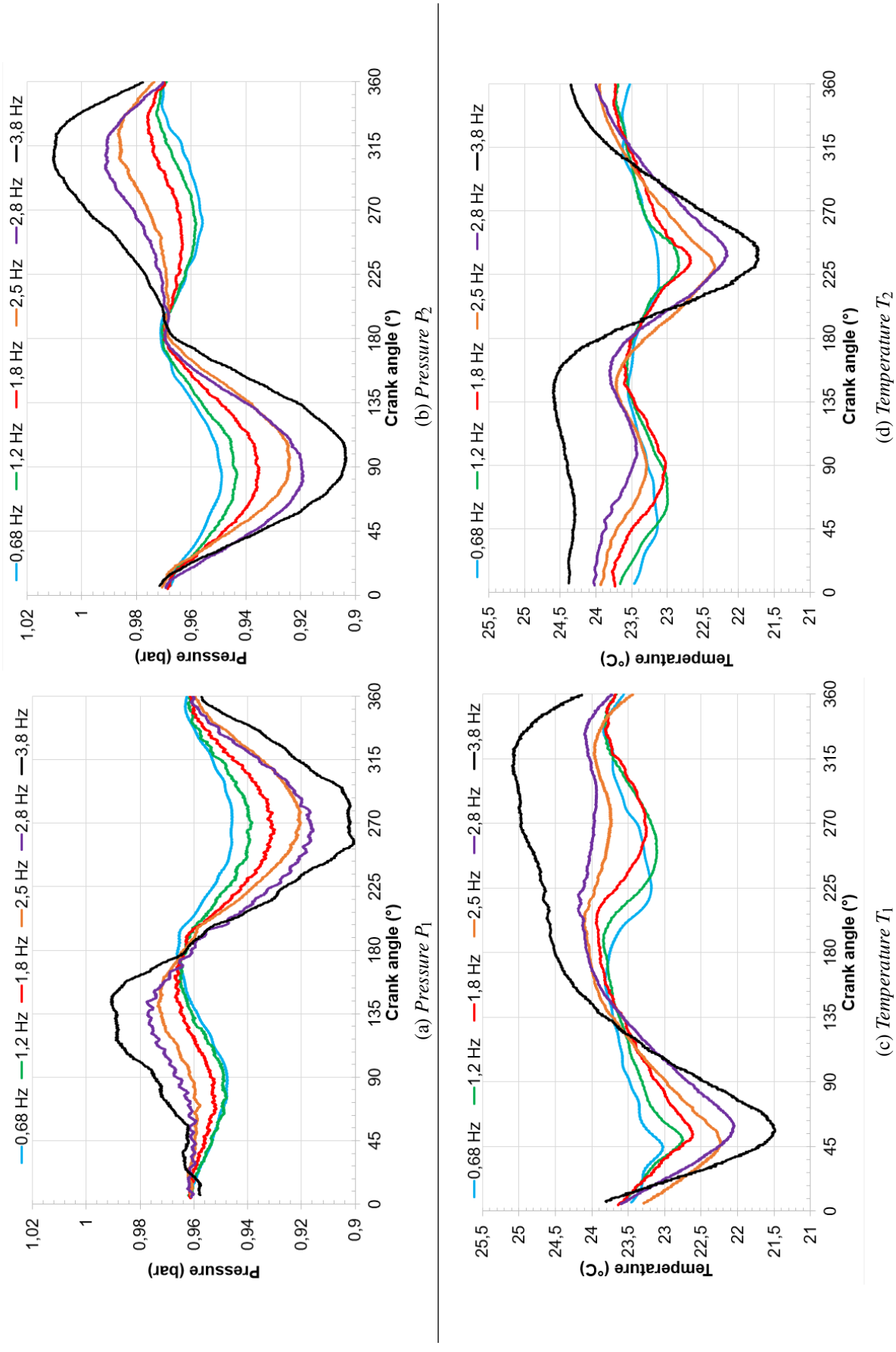

Figure IV.24: Measurements along a period for different frequencies for the channel $D_h = 1000\mu$m, $\alpha = 1$, $L_{ch} = 50$ mm. (a) Pressure P_1, (b) Pressure P_2, (c) Temperature T_1, (d) Temperature T_2

IV.3.2.2 Observations and discussions

i) Double frequency at low frequency (low Womersley number)

For the channels with the highest hydraulic diameter, *i.e.* D_h = 1 mm and at low frequencies f $\leq$ 3 Hz, as shown in figure IV.26 (a), both pressure and temperature signals exhibit two troughs in the same period, instead of just one expected. Figure IV.26 (b) shows the pressure and temperature signals at slightly higher frequencies for which we can observe that the phenomenon starts to be attenuated. At higher frequencies (figure IV.26 (c)), the phenomenon disappears leaving a signal with only one trough. These two troughs observed at low frequencies are not identical in terms of amplitude.

This phenomenon was observed by Ibrahim *et al.* [175]. The authors attributed it to the movements of the pistons, which are not perfectly sinusoidal. They explained that in the case of pistons 180° out of phase, a small change in phase shift can generate this asymmetry. Dellali [5] also studied alternating flow in porous channels as well as in empty tubes. The author highlighted the same phenomenon (figure IV.26 (d)), attributing this "double period", considering incompressible flow, by the preponderance of inertial effects over viscous effects. The authors observed the same trend for gas flow in empty channels while observing, for gas flow inside porous channels, the same trend as for moderate frequencies in our cases. Since for the same frequency, the flow velocity will be higher in the porous channel than in the empty channel with the cross-section lower, this is consistent with the observations made in our channels with the phenomenon disappearing as the frequency, *i.e.* the flow velocity, increases.

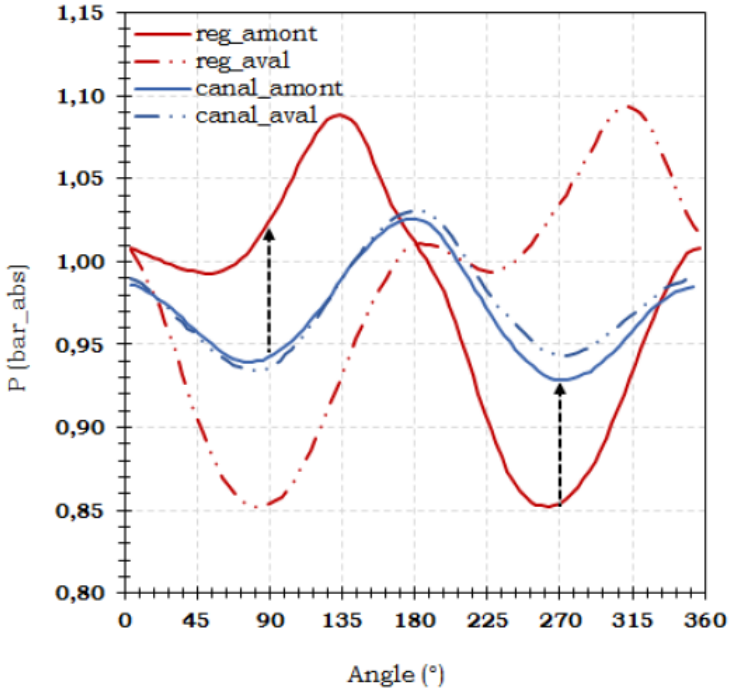

Figure IV.25: Measurements observed in empty and porous channels (from Dellali [5])

ii) Phase lag of pressure and temperature signals

As the frequency increases, we can also observe a phase lag that increases for both pressure and temperature. Figure IV.27 shows the variation of the phase angle θ at which the maximum of both

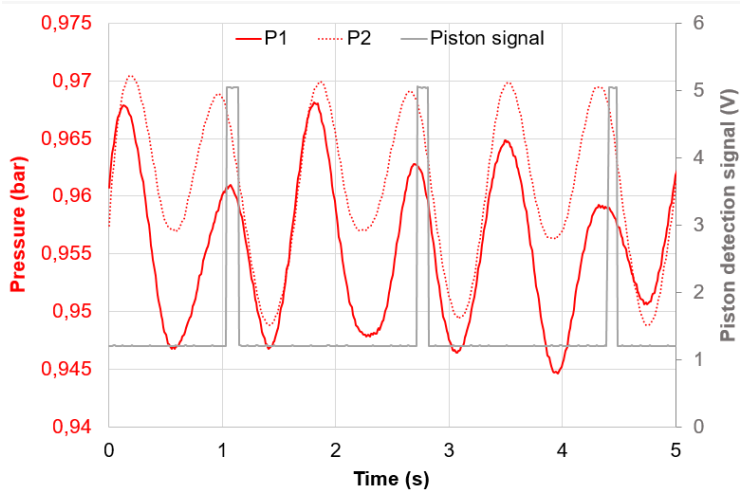

(a)

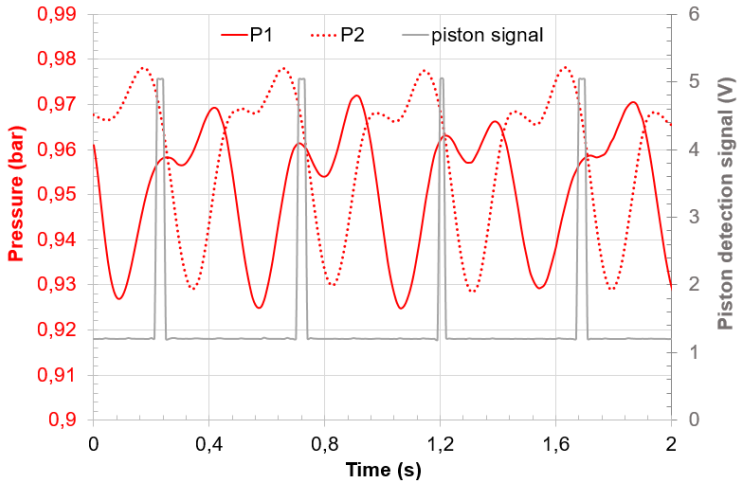

(b)

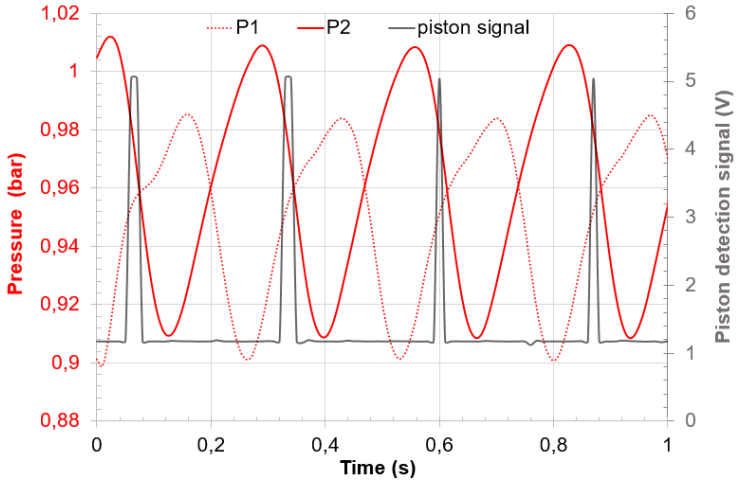

(c)

Figure IV.26: Pressure measurement for alternating gas flow in the channels with a hydraulic diameter of 1 mm and length of 50 mm at (a) 0.68 Hz, (b) 2.1Hz, (c) 3.8 Hz

pressure and temperature signals are obtained. The calculation of phase lag $\Delta\theta$ between pressure and temperature signals represented in figure IV.27 is shown in figure IV.28. It corresponds to the difference between the phase of temperature maximum signal with the one for pressure signal. As no difference was observed between signal obtained on side 1 with the signals measured on side 2, we chose to represent only the phase of pressure and temperature on side 1.

We recall that for a crank angle of 0°, the piston 1 was at its top dead center. Therefore, the phase angle of the maximum of the signals should also correspond to the phase lag between pressure and piston displacement (volume of fluid displaced) as well as temperature and piston displacement. However, if we wanted to represent the phase lag between pressure (or temperature) signal and piston displacement, we would need to correct the values as phase lag cannot be higher than 360 °. Assuming that the phase shift between piston displacement and fluid velocity is not significant, this observed increase in phase shift is consistent with Womersley's observation. In his study, focused on flow in arteries, Womersley made several assumptions or simplifications such as the artery being considered as a rigid tube (arterial expansion neglected), the pressure gradient being assumed to be a function of time only. Moreover, it is important to note that his pressure determination was also not made at the same time as velocity determinations. From his study, he noted that the phase shift between pressure and flowrate increased as the Womersley number increased [75].

We can also observe in figure IV.27, that the phase of temperature signals increases much more than that of pressure signals. As this was discussed, one possible explanation would be that, in our case, compressibility effects occur. Indeed, the compressibility of the gas results also in significant variation of fluid density. A difference can also be seen for channels as a function of hydraulic diameter, this could be due to the higher influence of the fluid compressibility with lower hydraulic diameter.

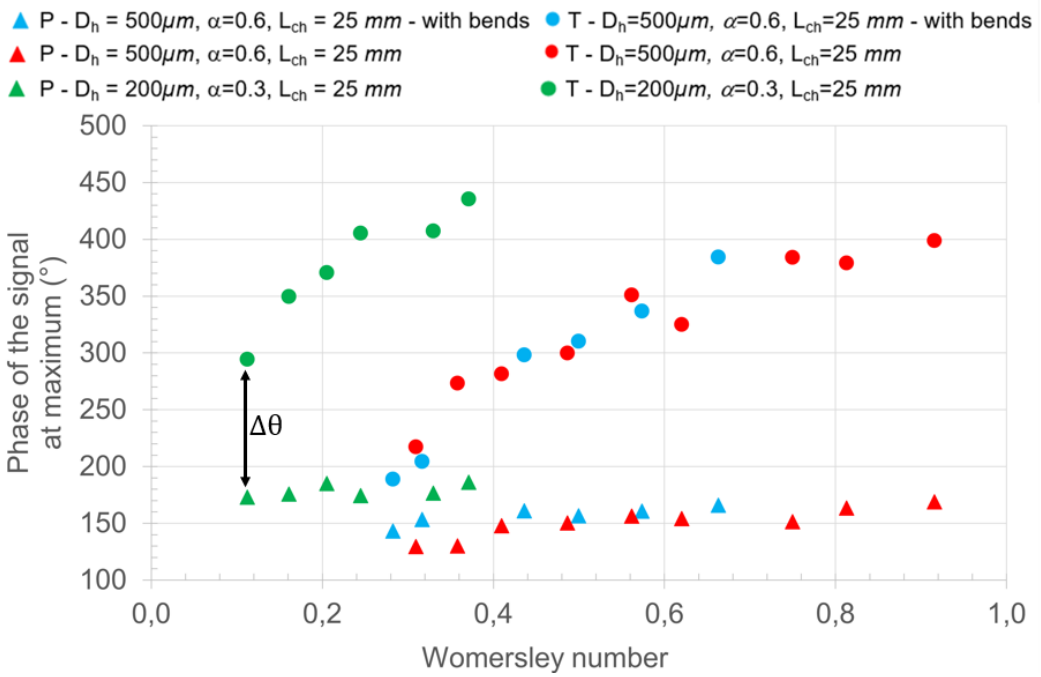

Figure IV.27: Phase angle for a maximum of both pressure and temperature signal as a function of Womersley number

Figure IV.28 shows the phase lag between pressure and temperature as a function of Womersley number. We can observe that for the channel with a hydraulic diameter of 500 μm at a low Womersley number, the phase lag between pressure and temperature does not increase considerably. However, as the Womersley number increases, the phase lag between pressure and temperature increases sharply.

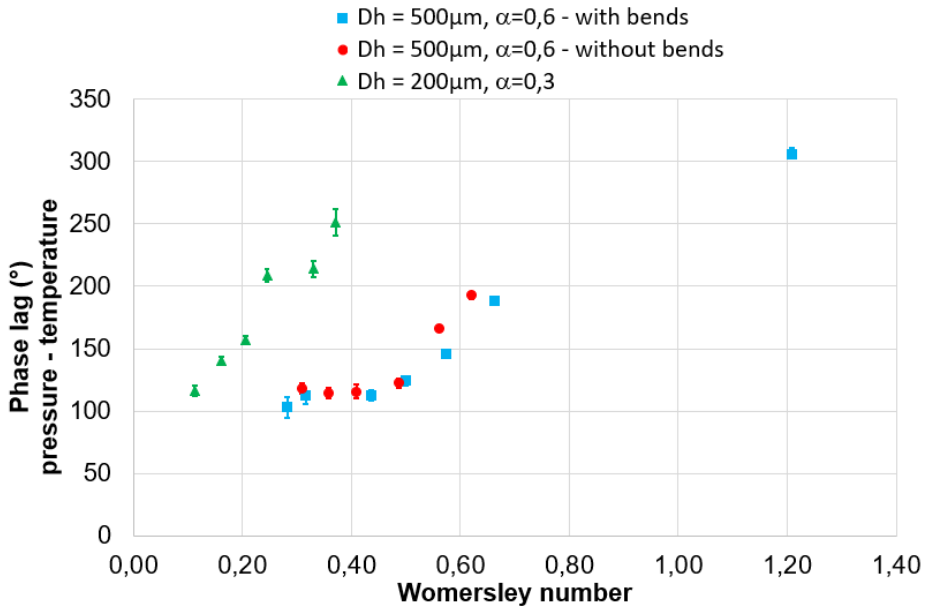

Figure IV.28: Phase lag between pressure and temperature versus Womersley number

IV.3.3. pressure difference

IV.3.3.1 Simplified analytical model of the experimental setup

A simplified analytical model of the experimental setup was established, assuming the gas to be ideal, to analyze the trends exhibited on the results obtained experimentally. Details on this model are presented in appendix A.

This model consists in calculating the pressure difference $\Delta P(t)$ by representing :

1. The relations between pressure and volume - under the action of the piston - on each side of the micro-channel, by using the ideal gas law.

2. The gas flow inside the microchannel by using the model proposed by Womersley [75] who considered sinusoidal variations of the pressure gradient generating this micro-flow.

It should be reminded that this model is based on several assumptions that may restrict its validity in some experimental situations:

1. Compressibilty of the fluid, which was exhibited for alternating gas flow, was neglected in the model.

2. The temperature difference on each side of the micro-channel is supposed to be low enough to be neglected in a first approximation - which may be rather true.

3. The microchannel cross-section is not rectangular but circular, to be in line with Womersley's paper - which may not change too much the results for equivalent hydraulic diameters.
4. Another key assumption is that the converging and diverging sections that enable a matching of cross-sections between the piston and the micro-channel are not taken in account at all.

As was already noticed in the analysis of steady-state flows, the contribution of converging and diverging sections may be significant compared to the contribution of the microchannel. Therefore the last assumption may restrict significantly the precision of the model.

Nevertheless, the general behavior of the pressure drop and flow measurements versus oscillation frequency or channel diameter is quite correctly described in several cases as can be seen in figures 2 and 3 in appendix A:

- the time variation of the pressure drop is well represented, especially the phase lag between this pressure drop and the volume oscillation versus frequency is quite close to the observations.
- the amplitude of pressure drop versus frequency and channel radius has a similar shape as the experimental one : for a given channel radius, it starts (as expected) from zero and grows strongly with frequency, before stabilizing to a limit value, whereas the experimental results often show a larger pressure drop and a slow growth instead of a clear stabilization with increasing frequency.

On the other hand, this simplified model is not able to represent :

- the measured temperature variations - which is expected because they have been neglected from the beginning.
- the frequency doubling observed at low Womersley numbers - which may be more related to the presence of converging and diverging sections than to the properties of the microchannel.

Even though, this model does not describes correctly the detailed behaviour of the observed alternating flow, it can still provide general trends and rough estimations that can serve as references for the experimental results.

IV.3.3.2 Analysis of results

In this section, we no longer consider the signals on either side of the channel, but the pressure drop. Figures IV.29 and IV.30 show the pressure drop for each channel configuration for different frequencies. We can first observe that the pressure drop increases as the frequency increases, this is consistent since for steady flow the pressure drop is related to the square of the velocity. Therefore, since the fluid velocity increases with the increasing frequency, the pressure drop increases as well. This is due to the friction contribution which increases as the fluid velocity increases. Indeed, at higher frequencies, when the gas is compressed, respectively expanded, the fluid viscosity and friction increases, respectively decreases.

Secondly, we can also notice a phase lag that increases as the frequency increases. This is due to the increase in the phase lag observed for both pressure P_1 and P_2. Since the phase lag between pressures P_1 and P_2 remains almost the same at a value around 180 °, the phase lag observed in the pressure drop is related to the phase lag that we observed for pressure P_1 and P_2.

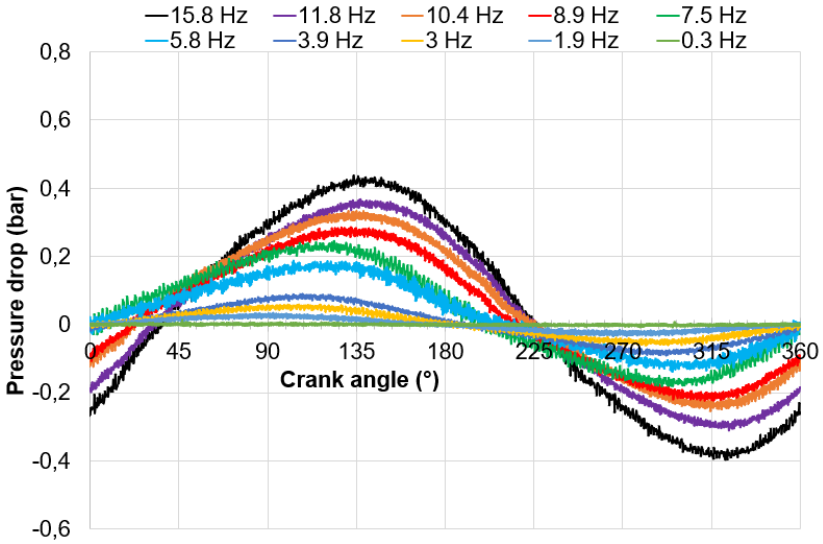

(a)

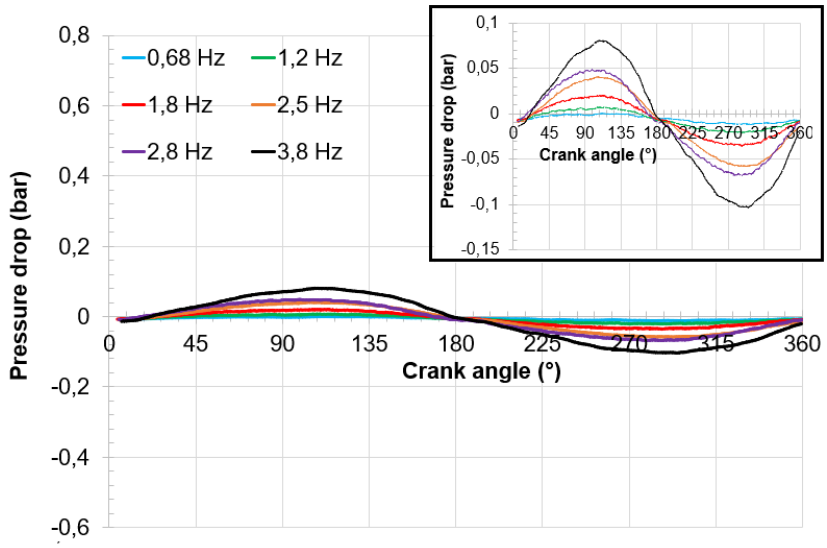

(b)

Figure IV.29: Pressure drop along a period for different frequencies in the channels D_h = 1 mm, α = 1, (a) L_{ch} = 25 mm, (b) L_{ch} = 50 mm

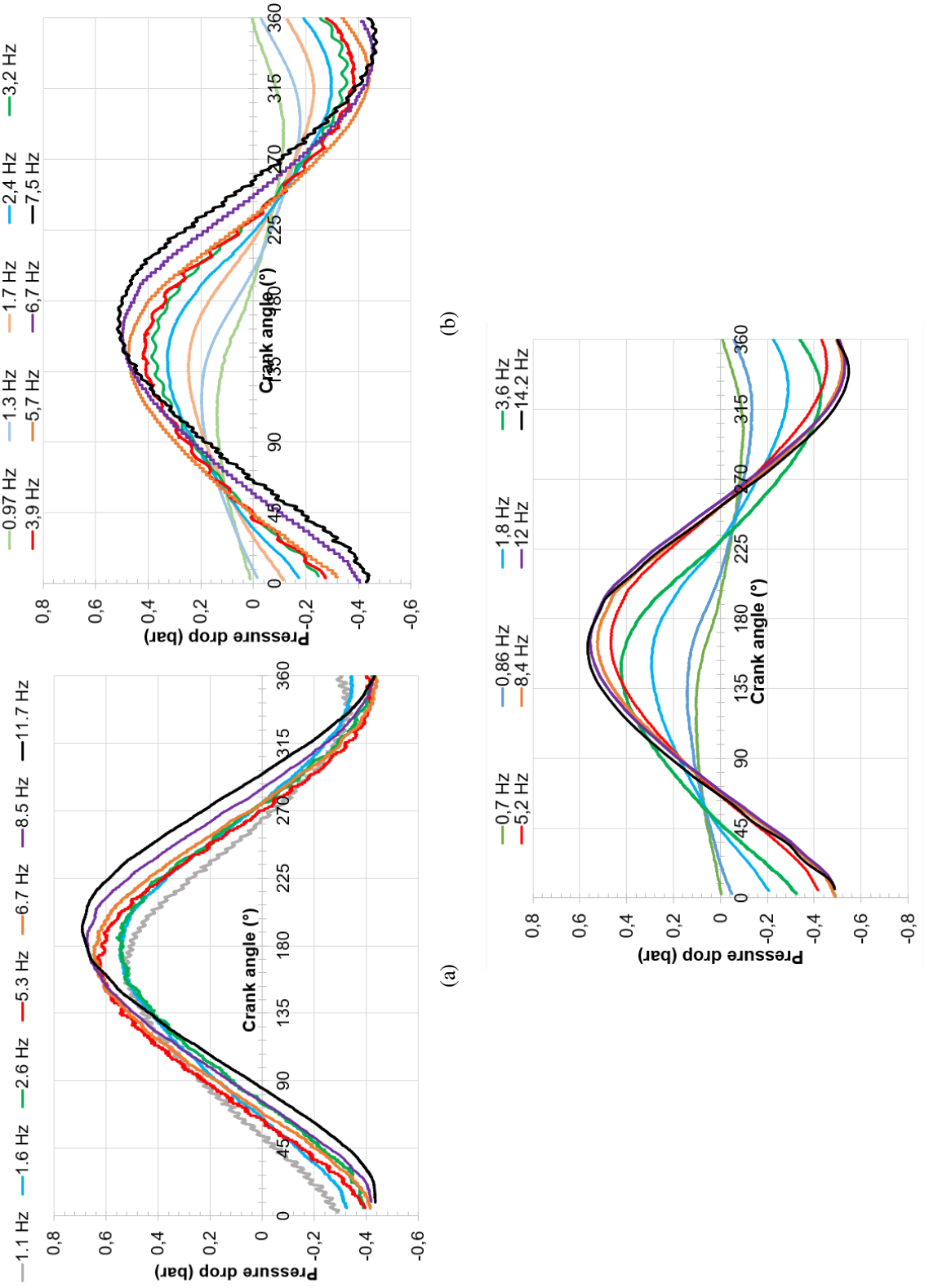

Figure IV.30: Pressure drop along a period for different frequencies (a) channel $D_h = 200\mu$m, $\alpha = 0.3$ and length of 25 mm, (b) channel $D_h = 500\ \mu$m, $\alpha = 0.6$, $Lch = 25$ mm without bends, (d) channel $D_h = 500\ \mu$m, $\alpha = 0.6$, $Lch = 25$ mm with four bends.

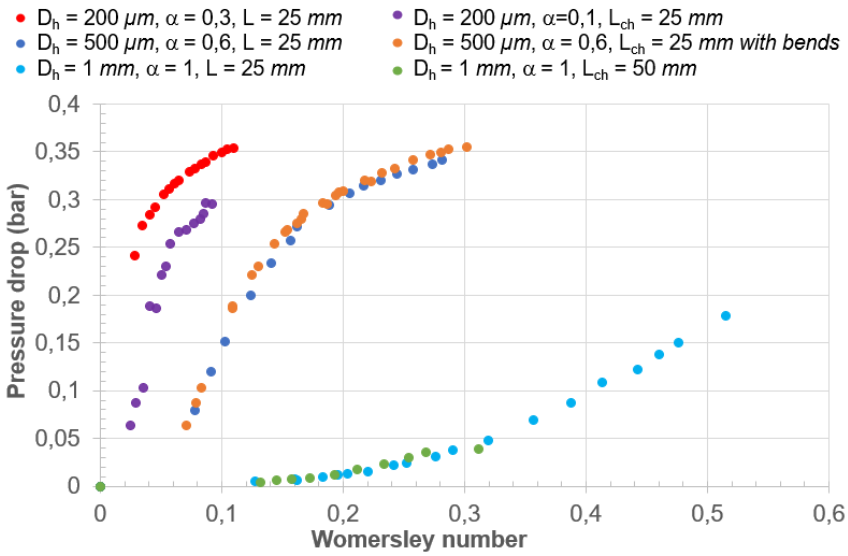

Figure IV.31: Pressure drop versus Womersley number for all channel configurations

Figure IV.31 shows pressure difference for all channel configurations versus Womersley number. Difference are clearly observed between the channels with hydraulic diameter of 1 mm and the other channels. Since change in hydraulic diameter was related to a change in aspect ratio for the channels tested, we cannot conclude with absolute confidence the contribution of hydraulic diameter or aspect ratio alone on pressure difference obtained. However, pressure difference should be inversely proportional to hydraulic diameter, which is consistent with what we observe on this figure. The influence of the other parameters (aspect ratio, bends and channel length) will be compared further.

As can be seen from the figure IV.31, pressure difference increased sharply at low Womersley numbers (*i.e.* low frequencies) while increasing in a lesser extent for higher Womersley numbers. Presumably, if measurements were taken at higher Womersley numbers (*i.e.* frequencies), it might be possible to observe that pressure difference reached a maximum value (as observed analytically in appendix A). This phenomenon could be due to a plugging effect, flow rate being not enough anymore to allow the flow to cross the channel within a period. Experimentally, a fairly clear similar trend was observed for channels with hydraulic diameters of 200 and 500μm, since the curves show a lower rate of increase in pressure difference: extrapolating the curves, they seem to tend towards a plateau, which is in agreement with what the simplified analytical model predicts. On the other hand, no such observations were made for the two channels with a hydraulic diameter of 1*mm*, which could highlight the influence of hydraulic diameter (as well as aspect ratio, since these two parameters are correlated with the channel tested).

IV.3.4. Temperature difference

Figures IV.32 to IV.34 show the temperature difference measured for each channel configuration for different frequencies, except channel with D_h = 1 mm, L_{ch} = 25 mm and channel with D_h = 200 μm, α = 0.1 for which technical issues occured.

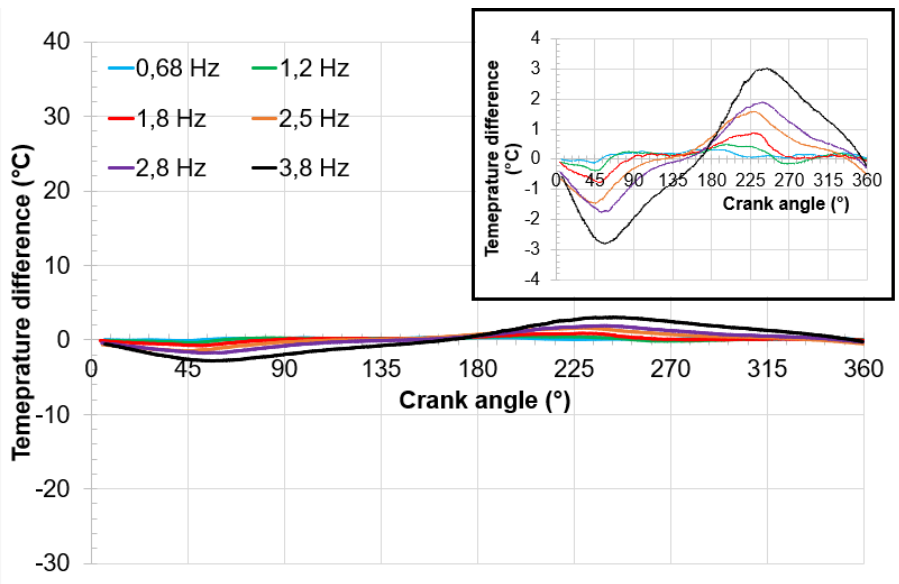

Figure IV.32: Temperature difference along a period for different frequencies in the channel D_h = 1 mm, α = 1, L_{ch} = 50 mm.

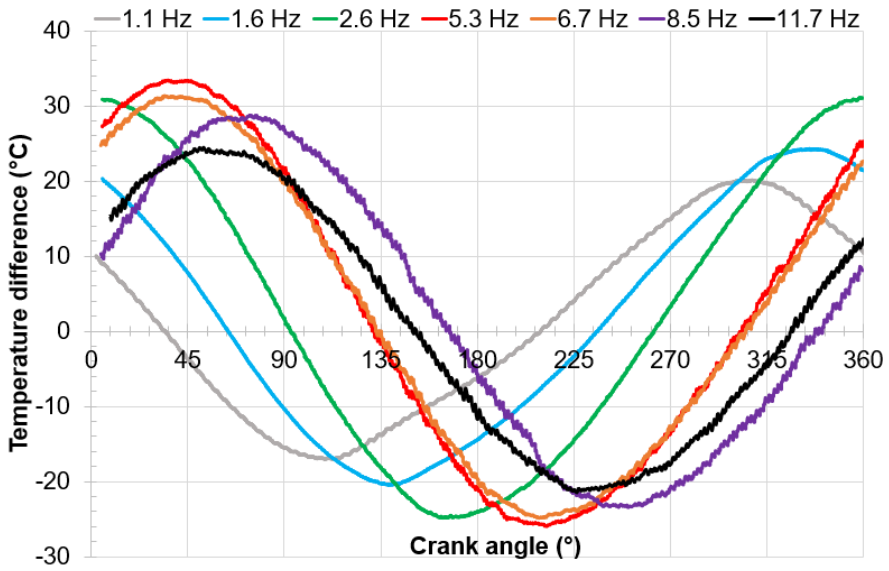

Figure IV.33: Temperature difference along a period for different frequencies in the channel D_h = 200 μm, α = 0.3, L_{ch} = 25 mm.

We can observe the same trend as observed for the pressure drop. Both the amplitude of the temperature difference and phase lag increased as the frequency increased. This is consistent with the fact that, as fluid velocity increases, more energy was dissipated by viscous friction, increasing the temperature. The phase lag between temperature T_1 and T_2 contributed to the temperature being increased at one end of the channel while being at its minimum at the other channel end, which results in the higher temperature difference observed.

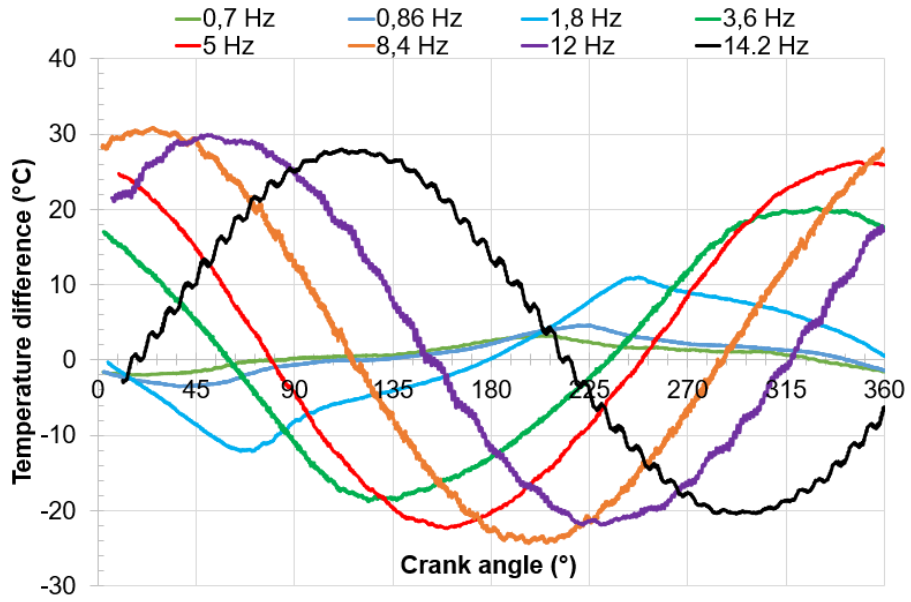

(a)

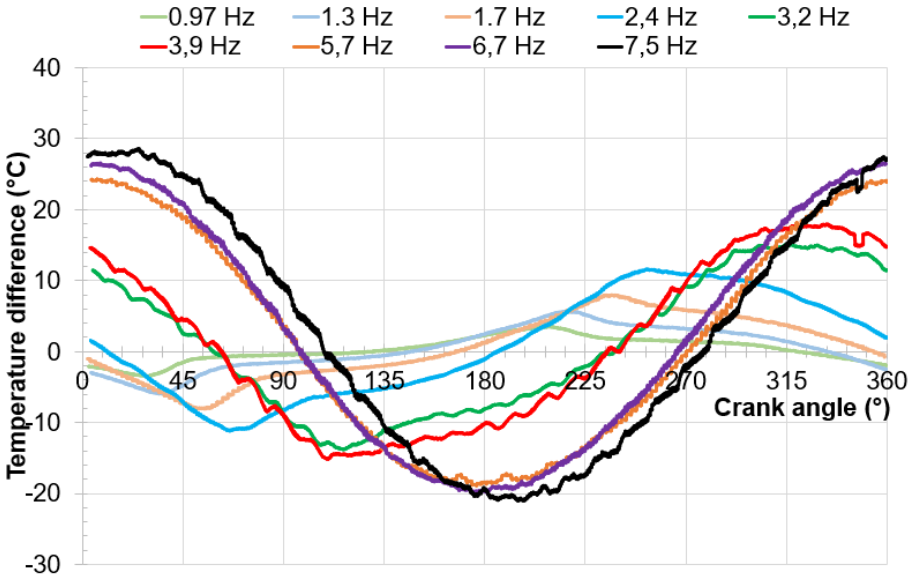

(b)

Figure IV.34: Temperature difference along a period for different frequencies (a) channel D_h = 500 μm, α = 0.6, L_{ch} = 25 mm without bends (b) channel D_h = 500 μm, α = 0.6, L_{ch} = 25 mm with four bends

Figure IV.35 shows the variation of the temperature difference ΔT as a function of the Womersley number. Similar to the observation for the pressure drop versus Womersley number, we can observe difference of thermal behavior between each different hydraulic diameter. For the channels with the highest hydraulic diameter, the temperature difference increases gradually as a function of the Womersley number, whereas it is not the case for the smaller hydraulic diameters. We can indeed observe that, for channels with smaller hydraulic diameters, temperature differencesΔT follow the same trend as that observed for pressure difference: they tend to reach a maximum value. Even in

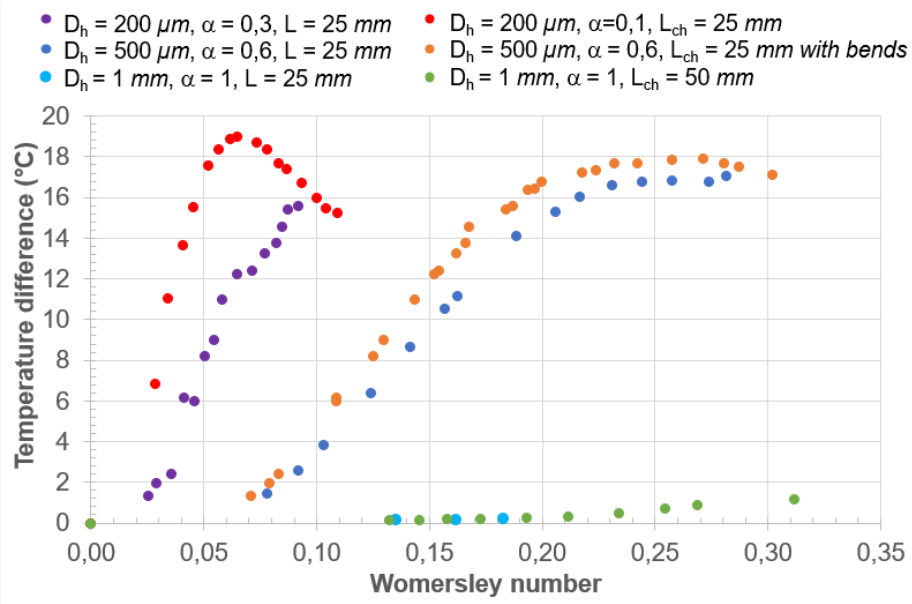

Figure IV.35: Temperature difference versus Womersley number

the case of the smallest channel (200 μm), we can see a further step in the decrease of the ΔT as the Womersley number (*i.e.* frequency) increases.

This behavior could be attributed to competition between two effects. Initially, frictional heating effects dominate, resulting in an increase in ΔT with frequency. Then, above a certain frequency, for hydraulic diameters of 200 and 500 μm, we see a change in curvature, followed by a decrease in ΔT for D_h = 200 μm. If we compare this curve with the pressure drop curve on figure IV.31, we see that the changes in curvature occur for the same Womersley values. While pressure difference increase less steeply and tend to reach a plateau, as frequency increases, flow velocity should theoretically increase further and, consequently, heat exchange with the wall should be higher. This would lead to greater heat dissipation to the environment, resulting in a decrease in the observed temperature difference. It should be noted that here too (as was observed for pressure difference), the above observations do not occur for channels with a hydraulic diameter equal to 1 mm, which could confirm the non-negligible influence of hydraulic diameter coupled (in our work) with aspect ratio.

IV.3.5. Comparison between steady and alternating flows

Both mean pressure difference and temperature difference seemed significantly higher than those observed in the case of steady flow. To make a comparison between steady and alternating flow, an estimation of mean flow rate $\bar{\dot{V}}_{osc}$ was made for alternating flow. For a given flow rate $\bar{\dot{V}}_{osc}$ close to a flow rate tested in steady flow $\dot{V}_{std}$, we can compare values of both pressure difference and temperature difference. Assuming that at low frequencies, the fluid flow behavior is close to an incompressible flow, at a given frequency, we can calculate the mean flow rate in a half period. Knowing the stroke of the piston c_{piston} as well as the radius of the piston r_{piston}, we can calculate the volume swept by the piston in a half period. This volume is related to the flow rate by the frequency:

$$\bar{\dot{V}}_{osc} = 2\, f\, c_{piston}\, \pi\, r_{piston}^2 \tag{IV.44}$$

It is important here to notice that the values given for alternating flow are therefore rough estimates based on an incompressible flow. However, this assumption is not completely irrelevant either, since the Mach numbers involved and the density variations at low frequencies were not as great as at higher frequencies. Nevertheless, the intention, here, is to give an order of magnitude for pressure difference and temperature variations.

Other quantities such as density and viscosity, which vary over time, involved in the mean Reynolds number calculation, were taken with their mean values over time and between inlet and outlet. For instance, several frequencies were similar to the flow rate tested in a steady flow, and the comparison for steady and alternating flow in the channel with hydraulic diameter of 500 μm and aspect ratio 0.6 is given in the table IV.6. We can observe that the pressure drop is up to 20 times higher for alternating flow than for steady flow while the temperature difference is around 100 times higher. We attribute that to the inertial effects which are significantly higher in alternating flow due to the density variation which results in fluid acceleration and therefore higher contribution of fluid friction, but also due to flow changing direction which also causes flow acceleration and deceleration.

Table IV.6: Comparison between pressure drop and temperature variation between 1 and 2 for steady (std) and alternating (osc) flows. Channels with D_h =500 μm, α= 0.6 and L_{ch}=25 mm

Flow rate V $(mL.min^{-1})$	**Frequency** f (Hz)	**Reynolds number**	ΔP (bar)		ΔT $(°C)$	
			ΔP_{std}	$\Delta \bar{P}_{osc}$	ΔT_{std}	$\Delta \bar{T}_{osc}$
75	0,97	155	400	6337	0,02	1,41
90	1,3	186	525	10276	0,03	2,58
120	1,7	248	639	13311	0,04	3,87
165	2,4	341	1017	18044	0,06	6,42
225	3,2	465	1439	21287	0,09	8,55

IV.3.6. Influence of the channel design (geometrical parameters)

IV.3.6.1 Hydraulic diameter and aspect ratio

The influence of hydraulic diameter is difficult to highlight since for the tested channels when changing the hydraulic diameter of the channel, the aspect ratio vary as well. The influence of aspect ratio is shown in figure IV.36 by comparing the pressure drop for the two channels with the same hydraulic diameter of 200 μm and same channel length of 25 mm but different aspect ratio, one with an aspect ratio of 0.1, while for the other it is equal to 0.3. As expected the mean pressure drop is higher for the channel with the highest aspect ratio. This is due the difference in cross-section: the channel with an aspect ratio of 0.1 has a cross-section almost twice higher than the one with an aspect ratio of 0.3 (5.2 10^{-8} m^2 for α = 0.34 and 1.1 10^{-7} m^2 for α = 0.1). As the cross-section is lower for the channel with the highest aspect ratio, the flow velocity (which is inversely proportional to the cross-section) is higher. This higher velocity results in higher pressure drop corresponding to what we observe. The same observation can be conducted for the mean temperature difference. This is consistent since higher pressure drop results in higher fluid friction and therefore to higher contribution of viscous dissipation which increases the fluid temperature.

Unfortunately, we were not able to test these channels in steady flow in order to make the comparison and conclude if the influence of aspect ratio is more significant for alternating flow.

However, as is known in permament flow, but not always detailed in the models, we see here the limit of the hydraulic diameter model, which is not sufficient on its own. Whereas in a channel with a circular cross-section, the theoretical pressure drop is a function of length, roughness, diameter, fluid properties and velocity, in a non-circular cross-section the diameter cannot be replaced by a hydraulic diameter alone: the aspect ratio must also be taken into account, as must probably other geometric criteria depending on the shape of the flow cross-section.

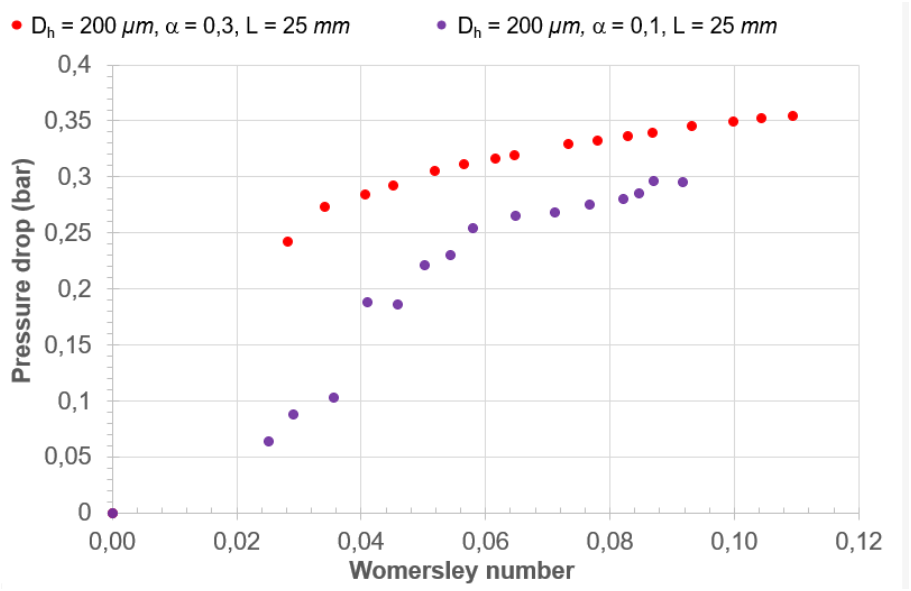

(a) Mean pressure drop

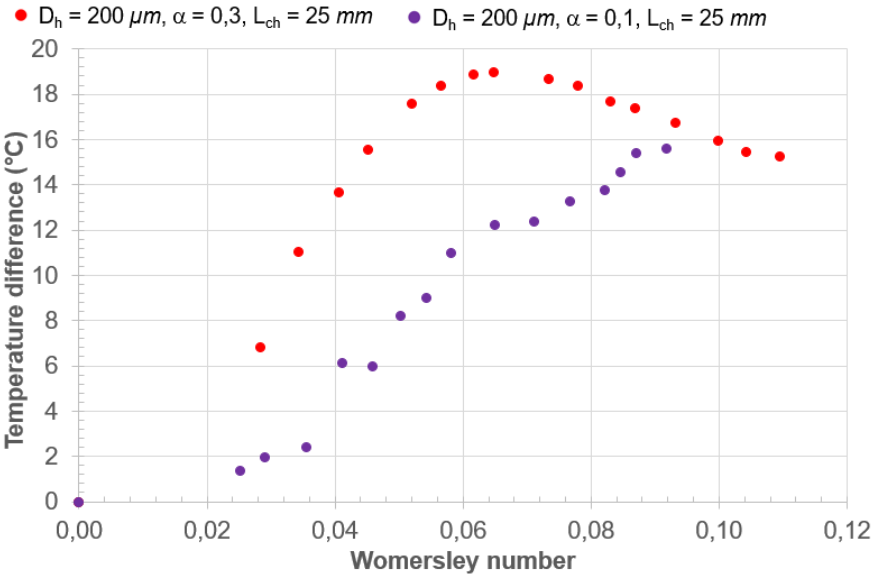

(b) Mean temperature difference

Figure IV.36: Influence of aspect ratio: Comparison for the pressure drop (a) and temperature difference (b) for channel with same hydraulic diameter $D_h = 200\ \mu$m, and same channel length $L_{ch} = 25$ mm, but with different aspect ratio, one with $\alpha = 0.1$, the other with $\alpha = 0.3$

IV.3.6.2 Influence of bends

Figure IV.37 emphasis on the influence of bends by comparing the pressure drop and temperature difference for straight channel and channel with bends with the same hydraulic diameter of 500 μm, aspect ratio of 0.6 and same channel length of 25 mm.

As expected, the pressure drop is higher for the channel with bends due to their additional contribution to the pressure drop. We can also observe that, even though, the influence of bends seemed to be negligible in figure IV.37, since the pressure difference considered in alternating flow is much higher than in steady flows, the contribution of bends remained considerable.

Table IV.7 gives a comparison (based once again on the rough estimation of mean Reynolds number for alternating flows) between the results for steady and alternating flows for both channels with hydraulic diameter of 500 μm, aspect ratio of 0.6 and channel length of 25 mm.

For the lowest frequency in table IV.7, we obtained, for alternating flow, a contribution of bends in the pressure difference nearly 1000 Pa, this contribution increased up to 2000 Pa for the highest frequency, while for steady flows the contribution of bends for the highest Reynolds number is around 350 Pa. The comparison showed that contribution of bends in alternating flows still represented almost 10 % higher pressure difference. In the case of the steady flow, this relative contribution was around 20 %. The relative contribution is therefore lower for alternating flows due to the higher pressure difference obtained for these flows.

Regarding temperature difference, it is much more hard to determine the relative contribution in the case of steady flows due to values obtained close to the accuracy of the sensors. However, once again, the contribution of bends increased this difference from around 0.5 °C for the lowest frequency to 2.3 °C for the highest frequency in table IV.7, while in the case of steady flows, this temperature difference is around only up to 0.15 °C.

Table IV.7: Influence of bends: Comparison of steady flows results with alternating flows

			Channel without bends D_h = 500 μm, α = 0.6, L_{ch} = 25 mm				Channel with bends D_h = 500 μm, α = 0.6, L_{ch} = 25 mm			
Flow rate ($mL.min^{-1}$)	**Frequency** (Hz)	**Reynolds number**	ΔP_{st}	$\Delta \bar{P}_{osc}$	ΔT_{st}	$\Delta \bar{T}_{osc}$	ΔP_{st}	$\Delta \bar{P}_{osc}$	ΔT_{st}	$\Delta \bar{T}_{osc}$
75	0.97	150	400	0.080	-0.03	1.44	404	0.088	-0.19	1.95
120	1.7	250	640	0.151	-0.04	3.85	774	0.186	-0.19	5.98
165	2.4	350	909	0.200	-0.05	6.39	1118	0.222	-0.19	8.21
225	3.2	460	1439	0.234	-0.09	8.64	1786	0.254	-0.16	10.97

IV.3.6.3 Influence of the channel length

The influence of channel length was performed by comparing results for both channels with hydraulic diameter of 1 mm, aspect ratio of 1 and different channel length 25 mm and 50 mm. This influence is shown versus Womersley number in figure IV.38.

The comparison of the influence of channel length for steady and alternating flows is complex since the pressure measurements and pressure drop calculated for these two channels in steady flows were close to the accuracy of pressure sensors. We recall that the influence of channel length for steady flows seemed to be not as significant as predicted by the theory due to the presence of converging and diverging sections that reduced the relative impact of channel length on the total pressure difference

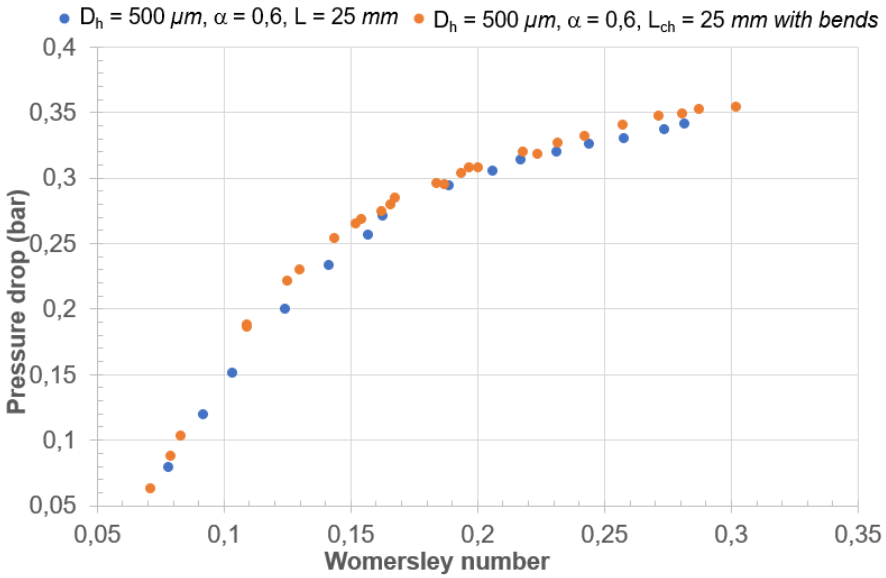

(a) Mean pressure drop

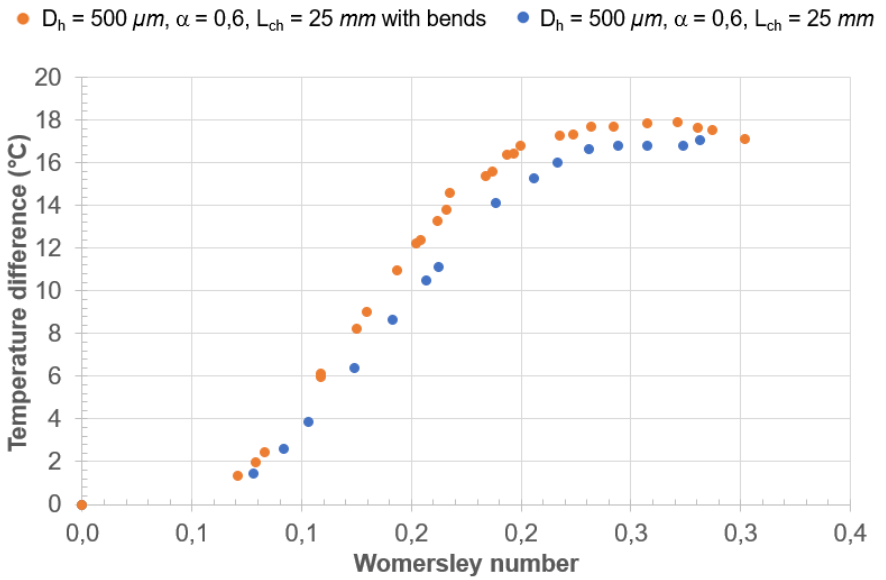

(b) Mean temperature difference

Figure IV.37: Influence of bends on characteristics of alternating flow. Comparison for the pressure drop and temperature difference for channel with same hydraulic diameter $D_h = 500$ μm, same aspect ratio $\alpha = 0.6$ and same channel length $L_{ch} = 25$ mm, one straight channel, the other channel includes bends.

generated. Moreover, since the values were close to the accuracy of the sensors, it is difficult to conclude the influence of channel length on the pressure drop.

Here, in the case of alternating flows, since the pressure considered is much higher and less close to the accuracy of the pressure sensors, the influence of channel length can be investigated. We observe that for the lowest frequency in table IV.8, the pressure difference for both channels are close. However, as the frequency increases, we observe, as expected, that the pressure difference for

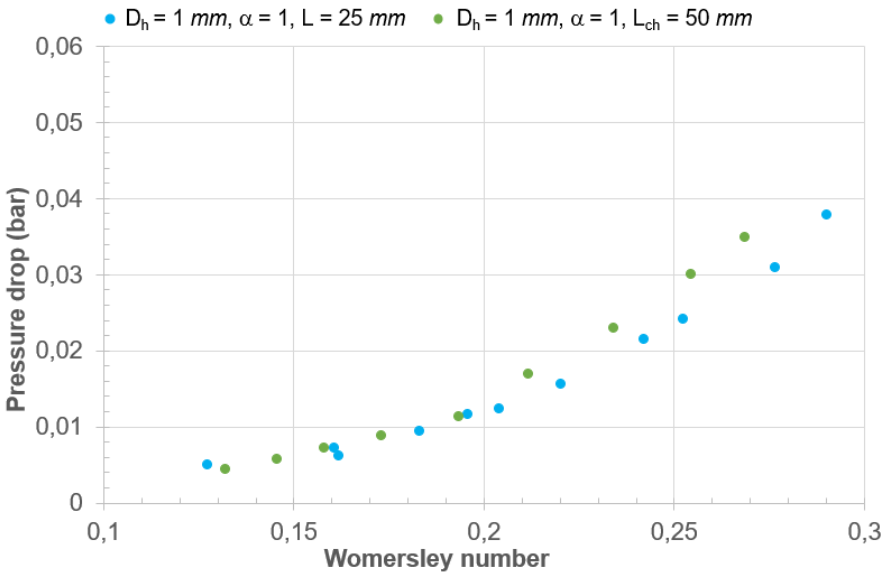

(a) Mean pressure drop

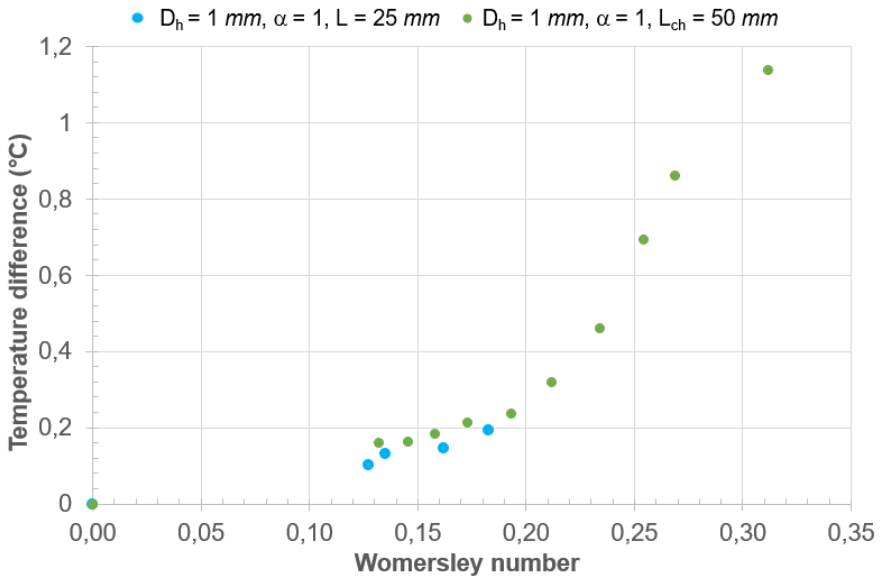

(b) Mean temperature difference

Figure IV.38: Influence of channel length: Comparison for the pressure drop and temperature difference for channels with same hydraulic diameter D_h = 1 mm, same aspect ratio α = 1 but different channel length 25 mm and 50 mm

the channel with the longest length are higher than for the other channel in a significant manner that shows the influence of channel length on the pressure drop.

Regarding temperature difference, we only determined the influence of channel length at low frequencies since the temperature sensors broke during the tests carried out on alternating flow in the channel with a length of 25 mm. The temperature difference is higher in the channel with the longest channel length as expected, however, this difference is not significant. Measurements, which would have been carried out at higher frequencies could validate this trend.

Table IV.8: Influence of channel length: Comparison of steady flows results with alternating flows

			Channel D_h = 1000 μm, α = 1, L_{ch} = 25 mm				Channel D_h = 1000 μm, α = 1, L_{ch} = 50 mm			
Flow rate (mL/min)	**Frequency (Hz)**	**Reynolds number**	ΔP_{st}	$Del\bar{t}aP_{osc}$	ΔT_{st}	$Del\bar{t}aT_{osc}$	ΔP_{st}	$Del\bar{t}aP_{osc}$	ΔT_{st}	$Del\bar{t}aT_{osc}$
45	0.61	50	55	509		0.1	59	451	-0.173	0.16
75	1.02	80	112	724		0.14	57	733	-0.238	0.18
105	1.5	120	109	1170		0.19	45	1140	-0.214	0.24
135	1.87	150	163	1567			204	1706	-0.094	0.32
180	2.53	200	227	2429			212	3014	-0.126	0.69
210	2.98	230	273	3102			243	3499	-0.169	0.86

To conclude on this part on the study on alternating flow, we have highlighted:

- Characteristics of alternating flow show similarities between macro and micro-scale:
  - The double frequency phenomenon have been observed at macroscale by Ibrahim *et al.* [175], but also at milliscale by Dellali [5]. Since this phenomenon was, in our case, only observed for the lowest frequencies and was more pronounced for the highest hydraulic diameter, we think it could be due to the contribution of inertial and viscous forces.
  - We have also observed the same trend for phase lag between pressure and piston displacement as those observed at the macroscale between pressure and flow.
- The influence of several parameters was investigated with the same trend as those observed for steady flows but were more pronounced with alternating flows.
  - pressure difference increased with the increasing length of the channels by 10 % - 25 %. The same observation could be made for temperature difference, even though, the temperature difference for both channels was closed, however, an increase of around 25 % was observed for the longest channel.
  - pressure difference obtained were, as expected, higher for channel with bends than for straight channel. The contribution of bends in the channel represented around 10 % higher pressure difference. As for temperature difference, the contribution of bends in the channel increased this difference by 25 to 35 %.
  - The influence of hydraulic diameter could not be taken into account separately from the influence of aspect ratio. However, the influence of the aspect ratio could be determined independently of the hydraulic diameter by comparing both channels with D_h = 200 μm and L_{ch} = 25 mm. When aspect ratio decreased, it significantly increased both pressure drop and temperature difference. For pressure difference, it was about 2.7 times higher for

the channel with aspect ratio of 0.3 than for the one with $\alpha = 0.1$ for the lower Womersley number considered, the influence of aspect ratio decreased with the increasing frequency down to a contribution of 14 % higher pressure difference for the channel with the lower aspect ratio. For steady flow, this parameter was not studied.

These results should be compared with an analytical study to verify that they agree with what is predicted by theory. An attempt of a simplified analytical model of the experimental setup based on an incompressible and isothermal flow was established for this purpose. It can be found in appendix A. However, this first draft requires further work, which will be subject of future works. Moreover, an in-depth study of more channel configurations would provide a better insight into the influence of parameters such as hydraulic diameter and aspect ratio. In addition, a study at higher frequencies could give a clearer idea of both pressure and temperature differences trends with increasing frequency.

Chapter conclusion

In this chapter, we presented the experimental setup used for steady and alternating flow as well as the acquisition setup and sensors used to carry out considered measurements (pressures, temperatures, flow rates, and piston displacements).

We first presented the results for steady flows.

- The results for pressure drop were compared with theoretical values taking into account the contribution due to converging and diverging sections at both ends of the channels which were included in the measurements. The experimental data were found in good agreement with the theory.
- Then, temperature variation on each side of the channels seemed similar to the results that were observed in the literature.
- Friction factors were calculated by removing the contribution of the converging and diverging sections according to their theoretical values. They were compared to correlations from the literature for which experimental conditions and channel dimensions were as close as possible to our experiment. The comparison showed good agreement.

In the second part of this chapter, we presented results for alternating flow in the test channels. The variations of pressure and temperature signals during a period were presented. The results were in line with expectations. We observed an increase in the amplitude of pressure and temperature variations in much greater proportions than those observed in the case of steady flow.
Moreover, a double period phenomenon was observed in the same way as it was mentioned by Ibrahim *et al.* [175] for oscillating flow at the macroscale and by Dellali [5] for alternating flow at the milliscale. A phase lag was also observed for both pressure and temperature which increased as the frequency increased. This is due, on the one hand, to the unsteadiness of the flow, which considerably increased the influence of inertial forces and their contribution to flow characteristics. On the other hand, the higher variations in fluid density induced far less negligible effects of fluid compressibility. The variation of pressure and temperature also increased as the frequency increased. This is consistent with viscous friction being more important as the frequency increased.

The influence of several parameters was determined. We found that:

- The aspect ratio had a significant influence. Both pressure drop and temperature difference increased while the aspect ratio decreased. This was related to the change in cross-section when the aspect ratio varied.
- The pressure drops and temperature difference in the channel with bends were observed, as expected, higher than those for the straight channel with the same hydraulic diameter, aspect ratio, and channel length. For alternating flows, we obtained pressure drops 10 % higher for channel with bends than for straight channel, while the increase in pressure drops was 20 % higher in the case of steady flows. Regarding temperature difference, channel with bends increased it by around 25% - 35 % (up to 55 % for the frequency of 1.7 Hz), while for steady flow, since the values were close to sensor's accuracy, it is more difficult to tell.
- The influence of channel length was also consistent with what was expected since we found higher pressure drops for the longest channel. For alternating flows, we obtained pressure drops 10 % - 25 % higher for the longest channel, while it seemed around 25 % higher for temperature difference. The values obtained in steady flows were close to the accuracy of sensors making it difficult estimate.

We have also observed that both pressure drop and temperature difference were much higher for alternating flows than those obtained for steady flows. This could be due to the contribution of inertial effects which were more important in the case of alternating flow.

Regarding the miniature Stirling engine that we aim to design, and according to the experimental observations carried out, we could say that the parameters that seem to have the greater influence on pressure drop and temperature difference are related to the hydraulic diameter and aspect ratio. These two parameters affect significantly both pressure drop and temperature difference. In contrast, bends and channel length seem to have less influence than expected.

However, these conclusions must be put into perspectives of observations made in steady flow on the increasing influence of pressure drops generated by converging and diverging sections as the flow velocity in the channel increased (*i.e.* as the flow rate, respectively, frequency increased in a steady flow, alternating flow). In alternating flow, we could not determine the weight of these sections when calculating the total pressure drops presented, since i/ we had no pressure measurements inside the channel and ii/ there are (to our knowledge) no correlations or models for these convergent/divergent sections in the literature on alternating flows. Thus, it is possible that the influence of bends and channel length was diluted in the contribution of converging and diverging sections.

Therefore, in future works, it would be useful to be able to determine the influence of converging and diverging sections alone for alternating flow, to clarify their influence. In addition, an in-depth study of the parameters would enable a better estimate of their influence on the flow characteristics.

CONCLUSION AND PERSPECTIVES

This thesis focused on the study of steady and alternating gas flows within milli- and micro-channels, providing a better understanding of the characteristics and behavior of alternating flows at this scale. Indeed, although these flows have been widely investigated on a macroscopic scale as part of the understanding of oscillating liquid flows (blood flow [75]), but also of alternating gas flows (typical of those generated within engines based on the Stirling engine principle [79] [88]), they are still quite unknown when it comes to channels whose dimensions are sub-millimetric.

As the review of the state of the art revealed, when channel dimensions are minimized, contributions such as rarefaction can occur. The rarefaction effects being negligible in our case, given the considered hydraulic diameters, its influence was not studied. On the other hand, the compressibility of the flow can become significant, even at low Mach numbers, well below the "classical" threshold between incompressible and compressible flow observed on a macroscopic scale. Indeed, for Mach numbers below 0.3, compressible flow behavior was observed on a micro-scale, depending on the ratio between P_{in} and P_{out}. As for the contribution of wall roughness, here again, the literature review highlighted the influence of roughness on flow characteristics at lower relative roughness values. Kandlikar *et al.* [31] proposed a hydraulic diameter whose definition takes wall roughness into account, to consider the reduction in cross-section when calculating the hydraulic diameter.
When it comes to alternating flows, at the macroscale, a review of results from the literature has indicated that the Reynolds number is no longer a suitable parameter for characterizing the flow since quantities such as velocity, pressure, and temperature vary with time. A dimensionless frequency term was proposed by Womersley [75] to characterize such flows. A phase shift between velocity and pressure was observed to depend on the Womersley number. Subsequently, many authors have used this dimensionless number to characterize the unsteadiness of their flows.

Following this literature review, which identified the parameters that seem to have a larger influence at the microscale, the design, and sizing of channels with dimensions similar to those of the micro Stirling engine [6], [5] was performed. This design includes the implementation of converging and diverging sections on either side of the channel, to match the cross-section of the pipes of the experimental system, while minimizing their impact on the flow as much as possible. The measurements considered for the study consisted of commercial pressure sensors and microthermocouples manufactured at FEMTO-ST Institute for global measurements. These measurements included minor losses generated due to converging and diverging sections and were positioned in such a way as to minimize disturbance of the flow. Other sensors were designed for local measurements close to the inlet and outlet of the studied channels. The designed pressure sensors consisted of a PDMS membrane with a thickness of 20 μm enabling measurements over the considered pressure range. The temperature

sensors consisted of Platinum thin film resistances deposited on the substrate with a thickness of 200 *nm*. Their resistance ranged from 300 Ω to 500 Ω at room temperature.

After designing the channels and sensors, the next step was to manufacture the devices using microfabrication technologies in the FEMTO-ST Institute's MIMENTO technology center. The process of making the channels with and without integrated sensors was presented, detailing each step one after the other. These processes were carried out alongside, to obtain channels that could be rapidly and easily tested without integrated sensors. Although the PDMS bonding for the fabrication of channels with integrated sensors was unsatisfactory, it nevertheless proved effective on unstructured substrates with a bonding strength of up to 2 *MPa*. Subsequently, although the fabrication of channels with integrated sensors was unsuccessful, it did provide an opportunity to characterize the temperature sensors fabricated. To improve the characteristics of these temperature sensors, an annealing process was carried out. Characterization of these sensors enabled to identification of the influence of annealing parameters (temperature, time) on their electrical, mechanical, and structural properties. We observed that annealing at 450 °*C* considerably increased the residual stresses in the layer, while at the same time altering negatively the electrical properties of the sensor, making it an unsuitable choice for our needs. We attributed this to diffusion of the chromium adhesion layer into the Pt layer, and oxidation of the adhesion layer near the surface. Conversely, annealing at 250 °*C* improved the electrical properties of these sensors, while still increasing the residual stresses in the layer but to a lesser extent, thus offering a good compromise for our needs.

Then, both steady and alternating were experimentally studied in our tested channels. For steady nitrogen flows, the pressure drops obtained were compared with theoretical values, whose calculation was detailed. The experimental results showed good agreement with the theory. The minor losses generated by the converging and diverging sections, though designed to be as small as possible, became significant as the flow rate increased due to their proportionality to the square of the flow rate, while pressure drop due to the channel itself was only proportional to the flow rate. The influence of bends was highlighted, by comparing two channels with the same hydraulic diameter, aspect ratio, channel length, and same converging and diverging sections. The straight channel exhibited a lower pressure drop than the channel with bends, as expected. For a Reynolds number of 480, the presence of bends in the channel design increased the pressure drops by more than 30 %. The friction factor for steady flows was calculated from the measured pressure drops for the channels with a hydraulic diameter of 500 μm, an aspect ratio of 0.6 and a Reynolds number ranging from 15 to 510. Friction factors were found close to the values from the literature, even though, differences could be observed, probably due to the various experimental conditions and channel geometries.

For alternating flows, as expected, the variation of pressure and temperature increased as the frequency increased due to higher friction contribution. However, for the smaller channel a decrease in temperature variation was observed at the higher frequencies similar to the variation of temperature observed for a steady flow, which might be due to the competing contribution of fluid friction and convective heat transfer between the fluid and the channel's wall.
The observed phase lag between pressure and temperature, which increased with increasing frequency, was mainly attributed to the compressibility of the fluid, inducing a significant variation in density.
In addition, the increase in pressure drop and temperature difference with the increasing frequency was consistent, once again, with the increasing contribution of viscous forces. We also observed that the pressure drop seemed to be bounded, which could be due to a plugging effect. This plugging

effect could also explain the observed decrease in temperature difference at the highest frequencies for the channel with the lowest hydraulic diameter.
Overall, we observed that the pressure drop and temperature difference were much higher in the case of alternating flow than for steady flows. This could be mainly due to inertial effects, which are more important in the case of alternating flow with a sudden change in fluid properties when the flow velocity is reversed. This results in a high acceleration and deceleration phase, which increased significantly the friction contribution, and thus pressure drop and temperature difference.
A comparison of the results obtained for each channel configuration revealed the influence of aspect ratio, bends, and channel length. The presence of bends, increasing channel length, and decreasing aspect ratio increased both pressure drops and temperature difference. The influence of bends was unexpected to be as low as observed. Indeed, on the tested range of frequencies for the alternating flow, the presence of bends in the channel results in a 10% increase in pressure drop compared with the case of a channel without bends. While the influence of channel length leads to an increase in pressure loss of up to 25%. Unfortunately, the influence of hydraulic diameter alone could not be properly studied, as it was correlated, for the channels studied, with the influence of aspect ratio (rectangular section). Therefore, when fabricating the miniature device designed for heat recovery, it seems that bends and channel length should not be taken as parameters that will considerably limit the efficiency of the device, while aspect ratio seems to have a much more influence. Moreover, even though, the influence of hydraulic diameter was not determined, it should be a parameter expected to have also a significant influence on both pressure drops and temperature difference, that is to say on the global efficiency of the micro Stirling engine.

Thus, among the prospects of this work, studying alternating flows for different aspect ratios, and different hydraulic diameters (by varying the geometry of the cross-section), could enable us to determine their contribution to pressure drops and temperature differences. This would allow us to determine which geometry is the most suitable for the design of the micro Stirling engine. The question of the effect of gas compressibility and fluid thermophysical properties could be addressed by reproducing these experiments with other gases and liquids. In addition, an important parameter to consider, but which we were unable to study for lack of precise control, would be the influence of wall roughness. The study of heat transfer, which is important when it comes to optimizing the design of a Stirling engine, could be done by imposing different wall temperature gradients between the two ends of the channel. An advanced study on heat transfer and Nusselt correlations could also provide insight into unanswered queries (influence of the gas viscosity, gas compressibility, entrance effects, rarefaction effects). Complementary measurements on the same isolated channels, to obtain adiabatic flow conditions, could shed light on these concerns, and could be compared with the work of Hong *et al.* [174], [13] and Rehman *et al.* [176], whose channel dimensions are close to ours, and whose flows were assumed to be adiabatic. From a technical point of view, various paths could still be explored to overcome the technological obstacles encountered. For instance, adhesive bonding using Perminex photoresist could be tested for the last bonding between the two silicon wafers. This photoresist has the advantage of being able to be structured before bonding, unlike SU-8 photoresist, and could therefore meet our bonding requirement. Preliminary tests on unstructured and structured wafers carried out by the cleanroom facility's staff have produced encouraging results towards this aim. Moreover, velocity sensors located upstream and downstream of the microchannel could provide a better view of the flow behavior. However, the implementation of a velocity sensor within the channel remains a major challenge, given the current available resources. Thus, it could enable to establishment of physical models of alternating flows at milli and micrometric scales.

BIBLIOGRAPHY

[1] Basanta Kumar Panigrahi, Rahate Ahmed, Muhammad Uzair Mehmood, Jin Chul Park, Yeongmin Kim, Wongee Chun, et al. Operation of a low-temperature differential heat engine for power generation via hybrid nanogenerators. *Applied Energy*, 285:116385, 2021. doi: 10.1016/j.apenergy.2020.116385.

[2] Jonghyeon Yun, Inkyum Kim, and Daewon Kim. Hybrid energy harvesting system based on stirling engine towards next-generation heat recovery system in industrial fields. *Nano Energy*, 90:106508, 2021. doi: 10.1016/j.nanoen.2021.106508.

[3] Seme Lanzuma Levi Enoka. *Harvesting Electrical Energy from Low-Temperature Difference Stirling Engine*. PhD thesis, The University of Utah, 2020.

[4] Hung-Di Huang and Wen-Lih Chen. Development of a compact simple unpressurized watt-level low-temperature-differential stirling engine. *International Journal of Energy Research*, 44(14):12029–12044, 2020. doi: 10.1002/er.5852.

[5] Emna Dellali. *Étude théorique et expérimentale des écoulements oscillants alternés d'un gaz au sein de micro et milli-régénérateurs de moteur Stirling*. Theses, Université Bourgogne Franche-Comté, October 2018. URL https://theses.hal.science/tel-02861908.

[6] A. Diallo. *Contribution à la conception et à la réalisation d'une micromachine thermique à cycle de stirling*. PhD thesis, Université de Bourgogne Franche-Comté, 2019. URL https://theses.hal.science/tel-02500736v1/document.

[7] William Sutherland. Lii. the viscosity of gases and molecular force. *The London, Edinburgh, and Dublin Philosophical Magazine and Journal of Science*, 36(223):507–531, 1893. doi: 10.1080/14786449308620508.

[8] FM White. Viscous fluid flow, 2005.

[9] Patrick H Oosthuizen and William E Carscallen. *Compressible fluid flow*, volume 179. McGraw-Hill New York, 1997. ISBN 978-1-4398-7792-0.

[10] Cyril Frank Colebrook, T Blench, H Chatley, EH Essex, JR Finniecome, G Lacey, J Williamson, and GG Macdonald. Correspondence. turbulent flow in pipes, with particular reference to the transition region between the smooth and rough pipe laws.(includes plates). *Journal of the Institution of Civil engineers*, 12(8):393–422, 1939. doi: 10.1680/ijoti.1939.14509.

[11] Frank M White. *Fluid mechanics*. Tata McGraw-Hill Education, 1979. ISBN 978-9814720175.

[12] Ascher H Shapiro. *The dynamics and thermodynamics of compressible fluid flow*. John Wiley & Sons, 1953. ISBN 978-0471066910.

[13] Chungpyo Hong, Yutaka Asako, Gian Luca Morini, and Danish Rehman. Data reduction of average friction factor of gas flow through adiabatic micro-channels. *International Journal of Heat and Mass Transfer*, 129:427–431, 2019. doi: 10.1016/j.ijheatmasstransfer.2018.09.088.

[14] Ryoji Kashiwagi, Chungpyo Hong, Yutaka Asako, Gian Luca Morini, and Mohammad Faghri. Identification of gas flow regimes in adiabatic microtubes by means of wall temperature measurements. In *Journal of Physics: Conference Series*, volume 1599, page 012019. IOP Publishing, 2020. doi: 10.1088/1742-6596/1599/1/012019.

[15] JN Pfahler, J Harley, H Bau, and J1 Zemel. Liquid transport in micron and submicron channels. *Sensors and Actuators A: Physical*, 22(1-3):431–434, 1990. doi: 10.1016/0924-4247(89)80008-1.

[16] J Judy, D Maynes, and BW Webb. Characterization of frictional pressure drop for liquid flows through microchannels. *International Journal of heat and mass transfer*, 45(17):3477–3489, 2002. doi: 10.1016/S0017-9310(02)00076-5.

[17] Puzhen Gao, Stéphane Le Person, and Michel Favre-Marinet. Scale effects on hydrodynamics and heat transfer in two-dimensional mini and microchannels. *International journal of thermal sciences*, 41(11):1017–1027, 2002. doi: 10.1016/S1290-0729(02)01389-3.

[18] C-Y Yang and T-Y Lin. Heat transfer characteristics of water flow in microtubes. *Experimental thermal and fluid science*, 32(2):432–439, 2007. doi: 10.1016/j.expthermflusci.2007.05.006.

[19] Jung-Yeul Jung and Ho-Young Kwak. Fluid flow and heat transfer in microchannels with rectangular cross section. *Heat and Mass Transfer*, 44(9):1041–1049, 2008. doi: 10.1007/s00231-007-0338-4.

[20] Chien-Yuh Yang, Chia-Wei Chen, Ting-Yu Lin, and Satish G Kandlikar. Heat transfer and friction characteristics of air flow in microtubes. *Experimental Thermal and Fluid Science*, 37:12–18, 2012. doi: 10.1016/j.expthermflusci.2011.09.003.

[21] Stéphane Colin. Rarefaction and compressibility effects on steady or transient gas flows in microchannels. In *ASME 2004 2nd International Conference on Microchannels and Minichannels*, pages 13–24. American Society of Mechanical Engineers, 2004. doi: 10.1115/ICMM2004-2316.

[22] Stéphane Colin. Gas microflows in the slip flow regime: a critical review on convective heat transfer. *Journal of Heat Transfer*, 134(2):020908, 2012. doi: 10.1115/1.4005063.

[23] Stéphane Colin, Pierre Lalonde, and Robert Caen. Validation of a second-order slip flow model in rectangular microchannels. *Heat transfer engineering*, 25(3):23–30, 2004. doi: 10.1080/01457630490280047.

[24] SG Jennings. The mean free path in air. *Journal of Aerosol Science*, 19(2):159–166, 1988. doi: 10.1016/0021-8502(88)90219-4.

[25] Satish Kandlikar, Srinivas Garimella, Dongqing Li, Stephane Colin, and Michael R King. *Heat transfer and fluid flow in minichannels and microchannels*. elsevier, 2005. ISBN 0-0804-4527-6.

[26] Stéphane Colin and Lucien Baldas. Effets de raréfaction dans les micro-écoulements gazeux. *Comptes Rendus Physique*, 5(5):521–530, 2004. doi: 10.1016/j.crhy.2004.04.005.

[27] Nishanth Dongari, Ashutosh Sharma IITK, and F. Durst. Pressure-driven diffusive gas flows in micro-channels: From the knudsen to the continuum regimes. *Microfluidics and Nanofluidics*, 6:679–692, 05 2009. doi: 10.1007/s10404-008-0344-y.

[28] H. Yu. *Lattice boltzmann equation simulations of turbulence, mixing and combustion*. PhD thesis, Texas A&M University, 2004.

[29] Chungpyo Hong, Yutaka Asako, Mohammad Faghri, and Jae-Heon Lee. Poiseuille number correlations for gas slip flow in micro-tubes. *Numerical Heat Transfer, Part A: Applications*, 56(10):785–806, 2009. doi: 10.1080/10407780903466436.

[30] Little W.A. Peiyi W. Measurement of friction factors for the flow of gases in very fine channels used for microminiature joule-thomson refrigerators. *Cryogenics*, 23(5):273–277, 1983. doi: 10.1016/0011-2275(83)90150-9.

[31] Satish G Kandlikar, Derek Schmitt, Andres L Carrano, and James B Taylor. Characterization of surface roughness effects on pressure drop in single-phase flow in minichannels. *Physics of Fluids*, 17(10):100606, 2005. doi: 10.1063/1.1896985.

[32] Guobing Zhou and Shi-Chune Yao. Effect of surface roughness on laminar liquid flow in micro-channels. *Applied Thermal Engineering*, 31(2-3):228–234, 2011. doi: 10.1016/j.applthermaleng.2010.09.002.

[33] Peng-Fei Hao, Zhao-Hui Yao, Feng He, and Ke-Qin Zhu. Experimental investigation of water flow in smooth and rough silicon microchannels. *Journal of Micromechanics and Microengineering*, 16(7):1397, 2006. doi: 10.1088/0960-1317/16/7/037.

[34] K Vijayalakshmi, KB Anoop, HE Patel, PV Harikrishna, T Sundararajan, and Sarit K Das. Effects of compressibility and transition to turbulence on flow through microchannels. *International journal of heat and mass transfer*, 52(9-10):2196–2204, 2009. doi: 10.1016/j.ijheatmasstransfer.2008.07.056.

[35] VK Natrajan and KT Christensen. The impact of surface roughness on flow through a rectangular microchannel from the laminar to turbulent regimes. *Microfluidics and nanofluidics*, 9 (1):95–121, 2010. doi: 10.1007/s10404-009-0526-2.

[36] Baomin Dai, Minxia Li, and Yitai Ma. Effect of surface roughness on liquid friction and transition characteristics in micro-and mini-channels. *Applied Thermal Engineering*, 67(1-2): 283–293, 2014. doi: 10.1016/j.applthermaleng.2014.03.028.

[37] Lewis F Moody. Friction factors for pipe flow. *Transactions of the American Society of Mechanical Engineers*, 66(8):671–678, 1944. doi: 10.1115/1.4018140.

[38] Stephen E Turner, Lok C Lam, Mohammad Faghri, and Otto J Gregory. Experimental investigation of gas flow in microchannels. *Journal of Heat Transfer*, 126(5):753–763, 2004. doi: 10.1115/1.1797036.

[39] GH Tang, Zhuo Li, YL He, and WQ Tao. Experimental study of compressibility, roughness and rarefaction influences on microchannel flow. *International Journal of Heat and Mass Transfer*, 50(11-12):2282–2295, 2007. doi: 10.1016/j.ijheatmasstransfer.2006.10.034.

[40] Marco Lorenzini, Gian Luca Morini, and Sandro Salvigni. Laminar, transitional and turbulent friction factors for gas flows in smooth and rough microtubes. *International Journal of Thermal Sciences*, 49(2):248–255, 2010. doi: 10.1016/j.ijthermalsci.2009.07.025.

[41] Yangpeng Liu, Guoqiang Xu, Jining Sun, and Haiwang Li. Investigation of the roughness effect on flow behavior and heat transfer characteristics in microchannels. *International Journal of Heat and Mass Transfer*, 83:11–20, 2015. doi: 10.1016/j.ijheatmasstransfer.2014.11.060.

[42] Xing Yuan, Zhi Tao, Haiwang Li, and Yitu Tian. Experimental investigation of surface roughness effects on flow behavior and heat transfer characteristics for circular microchannels. *Chinese Journal of Aeronautics*, 29(6):1575–1581, 2016. doi: 10.1016/j.cja.2016.10.006.

[43] Gh Mohiuddin Mala and Dongqing Li. Flow characteristics of water in microtubes. *International journal of heat and fluid flow*, 20(2):142–148, 1999. doi: 10.1016/S0142-727X(98)10043-7.

[44] David Pfund, David Rector, Alireza Shekarriz, Aristotel Popescu, and James Welty. Pressure drop measurements in a microchannel. *AIChE Journal*, 46(8):1496–1507, 2000. doi: 10.1002/aic.690460803.

[45] WL Qu, Gh Mohiuddin Mala, and DQ Li. Pressure-driven water flows in trapezoidal silicon microchannels. *International Journal of Heat and Mass Transfer*, 43(3):353–364, 2000. doi: 10.1016/S0017-9310(99)00148-9.

[46] Zhi-Xin Li. Experimental study on flow characteristics of liquid in circular microtubes. *Microscale thermophysical engineering*, 7(3):253–265, 2003. doi: 10.1080/10893950390219083.

[47] Roland Bavière, Frédéric Ayela, Stéphane Le Person, and Michel Favre-Marinet. An experimental study of water flow in smooth and rough rectangular micro-channels. In *International Conference on Nanochannels, Microchannels, and Minichannels*, volume 41642, pages 221–228, 2004. doi: 10.1115/ICMM2004-2338.

[48] X-Q Wang, Christopher Yap, and Arun Sadashiv Mujumdar. Effects of two-dimensional roughness in flow in microchannels. *Journal of Electronic Packaging*, 127:357–361, 2005. doi: 10.1115/1.1997164.

[49] Giulio Croce and Paola D'Agaro. Numerical simulation of roughness effect on microchannel heat transfer and pressure drop in laminar flow. *Journal of Physics D: Applied Physics*, 38(10):1518, 2005. doi: 10.1088/0022-3727/38/10/005.

[50] S Shen, JL Xu, JJ Zhou, and Y Chen. Flow and heat transfer in microchannels with rough wall surface. *Energy Conversion and Management*, 47(11-12):1311–1325, 2006. doi: 10.1016/j.enconman.2005.09.001.

[51] Timothy P Brackbill and Satish G Kandlikar. Effect of sawtooth roughness on pressure drop and turbulent transition in microchannels. *Heat transfer engineering*, 28(8-9):662–669, 2007. doi: 10.1080/01457630701326290.

[52] Pega Hrnjak and Xiao Tu. Single phase pressure drop in microchannels. *International Journal of Heat and Fluid Flow*, 28(1):2–14, 2007. doi: 10.1016/j.ijheatfluidflow.2006.05.005.

[53] Zhuo Li, Ya-Ling He, Gui-Hua Tang, and Wen-Quan Tao. Experimental and numerical studies of liquid flow and heat transfer in microtubes. *International journal of heat and mass transfer*, 50(17-18):3447–3460, 2007. doi: 10.1016/j.ijheatmasstransfer.2007.01.016.

[54] Masataka Hakamada, Yuuki Asao, Naobumi Saito, and Mamoru Mabuchi. Microfluidic flows in metallic microchannels fabricated by the spacer method. *Journal of Micromechanics and Microengineering*, 18(7):075029, 2008. doi: 10.1088/0960-1317/18/7/075029.

[55] Afshin J Ghajar, Clement C Tang, and Wendell L Cook. Experimental investigation of friction factor in the transition region for water flow in minitubes and microtubes. *Heat Transfer Engineering*, 31(8):646–657, 2010. doi: 10.1080/01457630903466613.

[56] Lap Mou Tam, Hou Kuan Tam, Afshin J Ghajar, Wa San Ng, Ieok Wa Wong, Ka Fu Leong, and Choi Keng Wu. The effect of inner surface roughness and heating on friction factor in horizontal micro-tubes. In *Fluids Engineering Division Summer Meeting*, volume 44403, pages 2971–2978, 2011. doi: 10.1115/AJK2011-16027.

[57] Z. Liu and Y. Pang. Influences of size and roughness of microchannels on friction factors under different pressures. *Engineering Mechanics*, 29(5):200–205, 2012. URL https://engineeringmechanics.cn/en/article/id/5644.

[58] Takuto Araki, Min Soo Kim, Hiroshi Iwai, and Kenjiro Suzuki. An experimental investigation of gaseous flow characteristics in microchannels. *Microscale Thermophysical Engineering*, 6 (2):117–130, 2002. doi: 10.1080/10893950252901268.

[59] Gian Luca Morini, Marco Lorenzini, Sandro Salvigni, and Marco Spiga. Analysis of laminar-to-turbulent transition for isothermal gas flows in microchannels. *Microfluidics and nanofluidics*, 7(2):181–190, 2009. doi: 10.1007/s10404-008-0369-2.

[60] Peter M-Y Chung, Masahiro Kawaji, and Akimaro Kawahara. Characteristics of single-phase flow in microchannels. In *Fluids Engineering Division Summer Meeting*, volume 36150, pages 1219–1228, 2002. doi: 10.1115/FEDSM2002-31211.

[61] Yutaka Asako, Kenji Nakayama, and Tetsuya Shinozuka. Effect of compressibility on gaseous flows in a micro-tube. *International journal of heat and mass transfer*, 48(23-24):4985–4994, 2005. doi: 10.1016/j.ijheatmasstransfer.2005.05.039.

[62] K Tang, JL Huang, T Jin, and MX Wu. An experiment-based comparative investigation of correlations for microtube gas flow. *Sadhana*, 40(2):537–547, 2015. doi: 10.1007/s12046-014-0326-6.

[63] P Vocale, D Rehman, and GL Morini. Numerical investigation of compressibility effects on friction factor in rectangular microchannels. *International Journal of Thermal Sciences*, 172: 107373, 2022. doi: 10.1016/j.ijthermalsci.2021.107373.

[64] Ding Ying-Tao, Yao Zhao-Hui, and Shen Meng-Yu. Gas flow characteristics in straight silicon microchannels. *Chinese Physics*, 11(9):869, 2002. doi: 10.1088/1009-1963/11/9/303.

[65] Chien-Yuh Yang. Friction characteristics of water, r-134a, and air in small tubes. *Microscale Thermophysical Engineering*, 7(4):335–348, 2003. doi: 10.1080/10893950390243608.

[66] Shou-Shing Hsieh, Huang-Hsiu Tsai, Chih-Yi Lin, Ching-Feng Huang, and Cheng-Ming Chien. Gas flow in a long microchannel. *International Journal of Heat and Mass Transfer*, 47 (17-18):3877–3887, 2004. doi: 10.1016/j.ijheatmasstransfer.2004.03.027.

[67] MJ Kohl, SI Abdel-Khalik, SM Jeter, and DL Sadowski. An experimental investigation of microchannel flow with internal pressure measurements. *International journal of heat and mass transfer*, 48(8):1518–1533, 2005. doi: 10.1016/j.ijheatmasstransfer.2004.10.030.

[68] Ian Papautsky, Bruce K Gale, Swomitra K Mohanty, Timothy A Ameel, and A Bruno Frazier. Effects of rectangular microchannel aspect ratio on laminar friction constant. In *Microfluidic Devices and Systems II*, volume 3877, pages 147–158. SPIE, 1999. doi: 10.1117/12.359332.

[69] Tariq Ahmad and Ibrahim Hassan. Experimental Analysis of Microchannel Entrance Length Characteristics Using Microparticle Image Velocimetry. *Journal of Fluids Engineering*, 132 (4):041102, 04 2010. ISSN 0098-2202. doi: 10.1115/1.4001292.

[70] E. Galvis, S. Yarusevych, and J. R. Culham. Incompressible Laminar Developing Flow in Microchannels. *Journal of Fluids Engineering*, 134(1):014503, 02 2012. ISSN 0098-2202. doi: 10.1115/1.4005736.

[71] E G Richardson. The amplitude of sound waves in resonators. *Proceedings of the Physical Society*, 40(1):206, dec 1927. doi: 10.1088/0959-5309/40/1/328. URL https://dx.doi.org/10.1088/0959-5309/40/1/328.

[72] EG Richardson and E Tyler. The transverse velocity gradient near the mouths of pipes in which an alternating or continuous flow of air is established. *Proceedings of the Physical Society*, 42 (1):1, 1929.

[73] Paul Lambossy. Oscillations forcees d'un liquide incompressibile et visqueux dans un tube rigide et horizontal. calcul de la force frottement. *Helv. Physica Acta*, 25:371–386, 1952. doi: 10.5169/seals-112314.

[74] EPW Helps and DA McDonald. Systolic backflow in the dog femoral artery. In *JOURNAL OF PHYSIOLOGY-LONDON*, volume 122, pages P73–P73. CAMBRIDGE UNIV PRESS 40 WEST 20TH STREET, NEW YORK, NY 10011-4211, 1953.

[75] John R Womersley. Method for the calculation of velocity, rate of flow and viscous drag in arteries when the pressure gradient is known. *The Journal of physiology*, 127(3):553–563, 1955. doi: 10.1113/jphysiol.1955.sp005276.

[76] Shigeo Uchida. The pulsating viscous flow superposed on the steady laminar motion of incompressible fluid in a circular pipe. *Zeitschrift für angewandte Mathematik und Physik ZAMP*, 7: 403–422, 1956. doi: 10.1007/BF01606327.

[77] Alexandre Meunier. *Contribution théorique et expérimentale à l'étude d'un système magnétocalorique: application au développement d'un prototype industriel de pompe à chaleur*. PhD thesis, Université de Franche-Comté, 2016. URL https://theses.hal.science/tel-01532205v1/document.

[78] Munekazu Ohmi, Manabu Iguchi, and Ikuo Urahata. Flow patterns and frictional losses in an oscillating pipe flow. *Bulletin of JSME*, 25(202):536–543, 1982. doi: 10.1299/jsme1958.25.536.

[79] Terrence W Simon and Jorge R Seume. A survey of oscillating flow in stirling engine heat exchangers. Technical report, 1988. URL https://ntrs.nasa.gov/api/citations/19880012938/downloads/19880012938.pdf.

[80] R C Tew and S M Geng. Overview of nasa supported stirling thermodynamic loss research. Technical report, 9 1994. URL https://www.osti.gov/biblio/10181260.

[81] SI Sergeev. Fluid oscillations in pipes at moderate reynolds numbers. *Fluid dynamics*, 1(1): 121–122, 1966. doi: 10.1007/BF01016289.

[82] JRS Park and MHI Baird. Transition phenomena in an oscillating manometer. *The Canadian Journal of Chemical Engineering*, 48(5):491–495, 1970. doi: 10.1002/cjce.5450480503.

[83] Manabu IGUCHI, Munekazu OHMI, and Kazunori MAEGAWA. Analysis of free oscillating flow in a u-shaped tube. *Bulletin of JSME*, 25(207):1398–1405, 1982. doi: 10.1299/jsme1958.25.1398.

[84] Munekazu Ohmi, Manabu Iguchi, Koichiro Kakehashi, and Tetsuya Masuda. Transition to turbulence and velocity distribution in an oscillating pipe flow. *Bulletin of JSME*, 25(201): 365–371, 1982. doi: 10.1299/jsme1958.25.536.

[85] Kyung H Ahn and Mounir B Ibrahim. Laminar/turbulent oscillating flow in circular pipes. *International Journal of Heat and Fluid Flow*, 13(4):340–346, 1992. doi: 10.1016/0142-727X(92)90004-S.

[86] TS Zhao and Ping Cheng. Experimental studies on the onset of turbulence and frictional losses in an oscillatory turbulent pipe flow. *International journal of heat and fluid flow*, 17(4):356–362, 1996. doi: 10.1016/0142-727X(95)00108-3.

[87] David Gedeon and JG Wood. Oscillating-flow regenerator test rig: hardware and theory with derived correlations for screens and felts. Technical report, 1996. URL https://ntrs.nasa.gov/api/citations/19960015878/downloads/19960015878.pdf.

[88] Makoto Tanaka, Iwao Yamashita, and Fumitake Chisaka. Flow and heat transfer characteristics of the stirling engine regenerator in an oscillating flow. *JSME international journal. Ser. 2, Fluids engineering, heat transfer, power, combustion, thermophysical properties*, 33(2):283–289, 1990. doi: 10.1299/jsmeb1988.33.2_283.

[89] Chin-Tsau Hsu, Huili Fu, and Ping Cheng. On Pressure-Velocity Correlation of Steady and Oscillating Flows in Regenerators Made of Wire Screens. *Journal of Fluids Engineering*, 121 (1):52–56, 03 1999. ISSN 0098-2202. doi: 10.1115/1.2822010.

[90] Sungryel Choi, Kwanwoo Nam, and Sangkwon Jeong. Investigation on the pressure drop characteristics of cryocooler regenerators under oscillating flow and pulsating pressure conditions. *Cryogenics*, 44(3):203–210, 2004. doi: 10.1016/j.cryogenics.2003.11.006.

[91] KC Leong and LW Jin. Characteristics of oscillating flow through a channel filled with open-cell metal foam. *International Journal of Heat and fluid flow*, 27(1):144–153, 2006. doi: 10.1016/j.ijheatfluidflow.2005.05.004.

[92] Q. Q. Shen and Y. L. Ju. A NEW CORRELATION OF FRICTION FACTOR FOR OSCILLATING FLOW REGENERATOR OPERATING AT HIGH FREQUENCIES. volume 985, pages 267–274, 03 2008. doi: 10.1063/1.2908556.

[93] Li Wen Jin and Kai Choong Leong. Pressure drop and friction factor of steady and oscillating flows in open-cell porous media. *Transport in porous media*, 72:37–52, 2008. doi: 10.1007/s11242-007-9134-3.

[94] M Kahaleras, F Lanzetta, G Layes, and Philippe Nika. Friction factor and regenerator effectiveness in an oscillating gas flow. In *Proceedings of the 5th Internantional conference on Heat Transfer and Fluid Flow in Microscale, Marseille, France*, pages 22–26, 2014.

[95] Gang Xiao, Hao Peng, Haoting Fan, Umair Sultan, and Mingjiang Ni. Characteristics of steady and oscillating flows through regenerator. *International Journal of Heat and Mass Transfer*, 108:309–321, 2017. doi: 10.1016/j.ijheatmasstransfer.2016.11.096.

[96] Emna Dellali, Sylvie Bégot, François Lanzetta, Eric Gavignet, and Jean-Yves Rauch. Pressure drop analysis of oscillating flows through a miniature porous regenerator under isothermal and nonisothermal conditions. *Experimental Thermal and Fluid Science*, 103:394–405, 2019. doi: 10.1016/j.expthermflusci.2019.01.027.

[97] M Karbaschi, A Javadi, D Bastani, and R Miller. High frequency oscillatory flow in micro channels. *Colloids and Surfaces A: Physicochemical and Engineering Aspects*, 460:355–360, 2014. doi: 10.1016/j.colsurfa.2014.03.062.

[98] L. S. Han. Hydrodynamic entrance lengths for incompressible laminar flow in rectangular ducts. *Journal of Applied Mechanics*, 27(3):403–409, 1960. doi: 10.1115/1.3644015.

[99] Charles W Hull. Apparatus for production of three-dimensional objects by stereolithography. *United States Patent, Appl., No. 638905, Filed*, 1984.

[100] Michael P Lee, Geoffrey JT Cooper, Trevor Hinkley, Graham M Gibson, Miles J Padgett, and Leroy Cronin. Development of a 3d printer using scanning projection stereolithography. *Scientific reports*, 5(1):9875, 2015. doi: 10.1038/srep09875.

[101] Zachary Zguris. How mechanical properties of stereolithography 3d prints are affected by uv curing. *Formlabs White Paper*, pages 1–11, 2016.

[102] VS Duryodhan, Shiv Govind Singh, and Amit Agrawal. Effect of cross aspect ratio on flow in diverging and converging microchannels. *Journal of Fluids Engineering*, 139(6), 2017. doi: 10.1115/1.4035945.

[103] Tianshu Liu, M Guille, and JP Sullivan. Accuracy of pressure-sensitive paint. *AIAA journal*, 39(1):103–112, 2001. doi: 10.2514/2.1276.

[104] Tianshu Liu, John P Sullivan, Keisuke Asai, Christian Klein, and Yasuhiro Egami. *Pressure and temperature sensitive paints*, volume 1. Springer, 2005. ISBN 978-3-030-68056-5.

[105] Chihyung Huang, James W Gregory, and John P Sullivan. Microchannel pressure measurements using molecular sensors. *Journal of Microelectromechanical systems*, 16(4):777–785, 2007. doi: 10.1109/JMEMS.2007.892914.

[106] Jia Li, Jing Ren, and Hongde Jiang. Film cooling performance of the embedded holes in trenches with compound angles. In *Turbo Expo: Power for Land, Sea, and Air*, volume 43994, pages 1415–1424, 2010. doi: 10.1115/GT2010-22337.

[107] Yu Matsuda, Ryota Misaki, Hiroki Yamaguchi, and Tomohide Niimi. Pressure-sensitive channel chip for visualization measurement of micro gas flows. *Microfluidics and nanofluidics*, 11 (4):507, 2011. doi: 10.1007/s10404-011-0825-2.

[108] Chih-Yung Huang, Chih-Min Lai, and Jia-Syuan Li. Applications of pixel-by-pixel calibration method in microscale measurements with pressure-sensitive paint. *Journal of Microelectromechanical Systems*, 21(5):1090–1097, 2012. doi: 10.1109/JMEMS.2012.2203106.

[109] Derek W Fultz and Jeffrey S Allen. Nonintrusive pressure measurement in microfluidic systems via backscattering interferometry. *Experiments in fluids*, 55(6):1754, 2014. doi: 10.1007/s00348-014-1754-0.

[110] Stephen Timoshenko, Sergius Woinowsky-Krieger, et al. *Theory of plates and shells*, volume 2. McGraw-hill New York, 1959. ISBN 978-0070858206.

[111] Yitshak Zohar, Sylvanus Yuk Kwan Lee, Wing Yin Lee, Linan Jiang, and PIN Tong. Subsonic gas flow in a straight and uniform microchannel. *Journal of fluid mechanics*, 472:125–151, 2002. doi: 10.1017/S0022112002002203.

[112] Shahnawaz Molla, Dmitry Eskin, and Farshid Mostowfi. Pressure drop of slug flow in microchannels with increasing void fraction: experiment and modeling. *Lab on a Chip*, 11(11): 1968–1978, 2011. doi: 10.1039/C0LC00478B.

[113] Kwanghun Chung, Hyewon Lee, and Hang Lu. Multiplex pressure measurement in microsystems using volume displacement of particle suspensions. *Lab on a Chip*, 9(23):3345–3353, 2009. doi: 10.1039/B911480G.

[114] Wuzhou Song and Demetri Psaltis. Optofluidic pressure sensor based on interferometric imaging. *Optics letters*, 35(21):3604–3606, 2010. doi: 10.1364/OL.35.003604.

[115] James L Kinsey. Laser-induced fluorescence. *Annual Review of Physical Chemistry*, 28(1): 349–372, 1977. doi: 10.1146/annurev.pc.28.100177.002025.

[116] WR Lempert and MM Koochesfahani. Molecular tagging velocimetry and thermometry. *Flow Visualization Technique and Examples*, pages 77–106, 2012. doi: 10.1142/9781848167926_0004.

[117] Masahiro Motosuke, Dai Akutsu, and Shinji Honami. Temperature measurement of microfluids with high temporal resolution by laser-induced fluorescence. *Journal of mechanical science and technology*, 23(7):1821–1828, 2009. doi: 10.1007/s12206-009-0609-8.

[118] Robin G Geitenbeek, Jeroen C Vollenbroek, Hannah MH Weijgertze, Corentin BM Tregouet, Anne-Eva Nieuwelink, Chris L Kennedy, Bert M Weckhuysen, Detlef Lohse, Alfons Van Blaaderen, Albert Van Den Berg, et al. Luminescence thermometry for in situ temperature measurements in microfluidic devices. *Lab on a Chip*, 19(7):1236–1246, 2019. doi: 10.1039/C8LC01292J.

[119] David Ross, Michael Gaitan, and Laurie E Locascio. Temperature measurement in microfluidic systems using a temperature-dependent fluorescent dye. *Analytical chemistry*, 73(17):4117–4123, 2001. doi: 10.1021/ac010370l.

[120] Peter Löw, Beomjoon Kim, Nobuyuki Takama, and Christian Bergaud. High-spatial-resolution surface-temperature mapping using fluorescent thermometry. *Small*, 4(7):908–914, 2008. doi: 10.1002/smll.200700581.

[121] J Coppeta and C Rogers. Dual emission laser induced fluorescence for direct planar scalar behavior measurements. *Experiments in Fluids*, 25(1):1–15, 1998. doi: 10.1007/s003480050202.

[122] Jun Sakakibara and Ronald J Adrian. Whole field measurement of temperature in water using two-color laser induced fluorescence. *Experiments in Fluids*, 26(1-2):7–15, 1999. doi: 10.1007/s003480050260.

[123] S Saeki and DP Hart. Investigation on yag (532) laser dyes for oil film thickness and temperature measurement. In *Proceedings of the third pacific symposium of flow visualization and image processing (Paper index number F3096)*, pages 18–21, 2001.

[124] Hui Hu, Manoochehr Koochesfahani, and C Lum. Molecular tagging thermometry with adjustable temperature sensitivity. *Experiments in Fluids*, 40:753–763, 2006. doi: 10.1007/s00348-006-0112-2.

[125] Hui Hu, Zheyan Jin, Daniel Nocera, Chee Lum, and Manoochehr Koochesfahani. Experimental investigations of micro-scale flow and heat transfer phenomena by using molecular tagging techniques. *Measurement Science and Technology*, 21(8):085401, 2010. doi: 10.1088/0957-0233/21/8/085401.

[126] Pramod Chamarthy, Suresh V Garimella, and Steven T Wereley. Measurement of the temperature non-uniformity in a microchannel heat sink using microscale laser-induced fluorescence. *International Journal of Heat and Mass Transfer*, 53(15-16):3275–3283, 2010. doi: 10.1016/j.ijheatmasstransfer.2010.02.052.

[127] F. Lanzetta and E. Gavignet. *Thermal Measurements And Inverse Techniques, Chap.3 - Temperature Measurements: Thermoelectricity and Microthermocouples*. CRC PRess, 2011. ISBN 978-1-4398-4556-1.

[128] Laurent Thiery, Nathalie Marini, Jean-Pierre Prenel, Michel Spajer, Claudine Bainier, and Daniel Courjon. Temperature profile measurements of near-field optical microscopy fiber tips by means of sub-micronic thermocouple. *International journal of thermal sciences*, 39(4): 519–525, 2000. doi: 10.1016/S1290-0729(00)00231-3.

[129] F Lanzetta, E Gavignet, P Nika, and C Meunier. Microthermocouples for the simultaneous measurements of temperature/pressure and temperature/velocity in microsystems. In *12th International Metrology Congress*, Lyon France, 2005.

[130] Mohamed Yacine Doghmane, François Lanzetta, and Eric Gavignet. Dynamic characterization of a transient surface temperature sensor. *Procedia engineering*, 120:1245–1248, 2015. doi: 10.1016/j.proeng.2015.08.840.

[131] Xugang Zhang, Hongseok Choi, Arindom Datta, and Xiaochun Li. Design, fabrication and characterization of metal embedded thin film thermocouples with various film thicknesses and junction sizes. *Journal of Micromechanics and Microengineering*, 16(5):900, 2006. doi: 10.1088/0960-1317/16/5/004.

[132] AZ Cygan, A Kardak, D Patterson, EJ Podlaha-Murphy, RV Devireddy, and MC Murphy. Modeling and fabrication of a micro thermocouple array. In *ASME International Mechanical Engineering Congress and Exposition*, volume 47756, pages 423–428, 2006. doi: 10.1115/IMECE2006-15247.

[133] Raymond A Serway. *Principles of physics - 2nd edition*. Saunders College Pub, 1998.

[134] Yves Moser and Martin AM Gijs. Miniaturized flexible temperature sensor. *Journal of Microelectromechanical Systems*, 16(6):1349–1354, 2007. doi: 10.1109/JMEMS.2007.908437.

[135] Roald M Tiggelaar, Remco GP Sanders, AW Groenland, and Johannes GE Gardeniers. Stability of thin platinum films implemented in high-temperature microdevices. *Sensors and Actuators A: Physical*, 152(1):39–47, 2009. doi: 10.1016/j.sna.2009.03.017.

[136] Frank Bernhard. *Handbuch der technischen Temperaturmessung*. Springer-Verlag, 2014. ISBN 978-3-642-24506-0.

[137] W Diehl. Platinum thin film resistors as accurate and stable temperature sensors. Technical report, 1984. URL https://ntrs.nasa.gov/api/citations/19850002015/downloads/19850002015.pdf.

[138] RP Reed. Aluminium 2. a review of deformation properties of high purity aluminium and dilute aluminium alloys. *Cryogenics*, 12(4):259–291, 1972. doi: 10.1016/0011-2275(72)90041-0.

[139] Bharat Bhushan and Zachary Burton. Adhesion and friction properties of polymers in microfluidic devices. *Nanotechnology*, 16(4):467, 2005. doi: 10.1088/0957-4484/16/4/023.

[140] Kurt E Petersen. Silicon as a mechanical material. *Proceedings of the IEEE*, 70(5):420–457, 1982. doi: 10.1109/PROC.1982.12331.

[141] Sedat Dogru, Bekir Aksoy, Halil Bayraktar, and B Erdem Alaca. Poisson's ratio of pdms thin films. *Polymer Testing*, 69:375–384, 2018. doi: 10.1016/j.polymertesting.2018.05.044.

[142] Tae Kyung Kim, Jeong Koo Kim, and Ok Chan Jeong. Measurement of nonlinear mechanical properties of pdms elastomer. *Microelectronic Engineering*, 88(8):1982–1985, 2011. doi: 10.1016/j.mee.2010.12.108.

[143] Miao Liu, Jianren Sun, Ying Sun, Christopher Bock, and Quanfang Chen. Thickness-dependent mechanical properties of polydimethylsiloxane membranes. *Journal of micromechanics and microengineering*, 19(3):035028, 2009. doi: 10.1088/0960-1317/19/3/035028.

[144] José Danglad-Flores, Stephan Eickelmann, and Hans Riegler. Deposition of polymer films by spin casting: A quantitative analysis. *Chemical Engineering Science*, 179:257–264, 2018. doi: 10.1016/j.ces.2018.01.012.

[145] Peter C. Sukanek. Dependence of film thickness on speed in spin coating. *Journal of The Electrochemical Society*, 138(6):1712, jun 1991. doi: 10.1149/1.2085860. URL https://dx.DOI.org/10.1149/1.2085860.

[146] SK Wilson, R Hunt, and BR Duffy. The rate of spreading in spin coating. *Journal of Fluid Mechanics*, 413:65–88, 2000. doi: 10.1017/S0022112000008089.

[147] John H Koschwanez, Robert H Carlson, and Deirdre R Meldrum. Thin pdms films using long spin times or tert-butyl alcohol as a solvent. *PLoS one*, 4(2):e4572, 2009. doi: 10.1371/journal.pone.0004572.

[148] ID Johnston, DK McCluskey, CKL Tan, and MC Tracey. Mechanical characterization of bulk sylgard 184 for microfluidics and microengineering. *Journal of Micromechanics and Microengineering*, 24(3):035017, 2014. doi: 10.1088/0960-1317/24/3/035017.

[149] Firdaus Prabowo, Adrian Law Wing-Keung, and Hayley H Shen. Effect of curing temperature and cross-linker to pre-polymer ratio on the viscoelastic properties of a pdms elastomer. In *Advanced Materials Research*, volume 1112, pages 410–413. Trans Tech Publ, 2015. doi: 10.4028/www.scientific.net/AMR.1112.410.

[150] Shari Farrens, S Sood, and SUSS MicroTec. Wafer level packaging: Balancing device requirements and materials properties. In *Proc. Pan Pacific Microelectron. Symp*, pages 22–24, 2014.

[151] Gerald Gerlach and Wolfram Dotzel. *Introduction to microsystem technology: a guide for students*. John Wiley & Sons, 2008. ISBN 978-0-470-05861-9.

[152] Stefan Mack. *Eine vergleichende Untersuchung der physikalisch-chemischen Prozesse an der Grenzschicht direkt und anodisch verbundener Festkörper*. VDI-Verlag, 1997. ISBN 978-3183436026.

[153] George Wallis. Field assisted glass sealing. *Electrocomponent Science and Technology*, 2(1): 45–53, 1975. doi: 10.1155/APEC.2.45.

[154] Pablo Morales Navarrete and Jie Yuan. A single-layer pdms chamber for on-chip bacteria culture. *Micromachines*, 11(4):395, 2020. doi: 10.3390/mi11040395.

[155] Xi Shu, Huiqin Liu, Yezi Zhu, Bo Cai, Yanxia Jin, Yongchang Wei, Fuling Zhou, Wei Liu, and Shishang Guo. An improved bulk acoustic waves chip based on a pdms bonding layer for high-efficient particle enrichment. *Microfluidics and Nanofluidics*, 22:1–7, 2018. doi: 10.1007/s10404-018-2052-6.

[156] Lance Kersey, Vincent Ebacher, Vahid Bazargan, Rizhi Wang, and Boris Stoeber. The effect of adhesion promoter on the adhesion of pdms to different substrate materials. *Lab on a Chip*, 9 (7):1002–1004, 2009. doi: 10.1039/B813757A.

[157] Saber Hammami, Aleksandr Oseev, Sylwester Bargiel, Rabah Zeggari, Céline Elie-Caille, and Thérèse Leblois. Microfluidics for high pressure: Integration on gaas acoustic biosensors with a leakage-free pdms based on bonding technology. *Micromachines*, 13(5):755, 2022. doi: 10.3390/mi13050755.

[158] Errong Jing, Bin Xiong, and Yuelin Wang. Low-temperature au/a-si wafer bonding. *Journal of Micromechanics and Microengineering*, 21(1):015013, 2010. doi: 10.1088/0960-1317/21/1/015013.

[159] Jie-Jun Wang, Tao Wang, Chuan-Gui Wu, Wen-Bo Luo, Yao Shuai, and Wang-Li Zhang. Highly precise ti/pt/cr/au thin-film temperature sensor embedded in a microfluidic device. *Rare Metals*, 40:195–201, 2021. doi: 10.1007/s12598-019-01301-7.

[160] Samara L Firebaugh, Klavs F Jensen, and Martin A Schmidt. Investigation of high-temperature degradation of platinum thin films with an in situ resistance measurement apparatus. *Journal of Microelectromechanical systems*, 7(1):128–135, 1998. doi: 10.1109/84.661395.

[161] J Puigcorbé, D Vogel, B Michel, A Vilà, I Gràcia, C Cané, and JR Morante. High temperature degradation of pt/ti electrodes in micro-hotplate gas sensors. *Journal of micromechanics and Microengineering*, 13(4):S119, 2003. doi: 10.1088/0960-1317/13/4/320.

[162] TC Tisone and J Drobek. Diffusion in thin film ti–au, ti–pd, and ti–pt couples. *Journal of Vacuum Science and Technology*, 9(1):271–275, 1972. doi: 10.1116/1.1316577.

[163] MP Moret, MAC Devillers, FD Tichelaar, E Aret, PR Hageman, and PK Larsen. Damage after annealing and aging at room temperature of platinized silicon substrates. *Thin Solid Films*, 434 (1-2):283–295, 2003. doi: 10.1016/S0040-6090(03)00453-X.

[164] Engin Ciftyürek, Katarzyna Sabolsky, and Edward M Sabolsky. Platinum thin film electrodes for high-temperature chemical sensor applications. *Sensors and Actuators B: Chemical*, 181: 702–714, 2013. doi: 10.1016/j.snb.2013.02.058.

[165] Aymen Zribi, Magali Barthès, Sylvie Bégot, François Lanzetta, Jean Yves Rauch, and Virginie Moutarlier. Design, fabrication and characterization of thin film resistances for heat flux sensing application. *Sensors and Actuators A: Physical*, 245:26–39, 2016. doi: 10.1016/j.sna.2016.04.040.

[166] U Schmid and H Seidel. Effect of high temperature annealing on the electrical performance of titanium/platinum thin films. *Thin Solid Films*, 516(6):898–906, 2008. doi: 10.1016/j.tsf.2007.04.128.

[167] Paul S Prevéy et al. X-ray diffraction residual stress techniques. *ASM International, ASM Handbook.*, 10:380–392, 1986.

[168] P Scherrer. Nanoscience and the scherrer equation versus the scherrer-gottingen equation. *Nach. Ges. Wiss. Göttingen*, 26(9):98–100, 1918.

[169] Monjoy Sreemany and Suchitra Sen. Effect of substrate temperature and annealing temperature on the structural, electrical and microstructural properties of thin pt films by rf magnetron sputtering. *Applied Surface Science*, 253(5):2739–2746, 2006. doi: 10.1016/j.apsusc.2006.05.040.

[170] Helcio RB Orlande, Olivier Fudym, Denis Maillet, and Renato M Cotta. *Thermal measurements and inverse techniques*. CRC Press, 2011. doi: 978-1-4398-4556-1.

[171] John David Anderson. *Hypersonic and high-temperature gas dynamics*. Aiaa, 1989. ISBN 978-1-56347-780-5.

[172] Isaak Evseevič Idel'čik. *Handbook of hydraulic resistance: coefficients of local resistance and of friction*. Israel Program for Scientific Translations, 1966. doi: 978-1-56700-251-5.

[173] J Pfahler. Gas and liquid flow in small channels, micromechanical sensors, actuators, and systems. In *ASME*, volume 32, pages 49–60, 1991.

[174] Chungpyo Hong, Taiki Nakamura, Yutaka Asako, and Ichiro Ueno. Semi-local friction factor of turbulent gas flow through rectangular microchannels. *International Journal of Heat and Mass Transfer*, 98:643–649, 2016. doi: 10.1016/j.ijheatmasstransfer.2016.02.080.

[175] Mounir Ibrahim, Meng Wang, and David Gedeon. Experimental investigation of oscillatory flow pressure and pressure drop through complex geometries. In *2nd International Energy Conversion Engineering Conference*, page 5560, 2004. doi: 10.2514/6.2004-5560.

[176] Danish Rehman, Gian Luca Morini, and Chungpyo Hong. A comparison of data reduction methods for average friction factor calculation of adiabatic gas flows in microchannels. *Micromachines*, 10(2):171, 2019. doi: 10.3390/mi10030171.

APPENDIX A:

ANALYTICAL MODELING OF THE EXPERIMENTAL SETUP

A.1 Modeling of the experimental setup

The device consists of a sealed fluidic system connecting two volumes V_1 and V_2 with the studied channel and the converging and diverging sections detailed in chapters 2 and 4. These volumes, located on either side of the channel, are made up of flexible tubes with a diameter of 5 *mm* and a length of 30 *cm*. The two 180° out-of-phase pistons that set the fluid in motion can be simulated by a displacer piston. Figure 1 shows a schematic illustration of the experimental set-up. We will call P_1 the gas pressure in the volume V_1 and n_1 the gas quantity in this volume. In the same way P_2 and n_2 will correspond to gas pressure and gas quantity in the volume V_2.

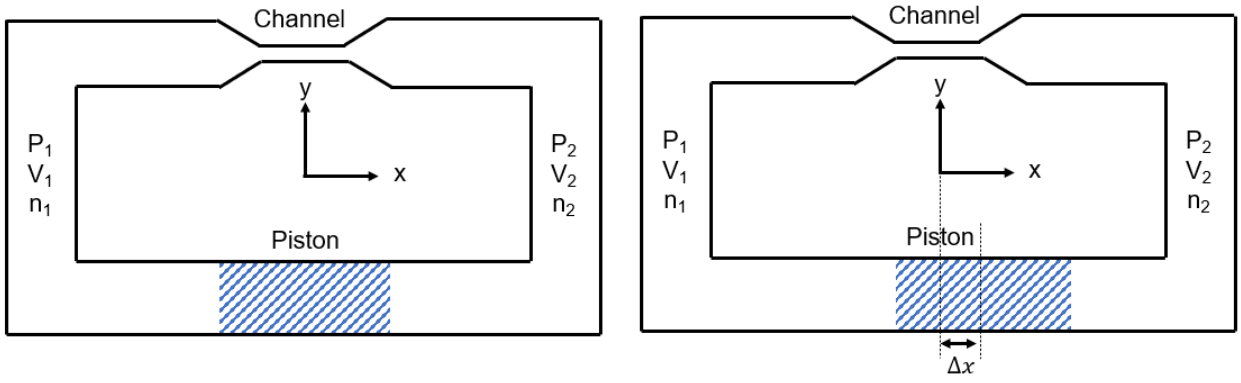

(a) $x = 0$ (b) $\Delta x > 0$

Figure 1: Schematic illustration of the experimental setup

Using ideal gas law, at each moment, we have the following equations:

$$\begin{aligned} P_1(t)\,V_1(t) &= n_1(t)\,R\,T_1(t) \\ P_2(t)\,V_2(t) &= n_2(t)\,R\,T_2(t) \end{aligned} \tag{45}$$

As the piston moves to the right in the scheme (figure 1 (b), $\Delta x > 0$), the volume V_2 decreases while the volume V_1 increases, resulting in an increase in pressure P_2 and a decrease in pressure P_1. This inequality between the pressures on either side of the channel generates a flow of gas through the channel. We assume that for $\Delta x = 0$, we have $V_1 = V_2 = V_0$. Therefore, the two volumes V_1 and V_2 can be expressed as:

$$\begin{aligned} V_1(t) &= V_0 + \Delta V(t) \\ V_2(t) &= V_0 - \Delta V(t) \end{aligned} \tag{46}$$

We will also assume that at each moment, a quantity Δn enter in the channel and the same quantity exit the channel (no gas is stored in the channel). Therefore, the gas quantity n_1 and n_2 in each volume separated by the channel can be expressed as:

$$\begin{aligned} n_1(t) &= n_0 + \Delta n(t) \\ n_2(t) &= n_0 - \Delta n(t) \end{aligned} \tag{47}$$

A.2 Relation between ΔP, ΔV and Δn

The pressure drops ΔP is given by:

$$\Delta P(t) = P_1(t) - P_2(t) = \frac{n_1(t) R T_1(t)}{V_1(t)} - \frac{n_2(t) R T_2(t)}{V_2(t)} \tag{48}$$

By using 46 and 47, this equation can be expressed as follows:

$$\Delta P(t) = R\left(T_1 \frac{n_0 + \Delta n(t)}{V_0 + \Delta V(t)} - T_2 \frac{n_0 - \Delta n(t)}{V_0 - \Delta V(t)}\right) \tag{49}$$

To simplify the model, we will consider isothermal flow as an initial approach, $T_1 = T_2 = T_0$. Therefore, the equation 49 becomes:

$$\Delta P(t) = 2\,R\,T_0\left(\frac{n_0\,\Delta V(t) - \Delta n(t)\,V_0}{V_0^2 - \Delta V^2(t)}\right) \tag{50}$$

Dividing the expression 50 by V_0^2, it can be expressed as follows:

$$\Delta P(t) = 2\,P_0 \frac{\frac{\Delta V(t)}{V_0} - \frac{\Delta n(t)}{n_0}}{1 - [\frac{\Delta V}{V_0}]^2} \tag{51}$$

To simplify the expression of the above equation, we will note:

$$\Delta P^*(t) = \frac{\Delta P(t)}{P_0} \qquad \Delta V^*(t) = \frac{\Delta V(t)}{V_0} \qquad \Delta n^*(t) = \frac{\Delta n}{n_0}$$

Finally, the equation 51 can be simplified with the following expression:

$$\boxed{\Delta P^*(t) = 2\frac{\Delta V^*(t) - \Delta n^*(t)}{1 - \Delta V^{*2}(t)}} \tag{52}$$

Since ΔV^* is given by the movement of the piston, this equation describes the relationship between the pressure drop ΔP^* and the variation of gas quantity Δn^*.

To determine $\Delta n(t)$ and $\Delta P(t)$, we will need another equation, which will be given by the relationship between pressure and flow velocity.

A.3 Relation between ΔP and U

The relation between pressure gradient and velocity was determined by the model used by Womersley [75] to characterize blood flow in arteries.

Considering an incompressible flow in a circular channel, the velocity verify the following equation:

$$\frac{\partial^2 U}{\partial r^2} + \frac{1}{r}\frac{\partial U}{\partial r} + \frac{\rho(P_1 - P_2)}{\mu l} = \frac{\rho}{\mu}\frac{\partial U}{\partial t} \tag{53}$$

The term with pressure gradient $\frac{P_1 - P_2}{L_{ch}}$ is the one responsible of the gas flow, while the term $\frac{1}{\nu}\frac{\partial U}{\partial t}$ correspond to the contribution of unsteadiness and is due to the fact that in our cases, velocity and pressure vary over time.

Since in our cases, the piston movement, we can assume that the variation of both pressure and velocity can be expressed as sinusoidal function. Therefore, in the following, we will focus only on periodic function of time. This will allow to decompose our functions into Fourier series. By finding the solution for a harmonic excitation at an angular frequency ω, we will be able to find all periodic solution to the problem.

Assuming that the pressure drops is sinusoidal, at a pulsation ω:

$$\Delta P(t) = P_0 B e^{i\omega t} \tag{54}$$

By resolving the equation 53, we obtain Bessel function and the flow velocity in the channel can be expressed as:

$$U(y,t) = \frac{1}{i\omega\rho l}\left[1 - \frac{J_0(Woyi^{3/2})}{J_0(Woi^{3/2})}\right]\Delta P(t) \tag{55}$$

By integrating the velocity over a section of the channel, we obtain the volume flow rate $\dot{V(t)}$. This gives the flow rate, which is expressed as the product of a complex coefficient dependent on frequency and the pressure drops function $\Delta P(t)$:

$$\boxed{\dot{V}(t) = \frac{\pi R^2}{i\omega\rho l} F(\omega)\Delta P(t)} \tag{56}$$

with $F(\omega) = 1 - \frac{2\alpha i^{3/2}}{\alpha^2 i^3} \frac{J_1(\alpha i^{3/2})}{J_0(\alpha i^{3/2})}$ and $Wo = R_h \sqrt{\frac{\omega}{\nu}}$.

Bessel functions make the calculation more complex, but since in our case the condition $Wo \ll 1$ will generally apply, we can use a decomposition of these functions into powers of Wo limited to the first terms with good precision. By developing Bessel functions for arguments that remain weak when $Wo \ll 1$, we find:

$$F(\omega) = \frac{iWo^2}{8}(1 - i\frac{Wo^2}{6} - \frac{5Wo^4}{384} + ...) \tag{57}$$

This approximation remains sufficiently accurate only when the condition $Wo \ll 1$ is met.

A.4 Expression of $\Delta n(t)$

We divide the surface S on which the gas flow exit the channel into a multitude of surfaces dS (which are not all subject to the same air velocity, since U depends on y). The air molecules added through dS during time dt to volume V_1 were previously contained in a cylinder of volume (U.dt).dS. If ρ is the density of air, then the mass added during time dt through dS will be $dm = \rho(U.dt)dS$. Dividing this mass dm by the molar mass of the air M, we obtain the number of moles added:

$$dn = \frac{dm}{M} = \frac{\rho(U.dt).dS}{M} \tag{58}$$

By integrating over the surface, we obtain the number of moles crossing this surface during dt and to know the total number of moles added between t_1 and t_2, we must also integrate dn over the duration $\Delta t = t_2 - t_1$. This gives:

$$\Delta n(t) = \frac{\rho}{M} \int_{\Delta t} \int_S U.dS.dt = \frac{\rho}{M} \int_{\Delta t} \dot{V}_\omega(t)dt \tag{59}$$

with $\dot{V}_\omega(t) = \int_S U(t).dS$ correspond to the flow rate integrated on the surface at time t (*cf.* equation 56).

With the pulsation ω being equal to $\frac{\nu Wo^2}{R^2}$ and that $\mu = \rho\nu$, flow rate can be expressed:

$$\dot{V}_\omega(t) = \frac{\pi R_h^4}{\mu L_{ch}} \frac{F(\omega)}{iWo^2} \Delta P(t) \tag{60}$$

N.B.: We can notice that when $\omega \to 0$, we have $\frac{F(\omega)}{iWo^2} \to \frac{1}{8}$ and $\dot{V}_0(t) = \frac{\pi R_h^4}{8\mu L_{ch}} \Delta P(t)$ which correspond to the Poiseuille's formula valid for a steady flow.

Therefore, flow rate can be written as:

$$\dot{V}_\omega(t) = \dot{V}_0 \left(1 - i\frac{Wo^2}{6} - \frac{5Wo^4}{384} + ...\right) \Delta P(t) \tag{61}$$

By replacing the expression of flow rate 61 in the equation 59 and keeping in mind that $\Delta P(t) = P_0 B e^{i\omega t}$, we get the expression for $\Delta n(t)$:

$$\frac{\Delta n(t)}{n_0} = \frac{\pi R_h^4}{\mu V_0 L_{ch}} \frac{F(\omega)}{iWo^2} \frac{\Delta P(t)}{i\omega} + C_n \tag{62}$$

Since the mean value over time of $\Delta n(t)$ is equal to 0, this results in $C_n = 0$. Therefore, $\Delta n(t)$ can be expressed:

$$\frac{\Delta n(t)}{n_0} = \frac{\pi R_h^4}{\mu V_0 L_{ch}} \frac{F(\omega)}{iWo^2} \frac{\Delta P(t)}{i\omega} \tag{63}$$

which can be simplified:

$$\boxed{\frac{\Delta n(t)}{n_0} = -iKG(\omega)\frac{\Delta P(t)}{P_0}} \tag{64}$$

with $K = \frac{\pi R_h^4 P_0}{8\mu V_0 L_{ch}}$ and $G(\omega) = \frac{1}{\omega}(1 - i\frac{Wo^2}{6} - \frac{5Wo^4}{384} + ...)$

With equation 52 and 64, we are now able to calculate the gas quantity $\Delta n(t)$ as well as the pressure drops $\Delta P(t)$ in the channel.

A.5 Determination of $\Delta P(t)$

In equation 52, the quantity $\frac{\Delta V(t)}{V_0}$ will always be assumed to be sinusoidal at pulsation ω. In the denominator of this equation, the term $\frac{DeltaV(t)}{V_0}$ is squared and will therefore produce a term at pulsation 2 ω, which multiplied by $\Delta P(t)$ will produce a term at pulsation 3 ω for $\Delta n(t)$. Moreover, if we assume that $\Delta P(t)$ contains a term at pulsation 2 ω, the equation 52 shows that this term must necessarily be zero.

Finally, it is reasonable to assume that $\Delta P(t)$ and $\Delta n(t)$ can be expressed, as a first approximation, by a Fourier development limited to pulsations ω and 3 ω.

$$\begin{aligned} \Delta V^* &= A_1 e^{i\omega t} \\ \Delta P^* &= B_1 e^{i\omega t} + B_3 e^{3i\omega t} \\ \Delta n^* &= N_1 e^{i\omega t} + N_3 e^{3i\omega t} \end{aligned} \tag{65}$$

By balancing the terms oscillating at the same pulsation in the equation 52, we obtain:

$$\begin{aligned} B_1 &= 2(A_1 - N_1) \\ B_3 &= A_1^2 B_1 - 2N_3 \end{aligned} \tag{66}$$

By doing the same with equation 64, we obtain:

$$\begin{aligned} N_1 &= -iKB_1 G(\omega) \\ N_3 &= -iKB_3 G(3\omega) \end{aligned} \tag{67}$$

Therefore, we can determine the terms in the expression of ΔP^* and Δn^*:

$$\begin{cases} B_1 = \frac{2A_1}{1-2iKG(\omega)} \\ B_3 = \frac{2A_1^3}{(1-2iKG(\omega))(1-2iKG(3\omega))} \\ N_1 = \frac{-2iA_1KG(\omega)}{1-2iKG(\omega)} \\ N_3 = \frac{-2iA_1^3KG(3\omega)}{(1-2iKG(\omega))(1+2iKG(3\omega))} \end{cases} \tag{68}$$

Figures 2 to 3 show a comparison between experimental pressure drops measured and the variation of ΔP obtained analytically. The model shows some same trends as those observed experimentally. We can observe analytically that the phase shift between pressure drop and the flow displacement (caused by the movement of the piston) increased as frequency increased in the same way as observed experimentally. The increase in the amplitude of pressure drop variations with increasing frequency is also found analytically. Nevertheless, we can observe differences between the values obtained analytically and those obtained experimentally. The most probable explanation could be due to the missing contribution of both convergent and divergent sections in the model, while experimentally we have observed that the contributions of these sections increased with the flow rate and should not be neglected. The other contribution which could explain the differences observed could be due to the converging and diverging sections, which have shown large contribution for steady flows and that were not modeled here, due to a lack of results on this matter with alternating flows. Moreover, analytical results were obtained in the case of circular channel, while our channels could be considerably impacted by their shape and specifically by their aspect ratio as it have been highlighted in chapter 4.

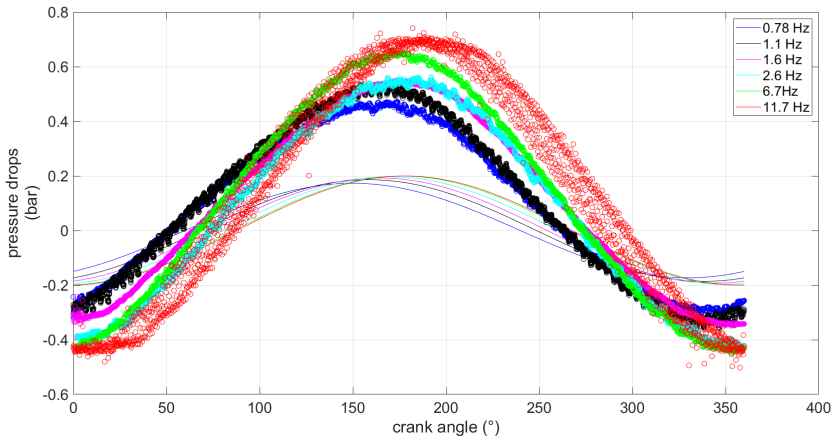

Figure 2: Comparison between analytical model (straight lines) and experimental values (circles) for the channels with $D_h = 200\ \mu m$, $\alpha = 0.3$, $L_{ch} = 25\ mm$ for several frequencies.

Figure 4 shows the amplitude of pressure drops versus frequency. We can observe that analytically pressure drops are bounded by a maximum. Beyond a frequency depending on channel dimensions, the channel acts as if it were plugged, the flow rate is no longer enough to allow the fluid to flow

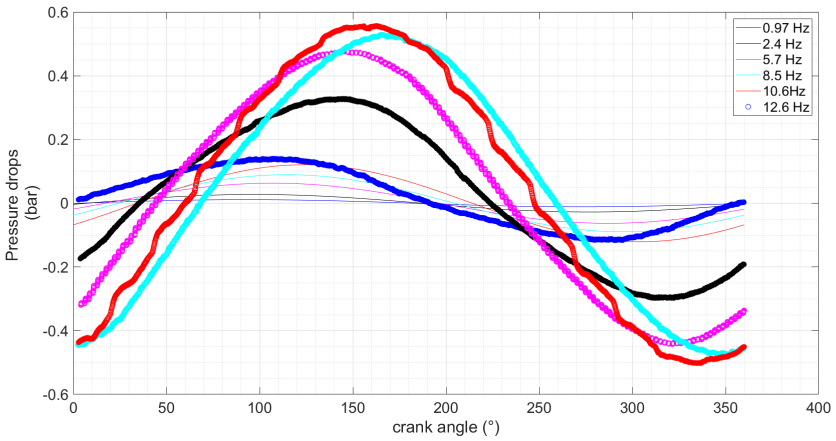

Figure 3: Comparison between analytical model (straight lines) and experimental values (circles) for the channels with $D_h = 500\ \mu m$, $\alpha = 0.6$, $L_{ch} = 25\ mm$ for several frequencies.

through the channel. As previously mentioned these pressure drops are inversely proportional to R_h^4. This is why, for the smallest channels, even at a low frequency, the pressure drops are significantly important. Moreover, the expression of B_1 and B_3 obtained in equation 68, shows that pressure drops maximum, obtained for $f \to \infty$ is equal to $2A_1$, cannot exceed twice the relative displaced volume $\Delta V/V_0$. Since the relative volume displaced was in our experiments around 10 % (piston stroke is equal to 3 *cm* and pipe volume on both side of the channel is around 30 *cm*), it is expected to obtain maximum of pressure drops around 0.2 *bar*.

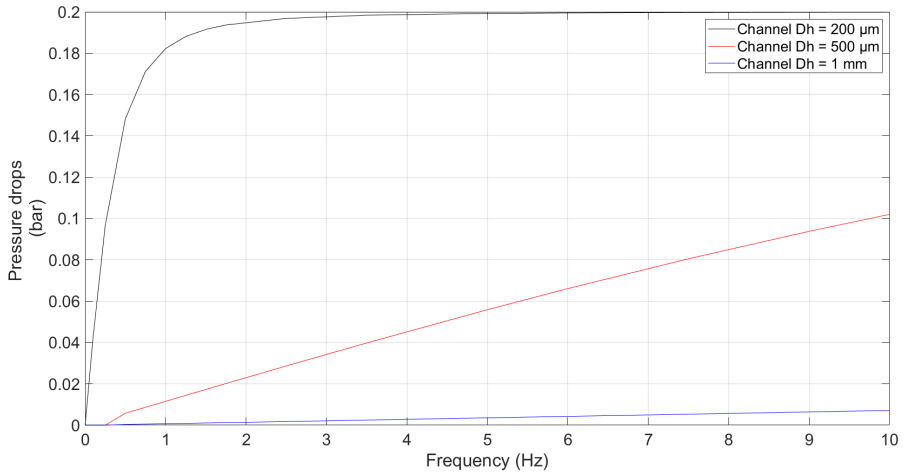

Figure 4: Analytical pressure drops versus frequency

APPENDIX B:

NUMERICAL MODELING OF THE EXPERIMENTAL SETUP

Numerical simulations were carried out prior to sizing the devices. These simulations provided a quantitative approach to the problem, enabling us to properly size the pressure and temperature sensors that we wanted to implement in the channel. These numerical simulations were carried out by Mr. Abdelhamid Blidia, an intern supervised as part of this thesis, using Ansys Fluent software. Figure 1 shows the geometry which was studied numerically. This includes channels as well as converging and diverging sections upstream and downstream of the channels. Although the dimensions of the system are not the same as those selected in the end for our channels and converging / diverging sections, this still allows us to determine overall trends.

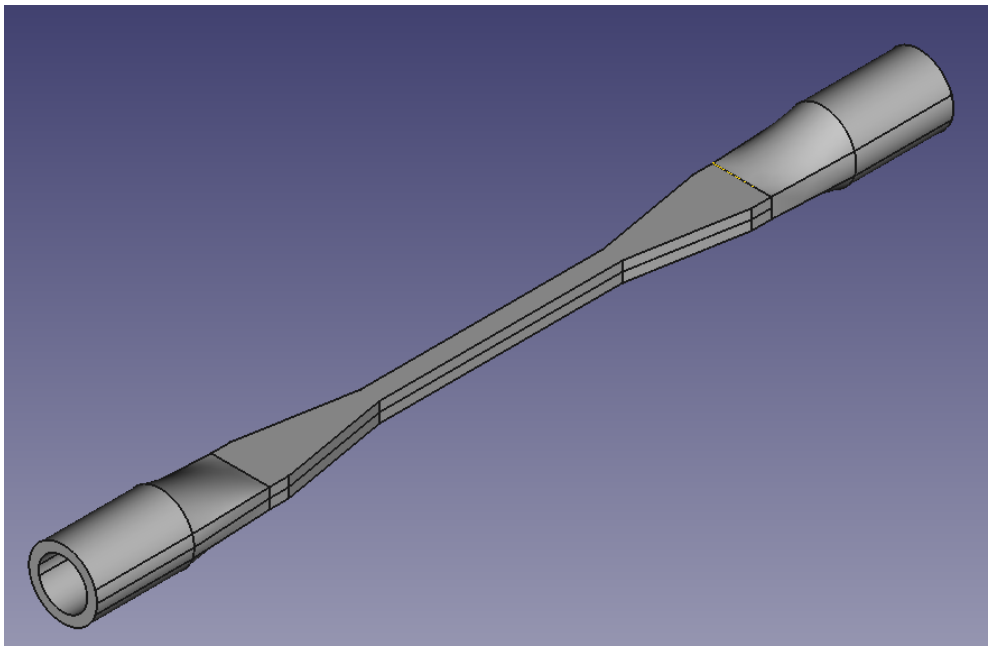

Figure 1: Numerical modelisation of channels and converging / diverging sections

B.1 Modeling of the experimental setup

B.1.1 Model

The study domain is divided into 7 parts: the two circular sections located at the ends of the domain, the two converging and diverging sections enabling the transition from a circular to a rectangular section, the two other converging and diverging sections implemented on the device realized by microfabrication techniques and the microchannel located in the center. The ends of the domain represent the location where pressure and temperature measurements are taken on the experimental bench.

Geometries with different roughness have been investigated numerically. To this extend, geometries were done with 3D max software. First smooth channel is done, then a "noise" function is applied allowing to create irregularities on the wall. Fig. 2 shows the different roughness simulated.

The simulations were carried out with a model without any slip boundary conditions. For steady flow, laminar model was used for straight channels, while for channels with bends, a k-Ω SST was used due to its better consideration of disturbance of flow near the bends. As for alternating flow, standard k-ε model was used. Viscous dissipation was added in the energy equation in order to take into account its contribution on the flow.

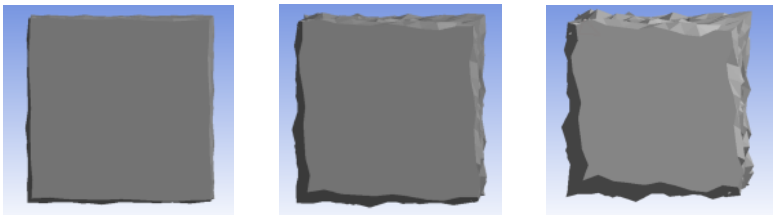

(a) (b) (c)

Figure 2: Different relative roughness simulated. (a) 2%, (b) 5%, (c) 8%

B.1.2 Fluid properties

Since the fluid used for both steady and alternating flows is gas, fluid properties calculation is important. Therefore, we have chosen the same expression of these properties as the one that were used in the experimental section.

- Density ρ have been calculated using the ideal gas state law
- Specific heat ratio C_P was determined using a temperature dependant polynomial law
- Thermal conductivity was obtained with law from kinetic theory as a function of the temperature
- Viscosity was also with law from kinetic theory as a function of the temperature

B.1.3 Mesh

Regarding the meshing of the study domain, a tetrahedral mesh structure with boundary layers applied close to the wall was adopted for the microchannel part, while a hexahedral mesh structure was generated for the ends of the domain in the case of alternating flow.

B.1.4 Boundary conditions

- Steady flow

  Regarding steady flows, the boundary conditions imposed are the following:

  - Inlet: Velocity and temperature imposed, the velocity corresponds to the range of flow rate tested in the experimental part
  - Outlet: Pressure and temperature imposed
  - Wall: adiabatic or isotherm conditions have both been tested
  - Symmetry: for straight channels only a quarter of the geometry have been simulated while for channels with bends a half of the geometry had to be simulated

- Alternate flow

  Regarding alternate flows, the boundary conditions imposed rigid wall at both ends of the device with a given temperature and velocity to model the displacement of pistons. The velocity was estimated with the range of frequency tested in the experimental part. The boundary conditions of channel's wall were still simulated with adiabatic or isotherm conditions.

B.2 Analysis of the results

B.2.1 Steady flow

As far as regular flows are concerned, the aim of these simulations is to validate that the models chosen for simulation are in good agreement with the experimental set-up.

1. Aspect ratio

   The influence of aspect ratio was investigated numerically for channels with hydraulic diameter of 200 μm and aspect ratio varying between 0.02 and 1. Fig. 3 shows the pressure drop and friction factor as function of Reynolds number for channels with different aspect ratio.

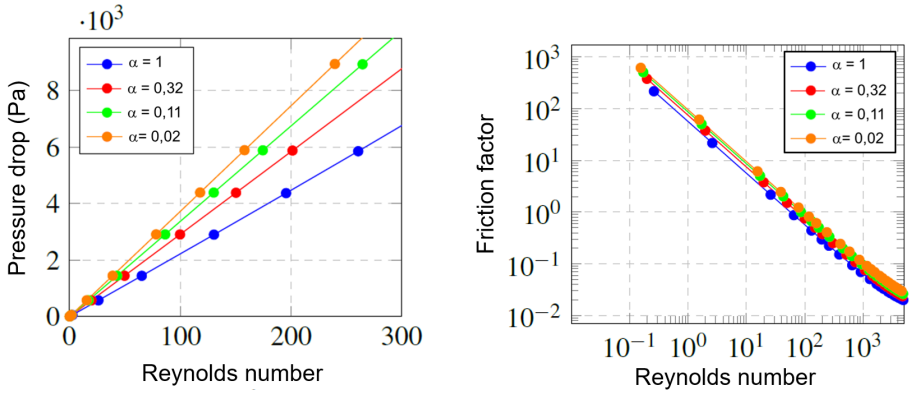

(a) (b)

Figure 3: (a) Pressure drop and (b) friction factor versus Reynolds number for channels with hydraulic diameter of 200 μm and different aspect ratio.

An increase in pressure drop and friction coefficient can be seen as the aspect ratio decreases. This variation could be due to the fact that decreasing the aspect ratio flattens the parabolic velocity profile. In fact, in the case of microchannels with a square cross-section, the velocity profiles are identical in the two directions perpendicular to the flow (x and y), whereas in the case of microchannels with a rectangular cross-section, whose aspect ratio is lower, a flatter profile can be observed in the y direction for which the dimension is the lowest, which may explain the increase in the pressure drop obtained ΔP, since friction forces increase when the velocity gradient at the wall increases, which is the case for flattened profiles.

According to this numerical result, the pressure difference ΔP should also increase with the decreasing aspect ratio for alternating flows. However, experimentally, for alternating flow, the opposite behaviour was observed with a decrease of ΔP with the decreasing aspect ratio, which was explained by the difference of cross-section which changes the velocity of the flow for a given frequency and therefore the friction behavior of the flow. This reveals that further numerical investigations on alternating flow are required to explain with absolute confidence the experimental observations that were made.

2. Channel roughness

The influence of channel roughness on the flow characteristics was investigated with relative roughness ranging from 0% to 8% for channels with hydraulic diameter of 200 μm. Fig. 4 shows pressure drops and friction factor as function of the Reynolds number for different relative roughness. Channel with relative roughness of 2% showed friction factor 5% higher compared to smooth channels while channel with relative roughness of 5% had friction factor 13% higher. This was consistent with the studies of various authors such as Wu *et al.* (1983), Acosta *et al.* (1985) and Xu *et al.* (2000).

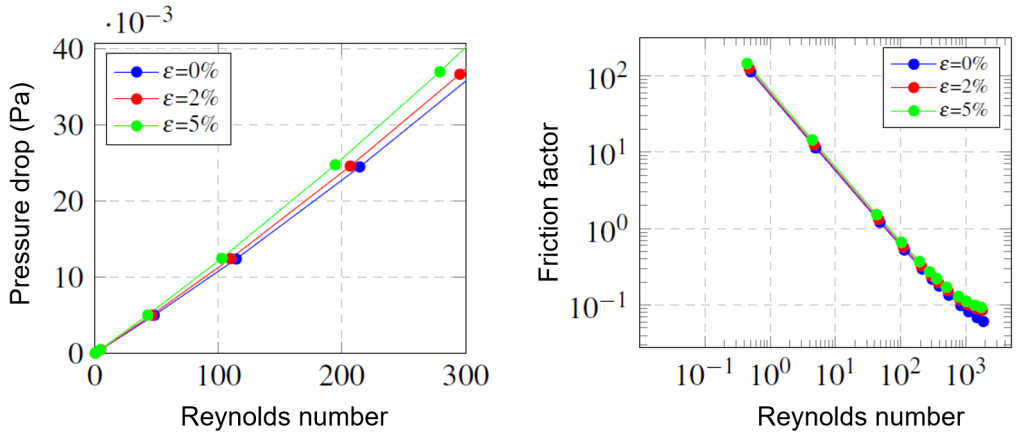

Figure 4: (a) Pressure drop and (b) friction factor versus Reynolds number for channels with hydraulic diameter of 200 μm and different relative roughness

3. Inlet temperature

While the experimental study in this thesis did not focus on the heat transfer aspects involved in these flows, numerical investigations were carried out to determine in particular the influence

of inlet temperature. The thermal boundary condition applied for these simulations was to consider adiabatic wall. Fig. 5 shows the product of friction factor and Reynolds number C_f.Re and heat transfer coefficient as function of the Reynolds number.

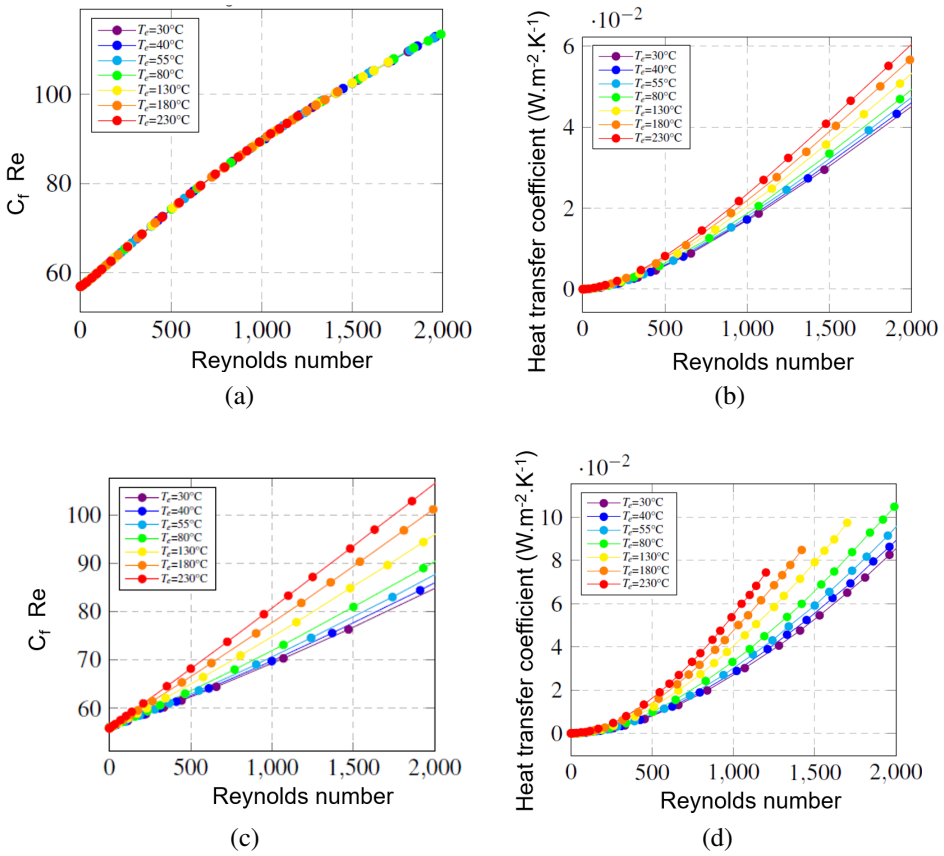

Figure 5: (a) C_f. Re and (b) heat transfer coefficient for the channel with hydraulic diameter equal to 1 mm and aspect ratio of 1. (c) C_f. Re and (d) heat transfer coefficient for the channel with hydraulic diameter equal to 100 μm and aspect ratio of 1.

We can observe that C_f.Re increased for the channel with hydraulic diameter of 100 μm with the increasing inlet temperature, while for the channel with hydraulic diameter of 1 mm, no significant variation was observed. Furthermore, an increase in the parietal heat transfer coefficient is also observed with increasing inlet temperature for both hydraulic diameters, with a greater variation for Dh = 100 µm than for Dh = 1 mm.

The increase in friction factor and parietal heat transfer coefficient is mainly due to the viscous dissipation of energy in thermal form, and to compressibility effects. Indeed, gas friction with the wall converts pressure energy into thermal energy, and in the case of an adiabatic wall, this energy is absorbed by the fluid either in the form of kinetic energy, which translates into a local acceleration of the fluid, or in the form of thermal energy, which is reflected in an increase in fluid temperature. This explains the increase in both velocity and temperature along the microchannel.

4. Contribution of converging and diverging sections

The contribution of converging and diverging sections, which was otherwise observed experimentally to be significant for moderate Reynolds number, was studied numerically. We recall that pressure drops due to converging or diverging sections can be expressed as:

$$\Delta P = \frac{1}{2}\zeta \rho U^2$$

with ΔP the pressure drops, ζ the minor loss coefficient, ρ the fluid density and U the mean cross-sectional velocity.

Fig. 6 shows the variation of minor loss coefficient for the converging and diverging sections as function of the Reynolds number for the different channel configuration simulated.

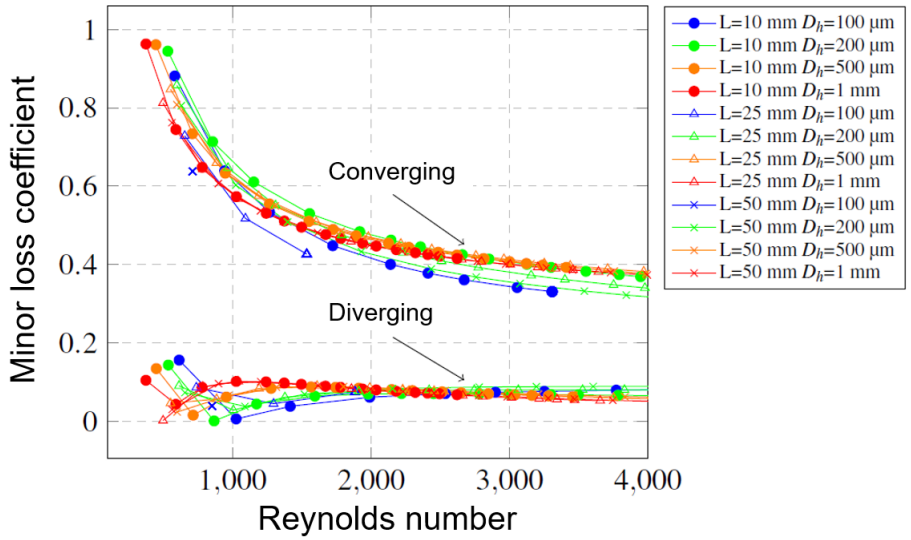

Figure 6: Minor loss coefficient for converging and diverging section versus Reynolds number

We can observe a slight variation of minor loss coefficient as hydraulic diameter vary. At low Reynolds number, the minor loss coefficient is higher for lower hydraulic diameter, while at higher Reynolds number, the minor loss coefficient is lower for lower hydraulic diameter. We can also observe that the coefficient approaches a limit value as the Reynolds number increases. For converging section, the coefficient tend to the limit value of 0.3, while for diverging section, the limit value seems to be equal to 0.1.

In comparison with the literature and for the same cross-section ratio and converging / diverging angle, the authors found experimental values on the macroscopic scale [12] slightly lower than the results obtained in the numerical simulation (ζ_{conv} = 0.28 and ζ_{div} = 0.08).

B.2.2 Alternating flow

Regarding alternating flow, due to excessive computation time, only flow modelling for a channel with a hydraulic diameter of 100 μm and an aspect ratio of 1 and for only one flow frequency (10 Hz) was simulated. In addition, only a quarter period could be simulated. Variations in the various parameters are shown in Fig. 7.

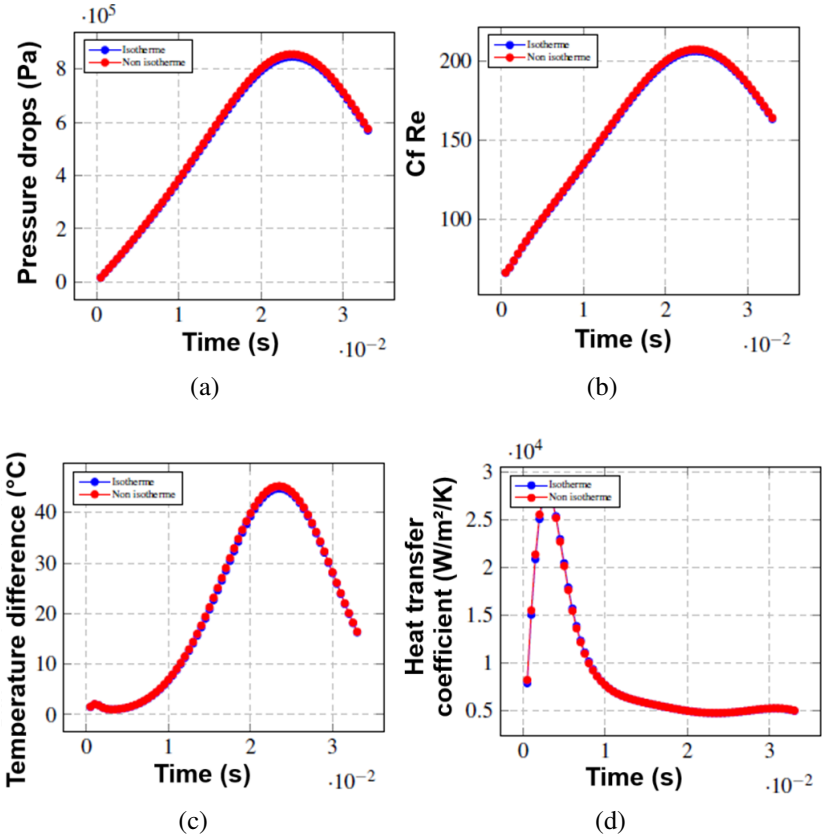

Figure 7: Time variation of (a) pressure drop, (b) C_f Re, (c) temperature difference and (d) heat transfer coefficient for an alternating flow in a channel with hydraulic diameter of 100 μm and aspect ratio of 1.

Although it was not possible to model the entire period of flow oscillation, it was possible to calculate a coefficient of friction based on the notion of RMS value, which seems much more relevant when characterizing alternating flows.

$$(C_f\ Re)_{eff} = \frac{(C_f\ Re)_{max}}{\sqrt{2}}$$

This effective friction coefficient was then compared with the friction coefficient values obtained for steady flow. For an RMS value of Reynolds number equal to 2012.9, we obtained $(C_f\ Re)_{eff} =$ 146.5, while for steady flows in the same channel configuration, $(C_f\ Re)_{std}$ = 105.2 was obtained at a Reynolds number of 2012. A higher coefficient of friction was therefore observed for alternating flow than for steady flow.

This numerical result must be set alongside the observations made experimentally on the comparison between permanent flow and alternating flow for a given flow rate (it should be remembered, however, that the flow rates obtained in alternating flow are based on rough estimations). The comparison showed that for alternating flows, pressure differences ΔP were higher than for steady flows at a given flow rate. Therefore, alternating flow seems to have higher friction contributions than steady flow in agreement with the numerical results.

These results should be completed with further simulations especially on alternating flow in order to bring better understanding of the experimental part.

Titre : Design, modélisation, fabrication et caractérisation d'un micro dispositif pour l'étude des écoulements alternés - application à la récupération et la conversion d'énergie

Mots clés : Ecoulements alternés, microfabrication, sonde Platine, membrane PDMS, récupération d'énergie.

Résumé : Cette thèse porte sur l'étude d'écoulements alternés au sein de canaux de dimensions milli- et sub-millimétriques. Ces travaux visent à contribuer à l'optimisation d'une machine miniature (dimensions sub-millimétriques) de récupération et de conversion d'énergie basse température (T < 200 ° C) basée sur le principe du cycle de Stirling. Ceci s'inscrit dans le contexte de valorisation de la chaleur perdue basse température encore non exploitée dans de nombreux milieux industriels. Dans les machines de type Stirling, les écoulements du fluide de travail sont alternés. Bien que ces écoulements soient assez bien connus à l'échelle macroscopique, ils le sont très peu à échelle milli et sub-millimétrique. Or une bonne compréhension de ce type d'écoulement à ces échelles est primordiale lors des phases de dimensionnement et design des machines. Afin de contribuer à la caractérisation des écoulement alternés à ces petites échelles, des canaux dont les dimensions sont proches de celles de la machine miniature ont été réalisés par des moyens technologiques de microfabrication au sein de la centrale technologique MIMENTO de l'Institut FEMTO-ST. Les canaux réalisés ont un diamètre hydraulique variant entre 200 μm et 1 *mm*, un rapport d'aspect compris entre 0.1 et 1 et deux longueurs de canal différentes (25 *mm* et 50 *mm*). Des canaux avec des coudes ont également été réalisés afin d'étudier leur influence sur les caractéristiques de l'écoulement. Ces canaux ont ensuite été implémentés sur le banc expérimental. Dans un premier temps, l'étude a porté sur la caractérisation des écoulements permanents, dans la gamme de Reynolds de 15 à 510, dont les résultats, en accord avec ceux issus de la littérature, ont servi de référence pour l'étude d'écoulements alternés, menée par la suite dans une gamme de Womersley allant de 0.02 à 0.67. La caractérisation des écoulements alternés a permis de déterminer que le rapport d'aspect et le diamètre hydraulique (bien que l'influence de ce dernier n'ait pu être déterminée séparément de l'influence du rapport d'aspect) des canaux affectent significativement l'écoulement. D'autre part, les travaux issus de cette thèse ont montré que les influences sur les caractéristiques de l'écoulement de la longueur du canal et de la présence de singularités (coudes) ne semblent pas aussi déterminantes qu'attendu. Par conséquent, parmi les paramètres testés au cours de cette thèse, le rapport d'aspect et le diamètre hydraulique des canaux sont des paramètres importants à prendre en compte dans le design de la micro machine Stirling, notamment afin de ne pas impacter considérablement son efficacité.

Title: Design, modeling, fabrication, and characterization of a micro-device for the study of alternating flow - Application to energy harvesting and conversion

Keywords: Alternating flows, microfabrication, Platinum probe, PDMS membrane, Energy harvesting

Abstract: This thesis focuses on the study of alternating flows within milli- and sub-millimeter-sized channels. The aim is to contribute to the optimization of a miniature (sub-millimeter dimensions) low-temperature (T < 200 ° C) energy recovery and conversion machine based on the Stirling cycle principle. This is in line with the recovery of waste heat which is still not exploited in many industrial environments. In Stirling-type engines, the working fluid flows in alternating directions. Although these flows are fairly well understood on a macroscopic scale, very little is known about them on milli and sub-millimeter scales. However, a good understanding of this type of flow at these scales is essential for engine dimensioning and design. In order to contribute to the characterization of alternating flows at these small scales, channels with dimensions close to those of the miniature machine were produced using microfabrication technology. The channels produced have a hydraulic diameter ranging from 200 μm to 1 *mm*, an aspect ratio between 0.1 and 1, and two different channel lengths (25 *mm* and 50 *mm*). Channels with bends were also built to study w their influence on flow characteristics. These channels were then implemented on the experimental bench. Initially, the study focused on the characterization of permanent flows, in the Reynolds range from 15 to 510, whose results, in agreement with those from the literature, served as a reference for the study of alternating flows, carried out in a second step with a Womersley number ranging from 0.02 to 0.67. The characterization of alternating flows has shown that the aspect ratio and hydraulic diameter (although the influence of the latter could not be determined separately from the influence of the aspect ratio) of the channels significantly affect the flow. On the other hand, work from this thesis has shown that the influences on flow characteristics of channel length and the presence of singularities (bends) do not appear to be as decisive as expected. Consequently, among the parameters tested in this thesis, the aspect ratio and hydraulic diameter of the channels are important parameters to take into account in the design of the micro Stirling machine, particularly so as not to impact its efficiency considerably.